Deliverable 1.25

PI-based assessment (application) on the results of WP2-WP4 for 20 MW wind turbines

September 2017

Agreement n.:	308974
Duration	November 2012 – October 2017
	DTU Wind

The research leading to these results has received funding from the European Community's Seventh Framework Programme under grant agreement

Document Name:	**PI-based assessment (application) on the results of WP2-WP4 for 20 MW wind turbines**
Document Number:	**Deliverable 1.25**
Author:	**P. Chaviaropoulos (NTUA)** **F. Rasmussen, A.B. Abrahamsen, D. Conti, A. Natarajan (DTU)** **G. Roukis, A. Makris (CRES)** **L. Sartori, F. Bellini, A. Croce (POLIMI)** **H. Polinder (TUD)** **D. Kaufer (RAMBOLL)** **J.A. Armendariz (CENER)** **A. Kumar (GL-GH now DNV-GL)** **D. Powell, P. Todd, R. Clark (Magnomatics)**
Document Type	Report
Dissemination level	PU
Review:	**P. Chaviaropoulos**
Date:	**September 2017**
WP:	**WP1: Conceptual Design**
Task:	**Task 1.2: Assessment of Innovation at the Subsystems Level**
Approval:	Approved by WP Leader

TABLE OF CONTENTS

(Innwind.EU, Deliverable 1.25, PI-based Assessment of 20MW Wind Turbines)

(Innwind.EU, Deliverable 1.25, PI-based Assessment of 20MW Wind Turbines)

LIST OF FIGURES & TABLES

(Innwind.EU, Deliverable 1.25, PI-based Assessment of 20MW Wind Turbines)

(Innwind.EU, Deliverable 1.25, PI-based Assessment of 20MW Wind Turbines)

CHAPTER 1   INTRODUCTION

1.1   Scope and Objectives

The objective of this report is to summarise and evaluate the main innovative concepts proposed by the technical Work-Packages 1 to 4 for turbines rated at 20MW. The evaluation is prioritizing the best innovations on the basis of the performance indicators (PIs) proposed in Deliverable D1.22. A similar work for 10MW turbines has been presented in D1.24.

Following the SMART Description of the present deliverable the innovative concepts that would be evaluated at the components level were expected to include:

- A minimum of one solution for blade aerodynamic design (WP2)
- A minimum of one solution for blade structural design (WP2)
- At least one drivetrain solution (super conducting or pseudo direct drive), as described in WP3
- At least one concept for the fixed substructure (WP4)

The 20MW innovative concepts shall be compared against a 20MW Reference Wind Turbine which derived through the upscaling of the 10MW with proper adjustments. The definition of the 20MW RWT is also part of D1.25 which is presented in the companion report D1.25a entitled "20 MW Reference Wind Turbine, Aeroelastic data of the onshore version" [1]. The same document provides indicative loads for the design of the 20MW jacket.

Preparatory work has been also done for the reliability assessment accounting for correlation and system effects, and the implication on reduction of the number of inspections needed if the support structures are designed with reduced safety factors and reduced material consumption. This part of work is reported in the companion D1.25b [2].

Five innovative concepts covering the above SMART expectations are presented and discussed in the present document. The deliverable is concluded with a comparison of the PIs [3] derived for the proposed innovative concepts against the PIs of the reference design. The emphasis is put on the Levelized Cost of Electricity (LCOE) and its main entries researched in INNWIND.EU, CAPEX, OPEX and Capacity Factor. Before any PI evaluation, each concept is assessed for its structural integrity and its cost performance following the procedures described in Deliverable D1.23.

1.2   Challenges in Designing for 10-20MW

Designing offshore wind turbines in the 10-20MW scale is pretty challenging. Due to the high CAPEX per MW of the turbine itself the designer can accept no compromises on its energy yield and loading. To cope with such challenges the project made in its early stage specific selections regarding turbines architecture narrowing down the design space where innovation was sought. Characteristic challenges and reasoning for the selections made are briefly presented below.

▪ *Upwind vs downwind rotor*

Market selection of the standard three bladed upwind concept occurred in the early 1980's after a very short concept competition phase, and the main focus thereafter in the industrial development has been the upscaling of this successful concept rather than challenging the conceptual characteristics like upwind vs downwind. The upwind rotor was chosen mainly in order to reduce the impact of the tower wake (on loads and noise), even though it was known that the downwind configuration offered some potential benefits related to better centrifugal de-loading by coning and unrestricted flapwise downwind blade bending and the possibility for free yawing and application of negative tilt, that might give more axial flow for wind turbines in complex terrain.

With the upscaling to multi MW turbines that requires more lightweight and thus more flexible blades the main design requirement became the avoidance of tower strike, and forward pre-coning and blade pre-bending was introduced. These blade characteristics are important parameters in the blade optimization, however, also subject to limitations, as they are also determining for the blade operational aeroelastic behaviour, where the main constraint still is to avoid tower strike.

Downwind operation offers some options for further weight reduction by allowing the blade to be more flexible at the cost of more tower wake interaction and the risk of blade vortex lock-in with increased blade passage noise.

For the above reasons most of the work in INNWIND.EU is addressed to upwind designs.

▪ *Three bladed vs two bladed rotors*

For three bladed designs critical n-P value appears to be the 3-P while 1-P and 6-P are normally outside the critical range for resonance. The 3-P excitation can be alleviated through an exclusion zone in the variable speed controller, which however compromises the power performance of the turbine and does not totally prevent the problem. If resonance is not avoided then the turbine will suffer from higher fatigue loads in the wind speed range where 3-P excitation takes place. With or without exclusion zone in control it is beneficial to translate the excitation zone at lower wind speeds which for offshore sites of economic interest have less probability of occurrence and, thus, they contribute less to the AEP and the lifetime fatigue loads. For a given rotor diameter and power curve, moving the 3-P resonance to lower wind speeds can be accomplished through i) increasing the design TSR which also increases the design tip-speed (increasing corrosion as long as noise is not a problem) and calls for slenderer blades or ii) reduce the system's first global frequency, which is more effectively done by increasing the tower height and consequently the support structure loading.

If the three-bladed / jacket design is challenging, the two-bladed / jacket seems impossible since one has to prevent 1-P, 2-P and 4-P excitation. In this case an alternative soft support structure has to be adopted. It has been shown that a semi-floater support structure can do the job.

For the above reasons INNWIND.EU is focused on three-bladed rotors although two-bladed rotors are also investigated but only in connection to a soft support structure such as the semi-floater.

(Innwind.EU, Deliverable 1.25, PI-based Assessment of 20MW Wind Turbines)

- *Kingpin vs traditional drive train support*

The main function of the nacelle is to support the rotational motion of the hub holding the turbine blades and to transmit the mechanical power from the blades into the shaft and finally into the drive train. Thus the shaft must be supported by either one or two main bearings, which should have a high reliability, because they are hard and expensive to replace at sea. Traditional drive trains have two main bearings holding the shaft and then a gearbox and generator sitting behind the main bearings. This concept is however not believed to be viable for turbines much large than 10 MW, because the two main bearings will be loaded differently and to a level beyond the current capacity of main bearings. In order to distribute the turbine rotor loads more evenly between two main bearings then it has been proposed to place the two bearings on a static pin going through the hub and on each side of the hub. This concept has been termed the King-Pin concept and is used for the INNWIND.EU nacelle.

- *Direct Drive versus geared concepts*

The function of the drive train in large offshore wind turbines is to convert the mechanical power provided by the turbine blades into electrical power flowing out through the cable connecting the turbine to the power grid on land. In order to do so one needs a generator, where rotating magnetic fields can induce a voltage in the windings of the generator. If the generator is loaded then there will also be a current running in the cable and the generator will provide a torque on the turbine shaft keeping the rotation speed of the turbine blades at the optimal rotation speed compares to the incoming wind speed. The electrical loading of the generator is provided by an electrical circuit connected to a transformer stepping up the generator voltage being a few kilo volts to 36-66 kilo volt of the wind farm collection cables. The collection cables from each turbine in the wind farm are connected to a transformer platform that brings the power to land trough the main power cable at a voltage of 100-200 kilo volts. The major design trends within drive trains for large offshore wind turbine can be categorized into two main types:

Geared
A gearbox is placed between the turbine shaft and the generator in order to convert high torque and slow speed of the turbine shaft to low torque and high speed of a generator, which can be small and cheap.

Pro's: Standard gearboxes and generators can be used and are therefore cheap.
Con's: There are many moving parts, which tend to break more often than what they are designed for. It is expensive to replace gearboxes offshore.

Direct drive
The high torque and slow speed of the turbine shaft is connected directly to a large generator, which is larger and more expensive than the generator sitting after the gearbox.

Pro's: Few moving parts and thereby higher expected reliability.
Con's: Direct drive generators are often large and heavy, whereby they must be designed as part of the turbine.

State of the art within drive trains for large offshore wind turbines is to reduce the number of gear stages in the gearboxes and connecting a medium speed generator to the gearbox. This is reducing the complexity of the drive train, but still allows for a reduced torque of the generator. Examples of this approach is found with the 9 MW MHI Vestas Offshore Wind V-

164 turbine and the 8 MW Adwen AD-8-180. Another trend is to use a permanent magnet direct drive generator as has been done by Siemens Wind Power for the 8 MW SWT-8.0-154 turbine and the 6 MW GE Haliade turbine. Drive trains based on a 3 stage gearbox is however still used for the large offshore turbines such as the Senvion 6.2M152.

For the reasons discussed above the innovative INNWIND.EU designs are focused to lightweight direct drive power trains.

- *Jackets versus other bottom-fixed support structures*

The water depth range at the site under consideration is usually the most important criteria for the type of support structure. But soil conditions, wind turbine size and experience from the designer also have major influence. As a rule of thumb monopile like structures are most suitable for shallow waters and jacket like structures are suitable for deeper waters. Nevertheless, it is not possible to define these limits exactly. In recent years the transition was approximately around 35-40m. The allowable range for each support structure concept regarding the water depth is changing because technology advances continuously and further influential parameters such as soil conditions, met-ocean conditions and the size of the wind turbine result in variable limits. For example a site with 50 m water depth and very stiff soil and small wave heights might still allow a competitive monopile design for 10 MW wind turbines, but it can also mean that shallow waters with soil in loose sand with extreme occurrence of scour and large wave heights require other solutions than a monopile. The design of the foundation always needs to follow an integrated approach considering many influential parameters of the site and the wind turbine appropriately. The most prevalent foundation design today is either the monopile or the jacket support structures, which are by far the most developed concepts. Innovative solutions such as suction buckets in combination with a monopile or jacket are currently been developed and are also been addressed in INNWIND.EU. One should keep in mind logistics for manufacturing and especially installation of very tall structures. For water depths beyond 60 m is can be problematic to handle the overall dimensions, e.g. required width and total height of the jacket. The total height of bottom fixed support structures could exceed the capacity of cranes with respect to possible lifting height and lifting distance.

Another aspect is the clustering due to water depth variations within the wind farm. Here the jacket support structure shows high flexibility while the overall stiffness (thus natural frequency) of the jacket is less affected than for monopiles. That finally means that the resulting wind turbine fatigue loads on the support structure are comparable for different jackets in the wind farm. The support structure frequency usually lies within the 1p and 3p frequency range of the wind turbine, whereas monopiles tend to reach the lower end (1p) and jackets tend to reach the upper end (3p) currently. This indirectly opens up easier realization for jackets in deep waters than for using monopiles.

In this project the water depth is 50 m and a large number of innovations of the wind turbine are addressed. The dynamic interaction of wind turbine loads and a monopile response is generally more problematic than for a wind turbine with a jacket. This mainly is a consequence of the hydrodynamic induced loading on the super structure. In order to allow innovations of the wind turbine being developed parallel to the support structure the jacket concept is chosen as the reference design in INNWIND.EU. It is a robust support structure which allows development of wind turbine innovations "quasi" independently from the foundation, but of course not the other way round (no matter which support structure is designed).

(Innwind.EU, Deliverable 1.25, PI-based Assessment of 20MW Wind Turbines)

The above justify why INNWIND.EU is using jackets as their baseline option for fixed offshore support structures.

- *Challenges in floating designs*

In floating configurations, as in bottom fixed platforms, the rotational speed of the wind turbine rotor can excite the tower natural frequency. In consequence, the accurate computation of the tower natural frequencies coupled with the floating platform has particular importance. In addition, the platform natural periods as rigid body have to be located sufficiently far from the central frequencies of the wave spectrum. For platforms using catenary mooring lines, these periods are low and typically avoid significant excitation from waves, but there is an exception with the heave natural periods for semisubmersibles. This period tends to be located inside the wave spectrum, around 15s-20s. The use of heave plates to damp the vertical motion can improve the behaviour of these platforms, increasing the damping.

The evaluation of the global damping of the platform for the different degrees of freedom is also an important challenge, because it embodies complex physical effects related to viscosity that not all simulation tools can capture. Detailed CFD simulations and experimental scale testing in wave tanks are required to accurately characterize the damping level including viscous effects that much influence the global platform dynamics.

The simulation of floating wind turbines requires integrated tools because physical effects such as rotor aerodynamics and platform hydrodynamics are strongly coupled. A great effort on the development of these tools has been performed in the last few years, although further research is still needed. An effect of particular importance for floating wind turbines is the non-linear hydrodynamics. The inclusion of these non-linearities can imply a high computational cost. These effects produce high frequency and low frequency excitation as result of the interaction between different wave components of the spectrum. The low frequencies can excite the natural periods of the platform in the case of catenary moored platforms and can have particular importance in the design of the mooring system. For TLP's, the high frequency components caused by non-linearities can also excite the platform natural frequencies.

A particular effect that can have importance in the design of TLP is the excitation of the tension lines by vortex induced vibration (VIV) phenomena. This effect requires complex simulations with structural models of the lines coupled with hydrodynamic models taking into consideration the fluid viscosity.

Specific control strategies for the floating wind turbines have to be developed to optimize designs. The dynamics of these systems are very different than onshore or bottom fixed systems. Floating wind turbines present low natural periods that increase the complexity of the control strategy.

Finally, more effort has to be performed during the design phase to aspects such as manufacturing, installation, operation and maintenance of the floater. These aspects can have a great impact on the final cost of the energy.

INNWIND.EU down-selected a semisubmersible three-leg floater with catenary mooring lines as its reference floater for 10MW designs.

(Innwind.EU, Deliverable 1.25, PI-based Assessment of 20MW Wind Turbines)

1.3 Overview of the report

In the following five Chapters we present in detail the individual innovative concepts selected from WPs 1 to 4. In each Chapter there is an introductory section providing a brief description of the concept. Most of the innovative concepts addressed here have been also investigated in D1.24 for the 10MW scale and their presentation here stays short to avoid duplication. In the next section we investigate the structural integrity of the proposed solution, starting from the design layout and dimensioning and proceeding to the load cases considered and its structural integrity verification according to the recommendations of Deliverable D1.23. In the next section we appreciate the impact of the proposed design on LCOE. We investigate separately its impact on the Annual Energy Production (AEP) on CAPEX and on OPEX (qualitatively, through the reliability surcharge index). When relevant, we proceed to an LCOE sensitivity analysis and we conclude each Chapter with some main findings and conclusions.

The following Chapters address the innovative concepts considered:

Chapter 2 LOW INDUCTION 20MW ROTOR (*Ref WP2, NTUA & CRES*)
The concept, which has been presented in detail in D2.11, suggest the use of a larger, less loaded, rotor as a strategy for increasing the wind turbine capacity factor and reducing the wake losses without burdening rotor and turbine loads. In the present report the LIR concept has been combined with a newly designed family of low-lift airfoils for 20MW blades reported in D2.14.

Chapter 3 20MW ROTOR DESIGN WITH BTC (*Ref WP2, POLIMI*)
The 20MW RWT Rotor is redesigned employing bend-twist coupling (BTC). BTC is a passive load control strategy where the blade, when loaded, deforms so as to induce aerodynamic load reduction. Passive load mitigation by BTC can be obtained by exploiting the anisotropic mechanical properties of composite materials.

Chapter 4 PDD 20MW GENERATOR (*Ref WP3, MAGNOMATICS, DTU in aeroelastic calculations*)
A magnetic gear is combined with an electrical machine to realize a magnetically geared drive of high torque density. The magnetic pseudo direct-drive (PDD) generator is realizing the possibility of applying magnetic gears in wind turbines. In a PDD generator, the magnetic gear and the electrical generator are mechanically as well as magnetically integrated.

Chapter 5 20MW JACKET DESIGN (*Ref WP4, RAMBOLL*)
The concept has been presented in detail in D4.36 and adopted as the INNWIND.EU 20MW Reference Jacket. Mass and cost functions for this reference have been established. The assessment of the material, welding and assembly costs has been performed which results in a cost saving potential of up to 20%. We adopt this 20% figure to assess the LCOE reduction potential due to advanced jacket design and manufacturing.

Chapter 6 ADVANCED CONTROL OF 20MW RWT (*Ref WP1, GH-GL (now DNV-GL)*)
The concepts have been presented in detail in D1.43 and D1.44. . The methodologies applied are a combination of mature advanced control methods and control methods using novel sensors and actuators. The control concepts applied include Individual Pitch Control (IPC), Individual Flap Control (IFC) of trailing edge flaps and extreme turbulence control.

Following **Chapters 2 to 6** with the presentations of the individual innovative concepts there is **Chapter 7** where their synthesis and cross-comparison is attempted with emphasis on their impact on LCOE.

LCOE and other performance indicators used in Chapter 7 are calculated with the INNWIND.EU cost model v developed in D1.23. The version of the cost model used is v1.02.1 of May 2016 which now includes OPEX modelling in terms of the turbine rated power and a factor expressing the reliability level of a given design. It is reminded that in the earlier versions of the cost model OPEX was treated in a flat way, accounting for 106 €/kW/y for all turbine designs, following EWII specifications.

The report closes with **Annex A** (*NTUA & DTU*) where we present a simplified procedure for translating design loads reduction of critical turbine subcomponents to relevant mass and cost reduction. Such a procedure is necessary for assessing the impact of innovations targeting to CAPEX reduction through design loads mitigation, before reaching the stage of a redesigned turbine, as in the case of advanced control of Chapter 6.

(Innwind.EU, Deliverable 1.25, PI-based Assessment of 20MW Wind Turbines)

CHAPTER 2   LOW INDUCTION 20MW ROTOR

2.1   Brief description of the concept

The present work builds on the Low Induction Rotor concept that can significantly improve LCOE in offshore wind applications. The LIR concept has been extensively presented in earlier INNWIND.EU deliverables and relevant publications (see [4] and [5]). It is there shown that the effectiveness of the concept is fully explored when combined with low-lift families of airfoils [6]. For completeness we shall briefly present in the following the LIR concept and the methods used for the design of low induction planforms.

For a pitch-variable speed HAWT design and for a given rotor radius the classical rotor aerodynamic design problem would seek to maximize the energy capture by maximizing the power coefficient C_P. According to the BEM theory this would happen for an axial induction value $\alpha=1/3$ and would correspond to a TSR design value λ which increases (along with CPMAX) as the aerodynamic performance of the blades k gets better (higher). As design λ increases the non-dimensional lift distribution gets smaller and, keeping the same family of blade profiles, the rotor solidity gets lower.

Suppose that one redesigns a reference rotor (designed for CPMAX), by letting its radius free but respecting all turbine related constrains (the rated rotational speed and power, the hub loading etc). Let R_0 be the initial rotor radius and let subscript "0" denote the reference design, the one with $\alpha=1/3$. The new design problem is formulated as:

$$\frac{C_P(\lambda, \alpha) \cdot R^2}{C_{P0}(\lambda_0, \alpha_0) \cdot R_0^2} \to \text{max},$$

$$\text{subject to } \frac{C_M(0)(\lambda, \alpha) \cdot R^3}{C_{M0}(0)(\lambda_0, \alpha_0) \cdot R_0^3} \cong 1$$

where $C_M(x)$ is the bending moment coefficient at x blade location (0 for the hub and 1 for the tip). In words: "maximize the power output up to the design wind speed without exceeding the initial aerodynamic root bending moment". By eliminating the radius dependence the optimization problem can be recast as:

$$\frac{C_P(\lambda, \alpha)}{C_{M(0)}(\lambda, \alpha)^{2/3}} \to \text{max}$$

For a typical 3-bladed turbine the solution of the optimization problem for α is shown in Figure 2-1. The optimal (α, R) combination is $\alpha=0.187$ and $R/R0 = 1.136$. The optimised blade will capture more energy at its design conditions: $[C_P(\lambda,\alpha).R^2] / [C_{P0}(\lambda_0,\alpha_0).R_0^2] = 1.087$; and will be less loaded than the initial one (design C_T and $C_M(x)$ will be smaller), operating at a lower axial induction value $\alpha=0.187$ instead of $\alpha_0=0.33$. We, thus, sacrificed C_P in order to increase energy capture with a larger rotor diameter, while maintaining the aerodynamic bending moments at their initial level.

Evidently, having a larger rotor means extra costs. Given that in offshore wind the rotor contribution to the turbine CAPEX is small while energy capture is directly driving LCOE, the LIR concept appears appealing for offshore cost of energy reduction.

(Innwind.EU, Deliverable 1.25, PI-based Assessment of 20MW Wind Turbines)
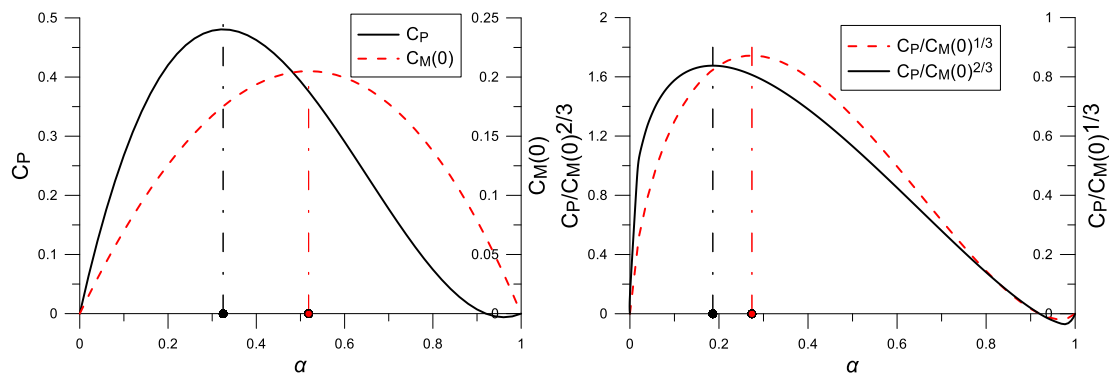
Figure 2-1 Plots of non-dimensional coefficients, candidates for blade optimization, versus axial induction coefficient α

2.2 Assessment of the Structural Integrity of the Proposed Design

2.2.1 Design layout and dimensioning

Aerodynamic design of the LIR blade

The aerodynamic design of the Low Induction 20MW Rotor builds upon the 20 MW RWT (Land Version) defined by NTUA [1]. It comprises the following steps:

STEP1: A high performance low lift airfoil of increased relative thickness (26%) is designed to replace the 24% high lift profile defining the outer 30% span of the 20MW reference blade. The reason behind this choice is to take advantage of the higher operational Reynolds number of a 20MW design (compared to the 10MW one) for increasing the thickness and, therefore, the flap bending resistance of the outer blade and its structural efficiency, maintaining the airfoils' aerodynamic efficiency and the energy capture of the rotor.

STEP2: Using the newly designed 26% low lift profile and a 30% profile [7] designed for a 10MW LIR, the optimization of the 20MW LIR blade planform is performed. The optimization leads to a 13% longer blade than the 20MW reference with similar loading capacity. Loads mitigation is accomplished by operating the LIR blade at the lower induction level where it is designed to reach its maximum performance using the dedicated low-lift profiles.

The LIR blade is fitted on the 20MW RWT maintaining its original variable speed range. The pitch schedule is slightly trimmed, without major interventions to the turbine controller, to comply with the 20MW power rating at higher wind speeds.

The design of the blade planform, for a given airfoil family, requires the derivation of chord, thickness and twist distributions that result in optimum energy yield for the wind turbine. The reference blade was used as a starting point for the design and constrains imposed on the new design were as follows:

- The length of the blade is increased, with a radius of 142.5m, keeping the same rotating speed.
- The thrust is constrained to remain less or equal to the thrust of the reference blade ($T \leq T_{ref}$), keeping the tower bending moment levels in check.

- Bending moment at the root blade is constrained in a similar manner ($M_{root} \leq M_{root-ref}$), so as to keep the loads on the blade similar to the reference blade.
- The maximum torque is also constrained not to exceed the reference value.

The result is a low induction blade, with reduced power density, but similar loads to the reference design. For the derivation of the optimum planform design a constrained optimization problem is setup, where the free variables are:

- Chord length at 3-4 different positions along the span. In this case a distribution that is very similar to the reference blade is used with identical values for maximum chord and root diameter in order to simplify the structural design.
- Blade twist value at 3-4 different positions along the span.
- Blade thickness and position where thickness switches to minimum value.
- Design Tip Speed Ratio. This is used to define the operating schedule for the wind turbine before pitching.

For the optimization problem a typical BEM method is used, calculating the operating envelope from cut-in to cut-off wind speeds. The resulting power is weighed based on the probability for a Weibull function with (c=10.38, K=2.0 – reference values). The objective function is then the capacity factor for the given wind conditions.

Optimization is performed using an evolutionary method to calculate optimum values for the free variables. The resulting blade shape (chord and twist distribution) is compared against the 20MW RWT blade shape in Figure 2-2. The newly designed 26% low lift profiles 10/90 and 20/80 are shown in Figure 2-3. The new airfoils have been designed to exhibit maximum L/D at lower lift values, C_L~0.8, (Figure 2-4), so as to be better suited for the low induction rotor.
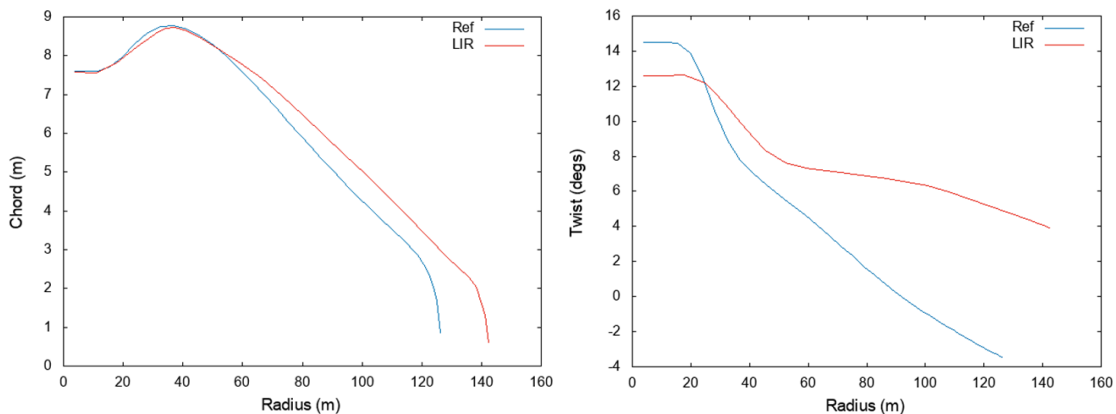
Figure 2-2   Planform characteristics of the 20MW LIR. Chord (up) and twist (down) distributions
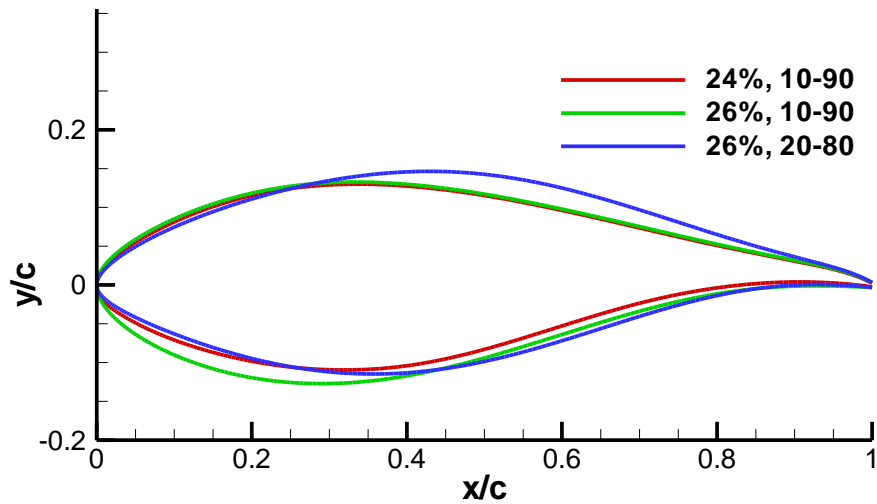
Figure 2-3   26% Low Lift profiles used in the present LIR design [8]
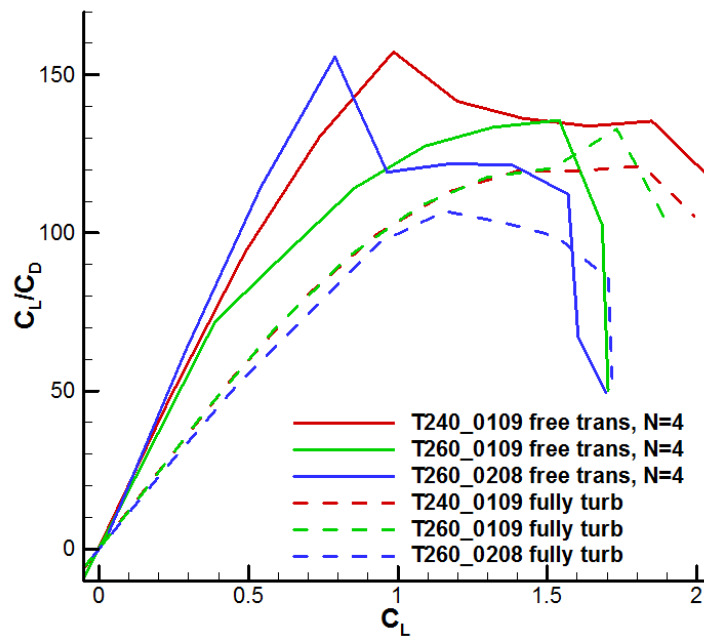
Figure 2-4   Performance (L/D) of the 26% LLs for transitional and fully turbulent flow conditions. The (more conservative) RANS results obtained with MaPFlow [8] are used in the present context

Structural design of the LIR blade

For the structural investigations performed by CRES the LIR blade is based on the NTUA aerodynamic design. The structural design of the LIR blade complying with the structural integrity requirements (as described in the following) was achieved with the introduction of carbon uniaxial layers on selective locations along the blade length to improve the stiffness of the blade keeping at the same time the mass of the blade as low as possible.

2.2.2   Load cases considered (from D1.23) and Results Obtained

The loading of the LIR blade was estimated by the Minimum Flap load envelop that was provided to CRES by NTUA. Following the aerodynamic design of the blade the solution to be acceptable for the reference wind turbine would mean that the root bending moments for the longer blade would be kept the same as the reference blade. Therefore, for deflection and strength estimations the LIR blade was subjected to 16.7% lower concentrated aerodynamic loads in both the edgewise and flapwise directions.

2.2.3   Structural integrity verification

To verify the suitability of the blade design for the wind turbine, as well as to verify the structural integrity, modal analysis, static strength analysis and buckling analysis were performed. The constraints set in order to have a feasible solution for the reference 20MW wind turbine, were as follows:

Dynamic behaviour   natural frequencies of the blade were to be as close as possible to the reference wind turbine blade. Avoidance of the 3p, 6p, 9p, etc. frequencies of the reference wind turbine.

Elastic stability   The LIR blade should perform comparable to the reference blade or even better. The loading applied to verify the structural design against elastic stability is considered the same extreme load case scenario as that used for the verification of stiffness and strength.

Stiffness, Strength   Stiffness and strength of the LIR blade should be comparable to the reference blade.

The analysis procedure used to verify the structural integrity of the blade was identical to that used in the benchmark study. The results of the analysis tools for the reference blade were compared with that of the other partners. Still in order to assure validity of results, the output data from the structural analysis procedure are compared against those of the reference wind turbine blade. For reference purposes, modal, stiffness and strength analysis, as well as elastic stability estimations were performed using FEM. The blade model comprised of 4-node SHELL181 elements suitable for modelling multi-layered composite materials.

The first five natural frequencies and their respective shape modes were calculated and presented in Table 2.1 and Fig. 2.2 -4 – 2.2-8 respectively.

Table 2-1 - Natural frequencies of the blade (all frequencies in Hz)

Mode No.	LIR blade	INNWIND.EU blade
1	0.44	0.43
2	0.58	0.67
3	1.36	1.237
4	1.75	2.004
5	2.73	2.52
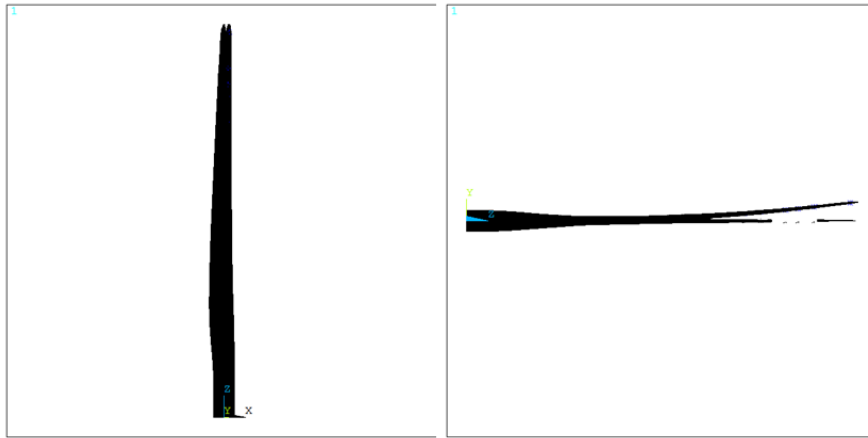
Figure 2.2-4 1st Mode Shape of 20MW LIR blade
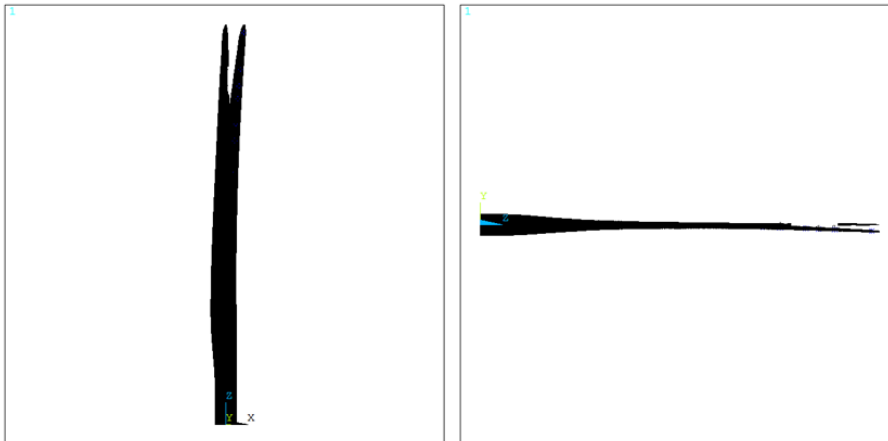
Figure 2.2-5 2nd Mode Shape of 20MW LIR blade
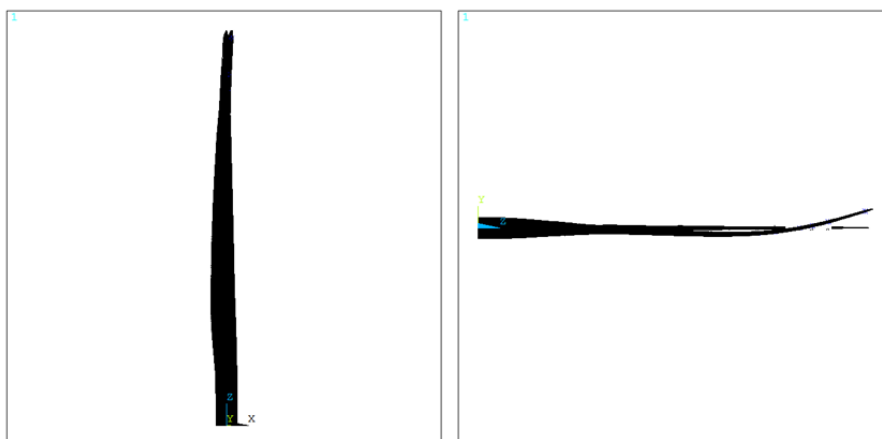
Figure 2.2-6 3rd Mode Shape of 20MW LIR blade
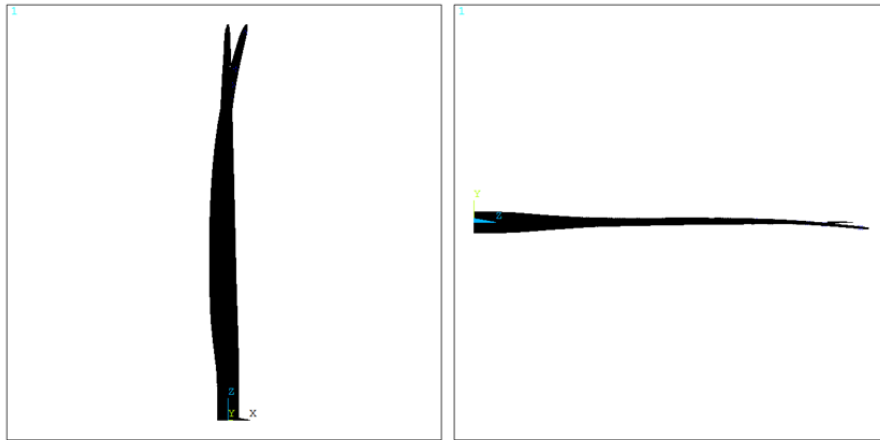
Figure 2.2-7 4th Mode Shape of 20MW LIR blade

Figure 2.2-8 5th Mode Shape of 20MW LIR blade

Buckling analysis was performed considering safety factors for the stiffness properties of the glass and carbon fabrics as also done within the benchmark. More specifically, the values of the stiffness properties were divided by a factor 2.042. The value of the factor was adopted following GL requirements. The first critical buckling load factor was calculated equal to 0.74 while the respective eigen-mode is presented in Figure 2.2-9. The critical location comprises the suction side of the blade. More specifically, buckling is observed in the spar cap region at the ca. 40% of the blade length. A direct comparison with the reference blade (buckling load factor 0.78) indicates that the LIR blade buckling behavior is comparable with the RTW one.
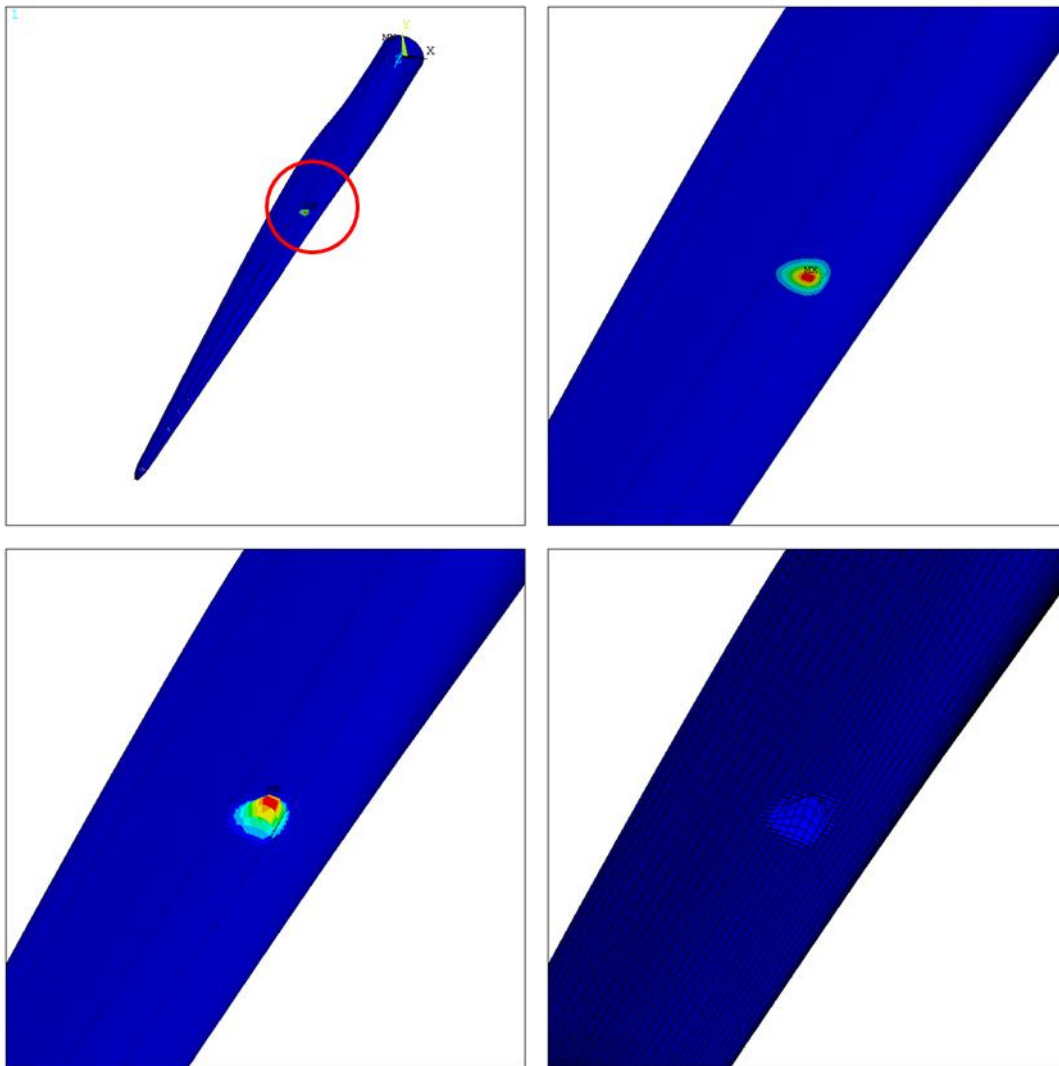
Figure 2.2-9 Buckling mode shape of the 20MW LIR blade

Strength analysis was performed calculating the Tsai-Wu failure index. Contour plots of the maximum Tsai-Wu value among the various layers for every element is presented in Figure 2.2-10. Critical part of the blade comprises the suction side near the spar cap close to the blade root with a failure index of 1.14. Reminding that the INNWIND.EU 20MW RWT reference blade indicated a maximum Tsai-Wu failure index equal to 4.03 (using CRES calculations), the current blade design is considered adequate. In Table 2.2 strength analysis results are presented in terms of the strength multiplication factor as defined in the benchmark study.
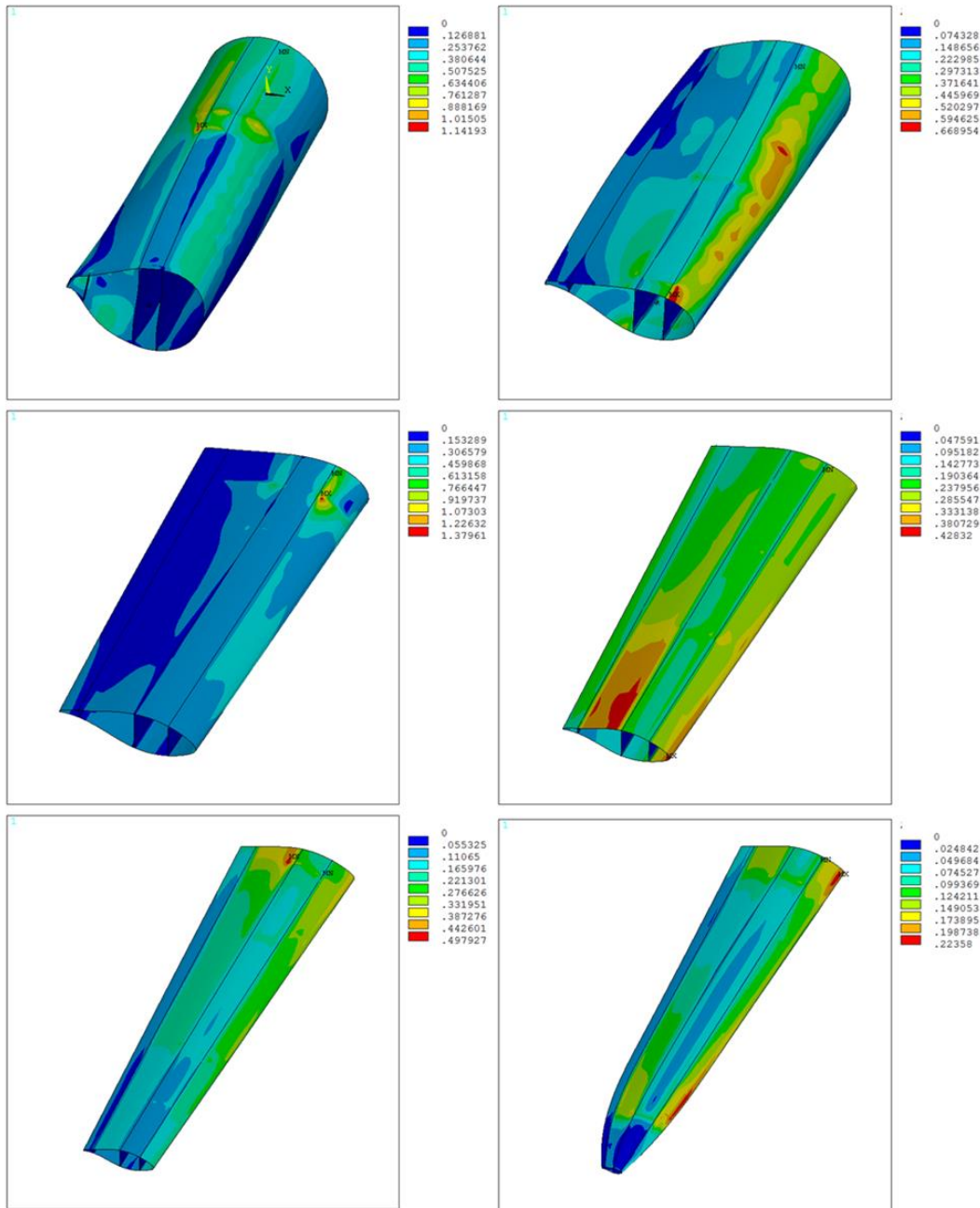
Figure 2.2-9 Detailed distribution of Tsai-Wu failure index of 20 MW LIR blade

The design of the LIR blade that complies with structural integrity requirements resulted in a lighter blade design compared to the reference one while the ratio of the carbon-layer mass to the overall blade mass is 45.6%. An overall summary is presented in Table 2.2.

Table 2.2 - Structural Integrity of the 20 MW RWT & LIR blades

Property	Reference Wind Turbine 20MW	Low Induction Rotor 20 MW
Length [m]	122.14	142.5
Mass [kg]	119840	98553
Carbon [kg]	-	45024
Tip Deflection [m]	19.95	11.46
Strength Multiplication Factor (higher factor implies higher strength)	0.248	0.72
Buckling Critical Load factor (higher factor implies better buckling behavior)	0.79	0.74
1st natural frequency [Hz]	0.43	0.44
2nd natural frequency [Hz]	0.67	0.58
3rd natural frequency [Hz]	1.237	1.36
4th natural frequency [Hz]	2.004	1.75
5th natural frequency [Hz]	2.52	2.73

It can be concluded that the introduction of carbon fabrics permits an efficient design of a 142.5 m rotor blade with respect to modal, stiffness, strength and buckling analysis. At the same time, the mass of the blade was kept in low values, decreased by 18% in comparison to the mass of the 122.14 m INNWIND.EU reference blade design.

2.3   LCOE Impact of the Proposed Design

2.3.1   Effect on Annual Energy Production

Wind turbine capacity factor

The wind turbine capacity factor calculated for LIR as a result of its planform optimization procedure is 0.546. This is 7.5% higher than the capacity factor of RWT which for the reference wind speed Rayleigh distribution with 9.2m/s mean is 0.508. It is anticipated that from the total of 7.5% wind turbine capacity factor increase 4.5% comes from the LIR concept and another 3.0% comes from the use of dedicated low lift airfoils. The improvement of AEP is a consequence of the increased LIR energy production below rated wind speed (see Figure 2-5).

(Innwind.EU, Deliverable 1.25, PI-based Assessment of 20MW Wind Turbines)
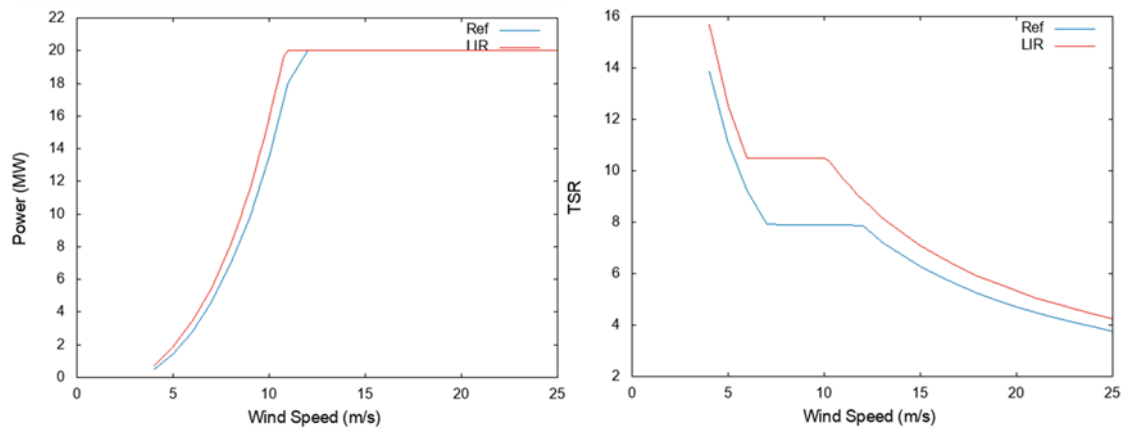
Figure 2-5   Power and variable speed schedule (as Tip-Speed-Ratio) versus wind speed The LIR design is considered with the low lift profiles family

Wind farm wakes

As already discussed in [3], LIRs are operating with reduced wake losses due to their lower thrust coefficients. The calculations presented in [3] support a reduction of the wind farm wake losses from 7% for the RWT to 5% for LIR, an improvement which directly reflects to the wind farm capacity factor as well.

Other wind farm losses including availability losses

We do not expect the LIR to affect the reliability of the turbine and, therefore, its availability losses.

2.3.2   Effect on CAPEX

Using a LIR instead of the original one of the 20MW RWT is affecting the CAPEX of the following turbine subcomponents

Blades

As already discussed the need for stiffening the longer blade of the LIR to limit its maximum deflection and trim its natural frequencies is satisfied by replacing the original all-glass blade with a hybrid one with carbon spar. This necessitates the development of a cost model for hybrid blades, given the fact that carbon fibre is three times more expensive than glass fibre.

The cost figures used for the 20MW LIR blade derive from the cost model developed for the hybrid 10MW LIR blade in [9]. The method involves the estimation of the baseline cost of a full glass blade and then correcting the cost estimation by the ratio of carbon fiber cost over glass cost. The method is well described in D1.24.

Firstly, the baseline blade cost is calculated:

Baseline blade cost: 13.084*98553-4452.2 =   1,285,015 $ (2002)

(Innwind.EU, Deliverable 1.25, PI-based Assessment of 20MW Wind Turbines)

It should be noted that CRES has estimated a weight for the reference blade of 119,840kg instead of the 117,849Kg reported for the reference wind turbine. Therefore, a correction for the weight estimation is done multiplying mass data by 0.9834. Correcting the baseline blade cost the blade cost assuming all glass manufacturing is 1,263,663 $(2002).

The material cost ratio estimated for a rotor of 100.758m is: 50.95%

From the carbon layer mass provided the carbon fibres are estimated to 45,024 kg, leading to a ratio over the whole blade mass of about 30.16%. When recalculating to percentage of fibres, the carbon fibres used comprise the 50.26% of the total fibres.

Moreover, it is assumed that the carbon fibres cost 3 times as much as the glass fibres and the percentage of fibers within the weight of the blade is ca. 60%.

Based on the above, the correction factor to be applied on the baseline cost estimated is:

(1-0.5095)+0.5095*(1-0.6)+0.5095*0.6*(1-0.5026)+0.5095*0.6*0.5026*3 = 1.307

Therefore, the cost of the hybrid glass/carbon blade is calculated to*: 1,651,971 $(2002)*

Tower

The LIR blade is 13% longer than the RWT one. However the 20MW RWT had already a longer tower than needed to maintain the acceptable minimum blade-sea surface distance. The longer tower of the RWT resulted from the need to reduce the first system's global frequency to avoid 3P excitation. The 20MW RWT tower is long enough to accommodate the longer LIR blade without further modification.

LIR tower mass = RWT tower mass = 1.780t
LIR tower cost = RWT tower cost = 5.85 M€ (2012)

Offshore Support Structure

It is anticipated that the static loads of the offshore support structure will be reduced due to the reduced rotor thrust. Nevertheless we have seen that such a reduction is not there for the fatigue loads that drive the jacket design. We shall therefore assume that no changes to the 20MW reference support structure are needed.

Other components

There is a small influence of LIR to other components CAPEX, such as the low speed shaft or the yaw mechanism due to the increasing rotor size. These extra costs are automatically taken into account by the INNWIND.EU cost model [10].

2.3.3 Effect on OPEX

Direct O&M costs, expressed in (€/kW/y) units are not affected by the introduction of LIR. At the same time we do not anticipate any LIR consequences on the turbine availability. Therefore, the replacement of the reference rotor with the LIR doesn't have any positive or negative effect on OPEX.

(Innwind.EU, Deliverable 1.25, PI-based Assessment of 20MW Wind Turbines)

2.4   Performance Indicators of 20MW LIR versus 20MW RWT

The comparison of LIR against the RWT in terms of key Performance Indicators is presented in the following Table.

ROTOR	Blade Mass (tn)	Blade Cost (k€ 2012)	Overall CAPEX (k€)	Turbine CF	Wind Farm CF	LCOE (€/MWh)
RWT - 20MW	118	1,274	68,000	0.508	0.437	96.50
LIR – 20MW	99	1,367	70,200	0.546	0.480	92.57

2.5   Conclusions

A 20 MW Low Induction Rotor has been designed aerodynamically and structurally. The rotor is tested on the 20MW RWT platform of INNWIND.EU. A hybrid glass-carbon has replaced the original all-glass blade of the RWT. The LIR is 13% longer and the hybrid design aims in increasing the extra requirements for stiffness and strength dye to the larger span. The hybrid blade:

- Has 16% lower mass than the (up-scaled) 20MW RWT blade
- Costs 7.3% more than the RWT blade
- Has a wind turbine capacity factor 7.5% higher than the RWT blade
- Yields a wind farm capacity factor 9.8% higher than the RWT blade due to the reduced wake losses corresponding to the lower thrust coefficient of the LIR

Although the turbine CAPEX increases by 3.2% the overall effect of LIR on LCOE is quite positive reducing it by 4.1%. The sensitivity of LCOE to the blade cost is relatively low. It is shown however that if a new LIR blade can be designed with the same cost of the RWT blade the LCOE would drop at 92.17 €/MWh.

(Innwind.EU, Deliverable 1.25, PI-based Assessment of 20MW Wind Turbines)

CHAPTER 3 20MW BLADE DESIGN WITH BTC

In this activity, a series of preliminary design studies have been conducted in order to optimize the Key Performance Indicators (KPI) of a 20 MW reference wind turbine. The starting point of the optimization process is the Baseline 20 MW developed by PoliMI for Deliverable 2.14. This configuration was obtained as part of a mass-minimizing solution, whose aim was to mimic as much as possible the aero-elastic properties of the 20MW RWT [1] the rotor of which was obtained throughout up-scaling from 10MW. As discussed in the corresponding report, this led to the design of a feasible structural layout for a given aerodynamic shape, which fulfils fundamental integrity constraints formulated in accordance with standard certification guidelines.

From here, we have performed a sequence of design steps in which several features of the rotor are optimized in order to reduce as much as possible the total blade mass as well as the ultimate and fatigue loads experienced by the turbine during its operational lifetime. In particular, the introduction of a geometric rotation in the alignment of the spar caps fibres (F-BTC) is exploited to significantly alleviate fundamental load figures, thanks to the introduction of a structural coupling between the out-of-plane deflection of the blade and its torsional deformation. Besides, other characteristics of the blade are optimized, including the rotor solidity and its prebend, so that the combination of the structural tailoring and the design refinements leads to additional aero-structural advantages in terms of mass, AEP and LCOE.

3.1   Introduction to the Innovative Concept

There is strong evidence in the literature that the anisotropic properties of composite laminates can be exploited to introduce desired behaviours in the dynamic response of rotor blades. This process of structural tailoring has been reported for example by [11] [12] [13] [14], while PoliMI presented a detailed application of a fiber-induced bend/twist coupling (F-BTC) to the structural design of the INNWIND.EU 10 MW Baseline during the Deliverable 2.22 [15] which resulted in significant load alleviations and related design advantages.
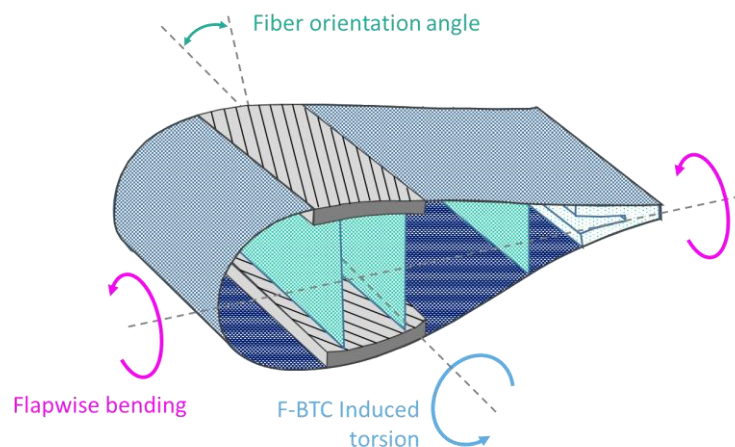
Figure 3-1 Detail of a typical blade section with F-BTC

In its general implementation, this technique can be exploited by introducing a certain rotation in the lamination of the composites associated to the different structural components, whereas the strongest beneficial effects are obtained when the fibers of the spar caps are rotated, as shown in Figure 3-1. From a structural perspective, the main consequence of the F-BTC is a modification of the fully-populated 6x6 stiffness matrix. In particular, the extra-diagonal term which takes into account the flapwise displacement and the torsional deformation, referred as $K_{Flap/Tors}$ is different from zero, as shown in Figure 3-2 (left) for the INNWIND.EU 10 MW rotor. It is evident how the magnitude of the $K_{Flap/Tors}$ term is positively correlated with the amount of fiber orientation, which means that larger rotations are associated to a stronger coupling effect. The same behaviour can be quantified by looking at the non-dimensional coupling factor α_{BTC}, which can be directly computed from the stiffness matrix members as follows:

$$\alpha_{BTC} = \frac{|k_{Flap/Tors}|}{\sqrt{K_{Flap} * K_{Tors}}}$$

The corresponding spanwise distribution of the α_{BTC} factor is illustrated for a varying amount of fiber orientation in Figure 3-2 (right), which confirms that a stronger effect is obtained for a larger amount of fiber rotation.
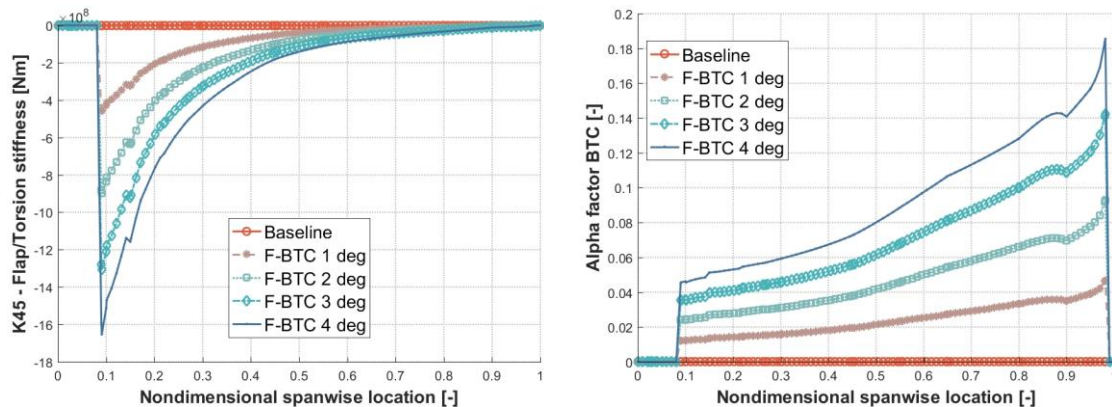
Figure 3-2 Flap/torsion stiffness and nondimensional BTC factor

The resulting effect is a built-in load alleviation mechanism: due to the non-zero extra-diagonal stiffness term, when the blade bends in the flapwise direction, part of the deformation energy is transformed into additional blade torsion. When the rotation of the fibers is properly tuned, an out-of-plane deformation towards the suction side of the blade results in a nose-in-the-wind rotation of the section, and therefore, the effective angle of attack is automatically reduced resulting in lower loads. This can be checked by recurring to simplified load cases.
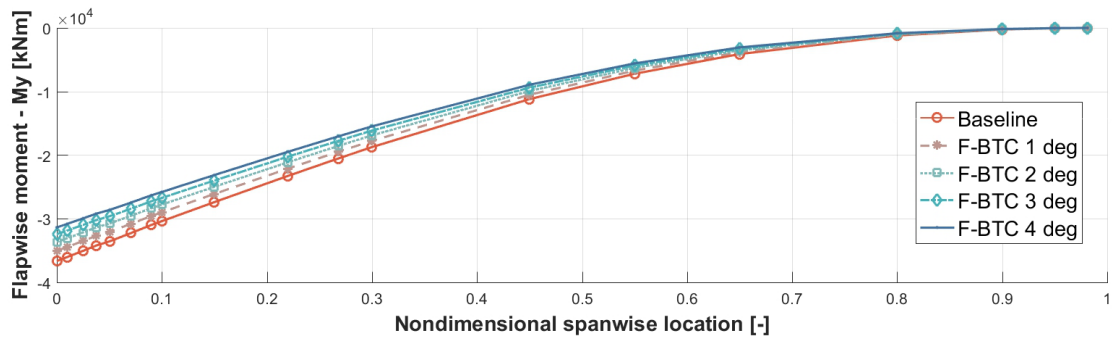
Figure 3-3 Parametric F-BTC: flapwise bending moment distributions along the blade span

For example, Figure 3-3 shows the spanwise distributions of the flapwise bending moment for a simplified condition in which the INNWIND.EU wind turbine is operating at its nominal conditions. These distributions have been obtained for different fiber angle only in the spar cap. In this example, the wind field is uniform, so that quasi-steady conditions can be obtained during the simulation. It can be seen that, for an increasing amount of fiber rotation, the resulting bending is progressively lowered. Please notice that, in this simulations, a negative value of the flapwise bending implies a loading towards the suction side of the blade.
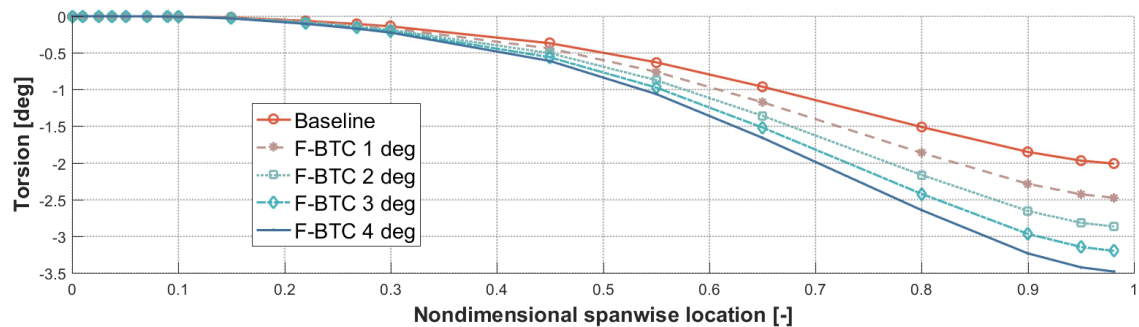
Figure 3-4 Parametric F-BTC: torsional deformation distributions along the blade span

The corresponding torsional deformations are reported in Figure 3-4, which demonstrates how the local twist angle is larger for an increasing amount of F-BTC: this confirms how a remarkable load alleviating effect is ascribable to a larger torsion of the blade sections, and to the corresponding reduction in the angle of attack. In the following, the F-BTC mechanism is introduced in the Baseline 20 MW in order to reduce the mass of the rotor as well as key ultimate and fatigue loads.

3.2   Assessment of the Structural Integrity of the Proposed Design

3.2.1   Design methodology

In this work, the design is formulated as a single-objective constrained optimization problem, which is solved by the multi-disciplinary design tool Cp-Max illustrated in Figure 3-5. In its more general formulation, the code is able to manage the complete design of rotor, blades and tower by targeting at the minimization of the CoE.

As described by Bortolotti et al. [16] the architecture of the code is based on a continuous interface among a primary (macro) loop, which handles the design of high-level characteristics of the machine like radius, solidity, cone and tilt angles and several submodules. These are responsible to conduct the detailed design of a specified subsystem in order to optimize certain performance of the wind turbine. It must be noticed that the mechanism is based on different nested optimization cycles so that, for each variation of the macro parameters, an entire loop of the sub-modules is required.

According to the needs, Cp-Max can be run as an integrated design tool, in which the macro design variables are sized through a full cycle of the underlying submodules. Otherwise, it is possible to bypass the macro loop and run the required submodules as standalone tools. This way, it is possible to save significant computational time where only certain aspects of the design should be investigated.

The main submodules employed in these activities are briefly described in the following:

- **Aerodynamic design submodule:**

  This module performs the optimization of the chord, twist and non-dimensional thickness (t/c) distributions along the blade. All quantities are described by means of a suitable parameterization, whose nodal points are the design variables of a dedicated optimization problem. The problem is solved by an SQP gradient-descent method, which targets at the maximization of the theoretical AEP. This is obtained through the computation of the Cp-TSR curves, which rapidly allow defining the regulation trajectory of the machine, and thus the ideal AEP. Possible constraints of this module include maximum chord and twist, as well as prescribed regularity of the distributions. The rotor solidity is also a constraint for the aerodynamic design submodule: if a solidity value is specified, the chord distribution is design to satisfy this value.

- **Prebend design submodule:**

  This module is able to perform the design of the prebend distribution along the blade. This is suitably discretized by means of Bézier curves, whose control points are the unknowns of a dedicated optimization problem. Here, the goal of the optimization is to design the prebend such that the deformed rotor area at rated conditions is maximized. This also represents an indirect requirement on the maximization (or at least preservation) of the AEP, under the assumptions that the effective disk area is directly correlated to the energy yielding of the wind turbine. Constraints can be imposed on the shape regularity, as well as on the maximum value of the prebend, which is usually determined by technological and manufacturing limitations.

- **Structural design submodule:**

  This module allows optimizing the total blade mass by sizing the thickness of all the structural elements along the blade. The design variables account for the thickness of all the composite fabrics (i.e. unidirectional, biaxial, triaxial) and that of the fillers (core, balsa, foam) so that a complete structural description of the blade is achieved at the end of the process. Ahead of the optimization, a set of

dynamic load cases is run by the multi-body solver Cp-Lambda [17] and the set of driving ultimate/fatigue loads is extracted and subsequently used to perform the design. Relevant constraints here are those prescribed by the international standards [18] and include frequency placement, maximum tip displacement, ultimate/fatigue integrity verification and a preliminary buckling verification of the structural elements. In this framework, each optimal solution is automatically feasible, that is, automatically satisfies the certification requirements. A detailed description of the module is provided by Bottasso et al. [19].

All modules are integrated within a dedicated data-flow, so the outcomes of each design submodule can immediately affect and influence the other submodules. So, for example, if the prebend optimization implies a different value of the blade/tower clearance, a subsequent structural optimization will be done by considering the updated value, so that the constraints can be updated accordingly.

As mentioned, due to the preliminary framework of this activity, in this work we performed a partial redesign of the wind turbine by targeting specified features of the rotor and by maximizing the corresponding objective functions. This was achieved through a series of design steps whose logic is depicted in Figure 3-6. Starting from the Baseline 20 MW illustrated in D2.14, we conducted several parametric analysis in order to obtain improvements of the Key Performance Indicators, which include at this level the rotor mass, the AEP and selected ultimate and fatigue load measurements.
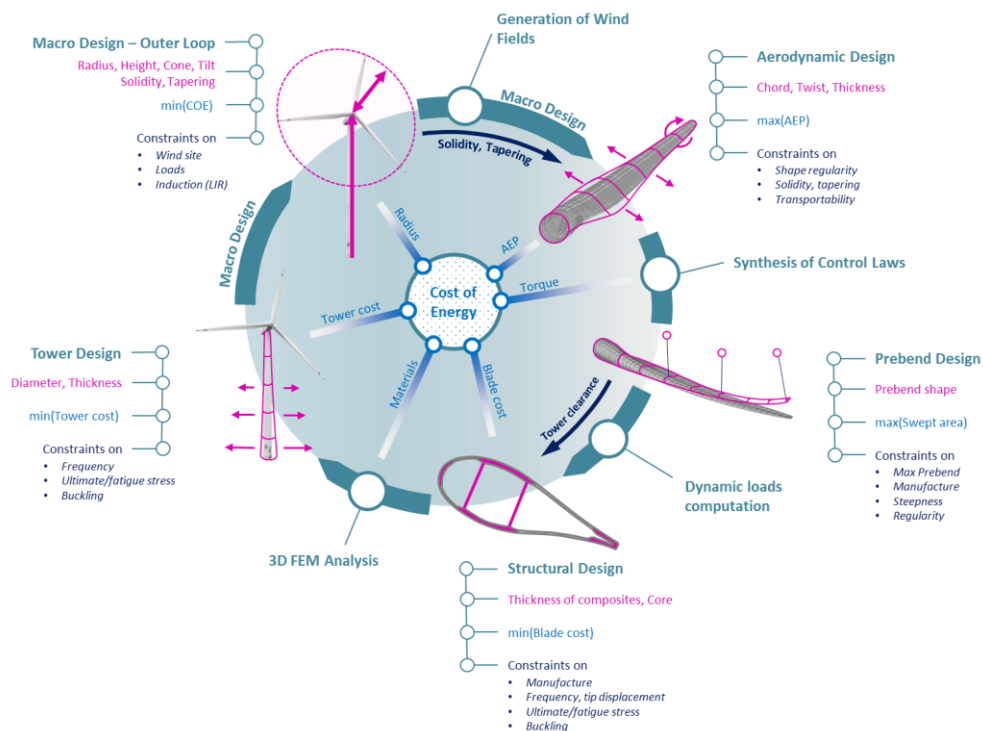
Figure 3-5 Cp-Max architecture

During each analysis we introduced perturbations of relevant design parameters and run the required design submodules in order to obtain improvements of specific performance. At the end of each parametric analysis, an optimal solution is chosen and used as the initial guess for the following study. According to the road map of Figure 3-6, we followed three main design steps:

1. **Prebend analysis**: the blade of the Baseline 20 MW is designed with a straight axis, which means that no prebend or sweep is applied. Considering that the maximum tip displacement is an active constraint of the design, at this step we introduced a varying amount of prebend in order to increase the blade/tower clearance and achieve a significant reduction of the rotor mass. Two different values of tip prebend have been tested, namely 2 and 4 meters. For each value, we used the prebend design submodule of Cp-Max to optimize the out-of-plane position of the blade axis. Then, a complete structural optimization loop was performed by the structural design submodule in order to obtain a mass-minimizing solution. As illustrated in Figure 3-6, apart from the expected mass reduction, a slight increase of the AEP was obtained, for approximately a comparable set of loads.
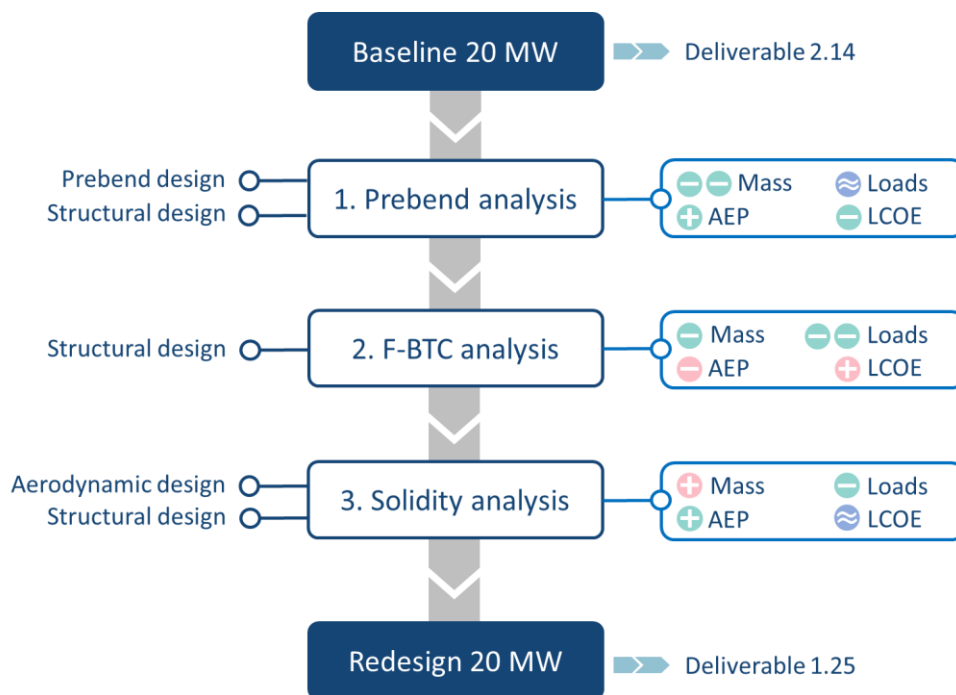
Figure 3-6 Road map of the redesign process

2. **F-BTC analysis**: starting from the optimized configuration with prebend, we then applied a parametric rotation to the fibers of the two spar caps. This way, we introduced a varying amount of F-BTC in the dynamic response of the rotor, which ultimately allowed obtaining a significant reduction of the key loads. For each configuration, a full structural optimization loop was performed to achieve mass-minimizing solutions. However, even though the mass is furtherly reduced, the introduction of the F-BTC led to a slight deterioration of the AEP, which is mainly

related to the larger torsional flexibility which makes the blade sections to operate away from the optimal aerodynamic efficiency.

3. **Solidity analysis**: In the last step of the design process, we started from the coupled F-BTC rotor designed at the previous step and progressively reduced the rotor solidity. For each value of solidity, we performed a redesign of the chord and twist distributions through the aerodynamic design submodule, in order to obtain AEP-maximizing solutions. Again, each configuration was then structurally optimized by the structural design submodule of Cp-Max. At this stage, we obtain a further reduction of the key loads, even though the lower solidity required a higher mass of the structural components. However, the AEP was globally increased so that approximately the same LCOE is achieved for all the parametric solutions.

3.2.2   Design assumptions

Structural Layout

All the solutions are based on the structural arrangement described in D2.14. The internal layout is shown in Figure 3-7, and is based on the common spar-box concept. The width and positions of all the sectional elements was kept as frozen during the entire design activity, while the thickness of the sectional components are recursively optimized by means of the structural design submodule of Cp-Max.
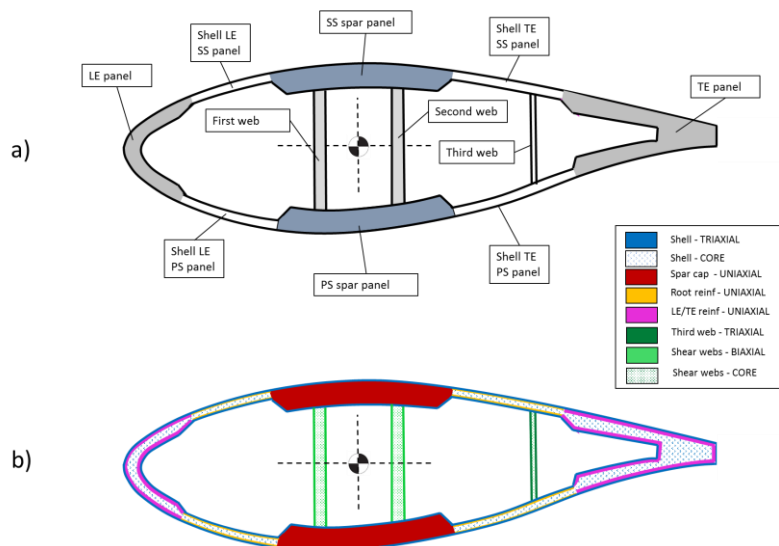
Figure 3-7 Sectional elements and structural components

Cost model

It is important to notice that we didn't employ the LCOE as merit function during the design process, since the main focus of the various steps was on the mass and loads mitigation. However, we thoroughly assess the COE during the process, in order to identify possible advantages in terms of cost reductions. In this activity, we computed the cost of energy

according to the INNWIND.EU cost model described by Chaviaropoulos [10] . The main assumptions that we adopted are the following:

- Plant capacity: we assumed an ideal wind farm with only a single wind turbine. So, the LCOE is directly computed for a unitary WT.

- Blade cost: this was obtained from the total blade mass following the scaling law:

$$Blade\ cost = 13.084 * Blade\ mass - 4452.2$$

- Tower cost: this was obtained from the total tower mass following the scaling law:

$$Tower\ cost = Tower\ mass * 4.35$$

- Conversion: we assumed that 1 USD = 0.75758 EUR.

- Actualization: we assumed a nominal discount rate of 0.0739 %

- AEP: in this work we use the turbulent energy production, which is obtained as an averaged measurement of the electrical power obtained during turbulent simulations (DLC 1.1)

- Capacity factor: for its estimation, we adopted the following simplified relation:

$$cf = \frac{AEP}{8760 * P_{Rated}}$$

Control

During the whole design process we used the external controller provided by Hansen and Henriksen (2013). The main settings/parameters were taken from the original datasheet of the 20 MW reference wind turbine.

To account for the modifications investigated during the design process, for each solution we defined an updated regulation trajectory. This was basically done by computing the envelope of the Cp-TSR curves ahead of the structural optimization loop. Subsequently, we computed the ideal rotor speed and a suitable pitch-scheduling look-up table. That information was then supplied to the controller, so that each configuration can operate close to its theoretical optimal point.

3.2.3 Load cases considered

Due to the significant amount of configurations investigated in this work, we used a basic set of DLC, which are defined according to IEC standards. The list of considered DLC is provided in Table 3-1 together with the corresponding definition and safety factors for the computation of the ultimate sizing loads. The list includes cases in normal operations as well as selected gust conditions, faults and storm situations. For the turbulent simulations only one seed was considered in order to save computational time. All turbulent winds were generated in accordance to the required wind turbine class through the Kaimal model.

(Innwind.EU, Deliverable 1.25, PI-based Assessment of 20MW Wind Turbines)

Table 3-1 List of considered DLC

DLC	Wind	No. of Seeds	Wind speed	Yaw mis.	Fault	SF
1.1	NTM	1	$V_{IN} : V_{OUT}$	-	-	1.35
1.3	ETM	1	$V_{IN} : V_{OUT}$	-	-	1.35
2.1	NTM	1	$V_{IN} : V_{OUT}$	-	Grid loss	1.35
2.3	EOG		V_{r-2} , V_r , V_{r+2} , V_{OUT}	-	Grid loss	1.1
6.1	EWM	1	V_{REF}	-8° : 8°	-	1.35
6.2	EWM	1	V_{REf}	180° : 180°	Grid loss	1.1

3.2.4   Parametric design results

In this paragraph, we provide fundamental results for each step of the design process described in the previous section. The investigated performances are ultimate and fatigue loads, the turbulent AEP, the total blade mass and the LCOE. It must be noticed that all the results are given as percent variation against the optimal solution identified at the previous step. Results of the first design step, on the contrary, are given as percent variation against the PoliMI Baseline 20 MW.

Step 1 - Prebend analysis

Starting from the PoliMI Baseline 20 MW, initially a parametric prebend was applied to the geometric description of the blade axis, in order to increase the blade/tower clearance and to relieve the maximum tip displacement constraint which drives the structural design of the initial solution. Configurations with a maximum prebend at tip of 2m and 4m were investigated, and each distribution was optimally designed by the dedicated submodule of Cp-Max. The final shapes are illustrated for both solutions in Figure 3-8.
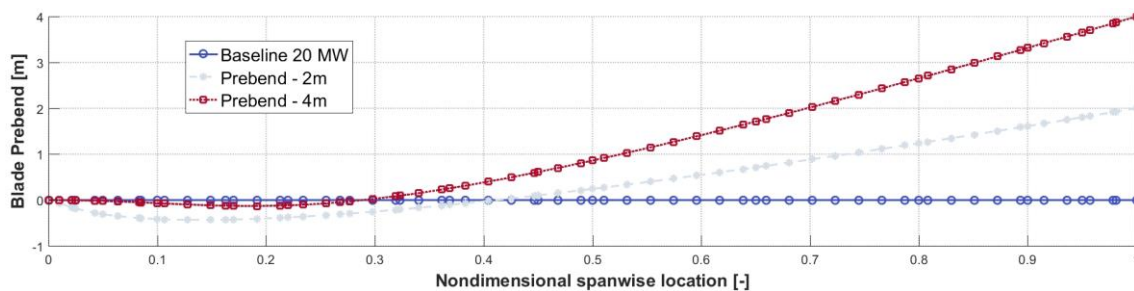
Figure 3-8 Step 1: optimal prebend distributions

The impact on the global performance is somewhat expected, and the main findings are summarized in Figure 3-9, which shows percent variations of total blade mass, AEP and LCOE of the two solutions with prebend against the Baseline 20 MW. As anticipated, the larger clearance ensures that a lighter blade can be designed for the same constraints, leading to a decrease of the blade mass. According to the formulation of the prebend optimization problem, the AEP is slightly increased in both cases, even though the huge

(Innwind.EU, Deliverable 1.25, PI-based Assessment of 20MW Wind Turbines)

flexibility associated to a larger prebend in part limits the energy gain. However, the LCOE predicted by the INNWIND.EU model is reduced in both cases.
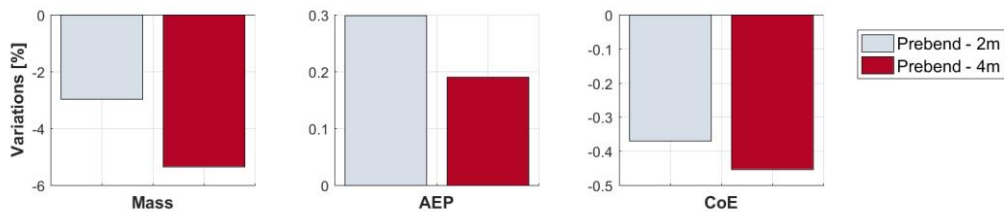
Figure 3-9 Step 1: performance variations against the PoliMI Baseline 20 MW

The percent variation of key ultimate and fatigue loads are provided in Figure 3-10 against the PoliMI Baseline 20 MW. Please notice that the first four dataset refer to ultimate loads, while the right-most columns represent fatigue DEL.

When ultimate loads are considered, they are expressed as the multi-directional 'combined' bending at each component. So, for example, the blade root bending refers to the composed flapwise/edgewise bending, whose magnitude is usually higher than the individual load components. The same applies to the hub, where the yawing/nodding bending is considered and to the tower, where the combined fore-aft/side-side is shown.
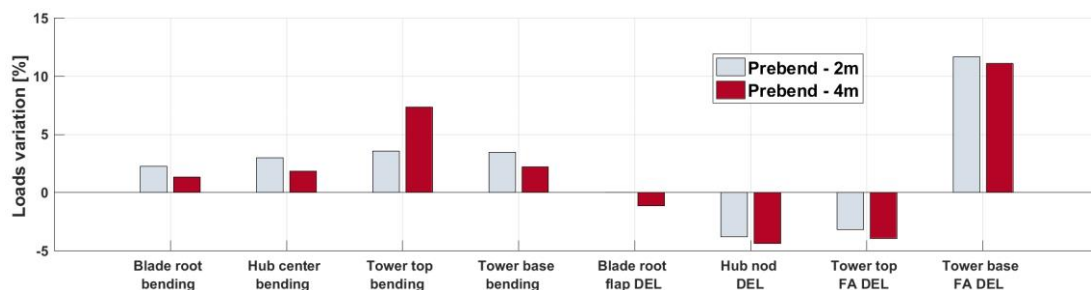
Figure 3-10 Step 1: ultimate and fatigue loads variations against the Baseline 20 MW

The results show that, with the exception of the tower base FA DEL, all key loads are encompassed in a range of approximately +/- 5% when compared against the baseline. Since the Prebend – 4m solution produces lower loads, it is considered the best one and used as starting point for the next step.

Step 2 – F-BTC Analysis

In the second step of the design procedure, we applied a parametric rotation to the fibers of the spar caps, in order to trigger the F-BTC mitigating effect. Three different configurations corresponding to rotations of 4, 6 and 8 degrees have been tested. Figure 3-12 gives the percent variation of the performance indicators against the Prebend – 4m solution, showing that an additional 2% of mass reduction can be achieved for the F-BTC 6 deg solution.

(Innwind.EU, Deliverable 1.25, PI-based Assessment of 20MW Wind Turbines)
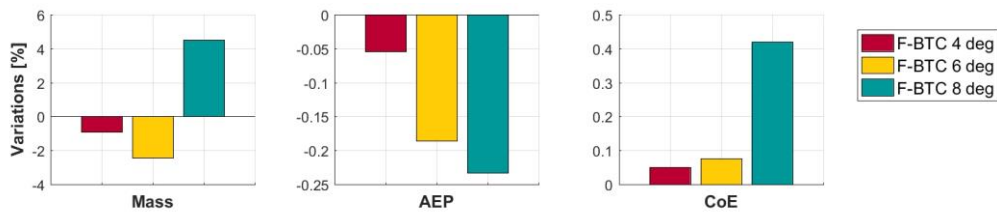
Figure 3-11 Step 2: performance variations against the Prebend – 4m solution
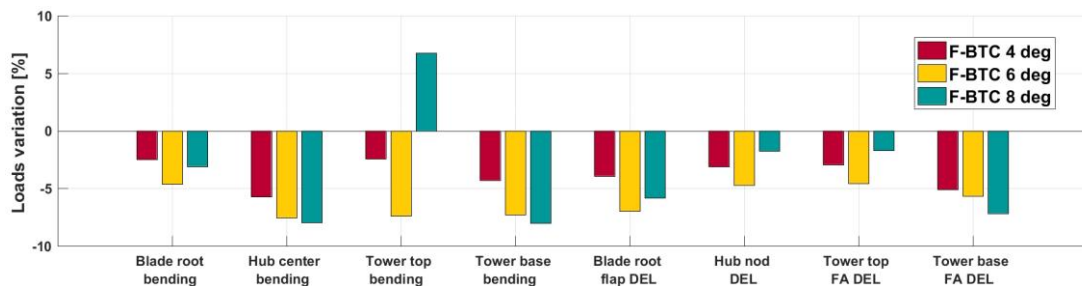
Figure 3-12 Step 2: ultimate and fatigue loads variations against the Prebend – 4m solution

However, the turbulent AEP is globally reduced, due to the increased torsional deformability which drives the sections away from their theoretical operating points. This results in a loss of aerodynamic efficiency which results in a slight loss of the energy production, and a corresponding light increase of the LCOE. However, the key loads are globally reduced, as shown in Figure 3-12.

In particular, the F-BTC 6 deg solution allows achieving a mitigation of about 5% in most load measurements, with an acceptable loss of LCOE. It must be noticed that, apart from the retuning of the pitch schedule, no advanced control strategy have been implemented in order to try to reduce the AEP losses. At the end of the second step, the solution F-BTC 6 deg is taken as the starting point for the last design step.

Step 3 – Solidity Analysis

In the last design step, we progressively redesigned the rotor of the 20 MW wind turbine for lower values of the rotor solidity. Three different configurations have been tested, with solidity equal to 98%, 96% and 94% of the initial one. For each configuration, we conducted a full aerodynamic design loop in order to redesign the chord and twist for the commanded solidity. At this stage, the optimization is done so that the AEP is maximized. Then, as done during the whole process, a full structural optimization ensures on one side that the blade mass is minimized but, at the same time, the satisfaction of fundamental integrity constraints is automatically achieved at the end of the loop.

Figure 3-13 shows the optimal chord distribution for each solution: as expected, the constraint on the commanded solidity forces the local chord to decrease and, unsurprisingly, higher reductions are obtained in the maximum chord region. The variations in the twist functions are on the contrary negligible, due to the fact that the airfoils are not changed, and thus the optimal angle of attacks for the various sections is approximately unchanged.

(Innwind.EU, Deliverable 1.25, PI-based Assessment of 20MW Wind Turbines)
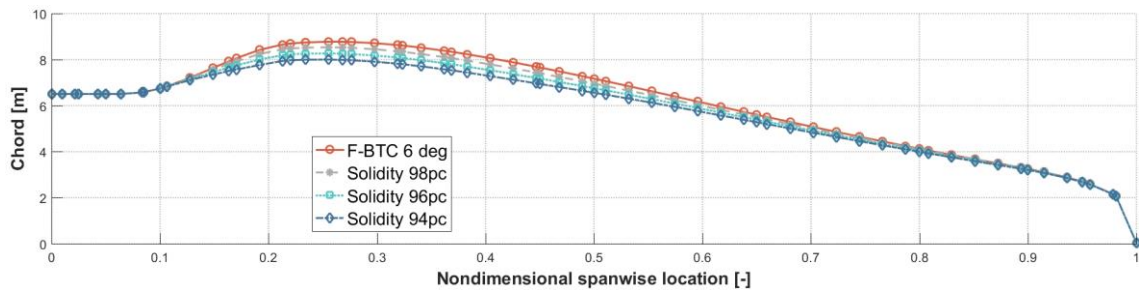
Figure 3-13 Step 3: optimal chord distributions
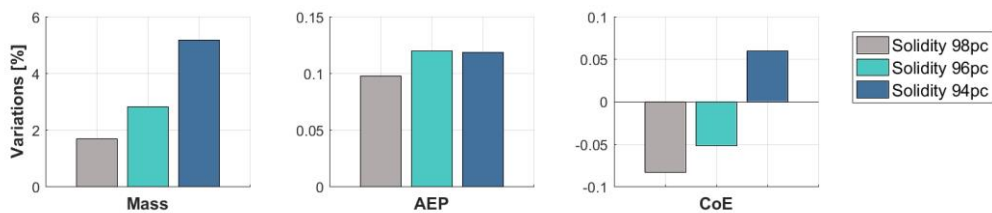
Figure 3-14 Step 3: performance variations against the F-BTC 6 deg solution

The usual comparison of the main performance is given in Figure 3-14, which clearly shows that the AEP is increased for all the solutions, mainly due to the dedicated chord optimization. At the same time, it is important to notice that reducing the planform of the blade implies that the structural components need to be thicker, since part of the stiffness and inertia properties associated to the sectional area are lost du to the reduced local thickness. The two effects, combined, lead to very small variations of the LCOE for all the solutions. On the contrary the key loads are globally reduced, as illustrated in Figure 3-15. This is mainly related to the reduced blade surface which naturally reduces the experienced loads.
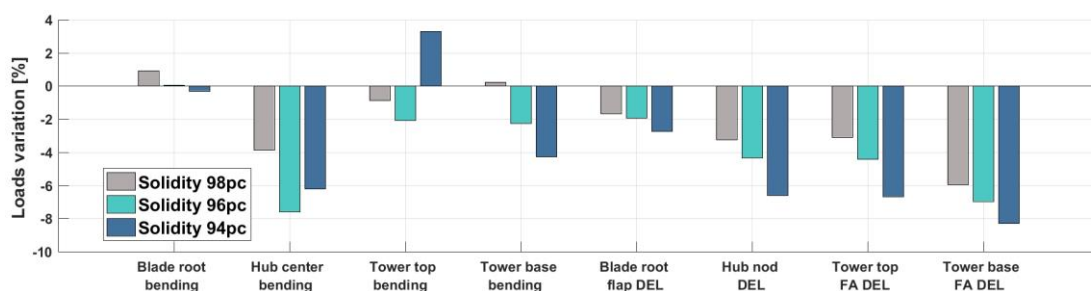
Figure 3-15 Step 3: ultimate and fatigue loads variations against the F-BTC 6 deg solution

At the end of the third step, we conclude that the solution with a solidity of 96% represents a good compromise between performance and load alleviation, so it is taken as the final configuration of this activity. The solution will be hereafter referred as Redesign 20 MW.

3.3   LCOE Impact of the Proposed Design

In the following Paragraphs, we present a direct comparison between the Baseline 20 MW presented in D 2.14 and the improved Redesign 20 MW developed as part of this activity.

(Innwind.EU, Deliverable 1.25, PI-based Assessment of 20MW Wind Turbines)

3.3.1 Effect on performance

The main differences in the aero-structural characteristics of the two solutions are provided in Table 3-2. Several high-level features of the 20 MW wind turbine have been kept frozen during the design process, then for example both solutions have the same diameter, hub height and cone and tilt angles. However the blade of the Redesign 20 MW rotor is characterized by an optimal prebend of 4 meters while the initial Baseline 20 MW rotor has a straight axis. Similarly, the optimized rotor has a fiber rotation of 6 degrees in both spar caps.

It can be appreciated how after the last step, the maximum chord of the Redesign 20 MW has been reduced to 8.27m and, as a consequence, the rotor works at a higher TSR due to the lower solidity. Although both rotors operate below the maximum tip speed of 90 m/s, the Redesign 20 MW has a slightly higher rotor speed and a slightly lower rated wind speed, which ultimately result in a higher AEP. Thanks to the different design steps, the total blade mass is reduced of about 5%, whereas the tower has not been redesigned, so that the total tower mass is identical for both wind turbines. This results globally in a cost saving of about 0.4% for the redesigned rotor. However, a different choice of the parameters of the cost model may result in slightly different considerations.

Table 3-2 Performance comparison

	Units	Baseline 20 MW	Redesign 20 MW	Variation %
Rated power	[MW]	20	20	
Rotor diameter	[m]	252.2	252.2	
Hub height	[m]	167.9	167.9	
Cone angle	[deg]	2.5	2.5	
Tilt angle	[deg]	5	5	
Rotor speed	[RPM]	6.77	6.82	+ 0.74
Max tip speed	[m/s]	89.4	89.93	+ 0.59
Optimal TSR	[-]	7.73	7.86	+ 1.68
Rated wind speed	[m/s]	11.56	11.45	- 0.95
Max chord	[m]	8.77	8.27	- 5.70
Max prebend	[m]	0	4	
Spar caps fiber rotation	[deg]	0	6	
Total blade mass	[kg]	113506	107772	-5.05
Total tower mass	[kg]	1779190	1779190	
AEP	[GWh/yr]	91.63	91.74	+0.12
LCOE	[EUR/MWh]	84.92	84.56	-0.42

3.3.2 Effect on loads

The application of the discussed redesign strategy led to a significant reduction of the main load metrics. Table 3-3 shows the fundamental ultimate loads considered during the design: it is important to notice how the blade root edgewise bending is heavily reduced,

as a consequence of the decreased blade mass. Important achievements include a 12% reduction of the combined hub/yaw bending at the hub centre and a 7% reduction in the tower base combined bending. It must be noticed that, although neither the hub nor the tower have been redesigned in this task, their accurate redesign could lead to additional economic advantages.

Table 3-3 Ultimate loads comparison

Sensor	Units	Baseline 20 MW	Redesign 20 MW	Variation %
Blade root flap	[MNm]	169.0	162.9	-3.61
Blade root edge	[MNm]	106.5	90.39	-15.14
Blade root flap/edge	[MNm]	172.8	167.1	-3.3
Hub thrust	[MN]	5.76	5.76	+0.0
Hub torque	[MNm]	42.89	42.29	-1.4
Hub yaw/nod	[MNm]	112.9	98.26	-12.9
Tower top FA/SS	[MNm]	105.3	102.5	-2.64
Tower top torsion	[MNm]	92.67	102.7	+10.8
Tower base FA/SS	[MNm]	148.0	137.1	-7.35
Tower base torsion	[MNm]	93.18	103.0	+10.5

Table 3-4 shows the main fatigue DEL considered in the design. Also in this case it is possible to notice a strong load mitigating effect: main achievements here include a 12% reduction of both the nodding and yawing DEL at the hub, while a 12% reduction is also obtained at the tower top FA DEL.

Table 3-4 Fatigue loads comparison

Sensor	Units	Baseline 20 MW	Redesign 20 MW	Variation %
Blade root flap DEL	[MNm]	83.84	75.63	-9.79
Blade root edge DEL	[MNm]	96.75	92.11	-4.80
Blade root torsion DEL	[MNm]	1.38	1.09	-21.0
Hub thrust DEL	[MN]	1.33	1.27	-4.51
Hub nod DEL	[MNm]	53.56	46.69	-12.83
Hub yaw DEL	[MNm]	49.93	44.31	-11.26
Tower top FA DEL	[MNm]	53.36	46.76	-12.37
Tower top SS DEL	[MNm]	8.42	7.57	-10.10
Tower base FA DEL	[MNm]	278.5	271.6	-2.48
Tower base SS DEL	[MNm]	204.4	164.9	-19.23

3.3.3   Effect on Annual Energy Production

As mentioned, the whole design process was based on the assessment of the turbulent AEP from the averaged time-histories during normal operating conditions (DLC 1.2). Table 3-5 shows the numeric data of the electrical power for both solutions.

Table 3-5 Averaged turbulent electrical power

Mean wind speed [m/s]	Mean electrical power [kW]	
	Baseline 20 MW	Redesign 20 MW
4	406	384
5	1095	1271
7	4344	4311

(Innwind.EU, Deliverable 1.25, PI-based Assessment of 20MW Wind Turbines)

9	8996	8981
11	15686	15716
13	19784	19774
15	19962	19969
17	19982	19977
19	19992	19992
21	19990	19983
23	19975	19994
25	19976	19997

3.3.1 Effect on CAPEX

The impact of the redesign activity on the capital expenditure is summarized in Table 3-6: as shown, the lower blade mass has a direct impact on the Turbine Capital Cost (TCC) and consequently on the wind turbine price. On the contrary, the computation of the Balance of Stations (BoS) depends mainly on the rated power of the wind turbine. Thus, since this value is the same for both rotors, the corresponding cost is unchanged. The combination of both cost items leads to a 0.46% saving in the Initial Capital Cost (ICC), which allows a similar saving on the annual Levelized Investment (LI). Due to a slight increase of the energy production for the Redesign 20 MW, the net result is a 0.4% reduction in the expected CAPEX.

Table 3-6 Contributions to the CAPEX

	Units	Baseline 20 MW	Redesign 20 MW	Variation %
Turbine Capital Cost – TCC	[kEUR]	25961	25728	-0.90
WT price/cost of components	[-]	1.4	1.4	
WT price	[kEUR]	36345	36019	
Balance of Stations - BoS	[kEUR]	34842	34842	
BoS price/cost multiplier	[-]	1	1	
Bos price	[kEUR]	34842	34842	
ICC (WT price + BoS price)	**[kEUR]**	**71187**	**70861**	**-0.46**
Capital Recovery Factor – FCR	[%]	0.074	0.074	
LI (ICC*FCR)	**[KEUR/yr]**	**5251**	**5227**	**-0.46**
Annual Energy Production	[GWh/yr]	91.62	91.74	+0.12
CAPEX (LI/AEP)	**[EUR/MWh]**	**57.31**	**56.97**	**-0.59**

3.3.2 Effect on OPEX

The impact of the redesign activity on the operations expenditure is summarized in Table 3-7. While the accountable O&M expenses are practically identical for both rotors, the higher AEP produced by the Redesign 20 MW leads to a 0.11% saving of the OPEX when compared to the initial Baseline 20 MW.

Table 3-7 Contributions to the OPEX

	Units	Baseline 20 MW	Redesign 20 MW	Variation %
Present value of total O&M – SO&M	[kEUR]	34301	34306	+0.01

(Innwind.EU, Deliverable 1.25, PI-based Assessment of 20MW Wind Turbines)

Capital Recovery Factor – FCR	[%]	0.074	0.074	
Annual Discounted O&M – DO&M	[kEUR/yr]	2530	2531	+0.04
Annual Energy Production	[GWh/yr]	91.62	91.74	
OPEX (DOE&M/AEP)	**[EUR/MWh]**	**27.61**	**27.58**	**-0.11**

3.4   Conclusions

In this work, we performed a preliminary aero-structural redesign of the Baseline 20 MW presented in the Deliverable 2.14. As part of the redesign activities, we conducted several parametric studies in order to find a suitable design strategy which can improve the performance of the Baseline 20 MW rotor.

In particular, we choose to concentrate on the load mitigation and on the total blade mass reduction rather than on the reduction of the LCOE. This choice is mainly driven by the significant ultimate and fatigue loads developed by the Baseline 20 MW, which make recommendable to adopt suitable countermeasures in order to reduce the key loads as much as possible. Future developments of this activity will focus on a proper cost-minimization design loop.

The design process was based on three different steps in which the prebend, the spar cap fiber rotation and the rotor solidity were investigated and optimized.

The resulting rotor shows a 5% reduction in the total blade mass while at the same time it achieves significantly lower loads when compared against those developed by the Baseline 20 MW. The final step led to an increase TSR which in turn ensure a slight improvement of the AEP (when computed from DLC 1.2) and a 0.4% reduction of the LCOE.

(Innwind.EU, Deliverable 1.25, PI-based Assessment of 20MW Wind Turbines)

CHAPTER 4 MAGNETIC PSEUDO DIRECT DRIVE 20MW GENERATOR (PDD)

4.1 Introduction to the Innovative Concept

4.1.1 State of the art and motivation

For many low-speed electrical machine applications it is usually weight/size and cost effective to employ a high-speed machine together with a mechanical gearbox. The disadvantages associated with mechanical gearboxes are concerns regarding reliability, acoustic noise, mechanical vibration, the need for lubrication and maintenance. In order to eliminate these concerns it is commonplace to use a direct drive machine, but careful design is required to ensure the size, mass and cost of the system do not become unfeasible.

The Pseudo Direct Drive (or PDD) is a magnetic and mechanical integration of a magnetic gear with a permanent magnet generator. This integrated approach is used to reduce the size and mass of the generator without recourse to a mechanical gearbox. The resulting drivetrain efficiency is very high as the generator is operated at higher speed (analogous to a single stage, "medium speed" system) and the "magnetic gearbox" losses are shared with the electromagnetic generator and are not additional as with a mechanical gearbox drivetrain.

A magnetic gear is a magnetic equivalent of a mechanical planetary system which has analogous components as shown in Figure 4-1. The torque is developed magnetically and there is no mechanical contact between the shafts.
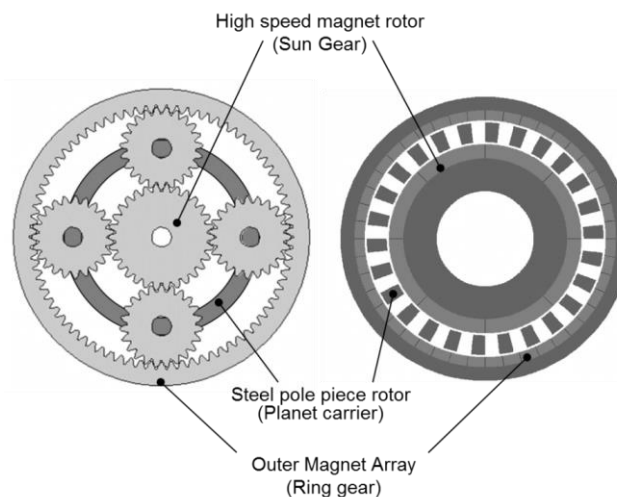
The PDD is a magnetic and mechanical integration of the magnetic gear system into the permanent magnet generator. The inclusion of a single stage gear gives the same uplift in performance to the generator system, i.e. increased rotor speed, reduced airgap torque and increased efficiency whilst allowing the size and mass of the generator to be minimized. The use of a highly integrated magnetic gear has a further series of key benefits such as:

(Innwind.EU, Deliverable 1.25, PI-based Assessment of 20MW Wind Turbines)

- The magnetic components service both the generator and the gear; hence the losses can be assumed to be shared and minimized leading to very high system efficiencies.
- The compliant nature of the gear leads to the attenuation of drive train oscillations and reduces acoustic noise.
- The magnetic gear, in very extreme circumstances, can be operated as a "torque fuse" which limits the damaging torque overload conditions that can occur during LVRT events or grid faults.
- There is no lubrication of the gear element (except bearings) and the service interval can be extended accordingly
- The integrated magnetic gear is placed in the centre of the machine and does not increase the overall volume envelope

Figure 4-2 shows a simplified diagram of a PDD. The pole-piece rotor (PPR) is driven by the blades which in turn rotates the high speed rotor that rotates inside the PPR. This action is caused by the magnetic gear, as in the same way as a mechanical planetary gear, if you hold one gear ring static a gear ratio exists between the other two rings. In this case the planet carrier (PPR) is driven whilst the ring gear (magnets mounted on the stator bore) are held static. Hence, the sun gear (high speed rotor) is forced to rotate, providing an alternating flux to the stator of the PDD. This is commutated in a conventional way to produce power.

Pole Piece Rotor (PPR) – Driven by the blades
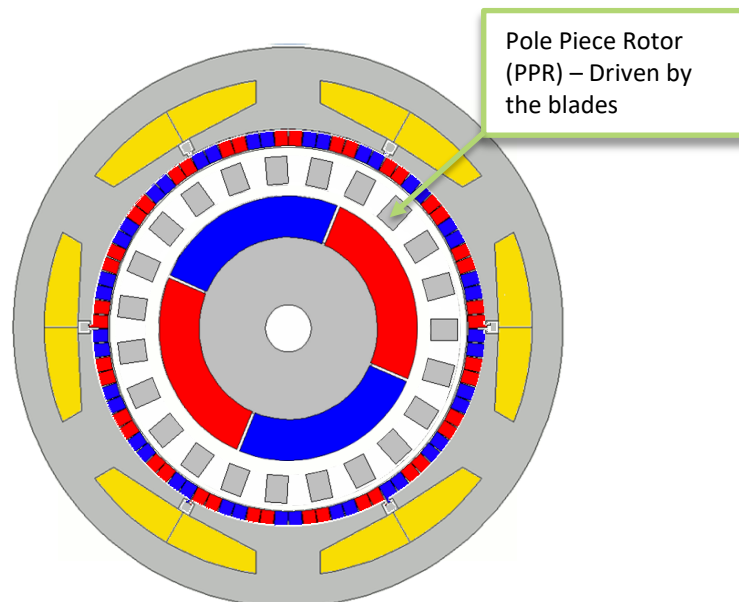
Figure 4-2 Depiction of the architecture of the PDD

4.2   Assessment of the Structural Integrity of the Proposed Design

The PDD essentially is a permanent magnet generator with magnetic gearing as shown in Figure 4-2, which allows a small gear ratio of order of 7 between input shaft rotor

connected to the main bearing and the generator rotor. This compact unit is front mounted on the 20 MW wind turbine, whose remaining configuration parameters are the same as the 20 MW RWT.

4.2.1 Design layout and dimensioning

Magnomatics have developed a full concept model of the 20MW PDD based on the electromagnetic analysis carried out by The University of Sheffield. The model includes all structural components and bearings and has been designed for a front-mounted topology. The generator is shown in various views from Figure 4-3 to Figure 4-9. The generator has been designed with a repeated modular electromagnetic structure to aid manufacturing if a modular build method is chosen, but it is also possible to use more conventional manufacturing methods.

The front-mounted design is connected to the structure as shown in Figure 4-10 (10MW PDD shown but the structure is identical).

The central king-pin is stationary and the main hub is attached to the pole-piece rotor of the PDD via a torque only connection. The pressurized rubber pads of the torsional coupling will only transmit the rotor torque to the generator, hence any non-torsional loads will result in very low reaction forces in the PDD rotor thus limiting deflections significantly. Electrical connections are routed through the king-pin to the upwind side of the generator.

As the non-torsional coupling allows movement between the blade hub and the PDD rotor, it is not possible to share the upwind main blade hub bearing with the PDD rotor as it would compromise the airgaps. Hence, two bearings are required for the pole-piece rotor and two bearings for the high speed rotor. The bearings are all mounted on the static shaft that protrudes from the king-pin and lubrication is provided by a conventional automated grease lubrication system. For the low speed (outer) bearings, the grease system is mounted on the static frame of the generator, whereas the high speed rotor bearing grease system is mounted on the high speed rotor assembly. Refills can be made at planned maintenance schedules for both systems, as access to the high speed rotor should be relatively easy through two doors in the frame and pole-piece rotor endplates, respectively.

With all front-mounted generators, the load reaction from the blades is taken through the king-pin, and hence the stator frame must be an open-ended structure which should be stiff enough to prevent significant deflection that may impair the operation of the generator (prevent airgap closure or eccentric rotation that would lead to noise and vibration). In this case, as shown in Figure 4-9, a number of thick stiffening webs have been included in the frame to increase stiffness without unduly increasing the mass. It is unclear at this stage whether the stator frame will be a single piece casting or a fabrication that is post-machined. As the electromagnetic architecture and winding design allows modularisation to be explored (stator constructed from a number of identical sub-assemblies) a number of stator frame designs could be explored for volume manufacture. Figure 4-3 to Figure 4-9 show various views of the 20MW PDD solid model.

Figure 4-3 – 20MW PDD generator concept model   Figure 4-4 – Cross section of active region
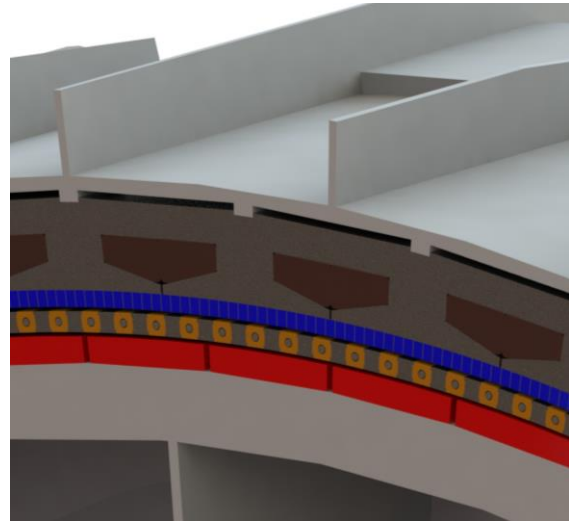
Figure 4-5 shows the generator in full cross-section where an average size man has been placed in the model for reference. It can be seen that maintenance on the internal workings (bearings, seals and grease systems) is not difficult in terms of access.
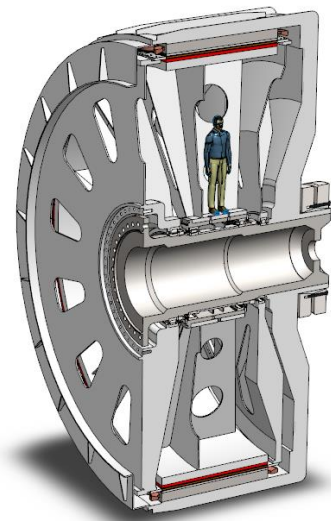
Figure 4-5 – 20MW PDD cross section showing an average height man for reference

(Innwind.EU, Deliverable 1.25, PI-based Assessment of 20MW Wind Turbines)
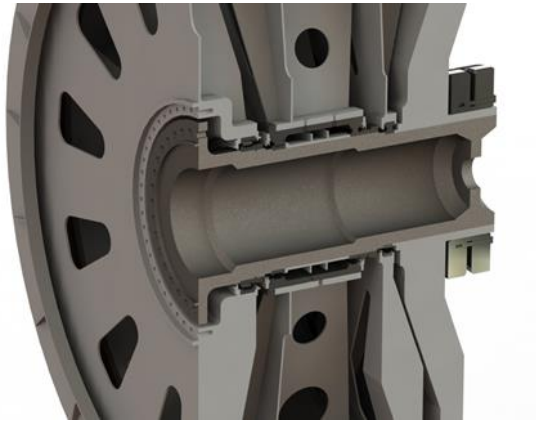
Figure 4-6 – King-pin stub-shaft and bearing details

Figure 4-7 – Active region cross section

Figure 4-8 – View of the PDD from the drive end
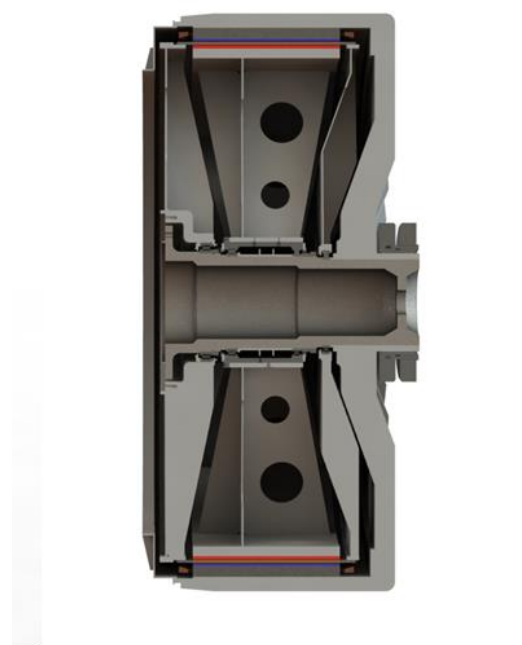
Figure 4-9 – Cross section showing stiffening webs to the stator frame and rotors
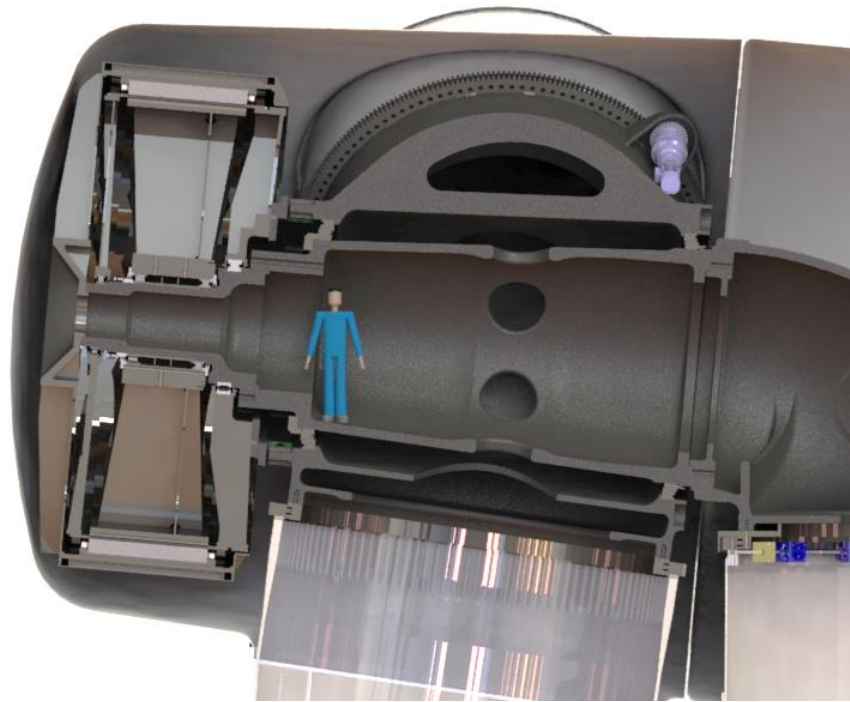
Figure 4-10 – 10MW PDD front mounted concept (identical to 20MW concept) – Courtesy of DNV-GL.

Figure 4-11 shows a general arrangement drawing of the 20MW PDD with key dimensions highlighted. The active dimensions are: 8950mm (diameter), 2400mm (length) and the overall frame dimensions are: 9420mm (diameter), 4525mm (length including frame and coupling). The total mass is 420 tons. This figure is 100 tons lighter than the estimated total mass from INNWIND sub-task 3.2.1 and is discussed in detail in section 4.3.2 of this report. Figure 4-12 and Figure 4-13 show details of the active region cross section and the active region detailed view, respectively.
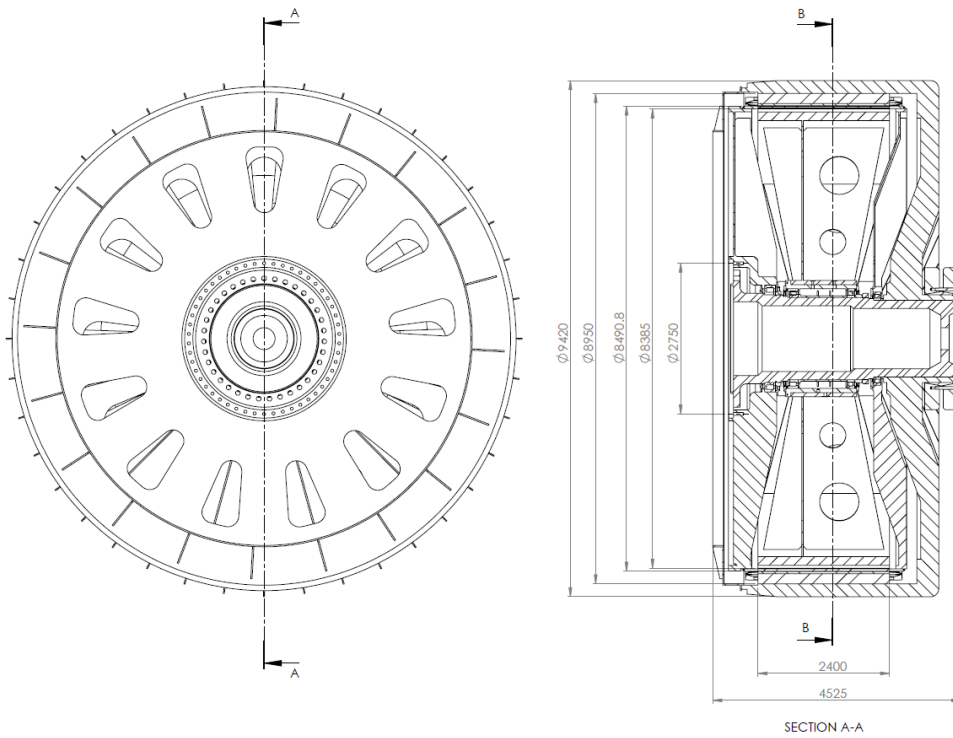
Figure 4-11- General arrangement of the 20MW PDD showing key dimensions
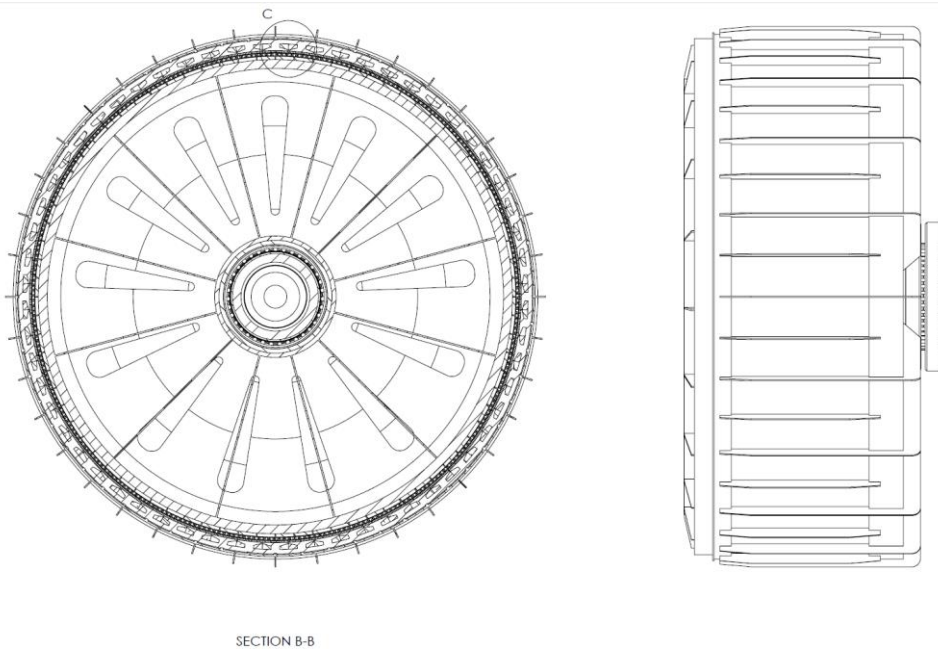
Figure 4-12 – Section B-B from above figure showing active region.
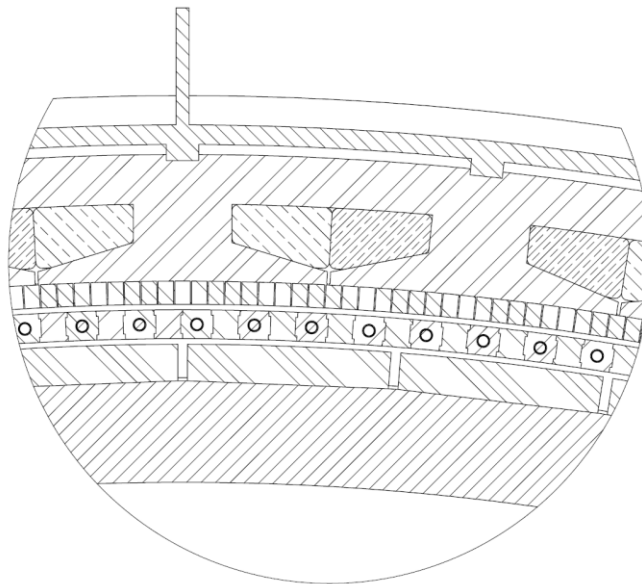
Figure 4-13 – Detail C – active region showing stator, windings, pole-piece rotor and high speed permanent magnet rotor.

In this study, the 20MW PDD generator designed for 20 MW turbines is implemented on an offshore steel jacket sub-structure. The 20 MW PDD design is evaluated in terms of fatigue and ultimate loads. The resulting loads are compared to the loads obtained on the baseline 20 MW RWT described in [1].

The 20 MW PDD turbine properties are described in Table 4-1 below and compared with the 20 MW RWT and 10MW PDD. The PDD generator is modelled as a concentrated mass located at 4 m upfront the rotor, whereas the nacelle weight, including other internal parts and components, is modelled as a concentrated mass located at 8.56 m downwind the yaw axis, acting as a counterweight. In the 20 MW RWT, the drivetrain weight is modelled as a concentrated mass added to the nacelle weight.

Table 4-1 Comparison of the RNA parameters of the 20 MW PDD turbine with the 10 MW PDD Turbine.

	10 MW PDD	20 MW PDD	20 RWT
Rotor size [m]	178	252	252
Distance along shaft from hub to Yaw axis [m]	5.31	7.13	10
Distance along shaft from hub to main bearing [m]	1.76	2.36	6.22
Hub mass [ton]	149.01	385.22	278
Hub inertia about low speed shaft [kg m^2]	2474705.87	12115772.17	1710000
Nacelle mass [ton]	240.01	587.85	1098
Nacelle inertia about Yaw axis [kg m^2]	9306677.45	45348724.05	3.607E+04
Nacelle CM downwind of yaw	-5.86	-8.56	3.83
Nacelle CM above yaw	2.27	2.68	3.39
Rated rotor speed	9.60	7.14	7.14

(Innwind.EU, Deliverable 1.25, PI-based Assessment of 20MW Wind Turbines)

Gear ratio	7.50	7.50	48
Generator inertia about LSS (Tons m^2)	1859	9600	19.247E+03
Drivetrain damping (free-free) [% critical]	5	5	5
Free-Free torsional frequency [Hz]	5.42	1.28	1.28

Modal analyses are performed for the overall structure at stand-still position. Resulting natural frequencies are presented in Table 4-2.

Table 4-2 Overall structure's natural frequency - 20 MW RWT and 20 MW PDD

Mode No.	RWT 20 MW	PDD 20 MW
1st fore-aft mode	0.163	0.161
1st side-side mode	0.169	0.166
1st fix-free mode	0.350	-
1st asymmetric flap with yaw	0.391	0.391
1st asymmetric flap with tilt	0.422	0.424
1st collective flap mode	0.452	0.451
1st assymetric edge1	0.656	0.657
1st assymetric edge2	0.666	0.668
2nd assymetric flap with yaw	0.960	0.930
2nd assymetric flap with tilt	1.050	1.030

4.2.2 Load cases considered

The design load cases are based on the IEC 61400-3. For the fatigue load analysis is considered DLC 1.2, whereas DLC 1.3 and 6.2 are assessed for the ultimate load analysis.

DLC 1.2: 16 load directions are simulated (full-cycle with 16 sectors and 22.5° step) for 11 wind speeds (5 - 25 m/s with 2 m/s step) accounting for yaw errors of ±10°. One seed per scenario is considered. Wind, wave are aligned. Overall 528 simulations are run.

DLC 1.3: 6 load directions are simulated (half-cycle with 6 sectors and 30° step) for 11 wind speeds (5 - 25 m/s with 2 m/s step) accounting for yaw errors of ±10°. Three seeds per scenario are considered. Wind, wave and currents are aligned. Overall 594 simulations are run.

DLC 6.2: 24 load directions are simulated (full-cycle with 24 sectors and 15° step) at 50 m/s. Three seeds per scenario are considered with no yaw misalignment. Wind, wave and currents are aligned. Overall 72 simulations are run.

The load sensors evaluated are presented in Table 4-3.

Table 4-3 Load sensors description

Load sensor		Wholer exponent m
MxTB	Tower bottom fore-aft	3
MyTB	Tower bottom side-side	3

(Innwind.EU, Deliverable 1.25, PI-based Assessment of 20MW Wind Turbines)

MxTT	Tower top tilt	3
MyTT	Tower top roll	3
MzTT	Tower top yaw	3
MxMB	Main bearing tilt	3
MyMB	Main bearing yaw	3
MzMB	Main bearing torsion	3
MxBR	Blade root flap	10
MyBR	Blade root edge	10
MzBR	Blade root torsion	10

The PDD generator is connected and supported to the main shaft using 2 main bearings as versus one main bearing for the reference wind turbine.

4.2.3 Structural integrity verification

Ultimate load analysis is conducted for DLC1.3 and 6.2. Figure 4-14 provides an overview of the computed ultimate loads normalized on the RWT 20 MW. It is seen a substantial reduction of ≈50% of the shaft bending moments at the main bearing (both the upwind and downwind bearings for PDD 20 MW) compared to the baseline model. This reduction is partly due to the fact that there are two main bearings used now. It is also observed an increasing MxTT–Tower Top tilt bending moment at the yaw bearing for the PDD 20 MW, resulting in ≈40% higher loads compared to the baseline. This follows from the overhanging additionally mass of the PDD generator located in front of the rotor at about 11.19 m from the yaw axis. For the other loads sensors evaluated in this study, a slightly difference about 1-2% is observed between the two models for the ultimate loads. Table 4-4 summarizes the ultimate loads in terms of moments and forces for the shaft at the main bearings, for tower top at the yaw bearing and at the interface between tower-jacket.
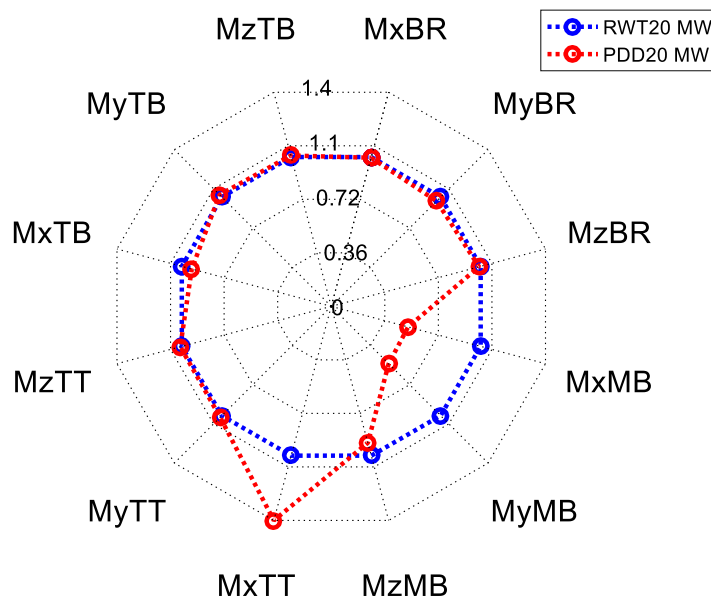
Figure 4-14 Comparison of ultimate loads - RWT 20 MW vs PDD 20 MW

(Innwind.EU, Deliverable 1.25, PI-based Assessment of 20MW Wind Turbines)

Table 4-4 Ultimate loads for shaft, tower top and interface - RWT 20 MW and PDD 20 MW

Shaft	MxMB [kNm]	MyMB [kNm]	MzMB [kNm]	FxMB [kN]	FyMB [kN]	FzMB [kN]
20 MW RWT	146269	143706	45823	9914	9847	6288
20 MW PDD (UW)	75253	75446	41881	5828	5762	3200
20 MW PDD (DW)	70096	68638	6415	5821	5903	3200
Tower Top	MxTT [kNm]	MyTT [kNm]	MzTT [kNm]	FxTT [kN]	FyTT [kN]	FzTT [kN]
20 MW RWT	131446	54095	151727	2592	5596	25103
20 MW PDD	188472	54934	153275	2795	5575	26869
Interface	MxTB [kNm]	MyTB [kNm]	MzTB [kNm]	FxTB [kN]	FyTB [kN]	FzTB [kN]
20 MW RWT	756871	419022	153937	3370	6760	43224
20 MW PDD	706477	427643	155521	3649	6934	45013

Figure 4-15, Figure 4-16 and Figure 4-17show the mean (black), maximum (blue), minimum (red) ultimate loads trends as function of wind speeds including DLC1.3 and DLC6.2. A square-marker is used for the baseline model and a star-marker for the PDD model.
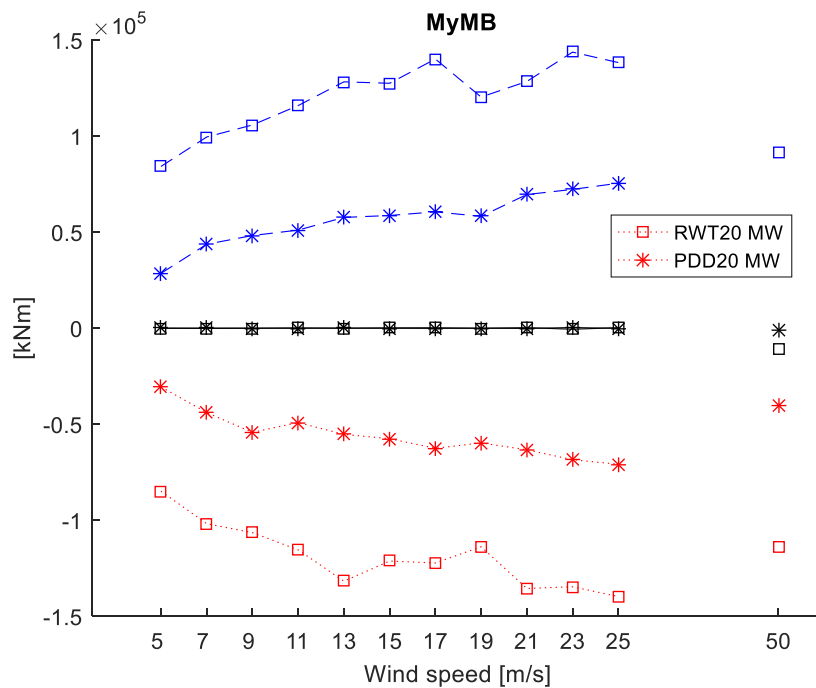
Figure 4-15 Ultimate loads for MyMB – RWT 20 MW and PDD 20 MW vs wind speeds

(Innwind.EU, Deliverable 1.25, PI-based Assessment of 20MW Wind Turbines)
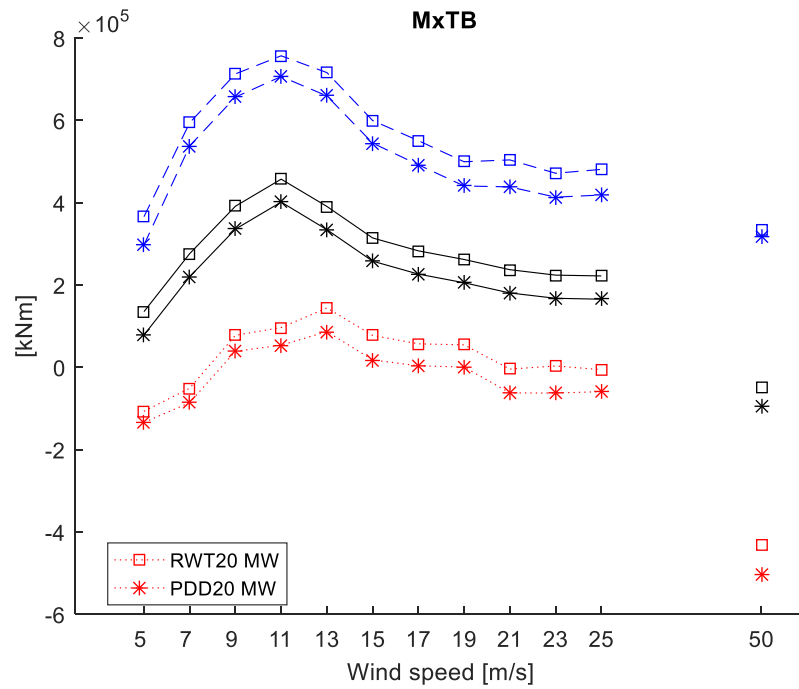
Figure 4-16 Ultimate loads for MxTB – RWT 20 MW and PDD 20 MW vs wind speeds
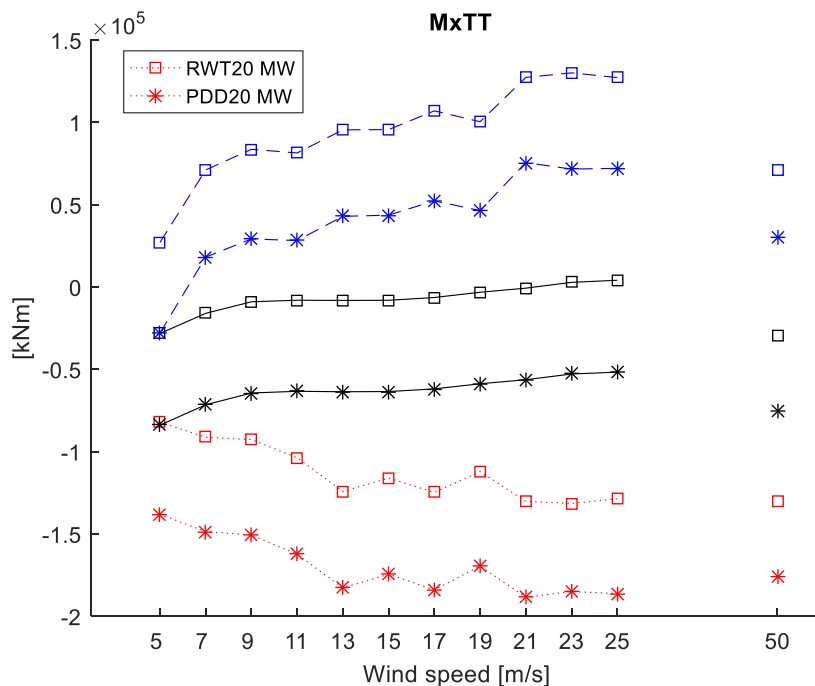
Figure 4-17 Ultimate loads for MxTT – RWT 20 MW and PDD 20 MW vs wind speeds

The fatigue loads are given as a damage equivalent load of 10^7 cycles corresponding to 25 years life time damage. Figure 4-18 illustrates the comparison of lifetime fatigue loads normalized on the RWT 20 MW. The PDD configuration delivers reduced fatigue loads of ≈60% at the shaft main bearings (2 in number) compared to the RWT (1 bearing). Even

though a fair comparison would require the RWT to be modelled as two-main bearings, these results indicate that PDD setup for 20 MW turbines has potential for delivering reduced fatigue loads at main bearings. Besides, a reduction of ≈30% of the shaft torsion is observed by the PDD. This is achieved due to the lower inertia of the PDD generator. Slightly increased tower top tilt and yaw moments are observed for the PDD setup. Table 4-5 summarizes the lifetime fatigue loads for the shaft, tower top and at the interface between tower-jacket.

Table 4-5 Fatigue loads for shaft, tower top and interface for RWT 20 MW and PDD 20 MW

Shaft	MxMB	MyMB	MzMB	FxMB	FyMB	FzMB
20 MW RWT	75643	75535	3381	13225	13200	956
20 MW PDD (UW)	33464	33438	2386	7674	7655	471
20 MW PDD (DW)	29570	29542	-	7639	7743	477
Tower Top	MxTT	MyTT	MzTT	FxTT	FyTT	FxTT
20 MW RWT	56177	5438	54424	483	977	881
20 MW PDD	58776	5938	56752	569	973	1112
Interface	MxTB	MyTB	MzTB	FxTB	FyTB	FxTB
20 MW RWT	84668	84758	55720	802	1889	1091
20 MW PDD	83250	83692	58067	1015	2002	1394
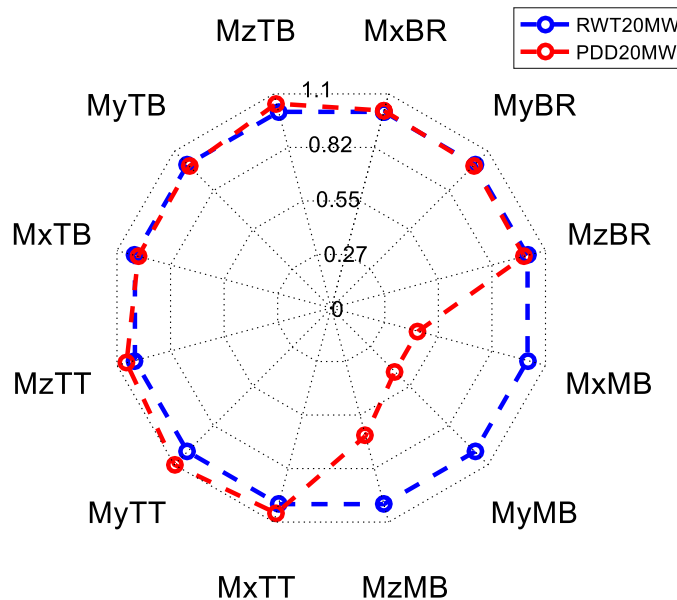
Figure 4-18 Comparison of lifetime fatigue loads - RWT 20 MW and PDD 20 MW

Figure 4-19, Figure 4-20, Figure 4-21, and Figure 4-22 illustrate the 1-Hz fatigue loads for the critical load channels. A square-marker is used for the baseline model and a star-marker for the PDD model.

(Innwind.EU, Deliverable 1.25, PI-based Assessment of 20MW Wind Turbines)
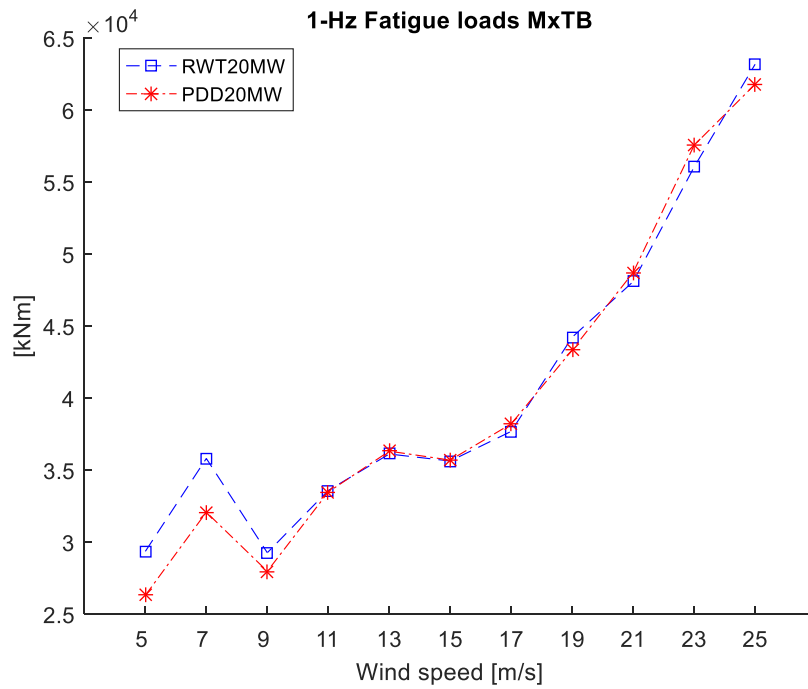
Figure 4-19 1-Hz fatigue loads for MxTB
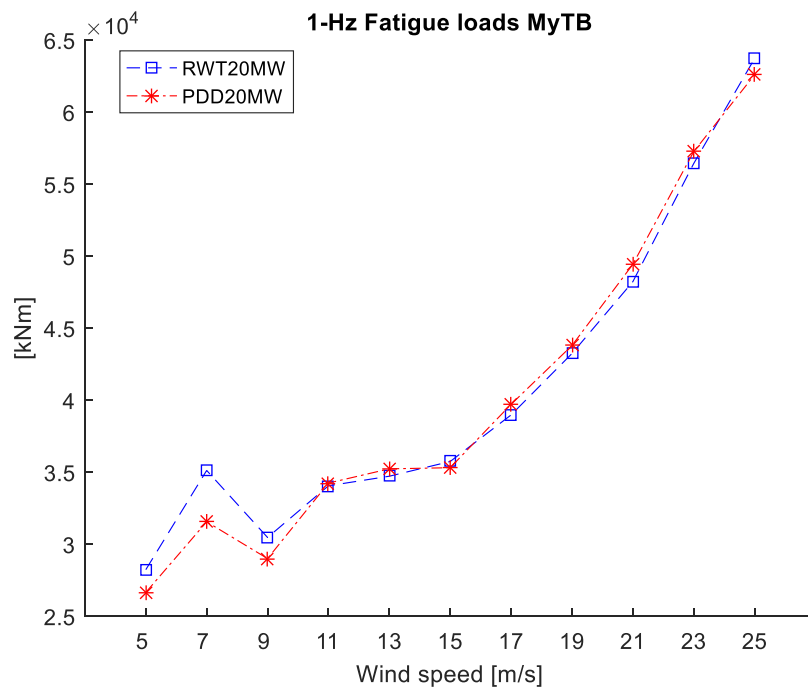
Figure 4-20 1-Hz fatigue loads for MyTB

(Innwind.EU, Deliverable 1.25, PI-based Assessment of 20MW Wind Turbines)
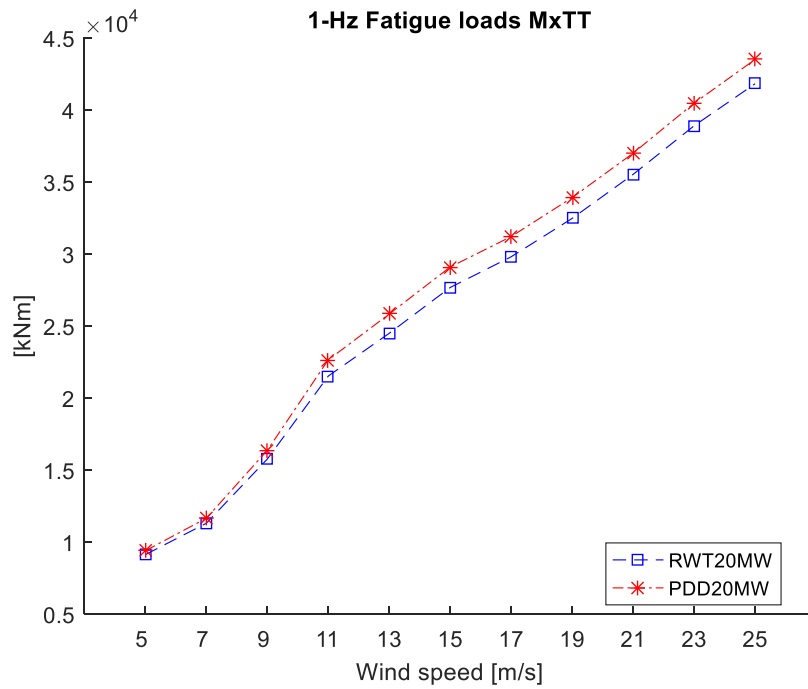
Figure 4-21 1-Hz fatigue loads for MxTT
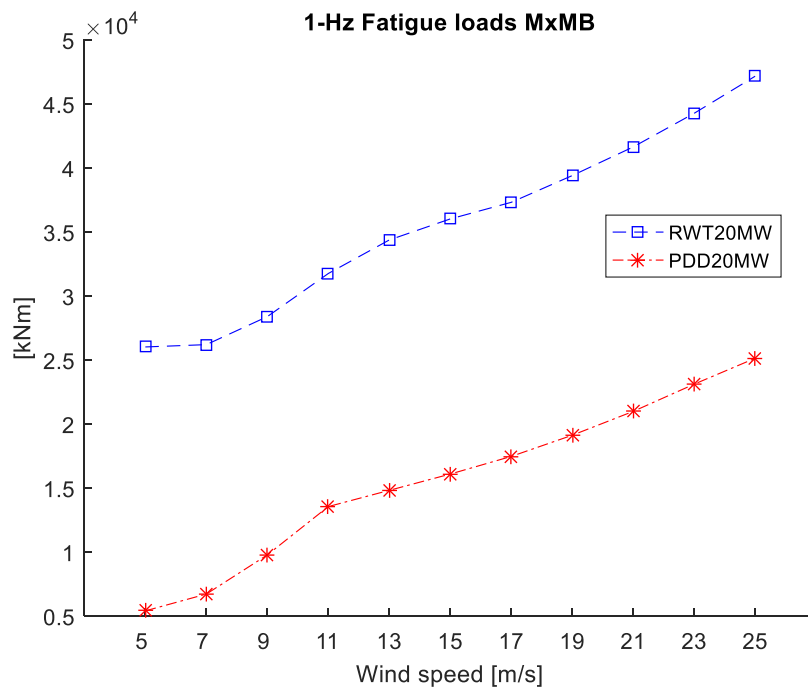
Figure 4-22 1-Hz fatigue loads for MxMB

(Innwind.EU, Deliverable 1.25, PI-based Assessment of 20MW Wind Turbines)

4.3 LCOE Impact of the Proposed Design

4.3.1 Effect on Annual Energy Production

For a given site and wind speed distribution, the Annual Energy Production is made up of a number of contributing factors. Some of these factors such as height and location of the turbine are common to all generator types, so can be disregarded in any comparison with the RWT. The two major factors that distinguish one generator's performance in terms of AEP from another are the energy conversion efficiency from the mechanical input at the shaft to the electrical power delivered to the grid, and the "up-time" of the generator (utilisation factor). As the power electronic converters for the RWT and the PDD will be nominally identical in terms of their operating efficiency, the key differential between RWT and PDD AEP is realised by the generator efficiency.

The basic efficiency curve for the 20MW PDD has been reported in INNWIND sub-task 3.2.1 (Penzkofer) at 98.75% at rated load. However, this basic analysis took no account of magnet eddy current losses or bearing losses. The original estimate of electromagnetic efficiency is shown in Figure 4-23.
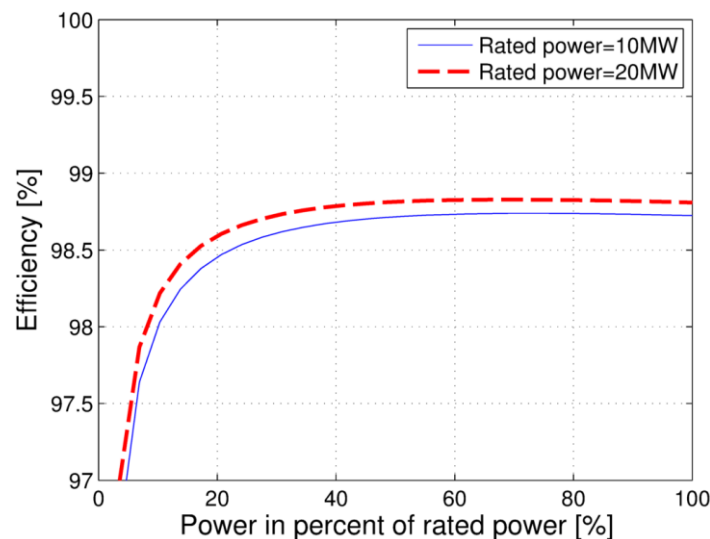
Figure 4-23 Electromagnetic efficiency of the 10MW and 20MW PDD designs from INNWIND sub-task 3.2.1.

Whilst the bearing losses are a function of the bearing type, loading, speed, lubrication quality and environment (predominantly imposed by the turbine structure and operating conditions), the magnet eddy current losses are a function of the individual size of the magnets. The physical dimension of the magnet segmentation is therefore considered to be a design variable in determining the operating efficiency of the PDD. Whilst eddy current losses in the magnets can rise to high levels if segmentation is not employed, the smaller the segmentation length, the lower the losses, and as the degree of segmentation is linked to manufacturing costs for the magnets, there is a trade-off between magnet costs and efficiency (CAPEX and AEP). This report does not discuss the cost/benefit analysis of the trade-off, but it highlights an opportunity in either reducing CAPEX by providing little segmentation of the magnets or increasing AEP through greater segmentation leading to an increase in AEP but higher CAPEX. Each of these will be

weighted accordingly in the calculation of LCOE for offshore operation. CAPEX is discussed in section 4.3.2 of this report.

3D analysis of eddy currents in the magnets of large PDDs has been carried out, and segmentation lengths proposed to meet sustainable thermal management targets and also efficiency targets. Although the magnet eddy currents have not been modelled for the 20MW concept design, it is reasonable to assume from past modelling on 300kW and 500kW generators that the efficiency will drop by around 0.25% (magnet segmentation is carried out to such a degree to meet this condition). Hence the efficiency at rated load will reduce from 98.75% (INNWIND sub-task 3.2.1) to 98.5% at rated load. As the magnet eddy current losses are a function of speed squared, the shape of the efficiency curve in Figure 4-23 would retain the same basic shape.

Overall efficiency is still higher than the RWT, where the PDD in general would allow for about 3% increased energy capture as compared to the RWT due to the high efficiency of energy conversion afforded by the mechanical and magnetic integration of an (effectively) medium speed PM generator and magnetic gear. The PDD avoids the inefficiency of both a mechanical gear system and the highly electrically stressed direct drive system.

Reliability can be a major contributor to AEP, and the subject of reliability and its effects on OPEX is covered in section 4.3.3 of this document. It is assumed that on reaching TRL 9 for multi-megawatt size generators that a PDD generator will have the same net effect on OPEX as a PMG due to the similar MTBFs. The effect on AEP is therefore dominated by the increase in energy capture afforded by the PDD (~3%) which is directly proportional to a reduction in LCOE.

A second order effect of a higher operating efficiency is the reduction in ancillary cooling equipment requirements, which in turn acts to reduce OPEX and boost reliability.

4.3.2   Effect on CAPEX

The cost of manufacture of large PDDs has been investigated with a large generator manufacturer and found to be close to the cost of an equivalent PMG. The comparison included raw material costs, processing costs, tooling and manufacturing labour. The costs for a 20MW PDD have not been considered beyond the raw material prices. In order to gain a useful level of detail, a concept model of the 20MW PDD has been developed and a basic bill of materials produced with all major components present, including bearings.

Table 4-6 shows the bill of materials (BOM) and mass breakdown of the 20MW PDD generator. It can be seen that the total mass of the PDD is around 420 tons which is 100 tons lighter than the estimated mass reported in INNWIND.EU sub-task 3.2.1. The difference is due to very basic early estimates based on simple ratios of active to structural material, whereas the latest estimate is based on a concept solid model as described in section 4.2.1. Table 4-7 shows the breakdown in terms of material type, the associated material prices per ton that have been assumed in the study, the resulting costs for each material and the total material cost of the 20MW PDD generator. It can be seen that the total material costs are around 3.6M€.

(Innwind.EU, Deliverable 1.25, PI-based Assessment of 20MW Wind Turbines)

Table 4-6 – Bill of Materials (BOM) for the 20MW PDD concept model

ITEM NO.	PART NUMBER	DESCRIPTION	QTY.	MATERIAL	MASS each [kg]	MASS total [kg]
1	20MW_28MNm_SM01585	Sub-Assembly, High Speed Rotor	1		129211.6	
1.1	20MW_28MNm_PM05916	High Speed Rotor Hub, 20MW	1	BS EN 10025 Grade S275	95734.16	95734.16
1.2	20MW_28MNm_PM05915	High Speed Rotor Magnet	80	Neo - N48SH	290	23200
1.3	20MW_28MNm_PM05914	Bearing Carrier, 20MW	1	BS 970 080M40 (EN8)	4924.27	4924.27
1.4	20MW_28MNm_PM05913	Seal Housing, HSR	2	BS EN 10025 Grade S275	255.06	510.12
1.5	20MW_28MNm_PM05912	Seal Retaining Plate	2	BS EN 10025 Grade S275	29.43	58.86
1.6	hsr free brg nu18_1500m1		1		750	750
1.7	hsr fixed brg nup28_1500m		1		1040	1040
2	20MW_28MNm_SM01584	Sub Assembly, Pole Piece Rotor and Shaft, 10 MW	1		66776.54	
2.1	20MW_28MNm_PM05911	Pole Piece	300	M450-65A	32.92	9876
2.2	20MW_28MNm_PM05910	Pole Piece Spacer Bar, 10MW	300	Glass Fibre EPC205	8.74	2622
2.3	20MW_28MNm_PM05909	Pole Piece Rotor End Ring, 10MW	2	BS EN 10088-2 1.4404 (316L)	2175.17	4350.34
2.4	PM05_20mw	PPR Endplate DE	1	BS EN 10025 Grade S355	31934.98	31934.98
2.5	20MW_28MNm_PM05907	Pole Piece Rotor End Plate Rear, 10MW	1	BS EN 10025 Grade S355	14437.13	14437.13
2.6	20MW_28MNm_PM05902	M16 Tie Rod, 10MW	300	Bumax 88 / 316L	4.64	1392
2.7	Washer ISO 7091 - 16		600			0
2.8	ISO 7042-M16-N		600			0
2.9	20MW_28MNm_PM05901	Bearing cover	1	BS EN 10025 Grade S275	214.72	214.72
2.1	hsr fixed brg nup28_1600m		1		1320	1320
2.11	hsr free brg nu18_1400m		1		625	625
3						
3.1	20MW_28MNm_SM01499	Stator Assembly, 20MW	1		176161.1	
3.1.1	20MW_28Nm_stator lams 2	Stator laminations	1	M450-65A	73965.61	73965.61
3.1.2	20MW_28MNm_PM05687	Stator Winding, 20MW	60	Copper 40%	238.46	14307.6
3.1.3	20MW_28MNm_PM05675	stator case, 20MW	1	BS EN 10025 Grade S275	71346.44	71346.44
3.1.4	20MW_28MNm_PM05665	Stator Magnet	1040	Neo - N48SH	14.43	15007.2
3.2	20MW_28MNm_PM05894	Input End Shield, 20MW	1	BS EN 10025 Grade S275	7306.87	7306.87
5	tas_3071-1000	Shrink disc	1	steel	13831.17	
5.1	tas_3071-1000_3		1	steel	819.34	819.34
5.2	tas_3071-1000_1		1	steel	6152.98	6152.98
5.3	tas_3071-1000_2		1	steel	6343.12	6343.12
5.4	tas_3071-1000_4		50	steel	10.31	515.5
6	20MW_28MNm_SM01583	Assembly, static Shaft	1		28201.33	
6.1	20MW_28MNm_PM05906	static shaft	1	BS 970 817M40T (EN24T)	26122.62	26122.62
6.2	20MW_28MNm_PM05905	Bearing Spacer	1	BS EN 10025 Grade S275	1202.12	1202.12
6.3	20MW_28MNm_PM05904	Locknut	1	Plain Carbon Steel	330.53	330.53
6.4	20MW_28MNm_PM05903	Bearing Spacer	1	BS 970 080M40 (EN8)	269.73	269.73
6.5	20MW_28MNm_TR1600 locknut	Locknut	1	Plain Carbon Steel	276.33	276.33
					TOTAL	416956

Table 4-7 – Material costs for the 20MW PDD concept design.

Material	Mass [tons]	EUROS/ton	Cost (kEUROS)
Copper Windings	14.3	15000	215
Magnets (N48SH)	38.2	60000	2292
Laminations (M400-65A)	83.8	3000	252
Glass Fibre Compsosite	2.6	15000	39
Structural steel (S355)	278.0	3000	834
TOTAL	417.0		3632

Whist there is a significant reduction in main shaft bending moments and torsion, it is not expected to result in a significant reduction in drive train CAPEX (other than what might be expected from the PDD itself), since the PDD would require two main bearings. Furthermore, the tower top mainframe and flange supporting the nacelle would need further material to support the significantly higher tower top bending moments for the PDD.

(Innwind.EU, Deliverable 1.25, PI-based Assessment of 20MW Wind Turbines)

4.3.3 Effect on OPEX

OPEX analysis considers all forms of expenditure to do with operations and maintenance of the offshore turbines. Section 4.2.1 described the PDD operation and Figure 4-3 to Figure 4-9 showed the detail of the 20MW PDD. Fundamentally, the PDD is a permanent magnet generator with an additional rotor, so it is sensible to make comparisons with direct drive PM generators to summarise the effect on OPEX of employing a PDD generator in a 20MW offshore wind turbine.

The output rotor (or pole-piece rotor) is connected to the blades via a torsional coupling (torque only connection), and the high speed rotor is free (unconnected) and rotates internally to the output rotor. At steady state speed, there is no torque on the high speed rotor, as this is reacted by the stator magnets. Hence, there is very little stress or strain in the high speed rotor other than the self-loading and it is isolated from any non-torsional loads. The high speed rotor bearings are therefore lightly loaded, and for a front-mounted design with flexible coupling between the output rotor and blade hub, there will be negligible influence from external sources due to wind loads. In addition, the bearings must straddle the static output shaft in the front-mounted design which results in the selection of over-sized bearings for the operating loads considered (~1.4m in diameter) and thus the bearings will have a long lifetime. Magnomatics have not investigated the lifetime of the high speed rotor bearings for such large generators, but the speeds and loads are well within SKF bearing guidelines.

Figure 4-24 shows a cross section of the 20MW PDD where the location of the various bearings has been highlighted. It can be seen that the two high speed bearings are mounted on the King-pin stub-shaft. It has been assumed that the static stub shaft will be sized to take the fatigue loads of the generator and also ensure displacement is within the specified tolerances for the bearings so as not to reduce their life expectancy. As the front-mounted generator is isolated to a large degree from the non-torsional loads of the blades, this is a valid assumption.

Given that the low speed bearings (DE and NDE bearings in Figure 4-24) are common to direct drive PMG designs, and that the high speed bearings are within established operating loads and speeds for the given lubrication type, it is assumed that the MTBF of the bearings can considered to be similar to that of the PMG's. Magnomatics have no test data to validate this assumption, and it is recommended that any follow-on programme will include the investigation of bearing lifetimes, but if the appropriate bearing selection can be made, then the lifetime can be similar to that of a PMG.

Rotor failure on PMGs is exceptionally rare, as much research has been poured in to magnet containment and retaining features, corrosion prevention and magnet eddy current loss modelling. Hence, the permanent magnet rotor can be considered to have a similar MTBF to PMG rotors.

The pole-piece rotor of the PDD is still the subject of de-risking through various demonstrator programmes at Magnomatics, with the latest rotor going on test in Q1 2018 at the Ocean Renewable Energy Centre in Blyth, UK. This is a 2m diameter pole-piece rotor for a 500kW wind turbine generator that carries the same design features and employs the same modelling as will be applied to an 8m diameter rotor for a 20MW generator. Although at present the MTBF for a PPR at a large scale is unknown, test data from other

smaller machines has shown that the modelling methods and manufacturing methods result in a simple robust structure.

The stator of the PDD carries the outer magnets and details of the magnet retaining features on a 500kW generator have been reported in INNWIND report 3.2.3. These features ensure the magnets remain bonded in position and prevent them from entering the airgap. A similar method has been tested on a 300kW PDD with very good results with 1000s of hours of operation without any degradation in the structure. The updated approach that is more amenable to large machine manufacturing is currently being trialled in the 500kW wind turbine generator under the DEMOWIND Compact High Efficiency Generator (CHEG) project in Q1 2018 – a collaboration between Magnomatics, ATB Laurence-Scott, ODSL and EDF.

Although the cumulative effect of all the features unique to a PDD compared to a PMG result in the PDD being assigned a lower TRL, consideration of the current stage of development of the PDD shows that it should be possible for a PDD to be as reliable as a PMG after more development iterations at increasing scale have de-risked the various novel technologies in the PPR and the magnet retaining features.

The technological differences between a PMG and a PDD should not result in increased maintenance schedules or lower MTBF, so the effects of the potential failure modes on OPEX can be considered to be neutral.
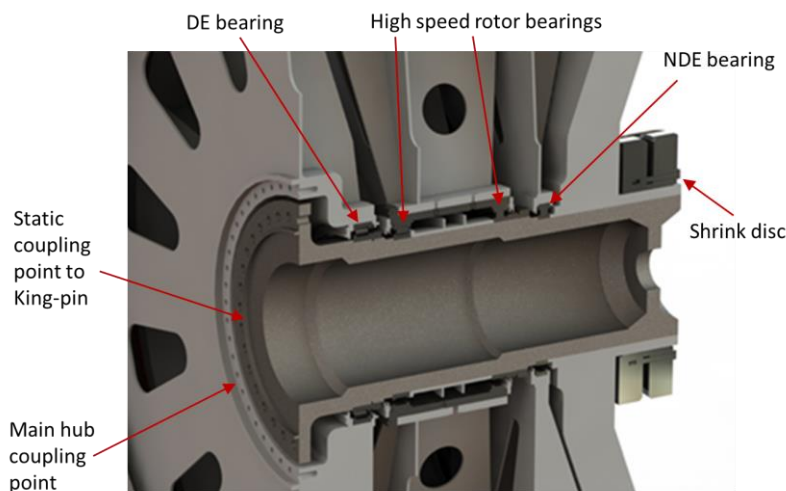
Figure 4-24 – Details of the king-pin stub-shaft and bearing locations.

The reduced fatigue on the main shaft due to the low inertia of the generator would allow longer life of the main shaft and main bearings. This can in turn reduce the OPEX due to reduction in unplanned maintenance, lower downtime and lower inventory costs.

4.4   Conclusions

A 20MW Concept design has been developed for the PDD and a detailed BOM produced from a solid model of the generator. The capital cost of the generator has been estimated

at 3.6M€ for materials but no further analysis was possible on manufacturing costs at this stage.

The PDD is assumed to offer no change in OPEX compared to the RWT. The largest contribution to a reduction in LCOE is due to the very high efficiency afforded by the magnetic gear and electrical machine integrated combination. Rated efficiency of 98.5% compared with the RWT drive-train results in an improved energy capture of around 3%. The calculation of LCOE is directly proportional to the AEP to a first order, so assuming that OPEX and CAPEX are similar, the higher energy transmission efficiency directly paves the way for a reduction of about 3% in LCOE.

It is the responsibility of ongoing and future programs to verify the efficiency, OPEX and CAPEX through engagement with OEMs and tier 1 suppliers on demonstrator programs that seek to push the boundaries beyond the current largest PDD which is rated at 500kW.

Ultimate and fatigue loads analysis is evaluated for 20 MW wind turbines setup with PDD. The 420 tons PDD is mounted upfront the rotor at a distance of 11.19 m from yaw-axis. For a more realistic comparison with the baseline 20 MW RWT turbine, the shaft of the PDD setup is supported by two main bearings located at respectively 2.36 m upwind and downwind the rotor. This model configuration achieves a significant improvement over a 1 main bearing RWT in both ultimate and fatigue loads on the shaft, which suggests the PDD as design solution for main shaft loads mitigation.

An ultimate load reduction of ≈50% has been demonstrated for the shaft bending moments (both tilt and yaw) and a reduction of fatigue loads of ≈60%. Besides, due to reduced inertia of the PDD generator, the fatigue torsion at the shaft is found 30% less than baseline configuration. Eventually, due to the additional mass located upfront the rotor in the PDD setup, increased ultimate loads of about 40% are observed for the tower-top tilt moment compared to the baseline.

(Innwind.EU, Deliverable 1.25, PI-based Assessment of 20MW Wind Turbines)

CHAPTER 5 20MW JACKET DESIGN

The jacket design for the 20 MW wind turbine is briefly described in this chapter. The structure has been developed using two design phases. Firstly, a jacket pre-design based on loads of a "land version" of the 20 MW reference wind turbine [1] is developed. This resulted in a first estimate of the overall jacket and pile geometry and dynamic properties of the full system. Secondly, a state-of-the art load iteration procedure under due consideration of the wind turbine and jacket and combined wind, wave loading and structural response is considered. This approach is usually applied in detailed design projects. An overview of the design assumptions is given and the results are summarized in this chapter.

5.1   Introduction to the Bottom-Mounted Jacket Design

Jacket type support structures are an adequate solution for medium water depths where monopile designs can reach manufacturing limits, dynamic limits (designs might become too soft), installation limits or cost effective limits and on the other end floating wind turbine concepts are mainly considered for much larger water depths. Wind farms using jacket support structures are typically located in water depths between approximately 35 m and 60 m. The development of new load mitigation concepts opens up the opportunity to realize monopiles also for increasing water depths. Hence the lower limit of the water depth for jackets will probably increase. However, the jacket concept is chosen as it is usually a robust design and geometry changes of the jacket have minor influences on the performance of the wind turbine components. Therefore optimization of the wind turbine rotor and drive train is possible considering only a pre-design of the jacket.

The main elevations and measures relevant for the jacket design considering the 20 MW reference wind turbine are outlined in Figure 5-1 in comparison to the 10 MW design. It should be noted that the assumption within the project consortium was to maintain the water depth and interface elevation (tower to transition piece interface) and also to apply a rather long offshore tower (extended by 12m) in order to achieve a relatively soft design that avoids unfavorable 3p excitations from the wind turbine, which was the case for the 10 MW jacket design. The resulting minimum distance between interface elevation and lowest blade tip elevation is therefore approximately 16 m for this 20 MW wind turbine configuration.

From the perspective of the foundation designer a much shorter offshore tower and somewhat higher TP would be recommended. This would improve the load transfer into the jacket and reduces bending moments on the support structure. Of course one has to evaluate if other requirements are contrary to this and does not allow the proposed modifications. A shorter tower will also influence the annual energy production because of the lower mean wind speed at a lower hub height. For example the mean wind speed at hub height is reduced by 0.4% assuming a wind profile exponent alpha of 0.12 and a reduction of 5 m of hub height.

The load analysis of the land version of the 20 MW reference wind turbine [1] considers three different onshore towers, called "Tower 1" to "Tower 3". They differ in the cross sections and material properties but have the same tower length of 163.14 m. The towers have different overall stiffness and thus the first natural frequency varies between 0.184 Hz and 0.208 Hz. For these three configurations the calculated wind loads time series are generated and can be used for the jacket pre-design. The loads are given at the

required jacket interface elevation, which is 141,9m below hub height (26m from tower bottom).

For the current design phase the transition piece is extrapolated and modelled as a beam framework with an estimated total mass considered as a single point mass. Such basic TP models have disadvantages regarding the correct stiffness and thus influences the load transition between the tower and the uppermost part of the jacket. However, considering the uncertainties in the current design phase with respect to the wind turbine loads and dynamic properties of the full model this is assumed a reasonable approach and does not justify to apply detailed finite element models of the transition piece yet,
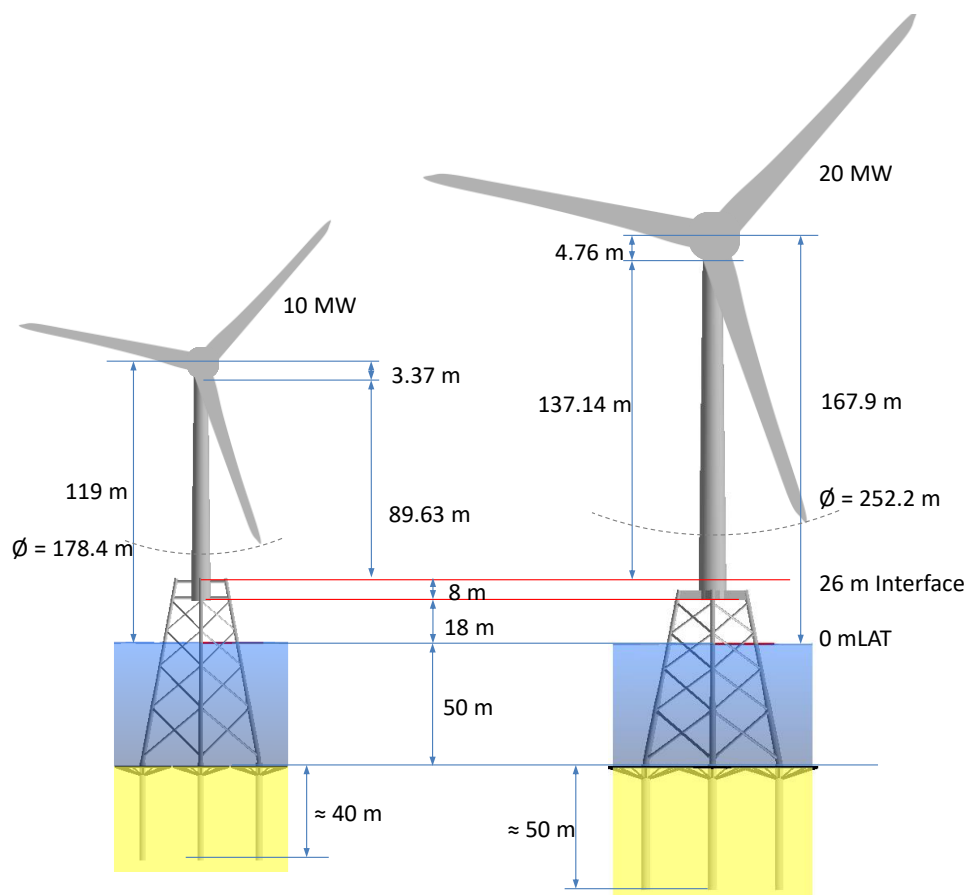
Figure 5-1 Main dimensions for the 10MW and 20MW support structure concept

5.2   Assessment of Structural Integrity

5.2.1 Final Design Layout and Dimensions

An overview of the main jacket geometrical parameters is shown in Table 5-1. Please refer to the jacket design report [20] for further model details, design assumptions and results of design load calculation in combination with the INNWIND.EU 20MW reference wind turbine. The design is driven mainly by the tubular joint fatigue criteria. The free members in between the joints are mass-optimized and if possible the standard cross-sections of

manufactures are considered. Typically steps in ¼ of inches are applied for wall thicknesses and full inches for diameters. The long members between two joints are discretized in four sub-elements. All members and details such as free tubular members, joints, circumferential single-sided and double-sided butt welds and attachment welds, are individual checked regarding excessive yielding and buckling in ULS with appropriate safety margins for loads and materials and regarding the achieved lifetime in FLS with a damage fatigue factor of 3.0. The design is based on the design guideline DNVGL-ST-0126.

The diameters and wall thicknesses of the offshore tower are taken from the scaled onshore tower model, but the length is shortened from the bottom to comply with the elevations given in Figure 5-1. Therefore the lower end of the onshore tower is cut at 26 m where it has a diameter of 11.1m. The total mass of the resulting offshore tower is approximately 1356 tons. The first natural frequency of the offshore model assuming a rigid support at tower bottom is approximately 0.3 Hz, which is significantly higher than the full model natural frequency including jacket and soil flexibility, see Table 5-1.

Table 5-1 Overview of jacket geometry and masses

Structural member	Dimensions	Value
Jacket		
Base Width	[m]	38
Top Width	[m]	20
Interface elevation	[m] wrt MSL	26
Transition Piece height	[m]	4*
Number of legs	[-]	4
Jacket legs diameter (outer)	[mm]	1829-2642
Jacket legs maximum wall thickness	[mm]	101.6
Jacket legs minimum wall thickness	[mm]	44.5
Number of x-braces levels	[-]	4
Diameter upper x-braces diameters (outer)	[mm]	914
Diameter middle upper x-braces diameters (outer)	[mm]	965 / 1219
Diameter middle lower x-braces diameters (outer)	[mm]	965 / 1219
Diameter lower x-braces diameters (outer)	[mm]	1168 / 1828
Braces wall thicknesses	[mm]	20 - 40.5
Number of Piles	[-]	4
Pile penetration	[m]	50
Pile diameter	[mm]	3500
Pile wall thicknesses	[mm]	34.9 – 73
Pile top elevation above mudline (Stick-up length)	[m]	1.8
Overlap length (grout length)	[m]	7.5
Mass		
Jacket structure	[t]	1670
Transition Piece (estimation)	[t]	450
Steel Appurtenances (estimation)	[t]	50
Piles	[t]	4x 230
Total lifting mass (no piles)	[t]	2170
Natural frequency overall structure		
1st eigenfrequency (1st bending mode)	[Hz]	0.165

(Innwind.EU, Deliverable 1.25, PI-based Assessment of 20MW Wind Turbines)

5.2.2 Design Load Cases and Load Calculation Method

The load calculations are based on IEC 61400-3 design load cases (DLC) with appropriate partial safety factors. It is assumed that the turbine has 100% technical availability, which is a conservative assumption because the jacket design is driven by operational wind loads and not from idling load cases. Wind and waves are aligned and 12 directions (30° increment) are considered. Turbulent seeds are combined with a yaw error of ±8 degree. The following DLCs have been applied:

- DLC 1.2   FLS (normal operation)
- DLC 6.4   FLS (idling operation)
- DLC 6.2   ULS (50 year extreme wind and wave conditions)

Serviceability limit state (SLS) is not considered in the present design level. The wind turbine manufacturer normally prescribes an allowable permeant rotation (tilt) of the structure against the horizontal plane. It is a combination of installation tolerance and settlement during service lifetime and has to be checked accordingly in a detailed design assessment. The 20 MW INNWIND.EU reference wind turbine does not prescribe allowable tilt angles. Furthermore such requirement is not a design driver for the primary steel of the jacket, but influences usually the required minimum pile penetration length.

The pre-design phase is carried out using the results of the onshore wind turbine model, thus a superposition approach of the loads is considered. In this approach the wind load time series ($F_x...M_z$) at interface elevation from the wind-only analysis are applied to the jacket and are combined with the wave loads from random sea states using airy wave theory and the JONSWAP spectrum. The considered significant wave heights and wave periods correlate with the mean wind speed. However, the dynamic interaction of loads and support structure response cannot be considered accurately in this approach. Furthermore all models from the wind-only analysis have a higher first natural frequency than the full offshore model including the jacket. Therefore it must be assumed that the wind loads and generally the load spectra will change in subsequent design iterations and requires also an update of the 20 MW wind turbine model and controller parameters to generally improve the design.

The conceptual design phase considers a sequential integrated simulation approach. A super-element approximation of the jacket and correlating wave loads has been calculated and both are implemented in the 20 MW reference wind turbine model in order to calculate the full system response of the offshore configuration shown in Figure 5-1. The resulting interface loads at tower bottom are subsequently applied in the design assessment of the detailed jacket together with the local wave loads to determine the local stresses in the jacket structure more accurately. However, an improved model of the 20 MW wind turbine, tower and controller is not developed in the project and thus it can be assumed that the results for the jacket are conservative.

5.2.3 Structural Integrity Check

Design assessment regarding NFA, ULS and FLS for the jacket is based on the DNV guideline, ref. [21] and [22]. Appropriate safety factors for loads and material are taken

into account. No tower design has been carried out. The given tower geometry is based solely on upscaling.

The purpose of the NFA analysis is to determine the natural frequency of the entire structure or the range of frequencies to be expected from varying design assumptions. The first natural frequency should be outside the 1P and 3P bandwidth of the wind turbine to avoid unfavorable resonance excitations. The 1P excitation corresponds to the rotor speed range and the 3P excitation corresponds to the blade passing frequency, which is three times the rotor speed range.
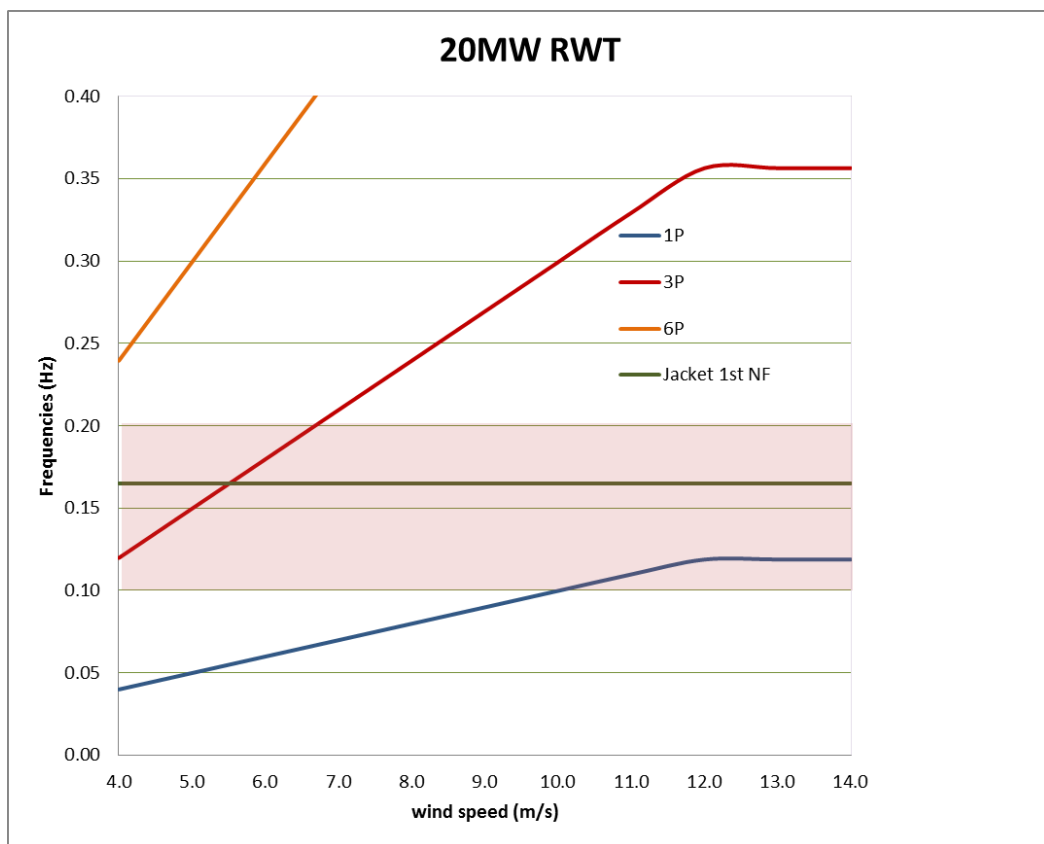
Figure 5-2 Operational and 1st jacket natural frequencies

However, the allowed soft-stiff range of the slow rotating 20 MW reference wind turbine is very small (0.11 - 0.12 Hz) and in practice it will not be possible to design the support structure for this range (see Figure 5-2). It will also not be possible to reach the stiff-stiff design which requires a natural frequency above 0.35 Hz or a soft-soft design which requires a frequency below 0.04 Hz. Furthermore, such low frequencies are within the wave periods and it would be reasonable to aim for higher natural frequencies if possible.

Finally this means that it cannot be fully avoided that the target frequency of the support structure will result in a 3p excitation, which requires an appropriate controller strategy. Resonance problems can hardly be avoided and ideally they occur at rotor speeds with low wind speed, thus lower aerodynamic loads.

(Innwind.EU, Deliverable 1.25, PI-based Assessment of 20MW Wind Turbines)

The obtained natural frequency of the system will be utilized in other analyses, such as the fatigue analysis, where the damping of the system is calculated by applying Rayleigh-damping.

The purpose of the extreme event analysis is to ensure that the jacket structure and piles are capable of supporting the WTG for the least favorable combination of environmental load conditions. The element stresses and tubular joints punching shear stresses are analyses for all members and load cases. The maximum allowed utilization has to be smaller than 1.0. The governing pile design loads are also calculated in ULS, which subsequently determines the minimum required pile penetration found in the geotechnical analysis. ULS criteria are fulfilled for the pre-design phase and the conceptual design phase.

The purpose of the time domain fatigue analysis is to ensure that the jacket structure is capable of supporting the WTG for the required design life of 25 years. In addition, site specific conditions in terms of water depth, marine growth, corrosion allowance and soil characteristics are applied for the turbine location. Hot spot stresses are calculated using the approach of stress concentration factors (SCF) and evaluated using a Rainflow counting method. S-N curves for different types of tubular joint welds, butt welds, cut-outs, conical sections and attachment welds are considered. The annual damage is calculated using the probabilities of every time series. The resulting fatigue lifetime is equal to the inverse of the annual damage. The results from the pre-design phase show sufficient lifetime throughout the jacket, but requires also post-weld treatment at a number of critical joints.

The conceptual design phase using integrated offshore load analyses show substantially different fatigue results. The lower part of the jacket (legs and braces) is prone to local bending vibrations, which cause high fatigue damage. Until the end of the work no final solution has been found since only the jacket geometry was modified without improvements of the wind turbine model or controller. Hence, a number of fatigue still details have insufficient lifetime and it is believed not realistic to develop a jacket design by increasing simply wall thicknesses or member diameters currently. It clearly shows the need for closer collaborations between wind turbine designer and foundation designer to solve these problems.

5.3   LCOE Impact

5.3.1   Effect on Annual Energy Production

The influence of the jacket, i.e. the motion of the structure, on the annual energy production of the wind turbine is negligible. The gained power is mainly driven by the mean wind speed and probability distribution of wind speeds, the rotor performance and the availability of the turbine.

5.3.2   Effect on CAPEX

Costs drivers for the support structure are the material costs (raw mass of the structure), the welding costs (number of welds and volume/length), the assembly costs and hourly rates for equipment and workers. Due to the complexity of such cost models and the volatile cost assumptions in the market it is more appropriate to consider lumped prices per tonnage of the structure. The lumped prices are defined for pile steel, jacket steel and

TP steel individually and thus expresses other cost shares through the specific mass of the component. Furthermore such lumped price cost models are sufficiently accurate when considering the present design maturity of the 20 MW offshore wind turbine in general. It should be noted that the 20MW reference wind turbine is up-scaled from the 10MW class (and also from the 5MW class) it is believed that the governing design loads are not realistic and probably too conservative.

5.3.3 Effect on OPEX

There are no OPEX related cost savings. The support structure is designed to survive the entire lifetime without maintenance of the primary steel components. However, it can be assumed that inspection services are required to validate the jacket design assumptions regarding corrosion allowance and scour development. Due to the larger dimensions of the structure the time needed for such work could be longer und thus result in higher OPEX costs. Precise OPEX cost estimates have not been estimated and generally contribute less to the overall project costs.

5.4 LCOE Sensitivity Analyses

A LCOE variation study using the INNWIND.EU cost model (v1.02.1 of May 2016) of the 20 MW reference wind turbine is performed. The influence of the CAPEX costs of the support structure on the LCOE is addressed. The LCOE calculation neglects variations of the installation costs because the structural optimization of the support structure will primarily influence member diameters, wall thicknesses and masses but will not end up in a substantial change of the general proportions. Thus the installation equipment and vessels will be unchanged. An impact on the installation time can be more relevant in cases where the optimization results in shorter pile penetration and thus can results in faster installation of the pre-installed piles. The results of the CAPEX variation study are shown in Table 5-2:

Table 5-2 LCOE variation study for bottom fixed support structure costs

	Support structure cost	LCOE	Change of LCOE
Ref. jacket design (TP, Jacket, Piles)	13.940 mio €	93.22 €/MWh	-
Jacket +10%	15.340 mio €	94.56 €/MWh	+1.44%
Jacket +5%	14.640 mio €	93.89 €/MWh	+0.72%
Jacket -5%	13.250 mio €	92.55 €/MWh	-0.72%
Jacket -10%	12.550 mio €	91.88 €/MWh	-1.44%
Jacket -20%	11.150 mio €	90.53 €/MWh	-2.89%

5.5 Conclusions

A pre-design of a 20MW jacket support structure with pre-installed piles has been successfully developed. The design is based on NFA, ULS and FLS assessments and clearly the fatigue requirements are most critical for the design. The natural frequencies of the whole structure are lower as initially anticipated in the load calculation of the 20 MW reference wind turbine. Therefore, it is not surprising that the differences between the pre-design loads (onshore loads) and the conceptual loads (integrated loads) are significant.

(Innwind.EU, Deliverable 1.25, PI-based Assessment of 20MW Wind Turbines)

Considering the fatigue results of the conceptual design it is believed very important to optimize the jacket including optimization of the wind turbine at the same time. Thus, stronger collaboration between wind turbine designer and foundation designer is required. The interaction between loads and response of the structure is significant for these large wind turbines. Traditional soft-stiff support structure designs are not feasible due to the narrow allowed range between 1p and 3p rotor frequencies of the very slow rotating rotor. The final FLS analysis show insufficient lifetimes and requires further design iterations including improvements of the wind turbine performance.

The foundation costs influence only the CAPEX of the wind turbine system there is no benefit for the energy yield. There is also no influence on operational costs in the scope of the primary steal design.

(Innwind.EU, Deliverable 1.25, PI-based Assessment of 20MW Wind Turbines)

CHAPTER 6 ADVANCED CONTROL OF 20MW RWT

In this chapter, we describe the control methodologies applied to the variations of the INNWIND 20 MW wind turbine. The methodologies applied are a combination of mature advanced control methods (TRL 9) and control methods using novel sensors and actuators (TRL ≤6). The controllers are designed to maintain wind turbine power capture levels whilst alleviating fatigue and extreme loading on the wind turbine. We show the pathways to load reduction for each method.

LCOE reduction facilitated by control design is most effective when combined in an iterative design procedure with all turbine components. Therefore, the design loads produced are not a complete indication of the load reduction potential of applying advanced control.

6.1   Introduction to the Innovative Concept

The innovative concepts presented here are explained in further detail in controller focused INNWIND.EU deliverables 1.43 and 1.44. The goal of each control feature is to reduce turbine loading. The loading margin can then be used in to reduce overall LCOE through:

- Increasing rotor size for larger AEP;
- Increasing capacity factor by increasing the operational conditions of the turbine (wind speed, turbulence intensity and sea state).
- Reducing loading requirements of turbine components

6.1.1   In-plane damping (TRL 9 – Essential)

The INNWIND 20 MW RWT shows very low damping (<2%) of the first collective in-plane mode of the turbine at 1.27 Hz. This coupled mode includes effects from the first and second blade edgewise collective mode, the 2nd and 3rd tower side-side modes. These modes are also at risk from destabilisation under closed-loop speed control. Therefore, in-plane damping is required to keep drivetrain in-plane loading at feasible levels. Traditionally the low-speed shaft (LSS) flexibility was the key determinant of the first in-plane frequency and showed the least damping; however, for the 20 MW RWT the drivetrain flexibility has a frequency of 3.65 Hz which is typically outside the bandwidth of any control loop and shows a reasonable damping level of 4.3%. Figure 6-1 and Figure 6-2 show the linear frequency response and step responses of the damped and un-damped systems at 12 m/s respectively. Note that damping has increased the response of the LSS around 2 Hz, though the energy content of the wind at 2 Hz is much less than at 1.27 Hz, so there is a net benefit in fatigue damage reduction. The damper takes the form of a bandpass filter from generator speed measurements to generator torque demand; an example frequency response of the filter is shown in Figure 6-3.

(Innwind.EU, Deliverable 1.25, PI-based Assessment of 20MW Wind Turbines)
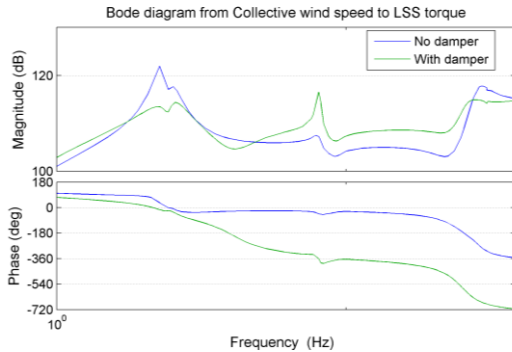
Figure 6-1 Frequency response of LSS torque to collective wind speed at 12 m/s
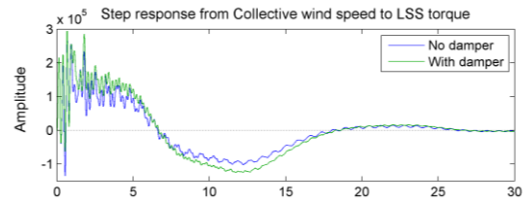
Figure 6-2 Step response of LSS torque to collective wind speed at 12 m/s
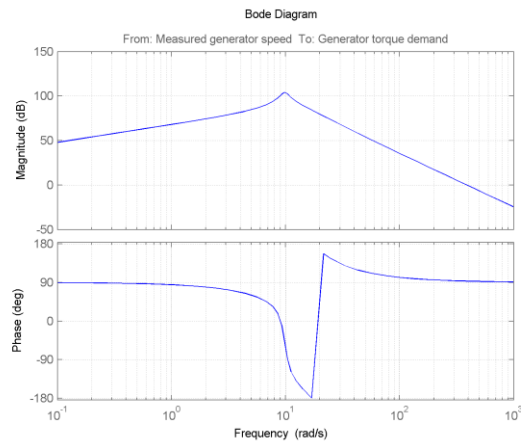
Figure 6-3 Frequency response of in-plane damper

6.1.2   Tower damping (TRL 9 – Essential)

Tower fatigue damage can be decreased by actively damping tower motions, particularly at the tower first fore-aft frequency. While the first fore-aft mode is relatively well damped due to the aerodynamic damping of the rotor, it is also very highly excited for the same reason. Figure 6-4 and Figure 6-5 show the linear frequency response and step responses of the damped and un-damped systems at 12 m/s respectively. The damper takes the form of an integrating controller with filtering from nacelle acceleration measurement to collective pitch angle demand; an example frequency response of the controller is shown in Figure 6-6.

(Innwind.EU, Deliverable 1.25, PI-based Assessment of 20MW Wind Turbines)
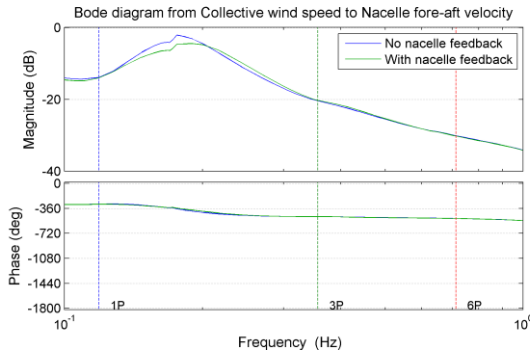
Figure 6-4 Frequency response of nacelle fore-aft velocity to collective wind speed at 12 m/s
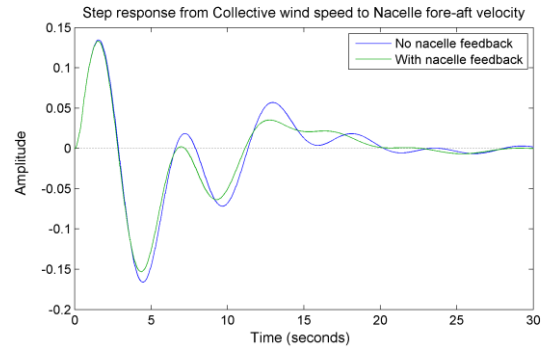
Figure 6-5 Step response of nacelle fore-aft velocity to collective wind speed at 12 m/s
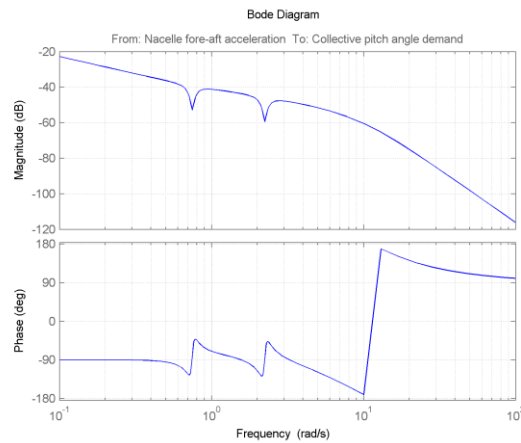
Figure 6-6 Frequency response of tower damper

6.1.3 Individual pitch control (TRL9 – Desired)

Individual pitch control (IPC) is a well-developed technology, though it has shown relatively small penetration into the wind turbine market [23]. As rotors get large, the asymmetries experienced over the swept area become more apparent and can induce significant fatigue loading on the blade roots, as well as mean hub and tower tilt/yaw loading – making this technology very appropriate for the 20 MW rotor. Industry standard IPC takes several similar forms [24] which typically demand a cyclic pitching as a function of azimuth angle and blade root load. The azimuthal variations are applied at harmonics of rotor rotational frequencies to target loading due to rotational sampling of the wind. In this work, IPC using the d-q axis transform has been applied to the 20 MW RWT (1P and 2P IPC), and 20 MW LIR (1P IPC) in Deliverable 1.44. In both cases, the controller uses blade-root load measurements to determine individual pitch angles that are decoupled form the collective-pitch control (CPC) loop and therefore should not impact power capture. Furthermore, because IPC is generally only active above rated wind speeds, the variable speed region of operation does not encounter an energy penalty when the blades deviate from the fine-pitch angle. A schematic of the IPC structure is shown in Figure 6-7.
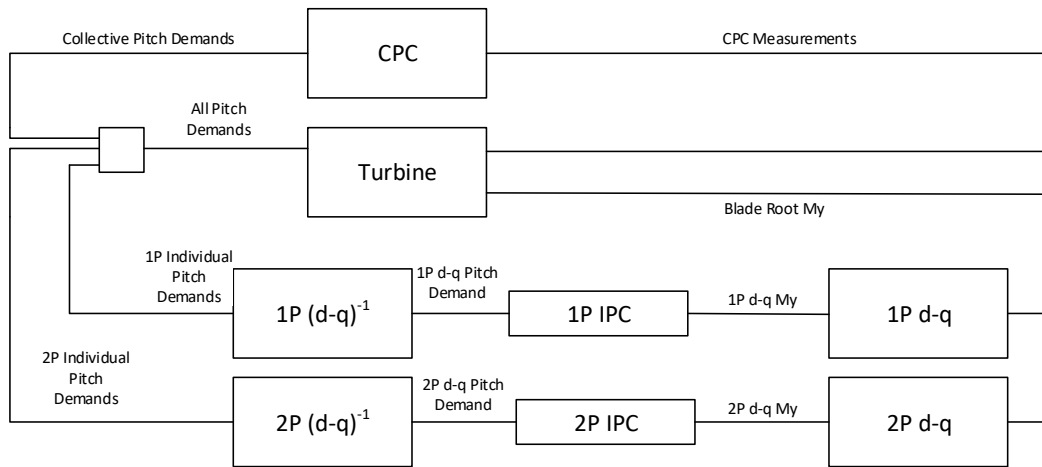
Figure 6-7 IPC Schematic

An example of the effects of 2P IPC compare to collective-pitch control (CPC) is shown in Figure 6-8 which illustrates how deterministic loading on the blade root from upflow, wind shear and direction error can be largely removed.
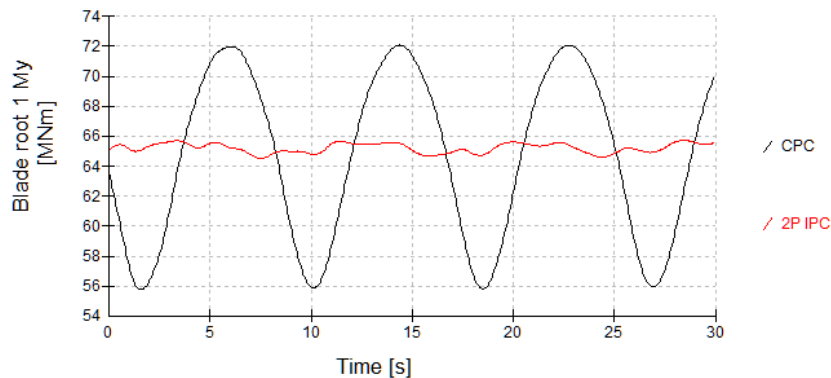
Figure 6-8 Blade root flapwise moment in steady flow with 8° upflow, 8° direction error and exponential wind shear with exponent 0.2.

6.1.4 Individual flap control (TRL < 6)

A study into several concepts of distributed control devices was conducted in Deliverable 2.31 and 2.32 for the INNWIND.EU project and have shown that trailing edge flaps (TEFs) present the highest TRL. When normalised for actuation levels, TEFs show similar fatigue load reduction potential to using IPC alone if using similar algorithms for load reduction. Combining IPC with flap actuation, some additional actuation may be possible if the superimposition of IPC and individual flap control (IFC) does not drive the blade into stall.

As blades become larger, with increased pitching inertia's and friction levels, the requirements on pitch systems can also increase. If TEFs can be used to reduce pitch activity, and at the same time provide the replacement actuation at lower costs there is a pathway to reductions in LCOE. TEFs provide this pathway as a smaller section of the blade is actuated. Another concern with IPC actuation is the constant cycling of pitch angle over a narrow range causing uneven wear in the pitch bearing and ring gear. If this cycling were passed on to a dedicated actuator such as a TEF, the actuation mechanism can be

(Innwind.EU, Deliverable 1.25, PI-based Assessment of 20MW Wind Turbines)

designed to be fully utilised with even wear leading to a more efficient mechanical design. Beyond fatigue loading TEFs also have the potential to assist in extreme load reduction by providing additional actuation during turbine failures and by reducing the difference between the pitch angles of each blade during faults.

Two methods of flap control have been studied at the 20 MW scale, IFC + IPC (IFPC) using blade root load feedback and intelligent shutdowns (IFPC-FB) and IFPC with the flap controller using inflow measurements from a spinner mounted anemometer for a feedforward approach (IFPC-FF). The former method is applied to the 20 MW RWT on advanced steel jacket and the latter is applied to the 20 MW LIR on advanced steel jacket. A schematic of the 2P IFPC-FB control structure is given in Figure 6-9and a schematic showing 1P IFPC-FF is shown in Figure 6-10. A demonstration of the flap reaction during an intelligent shutdown with IFPC-FB is given in Figure 6-11. This figure shows that at the onset of a collective-pitch runaway fault (algorithm failure), the individual pitch angles are much closer to the mean with IFPC and so the tower torsional loading is initially reduced, as the blades pitch to feather during the shutdown, the torsional moment is further relieved by deploying the flaps to counter the pitch angle asymmetries. Having TEFs do not induce design driving fault cases as the turbine can undergo a standard closed-loop shutdown because the pitch actuators are fully functional and can compensate the flap fault.
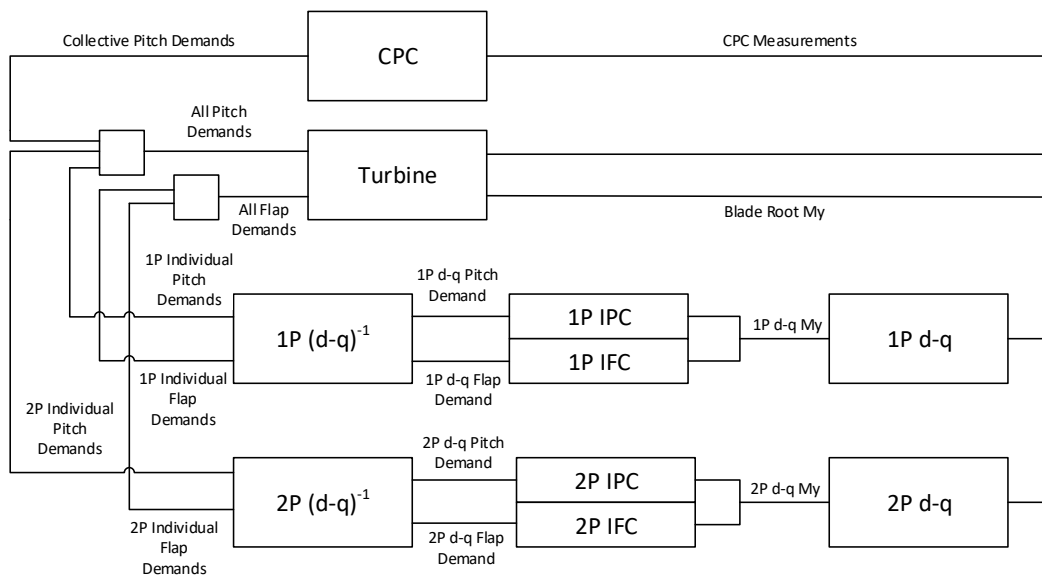
Figure 6-9 IFPC-FB schematic

(Innwind.EU, Deliverable 1.25, PI-based Assessment of 20MW Wind Turbines)

$$\beta_{flap}(U, \theta_{yaw}, \theta_{tilt}, \psi) = \beta_{f1}\cos(\psi + \Delta\psi_1) + \beta_{f2}\cos(2\psi + \Delta\psi_2)$$
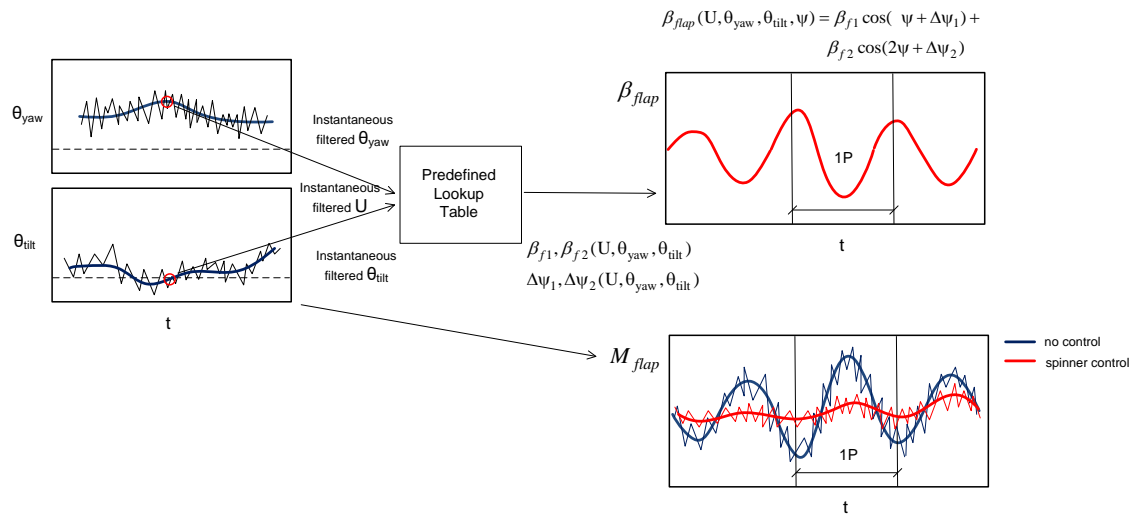
Figure 6-10 IFPC-FF schematic
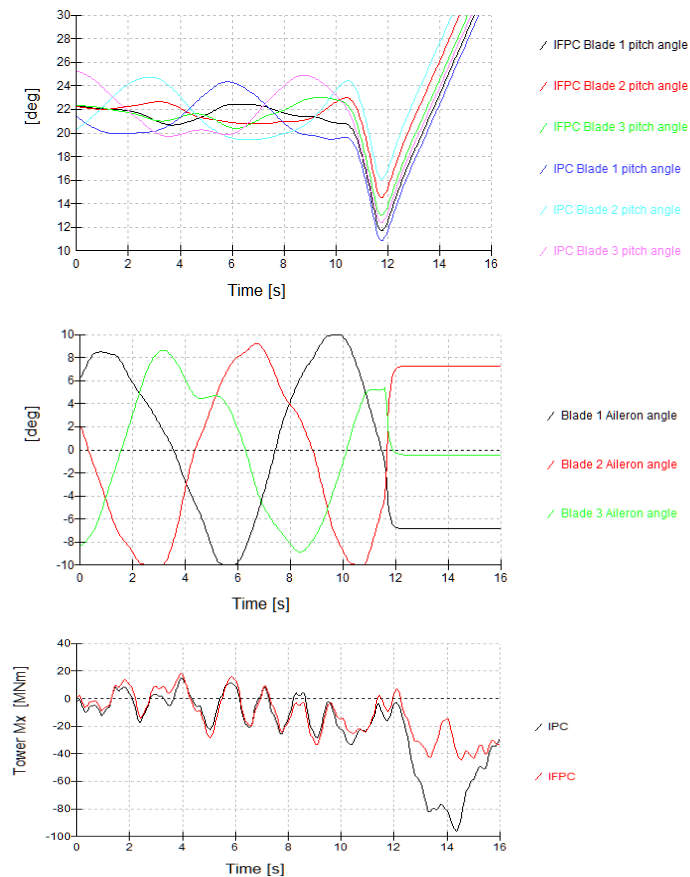
Figure 6-11 Time series response of DLC 2.2 eb2 (Collective pitch runaway) inder IPC and IFPC-FB

6.1.5 Extreme turbulence control (TRL < 6)

A new control strategy is proposed for reduction of extreme loads on wind turbine components during operation in extreme turbulence conditions, such as those specified in

DLC 1.3 of the norm IEC 61400-1 ed.3. The control algorithm is based on estimation of the turbulence in the wind, followed by reduction of the rated rotor speed whenever this turbulence estimate exceeds certain limit. An optimization approach is developed to calculate the limit on the turbulence so as to achieve the best balance between alertness and false alarms, i.e. maximizing the loads reduction capabilities of the algorithm during extreme turbulence conditions and minimizing the chances for power losses during operation under normal turbulence.

The Extreme Turbulence Control (ETC) concept is schematically represented in Figure 6-12, wherein the first three blocks are related to the estimation of the rotor-effective wind speed and turbulence. Details of the concept and the tuning of the concept are presented in Deliverable 1.44.
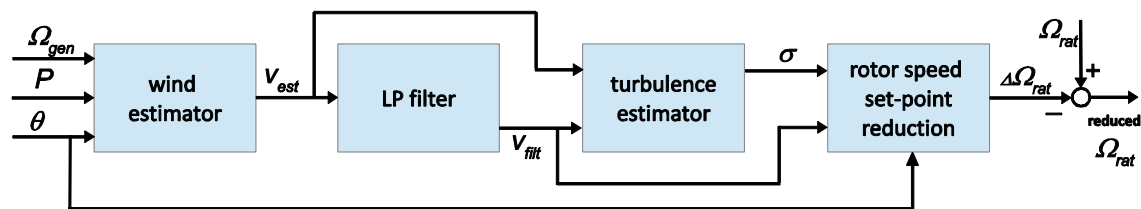
Figure 6-12 Schematic representation of the extreme turbulence control algorithm

6.2   Assessment of the Proposed Design

6.2.1   Individual Pitch Control

IEC fatigue and extreme load calculations have been conducted in Deliverable 1.44 comparing IPC to CPC on the 20 MW turbine with LIR on advanced steel jacket. The fatigue cases consider DLC 1.2, the extreme load cases consider DLCs 1.3 and 1.6.

The lifetime fatigue DEL reduction, of the blade root in the flap direction, achieved by using 1P IPC on the LIR and advanced steel jacket was found to be between 15% and 44% in Deliverable 1.44. This resulted in an increase in tower base fore-aft DELs of 3-4%.

The extreme loads on the blade root in the flapwise direction were reduced 6.9%, the tower base combined overturning moment was reduced by 3.5% and the tower base torsional moment was reduced 14.2%.

6.2.2   Spinner Anemometer Feedforward Individual Flap Control

IEC fatigue and extreme load calculations have been conducted in Deliverable 1.44 comparing IFPC to CPC on the 20 MW turbine with LIR on advanced steel jacket. The fatigue cases consider DLC 1.2, the extreme load cases consider DLCs 1.3 and 1.6.

The lifetime fatigue DEL reduction, of the blade root in the flap direction, achieved by using 1P IPC on the LIR and advanced steel jacket was found to be between 14% and 35% in Deliverable 1.44. This resulted in an increase in tower base fore-aft DELs of 3-7%.

(Innwind.EU, Deliverable 1.25, PI-based Assessment of 20MW Wind Turbines)

The extreme loads on the blade root in the flapwise direction were reduced 4.7%, the tower base combined overturning moment was reduced by 1.4% and the tower base torsional moment was reduced 6.4%.

6.2.3 Blade Root Feedback Individual Flap Control with Intelligent Shutdowns

IEC fatigue and extreme load calculations have been conducted in Deliverable 1.44 comparing IFPC to IPC on the 20 MW RWT on advanced steel jacket. IEC load cases considered are summarised in Table 6-1.

Table 6-1 Load cases considered for blade root feedback IFPC

DLC	Case Type
1.2	Fatigue
1.3	Extreme
1.4	Extreme
2.1	Extreme
2.2	Extreme
2.3	Extreme
2.4	Fatigue
4.1	Fatigue
4.2	Extreme
6.4	Fatigue

Fatigue results indicate the similar (within 1%) lifetime fatigue DELs are achieved for both IPC and IFPC (as desired in that study) across the hub, blades, tower base and specific jacket members, with a reduction in pitch actuator usage.

Extreme load results were driven by DLC 1.4, key results are summarised in Table 6-2 and the load reductions achieved on the hub asymmetric moment and tower base torsional moment when DLC 1.4 and DLC 1.3 are not considered, are given in Table 6-3.

Table 6-2 Extreme Load Reductions of IFPC with blade root feedback and intelligent shutdowns compared to IPC.

Component	Extreme Load Reduction
Blade Root Flap Moment	3.05%
Blade Root Flap Shear	2.28% - 3.62%
Tower Base Torsional Moment	4.37%
Tower Base Overturning Moment	1.52%
Mudline Member Torsional Moment	9.36%
Corner Member Torsional Moment	11.60%

Table 6-3 Extreme Load Reductions of IFPC with blade root feedback and intelligent shutdowns compared to IPC; not including DLC 1.4 or DLC 1.3

Component	Extreme Load Reduction

(Innwind.EU, Deliverable 1.25, PI-based Assessment of 20MW Wind Turbines)

Hub Asymmetric Moment	19.55%
Tower Base Torsional Moment	28.65%

6.2.4 Extreme turbulence control

IEC fatigue and extreme load calculations have been conducted in Deliverable 1.44 comparing ETC to a baseline controller on the 20 MW RWT. IEC load cases considered are DLC 1.2 and 1.3. Results show little impact on lifetime weighted damage equivalent loads (<1%) using this method as the target is for a reduction of extreme loading in DLC 1.3. A power production loss of 0.57% has been determined through DLC 1.2 calculations.
A summary of the extreme load reduction capabilities are given in Table 6-4.

Table 6-4 Summary of ultimate loads for InnWind 20MW RWT based on DLC 1.3

Component	Unit	REF	ETC	ratio [%]
blade flap	MNm	163.6	158.1	96.65
blade lead	MNm	87.39	85.23	97.53
blade XY	MNm	174.7	165.8	94.89
blade torsion	MNm	2.023	2.152	106.4
tower fore-aft	MNm	931.7	920.5	98.8
tower sideward	MNm	320.7	360.9	112.5
tower XY	MNm	948	921.4	97.19
shaft Y	MNm	131	108	82.43
shaft Z	MNm	109	110	100.9
shaft YZ	MNm	140	118	84.2
tower top tilt	MNm	145	121	83.89
tower top yaw	MNm	108	106	97.88
tip deflection	m	18.3	18.1	98.81

6.3 LCOE Impact of the Proposed Design

6.3.1 Effect on Annual Energy Production

With respect to the innovative features investigated, all are designed to not impact energy capture except for the ETC feature which de-rates the turbine in extreme turbulence. The use of individual flap control along with control on the 20 MW wind turbines on a jacket showed that both the blade root and tower base design loads can be reduced, thus aiding the LIR concept in increasing the rotor radius to increase AEP. The reduced fatigue and extreme loads on the turbine can allow increase availability, thus reducing OPEX and increasing capacity factors. Further about a 0.5% increase in AEP is feasible from the use of Spinner anemometer based feed-forward control using wind measurements.

6.3.2 Effect on CAPEX and LCOE

The Individual flap with pitch control and Individual pitch control aid in limiting the design loads, so that the increase in AEP does not result in an increase in design loads over the reference design. However their direct impact on reducing CAPEX is limited to primarily blade mass and main shaft mass savings. Since the blade or shaft CAPEX is a small

portion of the overall CAPEX when including the substructure, a limited influence on the overall CAPEX of less than 1% is seen from using active controls. However when the combined with the LIR concept and wind observers for feed-forward control, a net reduction in LCOE of at least 4% can be expected compared to the 20 MW reference, primarily derived from the larger AEP.

6.4   Conclusions

A range of control features have been applied to the INNWIND 20 MW RWT, 20 MW RWT on advanced steel jacket and 20 MW LIR on advanced steel jacket. In-plane damping and tower damping are considered essential features for the investigated configuration and together with CPC form a baseline control architecture for the 20 MW RWT. Further to this IPC, IFPC-FB, IFPC-FF and ETC have been applied with reductions in loading quantified.

IPC and IFPC have been shown to results in similar levels of fatigue load reduction on the blade roots but introduce slightly higher fatigue of the tower base.

IFC has been shown to lead to reduced extreme loading using intelligent shutdowns and through reducing pitch angle asymmetries at the onset of pitch faults. There is also the benefit of reduced pitch activity, though this has not been quantified for this study.

ETC has demonstrated reductions in extreme loading that occur in DLC 1.3 from extreme turbulence, with the largest impacts on blade root bending and all RNA tilting loads.

CHAPTER 7 SYNTHESIS AND CONCLUSIONS

The comparison of the studied concepts in terms of the Performance Indicators (PIs) set for the INNWIND.EU project is presented in Table 7-1 and Table 7-2. The first Table presents dimensional values of the PIs while the second shows percentage changes in comparison to the PI values of the 20MW Reference Wind Turbine. The combined effect of the rotor/drive train/support structure/control concepts is also included in the Tables.

The PI values used in the Tables may be slightly different than those presented in the earlier chapters of the report. This is the result of a harmonization procedure including the recalculation of all the PIs, whenever needed, with dedicated spreadsheets employing the cost model version of Ref [10].

For a better appreciation of the 20MW designs we include in the Tables the relevant PI values of the 10MW RWT. Moving from 10 to 20MW notable are the slight increase of the wind farm capacity factor due to less wake effects for the same installed capacity and the significant reduction of O&M cost from nearly 35 €/MWh to 28 €/MWh.

Table 7-1 Performance Indicators of the innovative concepts studied

ROTOR	Component Mass (tn)	Component Cost (k€)	Overall CAPEX (k€)	Turbine CF	Wind Farm CF	O&M (€/MWh)	LCOE (€/MWh)
RWT - 10MW	42	448	30,650	0.507	0.425	34.81	98.56
RWT - 20MW	118	1,274	64,550	0.508	0.437	28.08	93.22
Low Induction Rotor (LIR) 20MW	99	1,367	66,750	0.546	0.480	28.08	89.58
BTC Rotor 20MW (D = D RWT)	108	1,163	64,000	0.508	0.438	28.08	92.67
DRIVE TRAIN & NACELLE	Component Mass (tn)	Component Cost (k€)	Overall CAPEX (k€)	Turbine CF	Wind Farm CF	O&M (€/MWh)	LCOE (€/MWh)
RWT - 10MW	338	4,515	30,650	0.507	0.425	34.81	98.56
RWT - 20MW	914	11,300	64,550	0.508	0.437	28.08	93.22
PDD Generator 20MW	950	10,500	63,200	0.513	0.442	28.08	91.35
OFFSHORE SUPPORT STRUCT	Component Mass (tn)	Component Cost (k€)	Overall CAPEX (k€)	Turbine CF	Wind Farm CF	O&M (€/MWh)	LCOE (€/MWh)
RWT - 10MW	1,920	9,497	30,650	0.507	0.425	34.81	98.56
RWT - 20MW	3,090	13,950	64,550	0.508	0.437	28.08	93.22
Advanced Jacket (AJ) 20MW		11,160	61,800	0.508	0.437	28.08	90.53
ADVANCED CONTROL	Component Mass (tn)	Component Cost (k€)	Overall CAPEX (k€)	Turbine CF	Wind Farm CF	O&M (€/MWh)	LCOE (€/MWh)
RWT - 10MW			30,650	0.507	0.425	34.81	98.56
RWT - 20MW			64,550	0.508	0.437	28.08	93.22
Advanced Control (AC) 20MW							89.49
COMBINATIONS			Overall CAPEX (k€)	Turbine CF	Wind Farm CF	O&M (€/MWh)	LCOE (€/MWh)
RWT - 10MW			30,650	0.507	0.425	34.81	98.56
RWT - 20MW			64,550	0.508	0.437	28.08	93.22
LIR + BTC + PDD + AJ + AC (20MW)			62,100	0.551	0.485	28.08	80.74

(Innwind.EU, Deliverable 1.25, PI-based Assessment of 20MW Wind Turbines)

Table 7-2 Percentage improvement of PIs in comparison to the 20MW RWT

ROTOR	Component Mass (Δ%)	Component Cost (Δ%)	Overall CAPEX (Δ%)	Turbine CF (Δ%)	Wind Farm CF (Δ%)	O&M (Δ%)	LCOE (Δ%)
Low Induction Rotor (LIR) 20MW	-16.1%	7.3%	3.4%	7.5%	9.7%	0.0%	-3.9%
BTC Rotor 20MW (D = D RWT)	-8.5%	-8.7%	-0.9%	0.1%	0.1%	0.0%	-0.6%
DRIVE TRAIN & NACELLE	Component Mass (Δ%)	Component Cost (Δ%)	Overall CAPEX (Δ%)	Turbine CF (Δ%)	Wind Farm CF (Δ%)	O&M (Δ%)	LCOE (Δ%)
PDD Generator 20MW	3.9%	-7.1%	-2.1%	1.0%	1.1%	0.0%	-2.0%
OFFSHORE SUPPORT STRUCT	Component Mass (Δ%)	Component Cost (Δ%)	Overall CAPEX (Δ%)	Turbine CF (Δ%)	Wind Farm CF (Δ%)	O&M (Δ%)	LCOE (Δ%)
Advanced Jacket 20MW		-20.0%	-4.3%	0.0%	0.0%	0.0%	-2.9%
ADVANCED CONTROL	Component Mass (tn)	Component Cost (k€)	Overall CAPEX (k€)	Turbine CF	Wind Farm CF	O&M (€/MWh)	LCOE (€/MWh)
Advanced Control (AC) 20MW							-4.0%
COMBINATIONS			Overall CAPEX/MW (Δ%)	Turbine CF (Δ%)	Wind Farm CF (Δ%)	O&M (Δ%)	LCOE (Δ%)
RWT - 10MW			-5.0%	-0.2%	-2.8%	24.0%	5.7%
LIR + BTC + PDD + AJ + AC 20MW			-3.8%	8.6%	10.9%	0.0%	-13.4%

7.1 Blade Concepts

LIR concept (Chapter 2)

The new hybrid (glass-carbon) blade is lighter (16%) than the full-glass classically up-scaled 20MW RWT blade but more expensive (7.3%). This is due to its longer span and the use of expensive carbon. Nevertheless, the overall increase in turbine CAPEX is 3.4% because in offshore wind the blades represent a small fraction of the turbine and support structure cost. Despite the higher CAPEX the larger, less loaded rotor, increases the turbine yield (capacity factor CF) by 7.5%. As stated earlier, a 4.5% comes from the LIR planform and another 3% from the dedicated low lift profiles. Even more important is the increase of the wind farm capacity factor by 9.7% due to the lower wake losses of LIR rotors. This is the highest value achieved among the different rotor concepts. Overall, LIR promises a 3.9% reduction of LCOE compared to the 20MW RWT.

Bend-Twist Coupled Rotor (Chapter 3)

The conclusions here regarding the impact of the BTC concept on LCOE are similar to those extracted for 10MW designs. No real improvement in the cost of energy is expected maintaining the reference rotor diameter. Such designs may reduce primary the fatigue and secondary the ultimate loading of the blade itself but, also, of the support structure having an indirect effect on CAPEX reduction which, however, is not taken into account in the present context. The BTC blade is highly loaded (high Cp_max design) and 8.5% lighter and cheaper than the RWT blade. The overall CAPEX and LCOE improvement is small (1%) leading to an LCOE reduction of 0.6%. Due to the assumptions made we can consider that BTC improvements can be superimposed to LIR summing up their individual impacts to all PIs. Alternatively, the BTC concept could be used to increase the diameter of a Cp_max

(Innwind.EU, Deliverable 1.25, PI-based Assessment of 20MW Wind Turbines)

rotor maintaining the loads to their reference level. If this is possible for the design loads (ultimate and fatigue) of the individual load carrying components, it would also lead to an increased turbine capacity factor without using the LIR concept. Overall LIR+BTC or BLT alone can offer an LCOE reduction of 4 to 5%.

7.2   Drive Train Concepts

Magnetic Pseudo Direct Drive (PDD) (Chapter 4)
The PDD generator with highly efficient power electronics promises a good LCOE performance (2 % lower than the reference) combined with a significant nacelle/drive train cost reduction of 7%. The nacelle mass is slightly increased by 4% while the capacity factor increases by 1.1 % which, along with the reduced CAPEX, is the reason of LCOE improvement. The improved capacity factor comes as a combination of the highly efficient 20MW PDD generator (98.5% at full load) and the highly efficient power electronics.

7.3   Support Structure Concepts

Bottom Mounted Offshore Support Structure (Chapter 5)
An advanced design/manufacturing of the 20MW RWT jacket is expected to reduce the original cost of ~14 M€ by 20%. Such a reduction would decrease the overall CAPEX by 4.3% translated to 2.9% reduction of the LCOE.

7.4   Advanced Control

Advanced Control in 20MW (Chapter 6)
An LCOE drop of 4% can be expected due to the mitigation of design loads of the turbine and its support structure offered by advanced control. In the present context advanced control was mainly targeted in reducing blade than support structure loads. Such a reduction can be used for increasing the rotor diameter and improve LCOE through better energy capturing. Alternatively, one can target on the reduction of the support structure fatigue loads which are the design drivers of the jacket. For jacket structures load reduction is nearly proportional to mass reduction. Since the offshore turbine support structure has a significant contribution to CAPEX, the reduction of the jacket fatigue loads through advanced control can also lead to an LCOE reduction of order 4% without increasing rotor diameter.

7.5   Combination of Innovative Concepts and Overall Expectations

A simplified methodology for estimating the combined performance of the researched concepts would sum-up the percentage gains of the individual innovations as soon as they can be considered independent from each other. The combination of all innovative concepts studied is given in the lower parts of the PI Tables.

For bottom mounted designs at INNWIND.EU 20MW RWT conditions the following expectations regarding LCOE reduction look reasonable:

- Low induction rotors with conventional inner structure   4.0%
- Aeroelastically tailored rotors (adding on LIR)   0.5%
- Drive train (reduced CAPEX, increased efficiency)   2.0%
- Advanced Jacket   3.0%

(Innwind.EU, Deliverable 1.25, PI-based Assessment of 20MW Wind Turbines)

- Advanced control   4%

  Expected Overall   LCOE reduction   ~14%

Starting from the EWII LCOE value of 106.93 €/MWh corresponding to 5MW turbine sizes, and considering more realistic than the EWII O&M costs this time, this number dropped at 98.56 €/MWh (8.5% reduction) for the 10MW RWT and 93.22 €/MWh (14.7% reduction) for the 20MW RWT. These reductions were due to the larger turbine sizes along with the use of a lightweight rotor with thick profiles and the shift from traditional three-stage geared drive trains to medium speed single-stage drive while employing state of the art designed and manufactured jackets. An additional 14% reduction of LCOE can be expected for both 10 and 20MW designs, thanks to the advanced concepts researched in INNWIND.EU, getting LCOE close to 80 €/MWh for 20MW turbines (and 85 €/MWh for 10MW turbines).

(Innwind.EU, Deliverable 1.25, PI-based Assessment of 20MW Wind Turbines)

REFERENCES

[1] *INNWIND.EU Deliverable 1.25a, 20MW Reference Wind Turbine, Aeroelastic Data of the Onshore Version.*

[2] *INNWIND.EU Deliverable 1.25b.*

[3] *INNWIND.EU Deliverable 1.22.*

[4] *P.K. Chaviaropoulos, J. Beurskens and S.Voutsinas," Moving towards Large(r) Rotors – Is that a good idea?", Proc. EWEA 2013 Conference, Vienna,* 2013.

[5] *P.K. Chaviaropoulos and G. Sieros, "Design of Low Induction Rotors for use in large offshore wind farms", Proc. Scientific Track, EWEA 2014, Barcelona,* 2014.

[6] *P.K. Chaviaropoulos, G.Sieros, J.M. Prospathopoulos, K. Diakakis and S.G. Voutsinas, "Design and CFD-based Performance Verification of a Family of Low-Lift Airfoils", Proc. EWEA 2015, Paris,* 2015.

[7] *INNWIND.EU Deliverable 2.12, New Airfoils for High Rotational Speed Wind Turbines,* 2015.

[8] *INNWIND.EU Deliverable 2.14.*

[9] *INNWIND.EU Deliverable 1.24.*

[10] *INNWIND.EU Deliverable 1.23.*

[11] *Bottasso C.L., Campagnolo F., Croce A., Tibaldi C., "Optimization-based study of bend–twist coupled rotor blades for passive and integrated passive/active load alleviation", Wind Energy, Vol. 16, N.8, p1149-1166, 2013. DOI: 10.1002/we.1543 (2013)..*

[12] *Zahle, F., Tibaldi, C., Verelst, D. R., Bak, C., Bitche, R., and Blasques, J. P. A. A., Aero-Elastic Optimization of a 10MW Wind Turbine, Proceedings of the 33rd Wind Energy Symposium , Kissimmee, Florida, U.S.A., 2015.*

[13] *Lobitz DW, Veers PS, Eisler GR, Laino DJ, Migliore PG, Bir G. The Use of Twist-Coupled Blades to Enhance the Performance of Horizontal Axis Wind Turbines. Sandia Report SAND 2001-1303, Sandia National Laboratories, Albuquerque, NM, May 2001..*

[14] *Lobitz D, Veers PS, Laino D. Performance of twist-coupled blades on variable speed rotors. AIAA 2000-0062, 2000 ASME Wind Energy Symposium, Reno, January 10–13, 2000..*

[15] *A.Croce, Deliverable D2_22_PoliMI_16July2015.txt.*

[16] P. Bortolotti, C. L. Bottasso and A. Croce, "Combined preliminary-detailed design of wind turbines," *Wind Energy Science,* vol. 1, pp. 71-88, 2016.

[17] *Bottasso CL, Croce A. Cp-Lambda: User's Manual. Dipartimento di Ingegneria Aerospaziale, Politecnico di Milano, 2006–2011..*

[18] *IEC 61400-1. Wind turbines – Part 1: Design Requirements, 2005.*

[19] *Bottasso C.L., Campagnolo F., Croce A., "Multi-Disciplinary Constrained Optimization of Wind Turbines", Multibody System Dynamics, Vol. 27, N. 1, p. 21-53, 2012, ISSN: 1384-5640, doi: 10.1007/s11044-011-9271-x (2012)..*

[20] *INNWIND.EU Deliverable 4.36.*

[21] "DNVGL-ST-0126, Support structures for wind turbines, 2016".

[22] "DNVGL-RP-C203, Fatigue Design of offshore steel structures, 2016".

[23] J. Serrano-González, "Technological evolution of onshore wind turbines-a market-based analysis," *Wind Energy,* 2016.

[24] W. H. Lio, "Fundamental performance similarities between individual pitch control strategies for wind turbines," *International Journal of Control,* vol. 90, no. 1, 2017.

(Innwind.EU, Deliverable 1.25, PI-based Assessment of 20MW Wind Turbines)

A Simplistic Approach for Translating Load Reduction Potential to Cost Reduction

Innovative concepts in INNWIND.EU are often demonstrating a load reduction potential against a reference design which has to be translated to cost reduction when their impact on LCoE is sought. In the present note we propose a simplistic procedure for such a load-to-cost reduction translation which can be used in connection with the cost models and LCoE calculators developed in the project.

In our analysis we are assuming that we are dealing with structures composed by beam elements whose cross sections can be ideally modelled as thin-wall cylinders of radius R and thickness t. Such a model represents convincingly steel tower and substructures of an offshore wind turbine but it can be also used as an abstract representation of the blades or the drive train load carrying components.

Assuming a bending-tension (or compression) load case resulting from a bending moment M and an axial force F, the maximum normal stress in the cross section derives from the formula

$$\sigma_{max} = \frac{F}{A} + \frac{M}{W} \quad ; \quad A = 2\pi R t \, , W = \pi R^2 t \tag{A1}$$

where A is the cross section area and W its bending resistance. Load reduction can be connected to the expected area reduction by assuming that the maximum stress σ_{max} remains the same under the different loading conditions. We shall study as two individual cases, the pure axial and the pure bending load cases.

Let subscript 1 denote the reference design and subscript 2 the innovative design, the one with the reduced loads. If α stands for the load reduction ratio (Load2/Load1) then Eq. A1 yields:

For F-driven designs

$$\alpha = \frac{F_2}{F_1} = \frac{A_2}{A_1} = \frac{t_2}{t_1}\frac{R_2}{R_1} \tag{A2}$$

which is valid for both tension and compression loads, the latter under the consideration that the local buckling resistance of the section is retained through a proportional change of the radius and thickness ratios, that is $\frac{t_2}{t_1} = \frac{R_2}{R_1} = (A_2/A_1)^{1/2}$ and global buckling is not a failure mode.
Similar results would be obtained for shear-stress-driven designs (due to shear forces or torsion).

For M-driven designs

$$\alpha = \frac{M_2}{M_1} = \frac{W_2}{W_1} = \frac{R_2^2 t_2}{R_1^2 t_1} \tag{A3}$$

For maintaining local buckling resistance we, again, assume that $\frac{t_2}{t_1} = \frac{R_2}{R_1} = (A_2/A_1)^{1/2}$ and therefore

$$\alpha = \frac{M_2}{M_1} = \frac{R_2^2 t_2}{R_1^2 t_1} = \frac{R_2^3}{R_1^3} = \left(\frac{A_2}{A_1}\right)^{3/2} \tag{A4}$$

(Innwind.EU, Deliverable 1.25, PI-based Assessment of 20MW Wind Turbines)

If the load reduction potential is uniform along the idealized beam structure (which is normally the case) then the load reduction impact on mass (and cost) derives from Eq.A2 or Eq.A4 as

$$\frac{Cost_2}{Cost_1} = \frac{Mass_2}{Mass_1} = \frac{A_2}{A_1} = \alpha^\lambda \qquad\qquad (A5)$$

where *λ = 1 for axial force driven* designs and *λ=2/3 for bending moment driven* design. Note that $\frac{A_2}{A_1}$ should only use the areas affected by the fatigue load component represented by the load reduction potential a.

Fatigue considerations

For fatigue, the damage equivalent load over the design life is evaluated over all mean wind speeds of operation considering 100% availability and considering the site specific annual Weibull probability. Usually Miners rule is used to design the component to resist fatigue damage over the desired lifetime. The design equation as per the Miners rule assumes a coefficient of variation over the failure damage limit (usually about 0.25 with a mean of 1) and safety factors in the material parameters and variations in the damage equivalent load quantity. Therefore when assessing if a new turbine design has lower fatigue damage, it is necessary to not only look at the mean lifetime damage equivalent load, but also its variation. The mean lifetime damage equivalent load and its variation is evaluated based on varying wind turbulence seeds (at least 6 per mean wind speed bin) and wind direction (3 yaw directions, 0, +/- 10 degs).

Let $E(L_{1eq})$ and $\sigma(L_{1eq})$ be the expected damage equivalent load and its standard deviation for a sensor over its lifetime for the reference case and $E(L_{2eq})$ and $\sigma(L_{2eq})$ be the expected damage equivalent load and its standard deviation for the same sensor for the innovative turbine. The standard deviations are computed as the variation of the damage equivalent load over all wind turbulence seeds and wind directions per mean wind speed bin as used in the fatigue load computations. At least 6 seeds of wind turbulence are to be used in DLC 1.2, DLC 6.4 at each mean wind speed. The following steps are then evaluated to ascertain mass/cost reduction from fatigue damage reduction:

1) Calculate the new design damage equivalent load level for the new turbine components in terms of both the mean lifetime damage equivalent load, $E(L_{2eq})$ and its standard deviation $\sigma(L_{2eq})$.
2) Evaluate if there is a significant reduction in the fatigue loads as compared to the reference design by doing a 2-sample t-test. This test is available in a variety of tools: MS Excel, Matlab etc. This requires as input the mean fatigue lifetime load level for the new turbine and the reference, their respective standard deviations and the sample sizes used to compute the fatigue load (Usually this is the no. of seeds at each mean wind speed). The t-test is assessed with the hypothesis that the two samples have the same fatigue damage values at a 95% confidence level.
3) If the result of step 3 is that the p-value (from the t-test) is less than 0.05, then we accept that the mean values of fatigue damage are different in the two samples, which implies that there can be material cost savings.

(Innwind.EU, Deliverable 1.25, PI-based Assessment of 20MW Wind Turbines)

4) If step 3 is successful, then the new design fatigue load is taken as $L_{d2} = (E(L_{2eq}) + \sigma(L_{2eq}))$ and the baseline design fatigue load is taken as $L_{d1} = (E(L_{1eq}) + \sigma(L_{1eq}))$

5) Evaluate the savings in damage equivalent load as L_{d2}-L_{d1}

6) Repeat steps 1 -5 for all design driving load sensors of the structure in question. For example for the blade, the savings in fatigue damage due to the flap moment and edge moment need to be evaluated separately using the above steps 1-5.

7) The mass of the structure corresponding to each of the fatigue load components is to be correctly apportioned. For example for the blade, essentially the blade section nose and tail material and some of the shear webs resist the edge fatigue, while the rest of the blade section may resist the flap fatigue. Therefore the correct mass on which the blade edge fatigue damage acts on should be evaluated. It may be for example 30% of the total blade mass.

8) Use the respective design equations (bending or shear etc), Eq. A3 - Eq. A5 to convert the savings in one particular damage equivalent load value to savings in mass or cost. For example, Eq.A5 can be directly used as $\frac{A_2}{A_1} = \alpha^\lambda$ with $\alpha = \frac{L_{d2}}{L_{d1}}$ and the λ value corresponding to the loading conditions. Note that $\frac{A_2}{A_1}$ should only use the areas affected by the fatigue load component represented by $\frac{L_{d2}}{L_{d1}}$

The above simplistic models rely solely on the stress-load relation and can directly apply in designs driven by ultimate or fatigue loads. However, material strength resistance is necessary but not sufficient conditions in a real design. Constraints on maximum deflection of flexible bodies and system's natural frequencies should be also satisfied to ensure structural integrity and desirable system's dynamics. We shall elaborate on such constraints below.

Maximum deflection

Starting from the beam deflection equation

$$\frac{d^2 w(x)}{dx^2} = \frac{M(x)}{EI(x)} \tag{A6}$$

where $w(x)$ is the displacement along the beam axis $M(x)$ is the bending moment and $EI(x)$ the flexural stiffness, one can show based on the above assumptions for buckling resistance that for the reference and innovative designs are interrelated through:

$$d = \frac{w_{2max}}{w_{1max}} = \frac{\alpha}{\left(\frac{A_2}{A_1}\right)^2} \quad with \quad \alpha = \frac{M_2}{M_1} \tag{A7}$$

or

$$\frac{Cost_2}{Cost_1} = \frac{Mass_2}{Mass_1} = \left(\frac{A_2}{A_1}\right) = \left(\frac{\alpha}{d}\right)^{1/2} \tag{A8}$$

Eq. A8 can be anticipated as a constraint for the cost/mass ratio driven by the load reduction coefficient (corresponding to the conditions where the maximum deflection occurs) and the deflection margin ratio d. If d=1 (no extra deflection margin available) the above deflection constraint limits the λ value of Eq. A5 to ½ compared to the original M-

(Innwind.EU, Deliverable 1.25, PI-based Assessment of 20MW Wind Turbines)

driven value of 2/3. If d allows for values greater than one further mass/cost reduction can be achieved.

Natural frequencies

For a cantilever beam of length L, clamped at x=0, having a concentrated mass m_L at x=L, its lowest natural frequency can be estimated using Rayleigh-Ritz method from:

$$\omega^2 = \frac{\int_0^L EI(x)(\frac{d^2\xi(x)}{dx^2})^2 dx}{\int_0^L \rho A(x)\xi(x)^2 dx + m_L} \tag{A9}$$

where ω is the angular frequency, $EI(x)$ the flexural stiffness, $\rho A(x)$ is the linear mass and $\xi(x)$ the normalized mode shape with $\xi(L) = 1$.

Let us again consider the two designs, reference and innovative, and let

$$p = \frac{\omega_2}{\omega_1} \;,\; q = \frac{m_{L1}}{\int_0^L \rho A_1(x)\xi(x)^2 dx} \;,\; \mu = \frac{m_{L2}}{m_{L1}} \tag{A10}$$

It can be shown that the frequencies ratio p is given by

$$p^2 = (\frac{A_2}{A_1})^2 \frac{1+q}{(\frac{A_2}{A_1})+q.\mu} \tag{A11}$$

Solving Eq.A11 we obtain a frequency-driven constraint for the mass/cost ratio in terms of the "allowable" frequency range as

$$\frac{Cost_2}{Cost_1} = \frac{Mass_2}{Mass_1} = \left(\frac{A_2}{A_1}\right) = \frac{p^2 + p\sqrt{p^2 + 4q\mu + 4q^2\mu}}{2(1+q)} \tag{A12}$$

When q=0, in the blade case for instance, then $\left(\frac{A_2}{A_1}\right) = p^2$. As q increases $\left(\frac{A_2}{A_1}\right) \to p$. For wind turbine support structures with their RNA mass on top $\left(\frac{A_2}{A_1}\right) = p^{1.1}$ is a valid approximation.

The analysis above suggests that the frequency cost/mass reduction constraint is directly connected to the allowable level of component's natural frequency reduction without spoiling system's dynamics. For blades the frequency reduction effect on mass/cost is more pronounced (quadratic) than in support structures (linear).

Summarizing the above findings in a single table addressing specific wind turbine components we read

Component	Load ratio (α)	Cost or Mass Ratio (A2 / A1)			
		Strength	Fatigue $\alpha = L_{d2}/L_{d1}$	Deflection	Frequency
Blades	*M-driven*	α $^{2/3}$	α $^{2/3}$	(α/d) $^{1/2}$	P $^{2.0}$
Tower	*M-driven*	α $^{2/3}$	α $^{2/3}$	(α/d) $^{1/2}$	P $^{1.1}$
Jacket	*F-driven*	α	α	-	-

Note that α in the above table corresponds to the relevant load (ultimate, fatigue, or the one associated with the maximum deflection) reduction potential. Without losing the generality we may assume that α for strength and deflection are coinciding.

(Innwind.EU, Deliverable 1.25, PI-based Assessment of 20MW Wind Turbines)

Application examples and synthesis

Consider an application example where for an F-driven design a specific new concept can reduce the ultimate axial force on a load carrying component by 20%. Then α=0.8 and, from Eq.A5 for λ=1, this results to a mass (cost) ratio of 80% corresponding to 20% cost reduction. Here the cost-load benefit is 100%. On the other hand, a 20% ultimate moment reduction of an M-driven design corresponding to α=0.8 leads (Eq.A5 for λ=2/3) to a mass ratio of 0.86 and therefore to 14% cost reduction. In this case the cost-load benefit is lower, 14/20=70%. These cost benefit values are valid when no deflection or frequency constraints are imposed.

Blades and tubular towers can be considered as moment driven designs and therefore they can be handled with λ=2/3. Blades are subjected to deflection and frequency constraints. If no extra deflection margin is available (d=1) than their λ value drops from 2/3 to ½ and for the above examined case of α=0.8 the minimum allowable mass ratio is 0.894 and the cost-load benefit can go up to 53%. The difference from 53% to 70% can be only recovered by allowing for an increased (estimated to 5% by solving $\alpha^{2/3} = (\alpha/d)^{1/2}$ for d) blade deflection. Regarding the blade frequency constraint a full exploitation of the cost load benefit (λ=2/3) for α=0.8 would result to a p = 0.93 value corresponding to 7% reduction of its lowest (1st flap) frequency which is a rather affordable number

For 10+ MW bottom-fixed offshore turbines considered here one can probably exploit fully the cost reduction benefit of λ=2/3 corresponding to a 5% increase of tower-top maximum deflection for α=0.8 does not seem to be a problem, while the frequency reduction of 7% for the same α value is rather beneficial for the design in terms of preventing the tower excitation in the variable speed regime of turbine normal operation.

Multi-member truss-type constructions like jackets are rather axial force driven designs and a λ value closer to 1 can be used for them. Here, the deflection constraint does not seem to be a problem thanks to the high stiffness of the jacket while the frequency reduction is again beneficial for the large turbines of our consideration.

Clearly, the proposed model is very crude as it is based on many assumptions and simplifications. Nevertheless it provides some basic evidence on how load reduction can be translated to mass reduction and what the expected cost-load benefit could roughly be.

20 MW Reference Wind Turbine

Aeroelastic data of the onshore version of the turbine

April 2016

Agreement n.:   308974

Duration   November 2012 – October 2017

                                       DTU Wind

The research leading to these results has received funding from the European Community's Seventh Framework Programme under grant agreement

Document information

Document Name:	**20 MW Reference Wind Turbine** **Aeroelastic data of the onshore version**
Document Number:	**Deliverable D 1.25** (a)
Author:	**Panagiotis Chaviaropoulos, Alkis Milidis (NTUA)**
Document Type	Report
Dissemination level	PU
Review:	**Anand Natarajan (DTU)**
Date:	**April 2016**
WP:	**WP1: Conceptual Design**
Task:	**Task 1.2: Assessment of Innovation at the Subsystem Level**
Approval:	Approved by WP Leader

TABLE OF CONTENTS

INTRODUCTION

In this document we present the land version of the 20 MW Reference Wind Turbine of INNWIND.EU project and we present the methodologies used for defining its aeroelastic data needed for its performance and loading calculations.

The 20MW RWT is not designed from scratch but it derives from the upscaling of the 10MW DTU RWT. Contrary to the 10MW RWT which was an IEC-61400 Class IA design, the 20MW RWT is designed for Class IC. This is mainly expected to affect the fatigue loads which are the design drivers of some critical turbine subcomponents, among them its offshore support system, which have significant contribution to the turbine CAPEX (and, therefore LCoE).

Classical upscaling techniques are first used for configuring all turbine subsystems.. In a next step the initial data are trimmed to incorporate mass (cost) reduction expectations due to technology advancement and designing for a lower turbulent subclass. This is resulting in a 252.2m diameter 20MW rotor designed for an optimal TSR of 7.5, spinning with a tip speed of 90m/s and placed at a hub height exceeding 165m. The 122m long blades of the 20MW are expected to weight 118t each, while the nacelle mass is expected to be heavier than 1000t.

The design of a 20 MW offshore turbine includes further challenges regarding the proper selection of systems first global frequency (related to the support structure design) in connection to the variable speed schedule of the turbine which is essential for its high performance. Further deviations from classical upscaling are thus effected to avoid the cross-cutting of the rotor 3P frequency with the 1st global frequency at wind speeds that are critical for the turbine performance and loading. This is accomplished through a slight increase of the rotor Tip Speed Ratio and a parallel increase of the tower height by 12 meters.

The design summary of the turbine is cross compared against that of the 10MW RWT. The aeroelastic data of the turbine and its subcomponents are given in XLS spreadsheets accompanying this report. There are three such spreadsheets addressing three alternative towers. This is an option discussed and agreed with WP4 which will design the 20MW jacket.

Further, this report makes a first evaluation of the 20MW RWT (onshore version) in terms of its dynamics (natural frequencies of the system) and loads. Blade and tower root ultimate and fatigue loads are presented for two relevant IEC-61400 DLCs. The tower bottom loads are a prerequisite for the jacket design.

CHALLENGES IN DESIGNING FOR 20 MW

The design integration of the Rotor Nacelle Assembly (RNA) with the offshore support structure in a proper way that restrains dynamic loading is becoming challenging for very large (10+MW) turbines. The issue has been extensively studied in PART A of Deliverable 1.35 [1]. The lower eigenfrequencies of the turbine are mainly driven by the stiffness of the support structure including its foundation and the mass of the RNA. A proper design has to prevent significant resonances between such eigenfrequencies and excitations from the waves or the rotor frequency and its higher harmonics (3P and 6P for a 3-bladed rotor).

The classical upscaling for the land version of the 20MW wind turbine would yield a first global frequency of 0.18 Hz, which would move towards 0.20 Hz if a shorter tower was used that maintains the blade-sea clearance of the 10MW turbine. The replacement of the land tower with the offshore support structure is expected to further stiffen the 1st global frequency by 10% approaching 0.22 Hz. This last statement is claimed using our earlier experience for the 10MW turbine where the land and offshore versions have their first global frequency at 0.26 Hz and 0.29 Hz respectively.
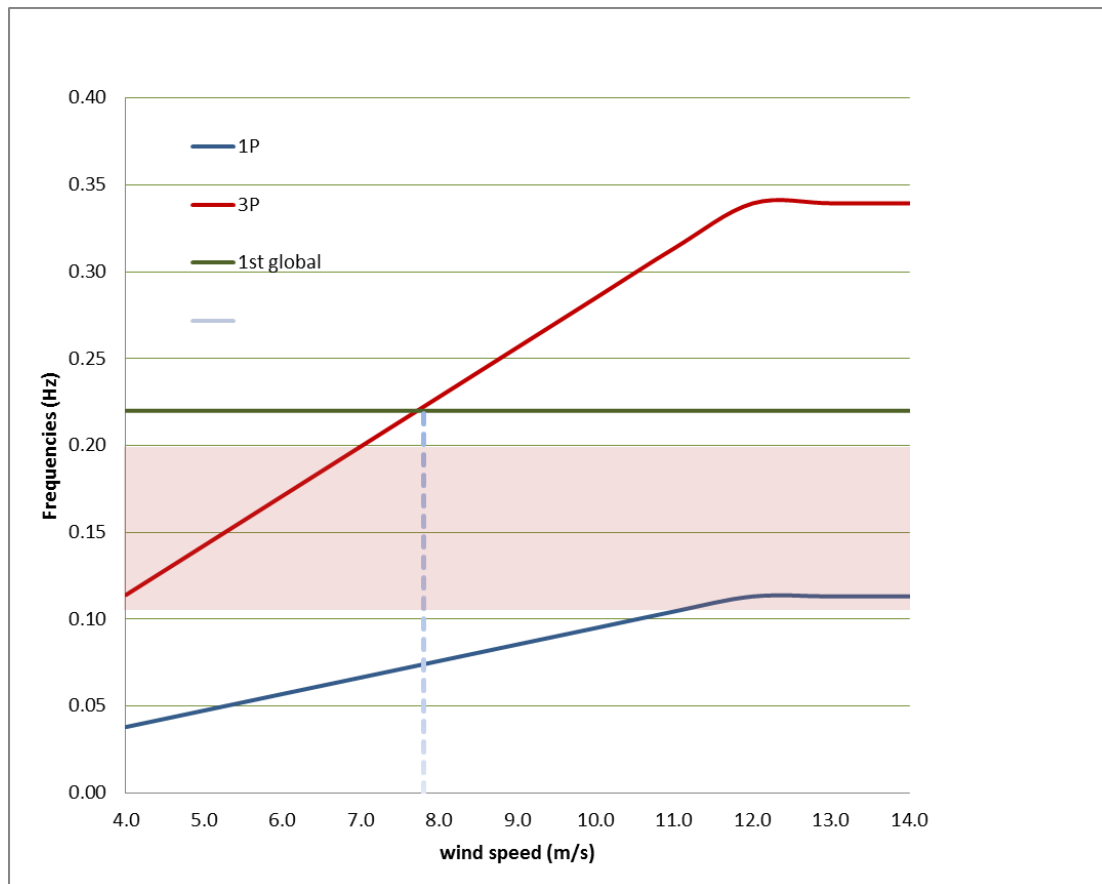
Figure 1   *Variable speed schedule vs system 1ˢᵗ global frequency – 20MW turbine using classical upscaling*

Deriving the rotor 1P frequency and variable speed schedule using classical upscaling we may form the Campbell diagram of Figure 1. It is seen that the 3P line cross-cuts the 0.22 Hz frequency at the wind speed of 7.8 m/s suggesting resonance there. In order to reduce the dynamic excitation a rotor speed exclusion window should apply in this region. This is already applied at the

10MW RWT offshore turbine, at speed range approximately ±10% around 6 rpm. The extent of the exclusion zone is a trade-off between loss in energy capture (due to deviation from the optimal TSR) and fatigue loading due to dynamic excitation of the support structure.

Both energy capture losses and fatigue loads are reduced when the resonance wind speed gets lower. This can be done by increasing the rotor speed or reducing the 1st global frequency or a combination of both.

Increasing the rotational speed of an existing blade (or operating it at a different TSR than its design value) is also having consequences on power production. Table 1 presents a study of the effect of rotor speed (through a TSR multiplier, noted as RPM x) and the late start of the variable speed schedule (above a given wind speed, noted as VS>value) on the capacity factor (CF) of a single turbine. The calculations have been performed assuming the INNWIND.EU reference site conditions (Rayleigh distribution with mean annual wind speed 9.3 m/s). The first two rows confirm that the 10MW RWT and the classically up-scaled 20MW turbine do have the same capacity factor. The third row shows that if the variable speed operation is also effected in the wind speed interval 4-7m/s this would result to a rather small increase of CF from 50.25% to 50.48%. The fourth row suggests that a 5% over-speeding of the reference rotor has a minor effect on CF reduction due to off-design operation. This effect is almost tripled when the over-speed becomes 10%.

	RPM x	Prated (MW)	Pmean (MW)	CF (%)	Max Flap Moment (kNm)
10 MW RWT (VS > 7 m/s)	1.00	10	5.025	50.25%	29091.75
20 MW Upscaled (VS > 7 m/s)	1.00	20	10.051	50.25%	82283.96
20 MW Upscaled (VS > 4 m/s)	1.00	20	10.095	50.48%	82299.42
20 MW Upscaled (VS > 4 m/s)	1.05	20	10.071	50.36%	85607.28
20 MW Upscaled (VS > 4 m/s)	1.10	20	10.013	50.07%	88698.62
20 MW Upscaled (VS >7 m/s)	1.10	20	9.920	49.60%	88683.79

Table 1   *Off-optimal-λ consequences to the single turbine capacity factor*

A 5% over-speed increases the tip speed of the blades from the original value of ~90m/s to ~95m/s. Further tip speed increase will result to higher power losses and burden corrosion effects. Thus the selection made for the 20MW RWT rotor is to use the geometrically up-scaled 10MW blade rotating 5% faster.

Table 2 shows the operating characteristics of the 20MW RWT rotor. Note that the TSR value in the variable speed range is now 7.91 (from 7.53) and the tip speed 94.12 m/s.

Reducing the 1st global frequency is more complicated. Ideally we would prefer to have a 1st global frequency of the offshore turbine close to 0.20 Hz. Higher values would move tower-rotor resonance at higher wind speeds while lower values might increase wave excitation loads. To do that the land version of the turbine should have an even lower 1st global frequency. At the tower design level this can be done either by increasing the tower height or increasing the tower mass. Through an investigation which is presented in a later section of the report, the decided to increase the tower height and have a blade-sea water clearance of 42m instead of the 30m of the 10MW RWT. Although a longer tower increases the ultimate and fatigue moments on the support structure this will be counterbalanced through the suppression of the dynamic loads (rotor-support structure interaction) and the reduction of turbulence induced loads (both ultimate and fatigue) since the design class is now IC compared to the IA of the 10MW RWT.

V (m/s)	RPM	1P (Hz)	3P (Hz)	OMEGA (rad/s)	Tip speed (m/s)	TSR
4.00	2.39	0.040	0.12	0.25	31.63	7.91
5.00	2.99	0.050	0.15	0.31	39.53	7.91
6.00	3.59	0.060	0.18	0.38	47.44	7.91
7.00	4.19	0.070	0.21	0.44	55.35	7.91
8.00	4.79	0.080	0.24	0.50	63.25	7.91
9.00	5.39	0.090	0.27	0.56	71.16	7.91
10.00	5.99	0.100	0.30	0.63	79.07	7.91
11.00	6.59	0.110	0.33	0.69	86.97	7.91
12.00	7.13	0.119	0.36	0.75	94.12	7.84
13.00	7.13	0.119	0.36	0.75	94.12	7.24
14.00	7.13	0.119	0.36	0.75	94.12	6.72
15.00	7.13	0.119	0.36	0.75	94.12	6.27
16.00	7.13	0.119	0.36	0.75	94.12	5.88
17.00	7.13	0.119	0.36	0.75	94.12	5.54
18.00	7.13	0.119	0.36	0.75	94.12	5.23
19.00	7.13	0.119	0.36	0.75	94.12	4.95
20.00	7.13	0.119	0.36	0.75	94.12	4.71
21.00	7.13	0.119	0.36	0.75	94.12	4.48
22.00	7.13	0.119	0.36	0.75	94.12	4.28
23.00	7.13	0.119	0.36	0.75	94.12	4.09
24.00	7.13	0.119	0.36	0.75	94.12	3.92
25.00	7.13	0.119	0.36	0.75	94.12	3.76

Table 2 *Operational characteristics of the 20 MW RWT*

The final selection of the 20MW RWT tower properties will be made after the 20MW RWT jacket is designed by WP4. This means that the design should be made in an interactive way with WP1 providing the tower bottom loads to WP4 for a given global configuration and WP4 gives back the resulting jacket design. To initiate the iteration we anticipate three alternative tower designs of different 1st global frequency as shown in Figure 2 (under Option 1 to 3 labelling) along with the variable speed schedule of the 5% over-speed rotor.
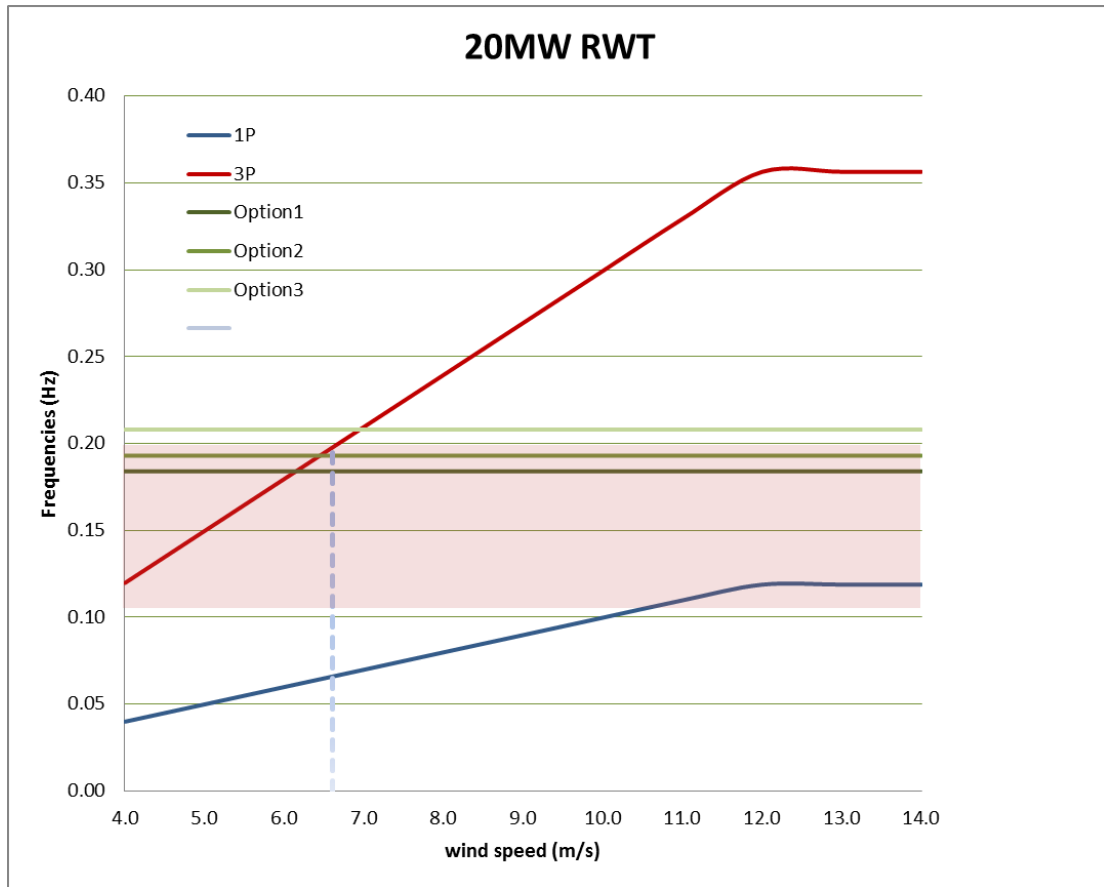
Figure 2   *Variable speed schedule vs system 1st global frequency – proposed design for the 20MW RWT*

CLASSICAL UPSCALING TECHNIQUES

Classical upscaling assumes geometric and aerodynamic rotor similarity, the later accomplished through the preservation of the tip-speed ratio of the rotor. The theory and application of upscaling (classical and beyond similarity) to wind turbine 10+ MW subsystems has been established in the UPWIND project, see [1], [3] and [4]. Here, we use classical similarity rules for a first appreciation of the 20MW RWT properties.

The classical upscaling method
- Maintains all aerodynamic-related stresses and deflections.
- Maintains the centrifugal stresses along the rotor.
- Maintains the aeroelastic stability characteristics of the rotor.
- Maintains the normalized (with the rotational frequency) natural frequencies of the W/T.
- Increases proportionally to the turbine size all stresses related to weight loading.
- Has an indirect effect (due to the deflection of the blades under their own weight) to the blade-tower clearance.
- May lead to higher than expected $\sim R^3$ tower-top weights due to drive train upscaling.

It is well known that classical upscaling is techno economically inefficient due to the so called "cubic law" for weight and cost. Nevertheless the method provides proper starting points for dimensioning critical turbine sub-systems, which can only be challenged by technological improvements in designing and manufacturing.

For the sake of completeness, we shall repeat in this section of the report part of the theory which is applied to calculate the distributed aerodynamic and structural properties of the 20MW blades along their span as well as the 20MW tower elastic properties. The basis for upscaling is the INNWIND.EU 10MW RWT. Upscaling of each property is effected through the so called "scaling factor" which is the exponent of the linear scale in the similarity rule governing the particular property. For instance, a volume property scales with R^3 and, therefore, its scaling factor is 3. Size independent properties (noted with I from invariant) have 0 scaling factor. Aerodynamic similarity suggests that the rotor angular speed has scaling factor equal to -1.

In the following paragraphs we present Tables showing the way that important geometrical, operational, structural and modal properties of the blades and the tower up-scale according to the classical theory.

3.1   Blades

Assuming geometric similarity for the external geometry of the rotor blades, i.e. the blade planform characteristics scale-up proportionally to the blade radius, the twist distribution and the airfoil types remain the same, we end-up with the following size dependency Table 3.

Innwind.EU, Deliverable 1.25, 20MW Reference Wind Turbine
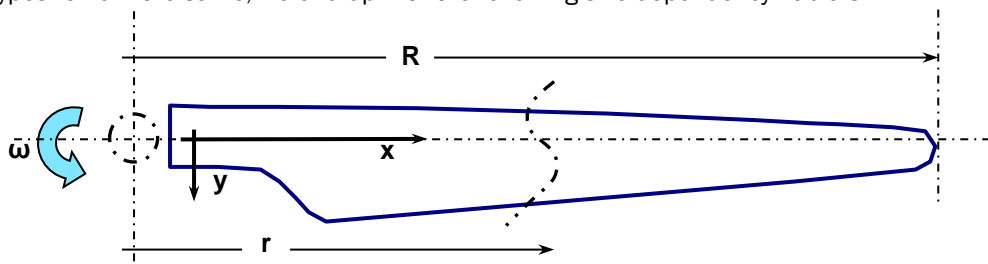
Symbol	Defining Formula	Description	Size-Dep.
R		Blade Radius	R
r		Local Radius	R
L	$L = R - r_0$	Blade length	R
x	$x = r / R$	Non-dimensional spanwise distance: $[x_h, 1]$ h=hub	I
$c(r)$		Chord distribution	R
$t(r)$		Max-Thickness distribution of airfoils	R
$c^*(x)$	$c^*(x) = c(r) / R$	Non-dimensional chord distribution	I
$t^*(x)$	$t^*(x) = t(r) / c(r)$	Non-dimensional Max-Thickness distribution	I
$twist(x)$		Twist distribution	I
$airf(x)$		Airfoil type	I

R: denotes linear dependency on blade radius.
I: denotes size independency.

Table 3   *Upscaling blade geometry properties*

To achieve aerodynamic rotor similarity we assume that the blade tip-speed and the collective pitch are size-independent, depending only on the actual wind-speed through the turbine control. It is notable, though, that the local Reynolds number *Re* increases proportionally to the turbine size. Aerodynamic airfoil similarity requires geometrically similar blades and equal Reynolds number, Mach number and reduced frequency (turbulence, 1P, tower passage) of the effective wind speed.

Symbol	Defining Formula	Description	Size-Dep.
ρ_a		Air density	I
U		Wind Speed	I
ω		Rotational Speed	$1/R$
ωR	$\omega R = function(U)$	Tip-speed	I
p	$p = function(U)$	Collective Pitch	I
$V(x)$	$V(x) = function(U, x)$	Effective Wind Speed	I
$Re(x)$	$Re(x) = V(x) * c(x) / \nu$	Reynolds Number (ν = air kinematic viscosity)	R
$M(x)$	$M(x) = V(x) / a$	Mach number (a = speed of sound)	I
$k(x)$	$k(x) = f * c(x) / 2V(x)$	Reduced frequency (f = frequency)	I (for 1P)

Table 4   *Upscaling operational conditions*

Assuming the geometric up-scaling of the internal blade structure (dimensions scale-up with R, increasing proportionally the number of layers of the same material) and ignoring possible second order effects, the following Table 5 results for the sectional properties.

Symbol	Defining Formula	Description	Size-Dep.
$A(x)$	$= R^2 \int ds^* = R^2 . A^*(x)$	Effective Area	R^2

$I(x) = \begin{pmatrix} I_{yy}(x) & I_{yz}(x) \\ I_{zy}(x) & I_{zz}(x) \end{pmatrix}$	$= R^4 \begin{pmatrix} \int z^{*2} ds^* & -\int y^* z^* ds^* \\ -\int z^* y^* ds^* & \int y^{*2} ds^* \end{pmatrix}$ $= R^4 . I^*(x)$	Moments of Inertia - Tensor	R^4
$I_p(x)$	$= R^4 . I_P^*(x)$	Polar Moment of Inertia	R^4
$J(x)$	$= R^4 . J^*(x)$	Torsion Constant	R^4
$W_y(x)$		Section Moduli – Y Bending	R^3
$W_z(x)$		Section Moduli – Z Bending	R^3
$W_t(x)$		Section Moduli – Torsion	R^3
$\bar{\rho}_m(x)$		Mean Material Density	I
$\bar{E}(x)$		Mean Young's modulus	I
$\bar{G}(x)$		Mean Rigidity modulus	I
$\bar{\rho}(x)$	$\bar{\rho}_m(x).A(x)$	Linear Density	R^2
$EI(x)$	$E(x).I(x)$	Bending Stiffness - Tensor	R^4
$GJ(x)$	$G(x).J(x)$	Torsional Stiffness	R^4

Table 5   *Upscaling blade structural properties*

Eigenvalue analysis relies on a single-beam model with uniform sectional properties along its span. Let L be the length of the beam. The angular natural frequencies ω_n of the different modes are proportional to $(K_m / M_m)^{1/2}$, where M_m stands for the generalized mass and K_m for the generalized stiffness. i is the radius of gyration scaling-up with R.

Table 6 the absolute blade natural frequencies are inversely proportional to R while the non-dimensional natural frequencies (normalized by the blade rotational frequency) are size independent.

	M_m	K_m	$\omega_n \approx \sqrt{K_m / M_m}$	$\overline{\omega_n} = \omega_n / \omega \approx$
Tension	$\bar{\rho}\,L \sim R^3$	$EA / L \sim R$	$\frac{1}{L}\sqrt{EA/\bar{\rho}} \sim R^{-1}$	$R^{-1}/R^{-1} \sim I$
Bending	$\bar{\rho}\,L \sim R^3$	$EI / L^3 \sim R$	$\frac{1}{L^2}\sqrt{EI/\bar{\rho}} \sim R^{-1}$	$R^{-1}/R^{-1} \sim I$
Torsion	$\bar{\rho}\,L\,i^2 \sim R^5$	$GJ / L \sim R^3$	$\frac{1}{L}\sqrt{GJ/(\bar{\rho}\,i^2)} \sim R^{-1}$	$R^{-1}/R^{-1} \sim I$

Table 6   *Upscaling blade natural frequencies*

3.2 Tower

Significant tower properties and relevant upscaling exponents deriving from the classic theory are given in Table 7.

Symbol	Defining Formula	Description	Size-Dep.
m_T	$= m_R + m_{nacelle}$	Tower-top mass	R^3 Assumed R^{3+} In reality
L_T		Tower Height	R
A_T		Tower Sectional Area	R^2
W_{Tb}		Tower Moduli , Bending	R^3
W_{Tt}		Tower Moduli , Torsion	R^3
EI_T		Tower Young's modulus	R^4
GJ_s		Tower Torsional Stiffness	R^4
$\sigma_{xx,Tc}$	$\sigma_{xx,Tc} = g(m_T + \overline{\rho_T} L_T)/A_T$	Axial Compression Stress due to Weight	R Assumed R^{1+} In reality
$\sigma_{xx,Tb}(U)$	$= (T(U)L - gm_T l)/W_{Tb}$	Axial stress due to bending, l is the offset of the nacelle centre of gravity	$I+R$ Assumed $I+R^{1+}$ In reality
$\tau_T(U)$	$\tau_s(U) = M_{Tt}(U)/W_{Tt}$	Shear Stress due to the Aerodynamic Torque M_{Tt}	I
$\overline{\omega}_{T,n}$	$\overline{\omega}_{T,n} = \dfrac{1}{\omega}\sqrt{\dfrac{EI_T / L_s^{3}}{\overline{\rho_T} L_T + m_T}}$	Non-dimensional bending frequency	I Assumed $I\cdot$ In reality

Table 7   *Upscaling tower properties*

DEVIATING FROM CLASSICAL UPSCALING

4.1 Rotor

Classical upscaling with cubic scaling factor for the mass is applied for the definition of the 20MW blades starting from the 10MW ones. The 10MW RWT all-glass blade is a state of the art design and it is difficult, therefore, to assume a lower scaling factor that could improve the 20MW mass and cost. The 20MW blade could be designed lighter if a proper integrated design approach was followed taking advantage of the lower turbulence sub-class (IC) that the design aims for. Nevertheless, the classically up-scaled 20MW blade is a good starting point to serve as a reference in the present context. No deviations from the classical theory are assumed here.

4.2 Nacelle – Hub

We take advantage of the lower turbine subclass to assume less than cubic mass scaling factors for the hub and the nacelle. For the nacelle we assume that its weight can be further reduced through technological interventions that maintain the current learning curve trends. The following values are used:

- Hub   :   SF = 2.8   Mass =   278 t
- Nacelle   :   SF = 2.6   Mass = 1 098 t

4.3 Drive train

The drive train weight is part of the nacelle weight discussed above. Drive train deviations from classical upscaling address the 5% increase of the rated rotor speed which now becomes 7.13 RPM. We further assume that we maintain the medium speed drive of the 10MW RWT with

- Rated Generator Speed: SF = -1.0   N = 339 RPM

yielding a Gearing Ratio of 48. No further deviations from classical theory are anticipated.

4.4 Tower

Significant deviation from the classical upscaling theory is normally encountered in offshore wind turbine design. The usual choice, which accounts the fact that the wind shear exponent is lower offshore than onshore (at least for flat terrain) and thus a longer tower is less cost effective, is that the tower height is not up-scaled with SF = 1 but in a way that maintains the blade water clearance to a prescribed level. In this case the new tower may derive by first up-scaling linearly the reference tower and then cutting its bottom part as much as needed to match the desired hub height.

The above described approach was also the starting point for designing the land version of the 20MW tower. The first global system frequency calculated in this case was 0.208 Hz (5th row of Table 8, corresponding to the SFs presented above for the RNA components). This is a rather high starting value which would further increase to 0.231 Hz if the lower 20m of the tower was made extra stiff, resembling the influence of the jacket (6th row of Table 8, "stiff" version).

To appreciate the influence of the tower design parameters on the 1st system frequency we performed several calculations assuming a tower / top-mass system and changing in a global way along the height the tower radius, thickness and height as depicted in Table 8. In the Table we present the 1st system frequency which derives from different combinations of the blades/ hub/ nacelle weight scaling factors, tower radius and wall thickness global multipliers and tower height.

In most of the cases we consider a "soft" and a "stiff" option, the later as defined in an earlier paragraph. The study showed that making the tower softer needs excessive extra mass (lowering the radius and increasing the wall thickness to maintain the level of bending resistance) if the tower height is not increased. As a more efficient way to soften the system frequency it was chosen to increase the tower height (we selected a value of 12m).

SF. Blade Weight	SF.Hub Weight	SF.Nacelle Weight	Tower Radius *	Tower Thickn *	Tower Height (+ m)	1st SYSTEM FREQ (Hz)	Soft / Stiff
3.00	3.00	3.00	1.00	1.00	0.00	**0.199**	soft
3.00	3.00	3.00	1.00	1.00	0.00	**0.221**	stiff
3.00	3.00	3.00	0.80	1.56	0.00	**0.195**	soft
3.00	3.00	3.00	0.80	1.56	0.00	**0.218**	stiff
3.00	2.80	2.60	1.00	1.00	0.00	**0.208**	soft
3.00	2.80	2.60	1.00	1.00	0.00	**0.231**	stiff
3.00	2.80	2.60	0.80	1.56	0.00	**0.205**	soft
3.00	2.80	2.60	0.80	1.56	0.00	**0.228**	stiff
3.00	2.80	2.60	1.00	0.90	0.00	**0.198**	soft
3.00	2.80	2.60	1.00	0.80	0.00	**0.188**	soft
3.00	2.80	2.60	1.00	1.00	0.00	**0.208**	soft
3.00	2.80	2.60	1.00	1.00	0.00	**0.231**	stiff
3.00	2.80	2.60	1.00	1.00	10.00	**0.195**	soft
3.00	2.80	2.60	1.00	1.00	10.00	**0.215**	stiff
3.00	2.80	2.60	1.00	1.00	12.00	**0.208**	stiff
3.00	2.80	2.60	1.00	1.00	12.00	**0.193**	soft
3.00	2.80	2.60	1.00	0.90	12.00	**0.184**	soft
3.00	2.80	2.60	1.00	1.00	20.00	**0.183**	soft
3.00	2.80	2.60	1.00	1.00	20.00	**0.205**	stiff

Table 8   *Alternative tower designs and their effect on 1st global frequency*

The baseline frequency of the longer tower "soft" (normal) version, hereafter called **Tower 2**, is 0.193 Hz which would increase to 0,208 Hz for the "stiff" version (**Tower 1**). In this case the stiffening is materialized by increasing artificially the rigidity of the first 15 meters of **Tower 2.** If the wall thickness of the tower might reduce by 10%, thanks to the lower ultimate fatigue and buckling loading of the selected IC turbine class, the baseline frequency would further reduce to 0.184 Hz (**Tower 3**). These three tower options are selected as alternatives for tower base load calculations communicated to WP4 for designing the 20MW jacket.

4.5   Control

Similar upscaling techniques have been used for the Standard DTU Controller parameters on the basis of their values for the 10MW RWT. The 5% over-speed is also taken into account. The full list of the controller parameters for the 20MW RWT is given in Appendix I. In red fond we present deviations from classical upscaling. Note that no exclusion zone is present but we compromise optimal variable speed generation by initiating at 7m/s wind speed corresponding to a minimum rotor speed of 0.45 rad/s. The value of "Constant 11" addressing the optimal Cp tracking factor

has been calculated explicitly using the exact values of its defining formula, taking into account the 5% rotor over-speed.

4.6   Design summary

Table 9 presents the design summary of the 20MW Reference Wind Turbine deriving from the above assumptions. Contrary to other properties the tower weight of the land version is given as a range of values from 1600 to 1780 tonnes corresponding to the two alternative "soft" designs discussed above.

	10	20
Rated Power [MW]	10	20
Number of blades [-]	3	3
Rotor Diameter [m]	178.33	252.2
Hub Height from m.s.l. [m]	119	167.9
Blade Length [m]	86.36	122.14
Rated Wind Speed [m/s]	11.4	11.4
Design Extreme Thrust Value [kN]	4600	9600
Minimum Rotor Speed [RPM]	6	4.45
Rated Rotor Speed [RPM]	9.6	7.13
Optimal TSR [-]	7.5	7.5
Gear Ratio [-]	50	48
Blade Mass [tons]	41.7	118
Hub Mass [tons]	105.5	278
Nacelle mass [tons]	446	1098
Tower mass [tons]	628.4	1600-1780
Tower Top Mass, RNA [tons]	676.7	1730
Water depth (mean sea level - m.s.l.) [m]	50	50
Access Platform a.m.s.l. [m]	25	25
Jacket Mass [Tons]	1210	-
Transition piece mass [Tons]	330	-

Table 9   *Design summary of the 20 MW RWT vs the 10 MW RWT*

FIRST ASSESSMENT OF THE 20 MW DESIGN

A first assessment of the 20MW RWT is presented in this section. An eigenvalue analysis of the 20MW blade and turbine are first presented. Then, loads are calculated for two critical load cases, DLC 1.2 (fatigue) and DLC 6.2 (ultimate) needed also for the design of the 20MW jacket.

DLC 1.2 is run for all operational wind speeds with a 2m/s binning, assuming normal turbulence IC conditions, using 6 turbulence generation seeds. Calculations are performed for 0, ±8° yaw misalignment values. DLC 6.2 is run for reference wind speed 50m/s (Class I) assuming turbulent wind conditions using 3 seeds. The yaw misalignment range considered is [-180°, 180°] discretized in steps of 15°. The sensors used for recording loads and deformations are placed at the three blade roots and at the tower height of 26m where the transition piece of the offshore foundation is planned to be. No safety factors have been applied to the calculated ultimate and fatigue loads. Turbulence is produced using a 3D Veers-type generator.

5.1   Blade natural frequencies

Table 10 shows the natural frequencies of the isolated 20MW reference blade calculated with the GAST.mb code of NTUA. As long as the 20MW derives by applying classical upscaling theory the natural frequency values are indeed those of the 10MW blade divided by the scaling factor $\sqrt{2}$.

Mode	BLADE ONLY		
1	1st Blade Flap		0.432
2	1st Blade Edge		0.640
3	2nd Blade Flap		1.219
4	2nd Blade Edge		1.925

Table 10   *Natural frequencies [Hz] of an isolated 20 MW RWT blade*

5.2   Turbine natural frequencies

Mode	Description	10 MW HAWC2 (Hz)	20 MW GAST (Hz) Tower 1	20 MW GAST (Hz) Tower 2	20 MW GAST (Hz) Tower 3
1	1st Tower SS	0.249	0.206	0.182	0.174
2	1st Tower FA	0.251	0.210	0.184	0.176
3	1st Drive Train	0.502	0.349	0.347	0.344
4	1st Blade Asym. Flapwise Yaw	0.547	0.372	0.365	0.363
5	1st Blade Asym. Flapwise tilt	0.590	0.382	0.379	0.377
6	1st Blade Collective Flap	0.634	0.448	0.446	0.446
7	1st Blade Asym. Edgewise 1	0.922	0.635	0.634	0.634
8	1st Blade Asym. Edgewise 2	0.936	0.647	0.646	0.645
9	2nd Blade Asym. Flapwise Yaw	1.376	0.919	0.914	0.906
10	2nd Blade Asym. Flapwise tilt	1.550	0.977	0.969	0.965
11	2nd Blade Collective Flap	1.763	1.241	1.239	1.240
12	2nd Tower SS	1.969	1.432	1.420	1.417
13	2nd Tower FA	2.247	1.784	1.626	1.619

Table 11   *Natural frequencies of the 20 MW RWT land version*

Table 11 presents the system natural frequencies of the land version of the 20MW turbine for the three tower options discussed earlier calculated with GAST.mb. A comparison against the land version of the 10MW RWT is also made. It is seen that in this full version of the turbine the 1st global frequencies corresponding to Tower 2 and Tower 3 are even lower than the approximate values of Table 8.

5.3   Blade root ultimate loads from DLC 6.2

Figure 3 and Figure 4 show the blade root flapwise and edgewise bending moment min-max values calculated for the different yaw angles considered. The results presented are seed-averaged and include all three tower models. Calculation results for yaw angles ±90o±15o are missing from the plots as the 20MW turbine (also the 10MW RWT) experiences severe edgewise vibrations at such crossflow conditions due to the highly negative aerodynamic damping experienced by their blades at angles of attack around ±90o. To a certain extent this is resulting from the very high Reynolds numbers under which such multi MW machines face even at idling conditions.
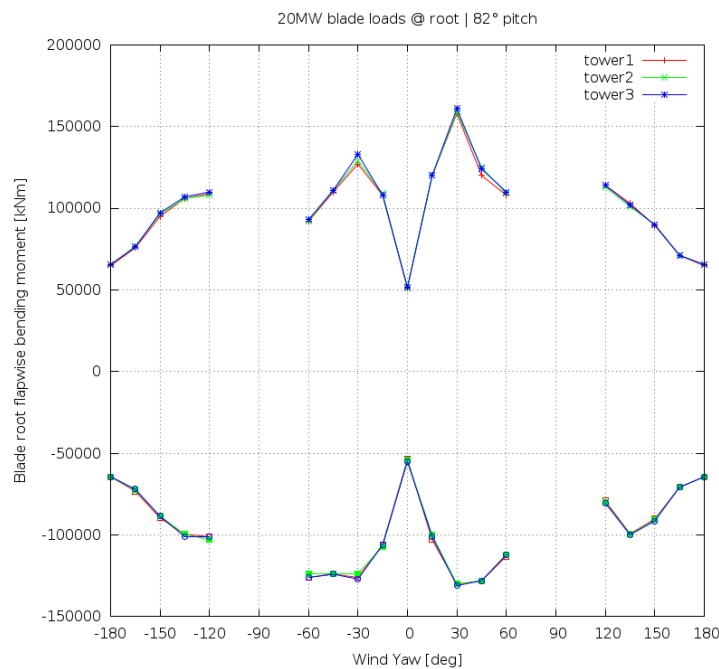

Figure 3   *Blade-root flapwise bending moment envelopes calculated for the three towers. Seed-averaged values.*

The pitch angle for the idling calculations was set to 82o, an unusually low value for feathering blades. Earlier results obtained for pitch angles closer to 90o demonstrated that due to the increased inertia of the 20MW rotor its idling speed is too small for such pitch settings. When the rotor torque is not adequately high the increased inertia of the 20MW rotor has the tendency to trap the blades at azimuthal zones of negative aerodynamic damping, resulting to instabilities and increased (edgewise) loads. Using lower pitch settings helps in increasing the idling torque so that the blades run through the unstable azimuthal zones without stacking in them. Evidently, there is an upper limit to the idling speed dictated by the multiples of the 3P frequency which has to stay away from the first global frequency of the system.
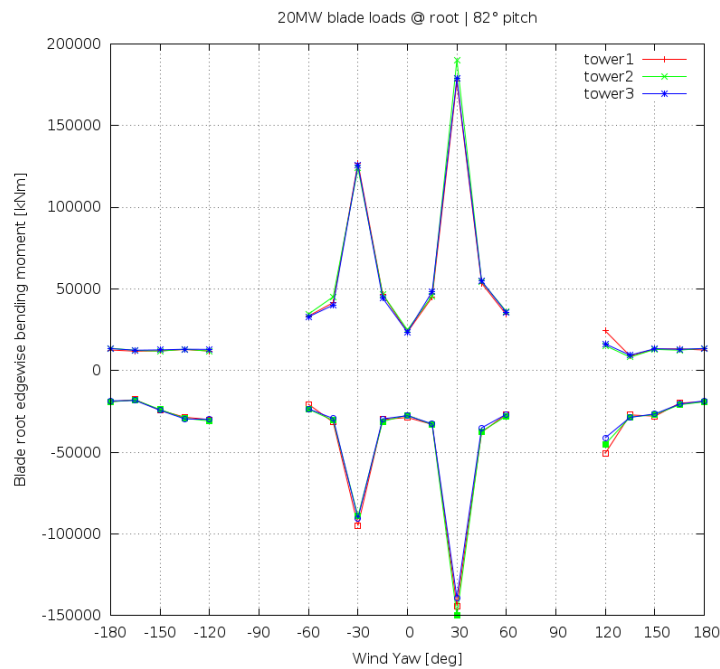
20MW blade loads @ root | 82° pitch

Figure 4   *Blade-root edgewise bending moment envelopes calculated for the three towers. Seed-averaged values.*

According to Figure 3 the FLAP+ ultimate bending moment at the blade root is +160MNm while the FLAP- is -130MNm. These values refer to the global coordinate system which is not taking account of the local blade twist (but only the pitch). In a similar way the EDGE+ root bending moment is close to +200MNm for the stiffer towers and the EDGE- is -150MNm. Both FLAP and EDGE ultimate loads derive at 30° yaw misalignment.

5.4   Tower bottom ultimate loads from DLC 6.2

Tower "bottom" loads are computed at 26m a.m.s.l. Figure 5, Figure 6 and Figure 7present seed averaged load envelopes for the fore-aft and side-side bending moments as well as the yaw moment.

The ultimate FOREAFT± loads are encountered at 30° yaw misalignment having values 550MNm and -450MNm respectively. The SIDESIDE± ultimate loads are encountered at 45° yaw misalignment reading +925MNm and -825MNm.

The ultimate yaw moments derive for yaw +30° and -30° with a level of +200MNm and -150MNm.

The combined tower bottom fore-aft / side-side bending moment envelope is shown in Figure 8. Its maximum value approaches 1000MNm at the yaw misalignment of 45°.
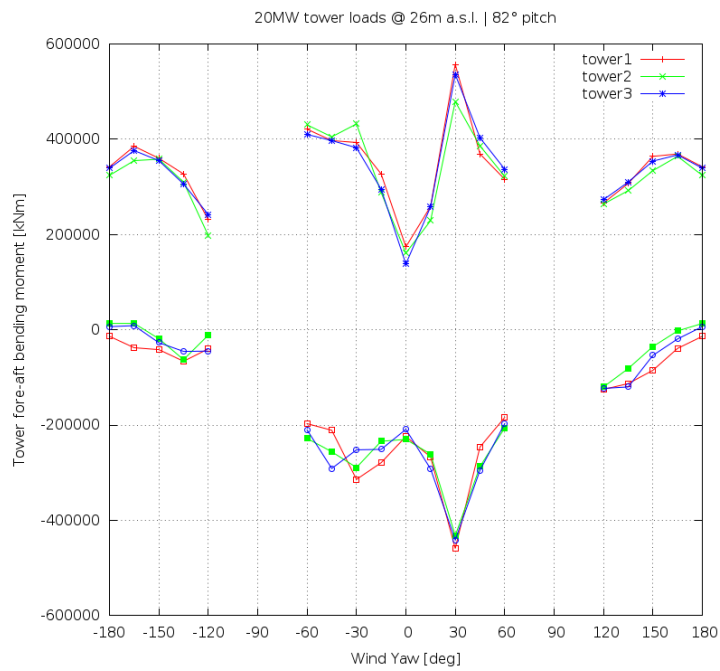
Figure 5   *Tower bottom (26m amsl) fore-aft bending moment envelopes calculated for the three towers. Seed-averaged values.*
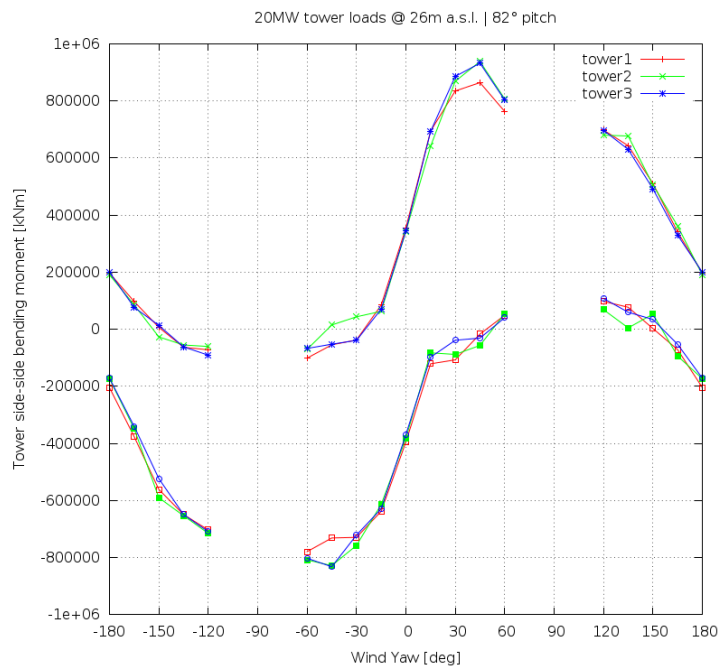

Figure 6   *Tower bottom (26m amsl) side-side bending moment envelopes calculated for the three towers . Seed-averaged values.*
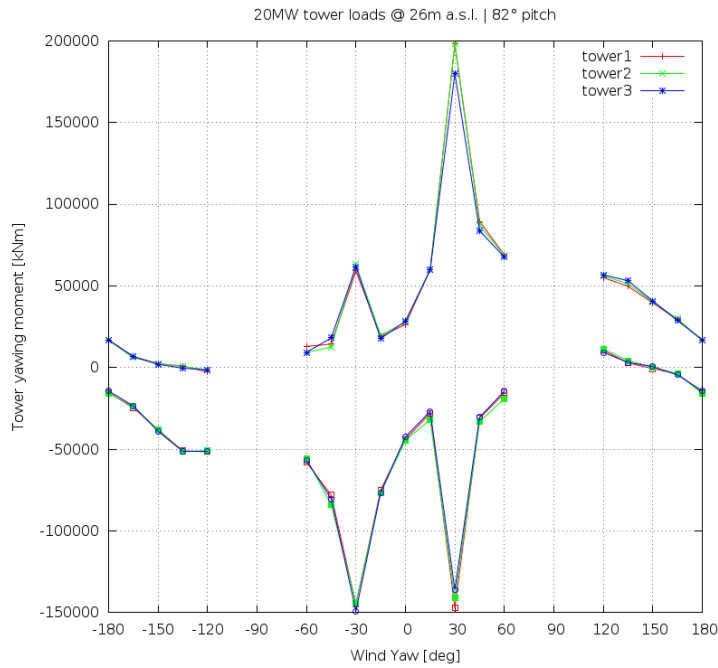
Innwind.EU, Deliverable 1.25, 20MW Reference Wind Turbine

Figure 7   *Tower bottom (26m amsl) yaw bending moment envelopes calculated for the three towers. Seed-averaged values.*
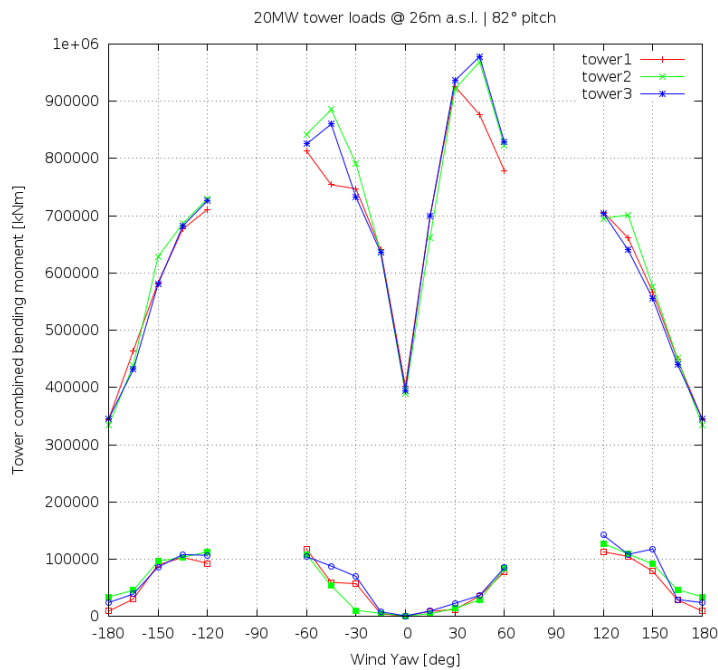

Figure 8   *Tower bottom (26m amsl) combined fore-aft/side-side bending moment envelopes calculated for the three towers. Seed-averaged values.*

5.5   Blade root fatigue loads from DLC 1.2

Characteristic values of blade root flapwise and edgewise moments calculated for Tower 1 for zero yaw as a function of the wind speed for all 6 turbulent seeds are presented in Figure 9 and Figure 10 respectively. The figure presents min-max values per seed (the coloured bars), mean value per wind speed for all seeds (continuous black line) and standard deviation mean for all seeds (continuous white line). The same notation and colouring scheme is used in all fatigue load plots.

In the present context we present blade toot results for Tower 1 and for the zero yaw angle. The full set of results, for all three towers and all three yaw angles are included in Appendix II. The influence of the yaw misalignment and the tower selection on blade root fatigue loads is rather small.
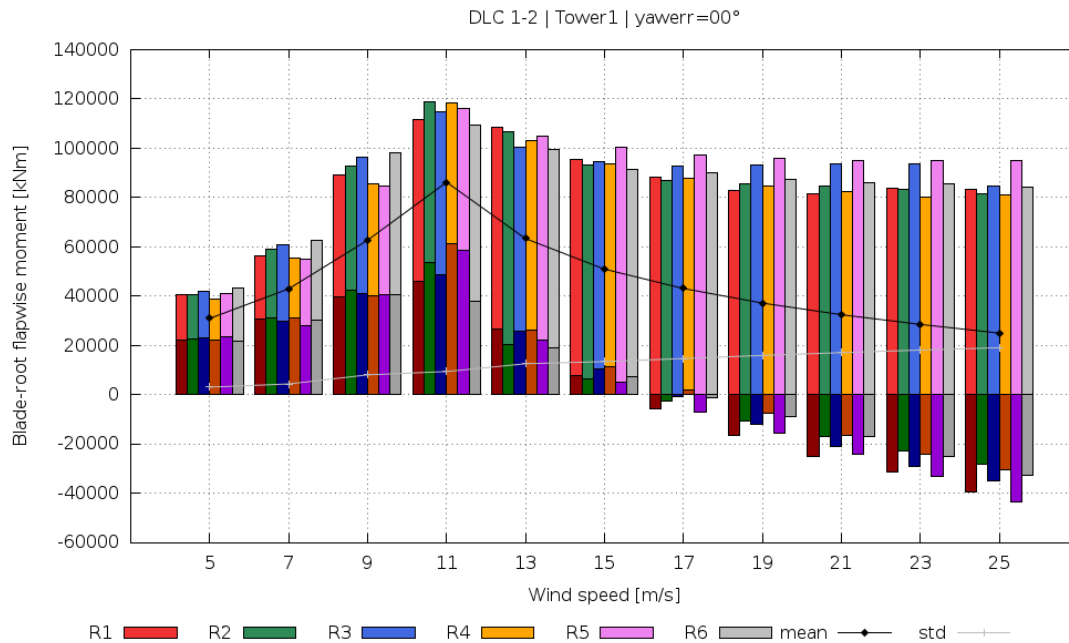

Figure 9   *Blade-root flapwise bending moments for Tower 1 and yaw angles 0 for all wind speeds and turbulent seeds*

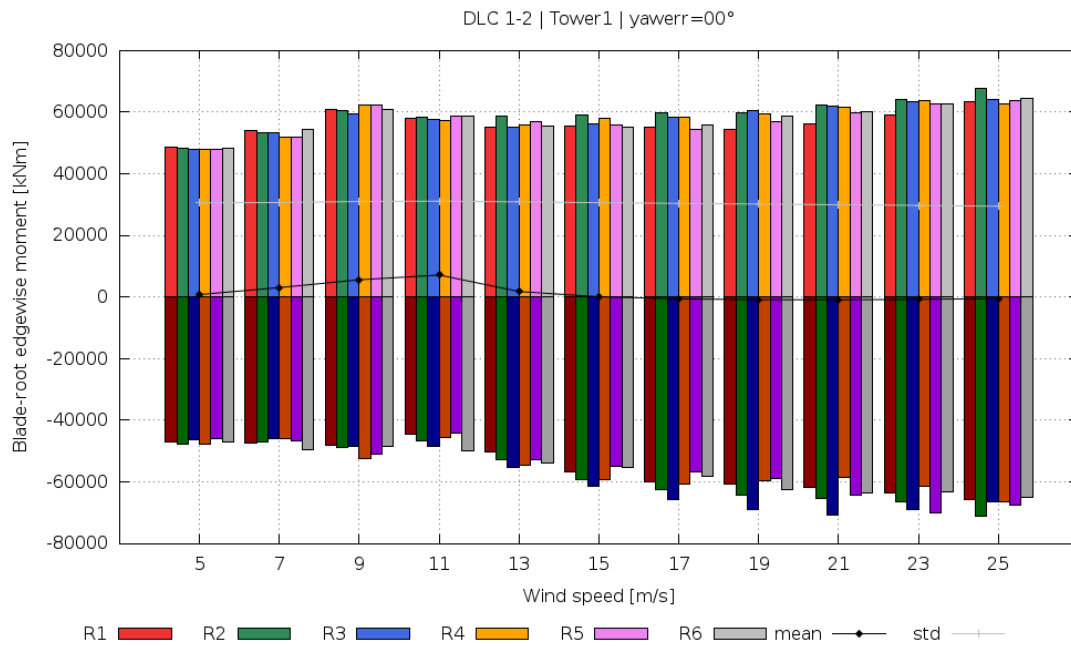*Innwind.EU, Deliverable 1.25, 20MW Reference Wind Turbine*

Figure 10   *Blade-root edgewise bending moments for Tower 1 and yaw angles 0 for all wind speeds and turbulent seeds*
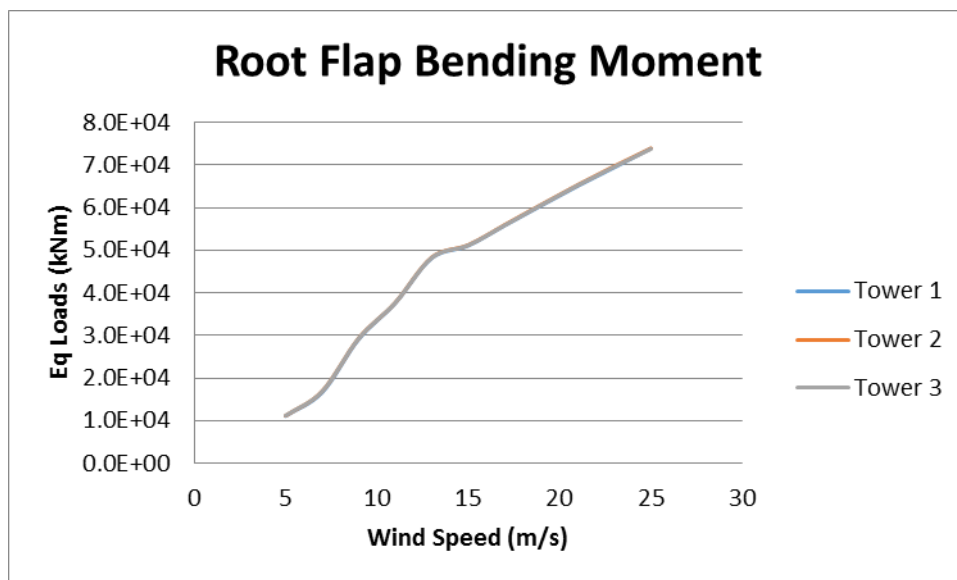

Figure 11   *Flapwise bending moment equivalent loads at blade root for all three towers and yaw angle 0, as a function of the wind speed. Seed averaged results, m=12.*

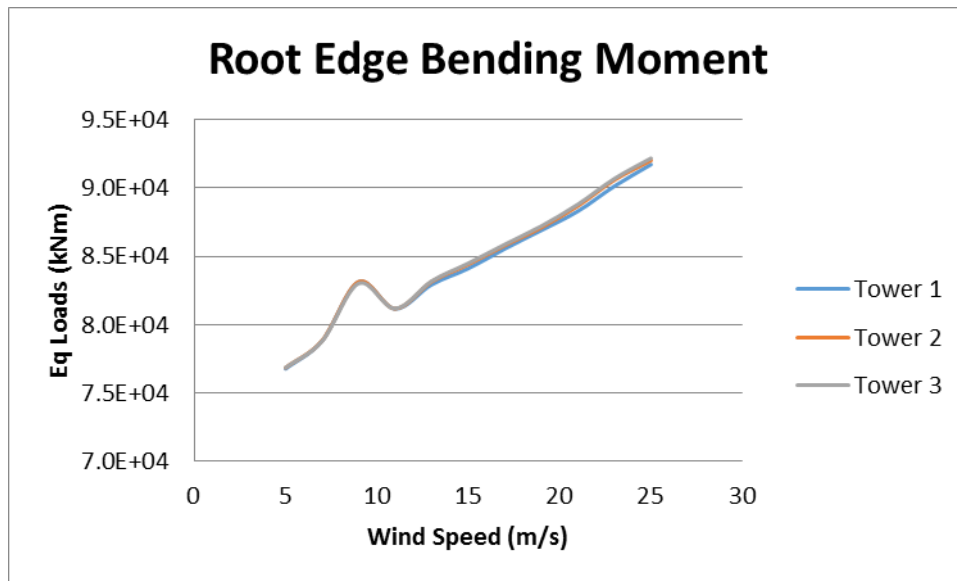*Innwind.EU, Deliverable 1.25, 20MW Reference Wind Turbine*

Figure 12   *Edgewise bending moment equivalent loads at blade root for all three towers and yaw angle 0, as a function of the wind speed. Seed averaged results, m=12.*

Figure 11 and Figure 12 present the correlation of the root flapwise and edgewise bending moment equivalent loads with the wind speed. The equivalent loads are seed-averaged, they are only shown for the yaw 0º case and have been calculated for m=12. The flapwise equivalent loads are characterized by their monotonic growth with the wind speed and their level are tower independent. Contrary, the edgewise loads, although tower independent too, they are characterized by an excitation at 9m/s which presently cannot be explained through a resonance mechanism either with 3P or 6P. The redesign of the blades in the course of the project should try to remedy this inconvenience.

5.6   Tower bottom fatigue loads from DLC 1.2

Characteristic values of tower bottom (26m a.m.s.l where the transition piece of the offshore version is planned to begin) fore-aft, side-side and yaw moments calculated for Tower 1 for zero yaw as a function of the wind speed for all 6 turbulent seeds are presented in Figure 13, Figure 14 and Figure 15 respectively. The figure presents min-max values per seed (the coloured bars), mean value per wind speed for all seeds (continuous black line) and standard deviation mean for all seeds (continuous white line).

In the present context we present blade toot results for Tower 1 and for the zero yaw angle. The full set of results, including fatigue equivalent loads, for all three towers and all three yaw angles are included in Appendix II. The influence of the yaw misalignment and the tower selection on blade root fatigue loads is, again, rather small.

The maximum magnitude of the mean fore-aft tower bottom bending moment is about 400MNm which is very close to the one expected from up-scaling calculations. Given that the maximum steady thrust of the 20MW RWT is expected to be ~2.1400=2800 kN (1400 kN is the value for the 10MW RWT) which multiplied with the lever of 168(hub height)-26=142m yields a similar value.

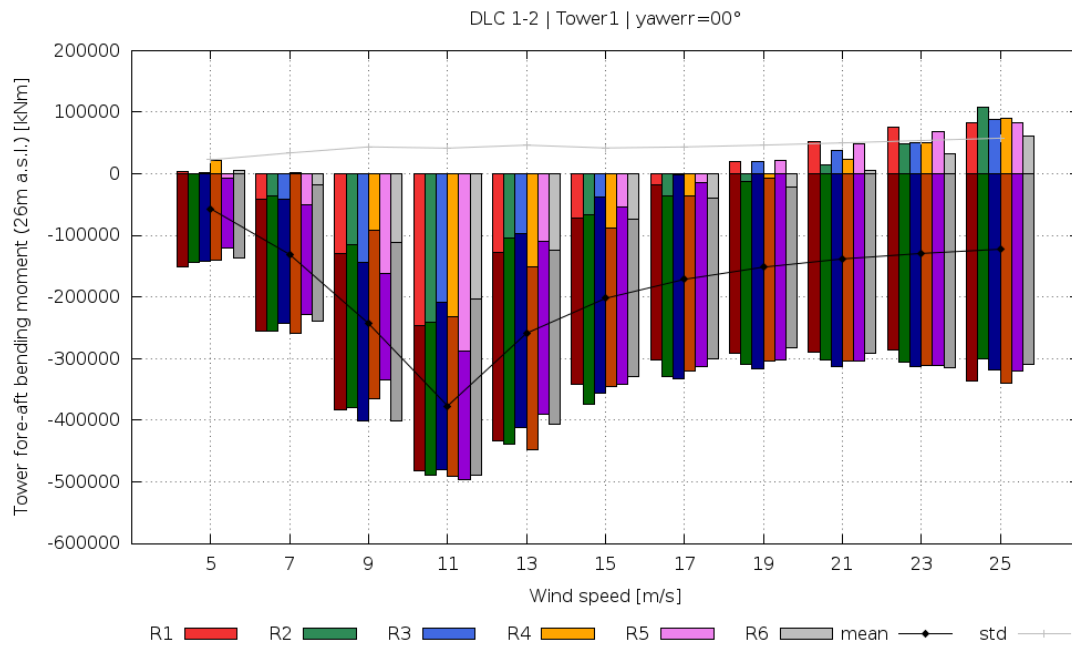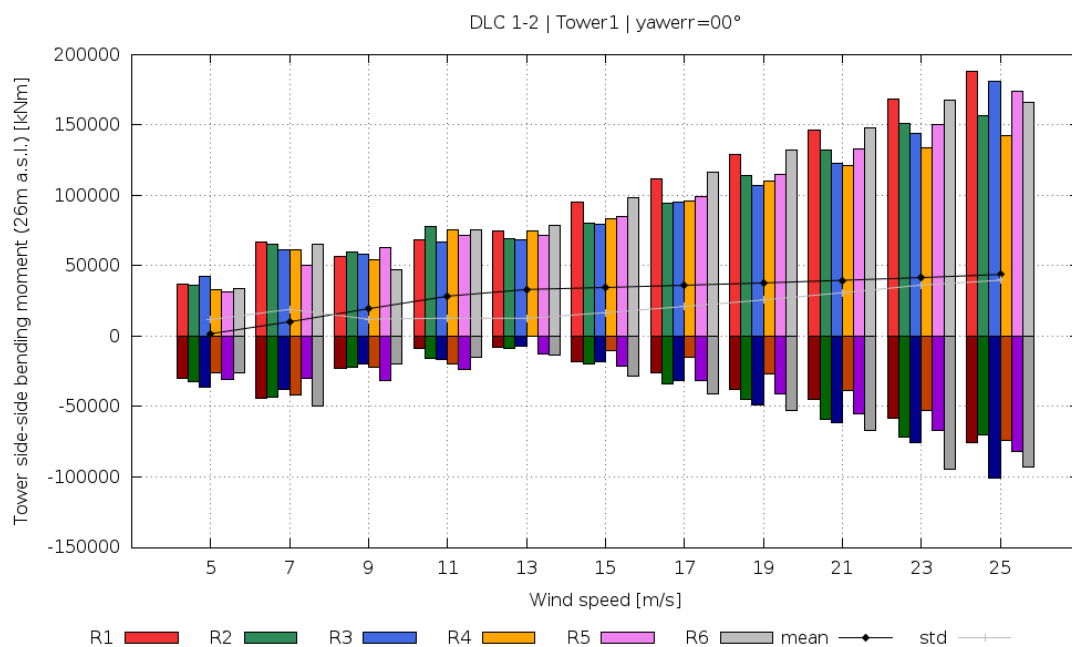*Innwind.EU, Deliverable 1.25, 20MW Reference Wind Turbine*

Figure 13   *Tower bottom (26m amsl) fore-aft bending moments for Tower 1 and yaw angles 0 as a function of the wind speed*

Figure 14   *Tower bottom (26m amsl) side-side bending moments for Tower 1 and yaw angles 0 as a function of the wind speed*
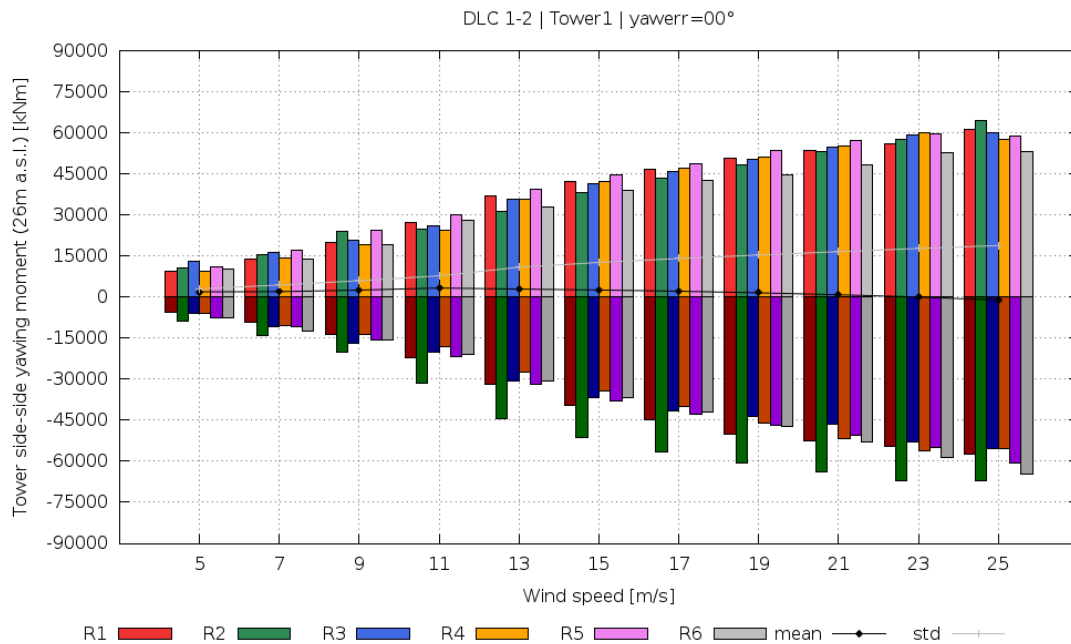
DLC 1-2 | Tower1 | yawerr=00°

Figure 15   *Tower bottom (26m amsl) yaw moments for Tower 1 and yaw angles 0 as a function of the wind speed*

Figure 16, Figure 17 and Figure 18 present the correlation of the fore-aft bending, side-side bending and yaw moment equivalent loads with the wind speed. The loads have been calculated at the tower bottom and are shown for all three towers. The equivalent loads are seed-averaged, they are only shown for the yaw 0° case and have been calculated for m=4. Notable is the tower fore-aft and side-side excitation at low wind speeds (7m/s) in particular for the stiffer Tower 1. Clearly, this is attributed to the matching 3P and 1st system global frequencies at such wind speed conditions. The tower yaw moment is unaffected.

Figure 16   *Tower bottom (26m amsl) fore-aft bending moment equivalent loads, for all three towers and yaw angle 0, as a function of the wind speed. Seed averaged results, m=4.*

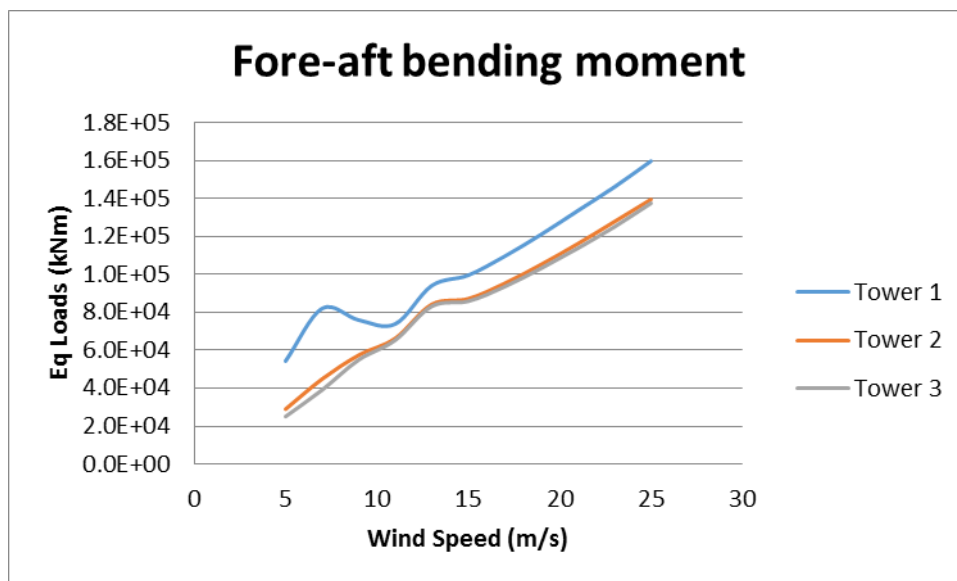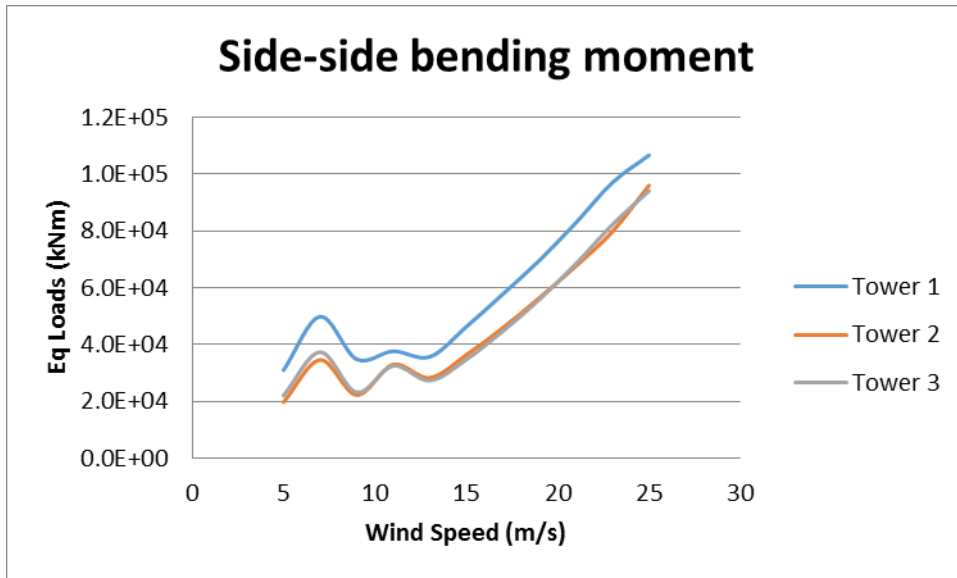Figure 17   *Tower bottom (26m amsl) side-side bending moment equivalent load, for all three towers and yaw angle 0, as a function of the wind speed. Seed averaged results, m=4.*
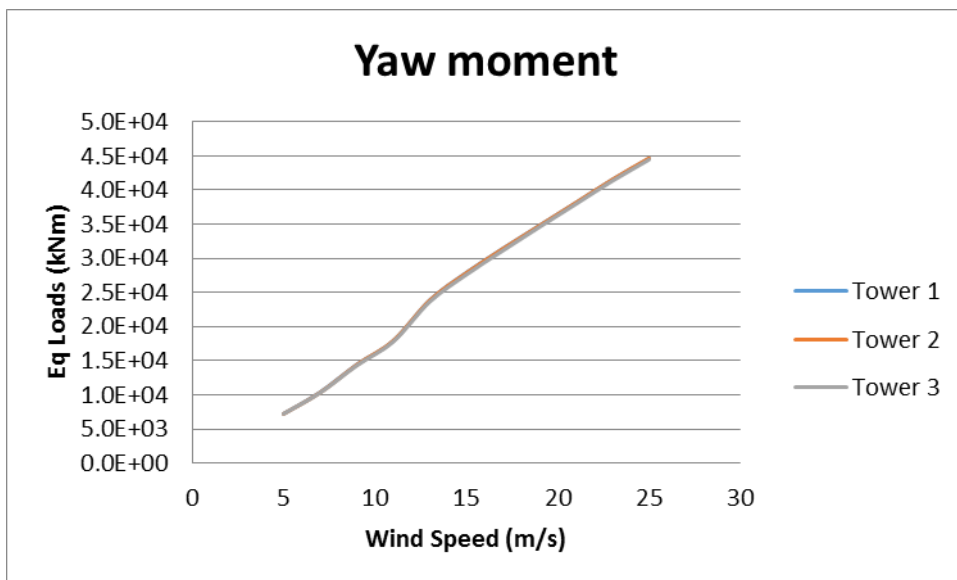

Figure 18   *Tower bottom (26m amsl) yaw moment equivalent loads, for all three towers and yaw angle 0, as a function of the wind speed. Seed averaged results, m=4.*

Innwind.EU, Deliverable 1.25, 20MW Reference Wind Turbine

SUMMARY

In this document we presented the design and a preliminary evaluation of the land version of the 20 MW Reference Wind Turbine of INNWIND.EU project.

The 20MW RWT derived from the upscaling of the 10MW DTU RWT and is intended to be a Class IC. Classical upscaling techniques were the starting point for configuring all 20MW turbine subsystems. In a second step the up-scaled data were adjusted to include learning curve expectations in terms for components mases and to face particular challenges regarding the proper selection of the first systems' frequency in connection to the variable speed schedule of the turbine.

The design summary of the turbine is compared against that of the 10MW RWT. The aeroelastic data of the turbine and its subcomponents are given in XLS spreadsheets that accompany this report.

System natural frequencies and loads are calculated for the 20MW RWT. Blade and tower root ultimate and fatigue loads are presented for two relevant IEC-61400 design load cases, D6.2 for ultimate and D1.2 for fatigue loads. The tower bottom loads extracted are delivered to WP4 for the design of the 20MW reference jacket.

REFERENCES

1. Berger F. et al. System design assessment for innovative support structures. INNWIND.EU D1.35, October 2015.

2. Chaviaropoulos PK. Similarity rules for W/T up-scaling. UPWIND Report, WP 1B4, 2007.

3. Sieros G, Chaviaropoulos P, Sorensen JD, Bulder BH, Jamieson P. Up-scaling Wind Turbines: Theoretical and practical aspects and their impact on the cost of energy. Wind Energy 2012. 15(1): 3-17.

4. Sieros G, Chaviaropoulos P.K. Aspects of up-scaling beyond similarity. Proceedings of 'The Science of Making Torque from Wind' Conference, Heraklion, Greece, 28-30/6/2010, Edited by S. Voutsinas and P. K. Chaviaropoulos.

5. Wind Turbine Design Cost and Scaling Model, by L. Fingersh, M. Hand, and A. Laxson, NREL/TP-500-40566, December 2006.

6. Chaviaropoulos, T, H.J.M. Beurskens and S. Voutsinas, Moving towards large(r) high speed rotors – is that a good idea? Proc. Scientific Track, EWEA 2013 Conference, Vienna.

7. Key Performance Indicators for the European Wind Industrial Initiative, SETIS-TPWIND, Version: 3, 7th November 2011.

8. Peter Jamieson, Innovation in Wind Turbine Design, A John Wiley & Sons, Ltd., Publication, ISBN 978-0-470-69981-2, 2011.

Innwind.EU, Deliverable 1.25, 20MW Reference Wind Turbine

APPENDIX I: CONTROL PARAMETERS OF THE 20MW RWT

20 MW Column: Parameters of the DTU Standard Controller for the 20MW RWT
10 MW Column: Parameters of the DTU Standard Controller for the 10MW RWT
SF : Linear Scaling Factor
Red Fond: Deviation from classical upscaling

1.4142		1.05	20MW	10MW	SF	DESCRIPTION
** Overall parameters						
constant		1	20000.00	10000.00	2	Rated power [kW]
constant		2	0.45000	0.52360	-1	Minimum rotor speed [rad/s]
constant		3	0.74617	1.00500	-1	Rated rotor speed [rad/s]
constant		4	4.4123E+07	1.5600E+07	3	Maximum allowable generator torque [Nm]
constant		5	100	100	0	Minimum pitch angle, theta_min [deg], if |theta_min|>90, then a table of <wsp,theta_min> is read from a file named 'wptable.n', where n=int(theta_min)
constant		6	90	90	0	Maximum pitch angle [deg]
constant		7	7.071	10.000	-1	Maximum pitch velocity operation [deg/s]
constant		8	0.14142	0.20000	-1	Frequency of generator speed filter [Hz] simulink 0.2
constant		9	0.7	0.7	0	Damping ratio of speed filter [-]
constant		10	0.35000	0.64000	-1	Used Frequency of free-free DT torsion mode [Hz], if zero no notch filter used simulink 0.64
** Partial load control parameters						
constant		11	5.1376E+07	1.3013E+07	5	Optimal Cp tracking K factor [kNm/(rad/s)^2], Qg=K*Omega^2, K=eta*0.5*rho*A*Cp_opt*R^3/lambda_opt^3
constant		12	2.73E+08	6.83E+07	4	Proportional gain of torque controller [Nm/(rad/s)]
constant		13	4.34E+07	1.53E+07	3	Integral gain of torque controller [Nm/rad]
constant		14	0	0	6	Differential gain of torque controller [Nm/(rad/s^3)]

** Full load control parameters						
constant	15	2	1			Generator control switch [1=constant power, 2=constant torque]
constant	16	0.5245	0.5245	**0**		Proportional gain of pitch controller [rad/(rad/s)]
constant	17	0.0999	0.1412	**-1**		Integral gain of pitch controller [rad/rad]
constant	18	0	0	2		Differential gain of pitch controller [rad/(rad/s^2)]
constant	19	2.00E-09	4.00E-09	-2		Proportional power error gain [rad/W]
constant	20	1.41E-09	4.00E-09	-3		Integral power error gain [rad/(Ws)]
constant	21	198.329	198.329	0		Coefficient of linear term in aerodynamic gain scheduling, KK1 [deg]
constant	22	693.222	693.222	0		Coefficient of quadratic term in aerodynamic gain scheduling, KK2 [deg^2] & (if zero, KK1 = pitch angle at double gain)
constant	23	1.3	1.3	0		Relative speed for double nonlinear gain [-]
** Cut-in simulation parameters						
constant	24	0.1414	0.1000	1		Cut-in time [s]
constant	25	5.6569	4.0000	1		Time delay for soft start of torque [1/1P]
** Cut-out simulation parameters						
constant	26	0	0	0		Cut-out time [s]
constant	27	0.1414	0.1000	1		Time constant for 1st order filter lag of torque cut-out [s]
constant	28	1	1	0		Stop type [1=linear two pitch speed stop, 2=exponential pitch speed stop]
constant	29	1.4142	1.0000	1		Time delay for pitch stop 1 [s]
constant	30	14.1421	20.0000	-1		Maximum pitch velocity during stop 1 [deg/s]
constant	31	1.4142	1.0000	1		Time delay for pitch stop 2 [s]
constant	32	7.0711	10.0000	-1		Maximum pitch velocity during stop 2 [deg/s]
** Expert parameters (keep default values unless otherwise given)						
constant	33	0.5	0.5	0		Lower angle above lowest minimum pitch angle for switch [deg]

constant	34	0.5	0.5	0	Upper angle above lowest minimum pitch angle for switch [deg], if equal then hard switch
constant	35	95	95	0	Ratio between filtered speed and reference speed for fully open torque limits [%]
constant	36	7.0711	5.0000	1	Time constant of 1st order filter on wind speed used for minimum pitch [1/1P]
constant	37	7.0711	5.0000	1	Time constant of 1st order filter on pitch angle used for gain scheduling [1/1P]
** Thrust shaving					
constant	38	0	0	0	!!! 0 - off
** Over speed					
constant	39	100	100	0	Over speed percentage before initiating shut-down
** Additional non-linear pitch control term					
constant	40	0	0	-1	Err0 [rad/s]
constant	41	0	0	-2	ErrDot0 [rad/s^2]
constant	42	0	0	-1	PitNonLin1 [rad/s]
** Storm control command					
constant	43	28	28	0	Wind speed 'Vstorm' above which derating of rotor speed is used [m/s]
constant	44	40	40	0	Cut-out wind speed (only used for derating of rotor speed in storm) [m/s]
** Safety system parameters					
constant	45	30	30	0	Overspeed percentage before initiating safety system alarm (shut-down) [%]
constant	46	3.5355	5.0000	-1	Max low-pass filtered tower top acceleration level [m/s^2] - max in DLC 1.3=1.1 m/s^2
** Turbine parameter					
constant	47	252.1967	178.0000	1	Nominal rotor diameter [m]
** Parameters for rotor inertia reduction in variable speed region					
constant	48	0	0	5	Proportional gain on rotor acceleration in variable speed region [Nm/(rad/s^2)]

					(not used when zero)
** Parameters for alternative partial load controller with PI regulated TSR tracking					
constant	49	0	0	0	Optimal tip speed ratio [-] (only used when K=constant 11 = 0 otherwise Qg=K*Omega^2 is used)
** Parameters for adding aerodynamic drivetrain damping on gain scheduling					
constant	50	0	0	4	Proportional gain of aerodynamic DT damping [Nm/(rad/s)]
constant	51	0	0	0	Coefficient of linear term in aerodynamic DT damping scheduling, KK1 [deg]
constant	52	0	0	0	Coefficient of quadratic term in aerodynamic DT damping scheduling, KK2 [deg^2]
** Speed exclusion zone					
constant	53	0.0000	0.5760	-1	Torque exclusion zone: Low speed [rad/s] = 5.5; 5.9 rpm
constant	54	0.000E+00	4.500E+06	3	Torque exclusion zone: Low speed generator toque [Nm]
constant	55	0.0000	0.6907	-1	Torque exclusion zone: High speed [rad/s] = 6.5 6.1 rpm
constant	56	0.000E+00	2.500E+06	3	Torque exclusion zone: High speed generator toque [Nm]
constant	57	0.0000	30.0000	1	Time constant of reference switching at exclusion zone [s]
** DT torsion mode damper					
constant	58	0.0000	3.4000	-1	Frequency of 1st free-free DT torsion mode
constant	59	0.0141	1.7700	-1	Frequency of DT torsion mode notch filter [Hz]
constant	60	0.0000	0.2000	-1	Damping of 1st DT torsion mode BP filter [Hz]
constant	61	0	-10000000	0	Gain of 1st DT torsion mode damper [-]
constant	62	0.0000	0.1000	1	phase lag of 1st DT torsion mode damper [s] => (n-1)*Ts; max n = 40
** Fore-aft Tower mode damper					
constant	62	0.0000	0.3000	-1	Frequency of BP filter [Hz]
constant	63	0.0000	0.4700	-1	Frequency of notch filter [Hz]

constant		64	0.0000	0.0200	0	Damping of BP filter [-]
constant		65	0.0000	0.0100	0	Damping of notch filter [-]
constant		66	0.0000	0.0400	0	Gain of damper [-]
constant		67	0.0000	0.3000	1	Phase lag of damper [s] => max 40*dt
constant		68	0.0000	0.1800	-1	Time constant of 1st order filter on PWR used for fore-aft Tower mode damper GS [Hz]
constant		69	0.0000	0.5000	0	Lower PWR limit used for fore-aft Tower mode damper GS [-]
constant		70	0.0000	0.8000	0	Upper PWR limit used for fore-aft Tower mode damper GS [-]
** Side-to-side Tower mode filter						
constant		71	0.0000	0.3140	-1	Frequency of Tower side-to-side notch filter [Hz]
constant		72	0.0000	0.0100	0	Damping of notch filter [-]
constant		73	0.0000	5.0000	-1	Max low-pass filtered tower top acceleration level before initiating safety system alarm (shut-down) [m/s^2]
** Safety system parameters						
constant		74	0	1	0	Time constant of 1st order filter on pitch angle used for switch [1/1P]
constant		75	0	1	0	Time constant of 1st order filter on tower top acceleration used for ShakeGuard [1/1P]
** Gear ratio						
constant		76	1	1	0	Gear ratio (To be used only if input #2 refers to HSS)

APPENDIX II: FATIGUE RESULTS FOR ALL TOWER VERSIONS OF THE 20MW RWT

Figure 19   *Blade-root flapwise bending moments for Tower 1 and yaw angles 0 and ±8 degrees as a function of the wind speed*

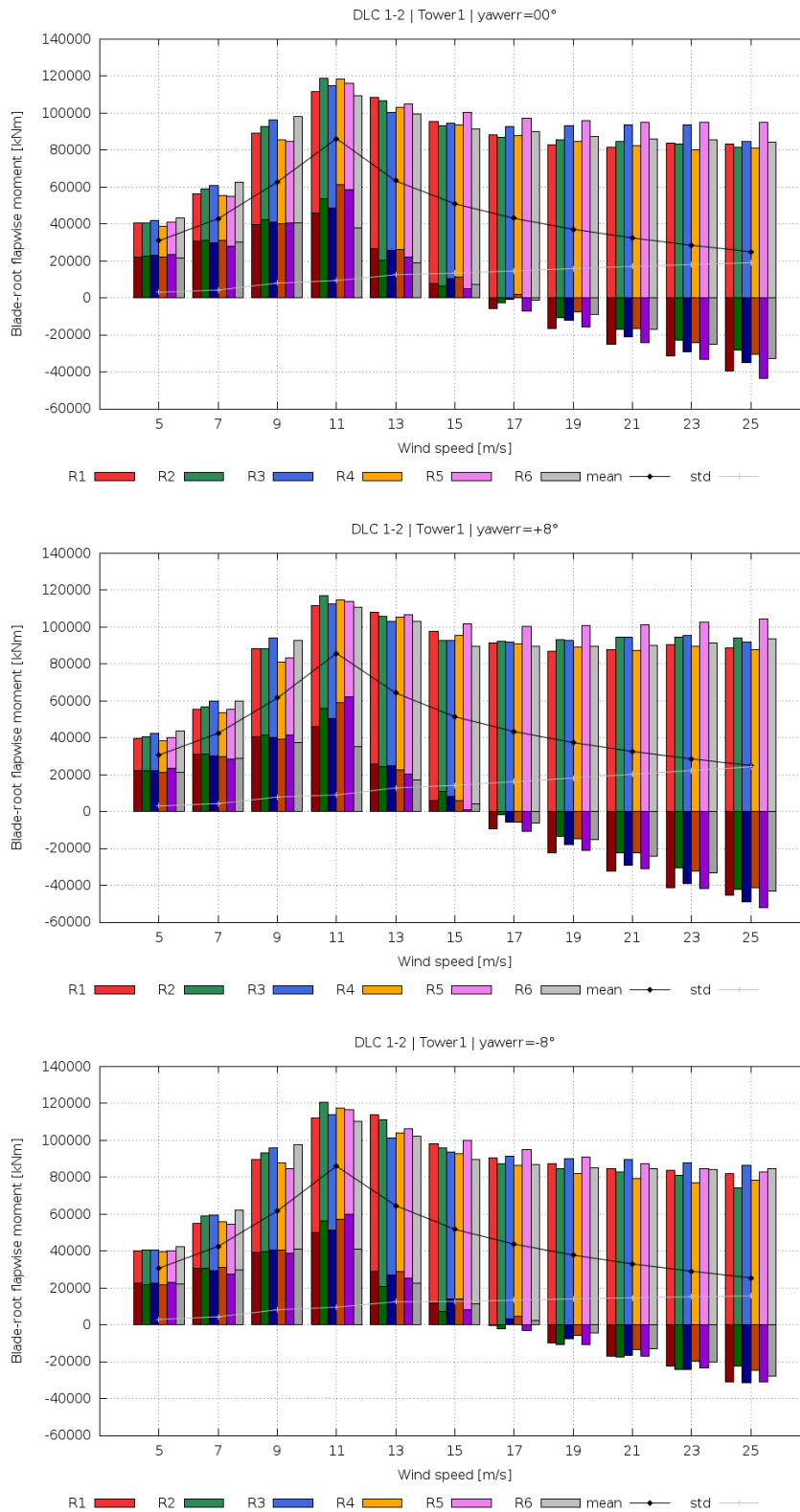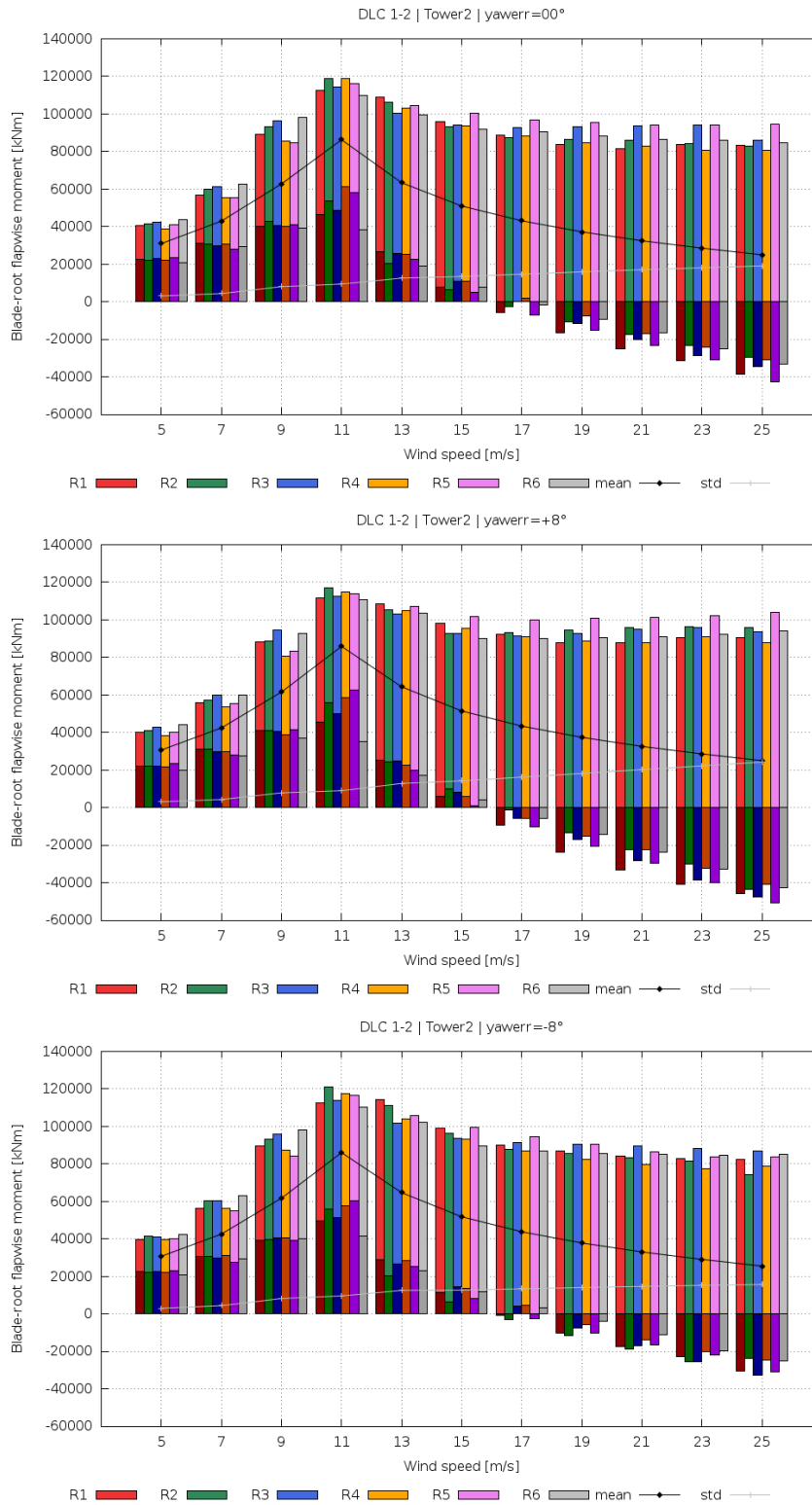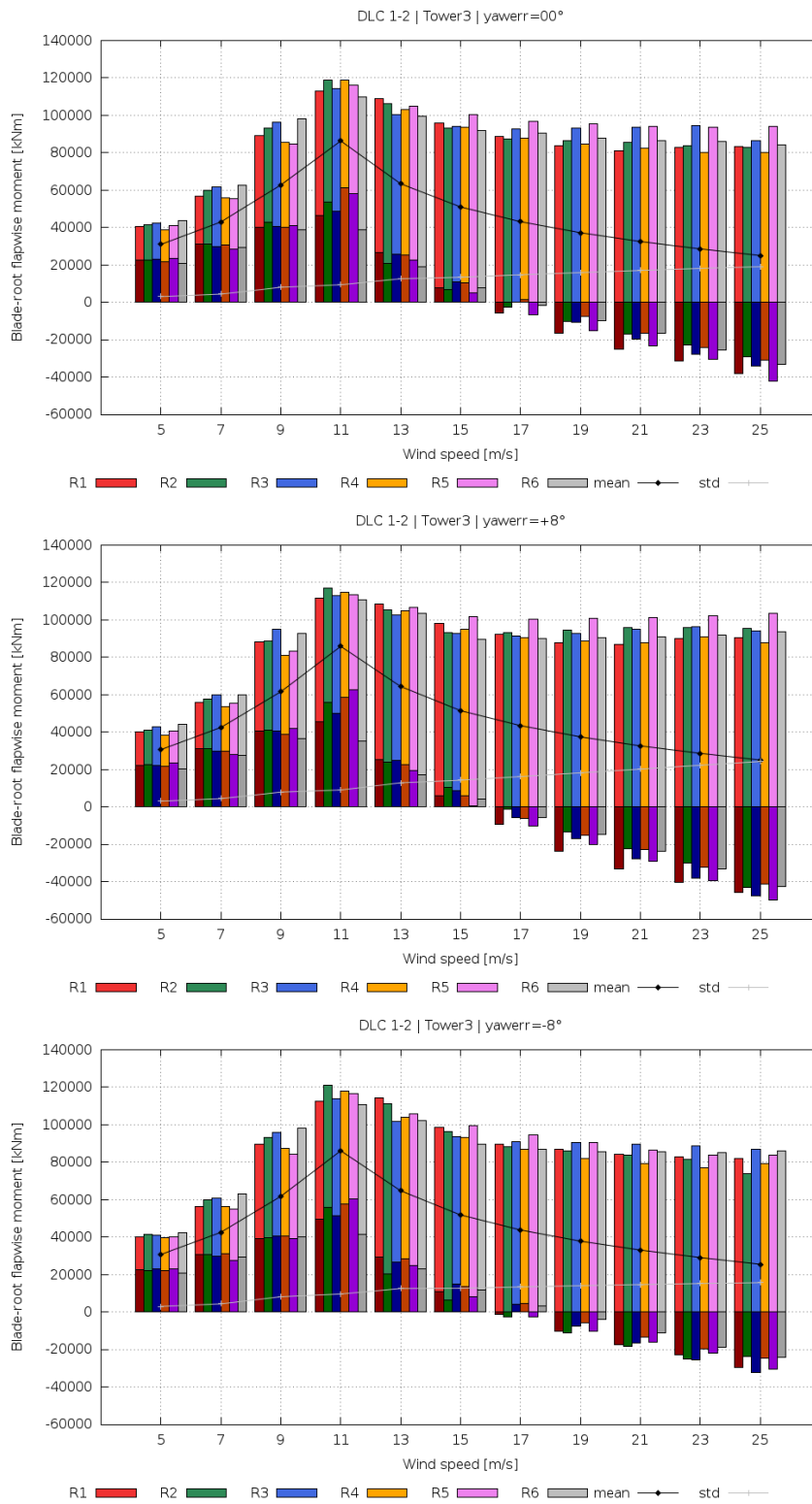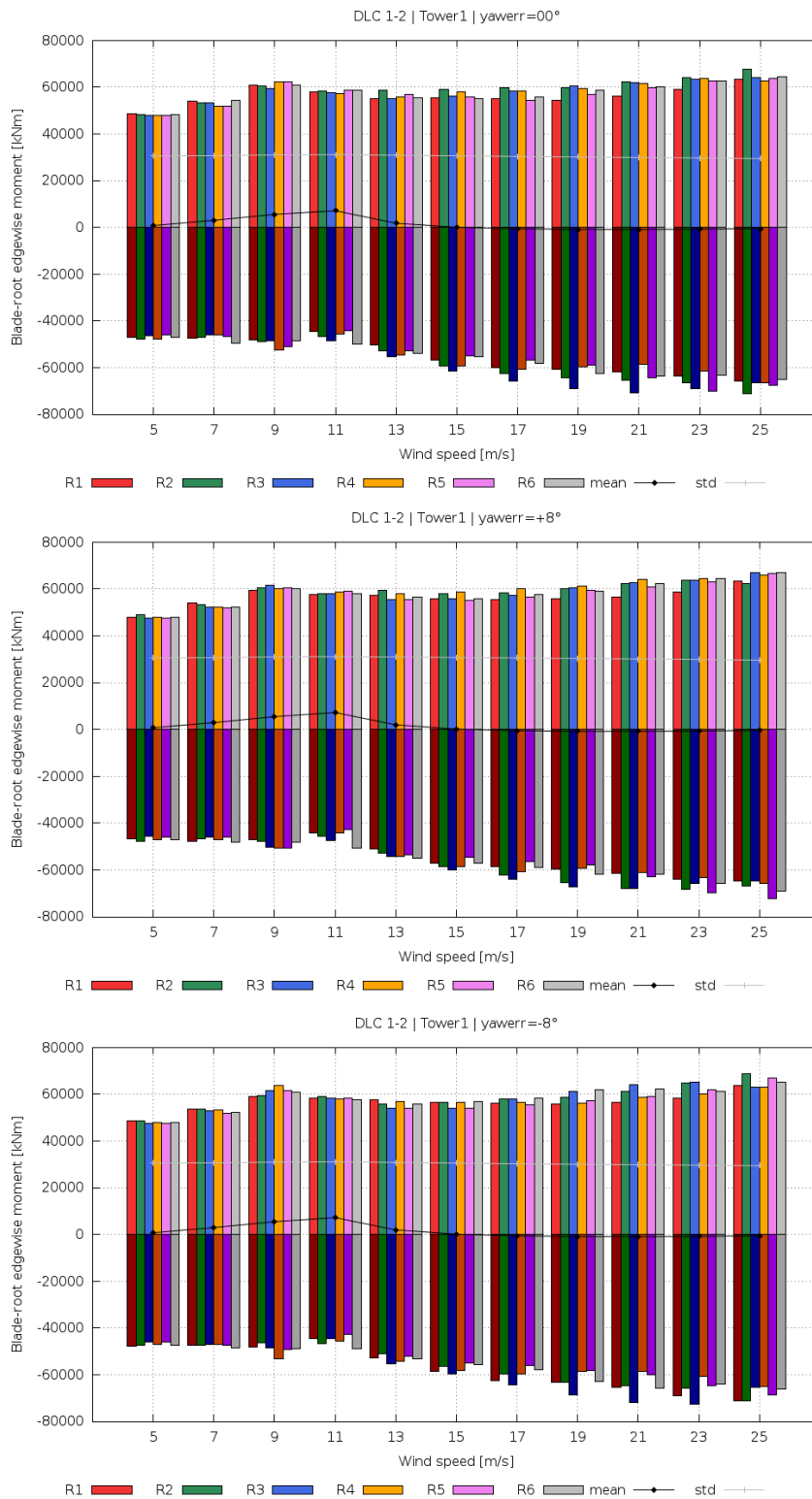*Innwind.EU, Deliverable 1.25, 20MW Reference Wind Turbine*

Figure 20 — *Blade-root flapwise bending moments for Tower 2 and yaw angles 0 and ±8 degrees as a function of the wind speed*

Figure 21   *Blade-root flapwise bending moments for Tower 3 and yaw angles 0 and ±8 degrees as a function of the wind speed*
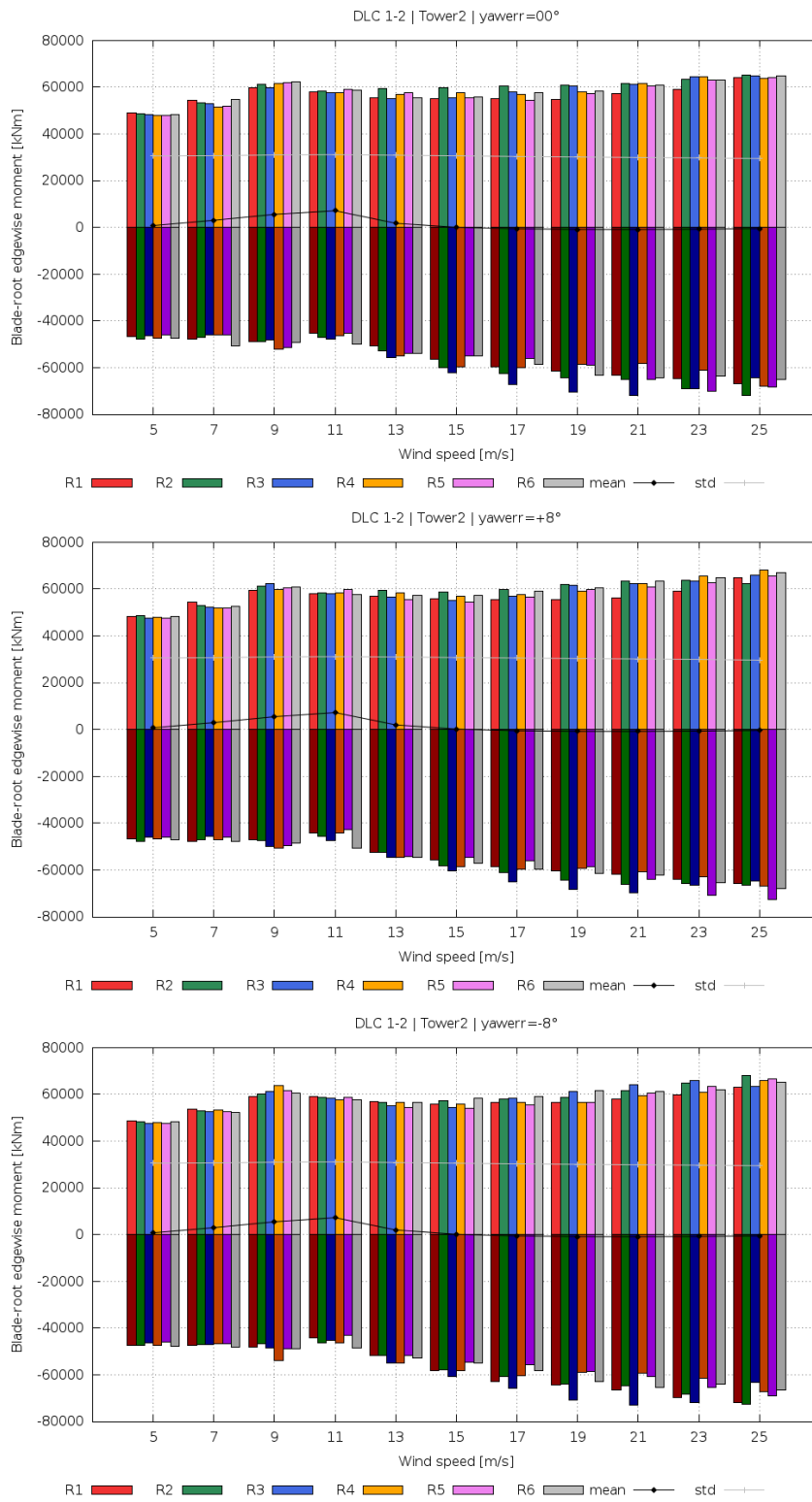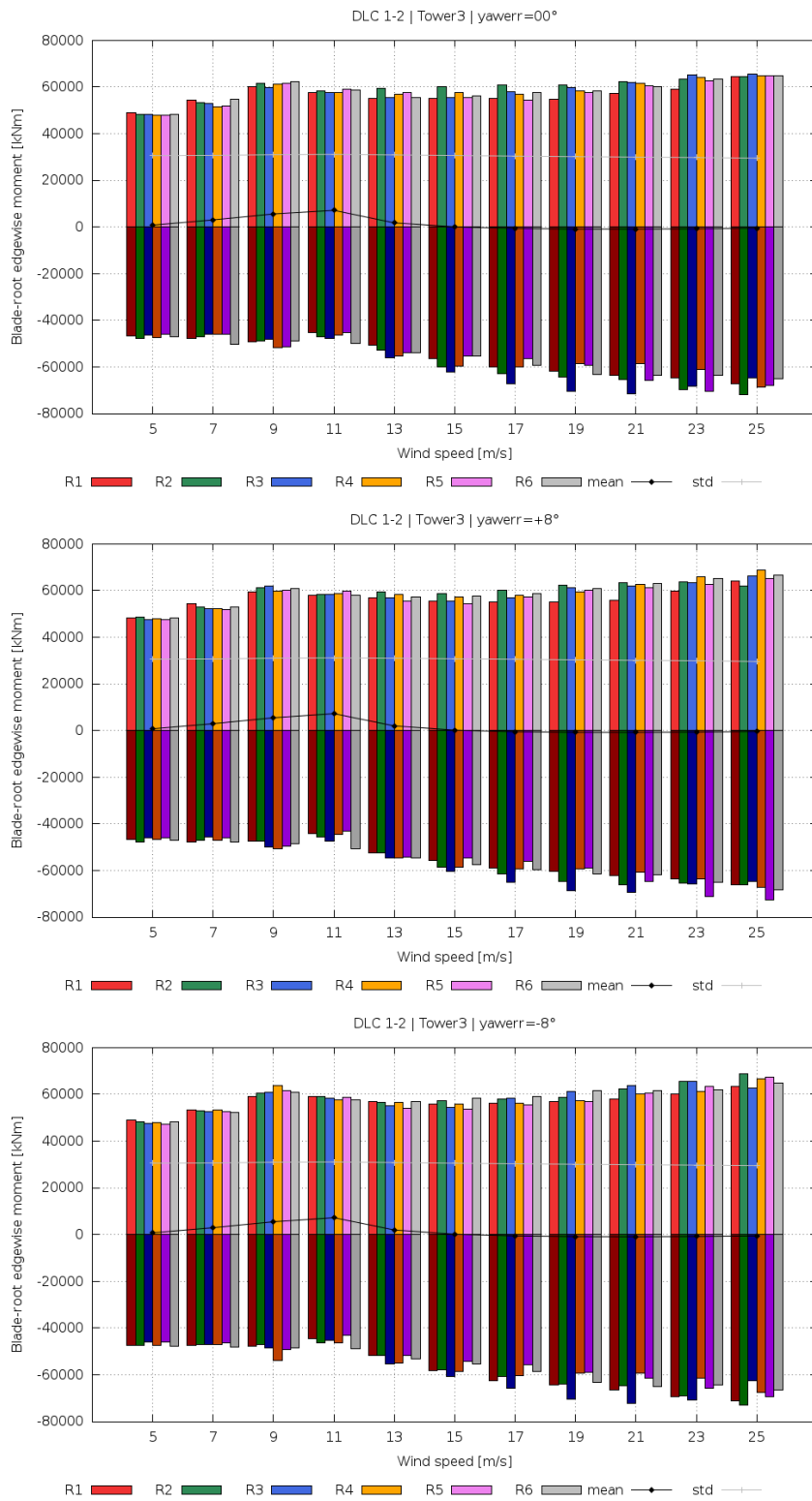
Innwind.EU, Deliverable 1.25, 20MW Reference Wind Turbine

Figure 22   *Blade-root edgewise bending moments for Tower 1 and yaw angles 0 and ±8 degrees as a function of the wind speed*

Innwind.EU, Deliverable 1.25, 20MW Reference Wind Turbine

Figure 23   *Blade-root edgewise bending moments for Tower 2 and yaw angles 0 and ±8 degrees as a function of the wind speed*

Figure 24   *Blade-root edgewise bending moments for Tower 3 and yaw angles 0 and ±8 degrees as a function of the wind speed*
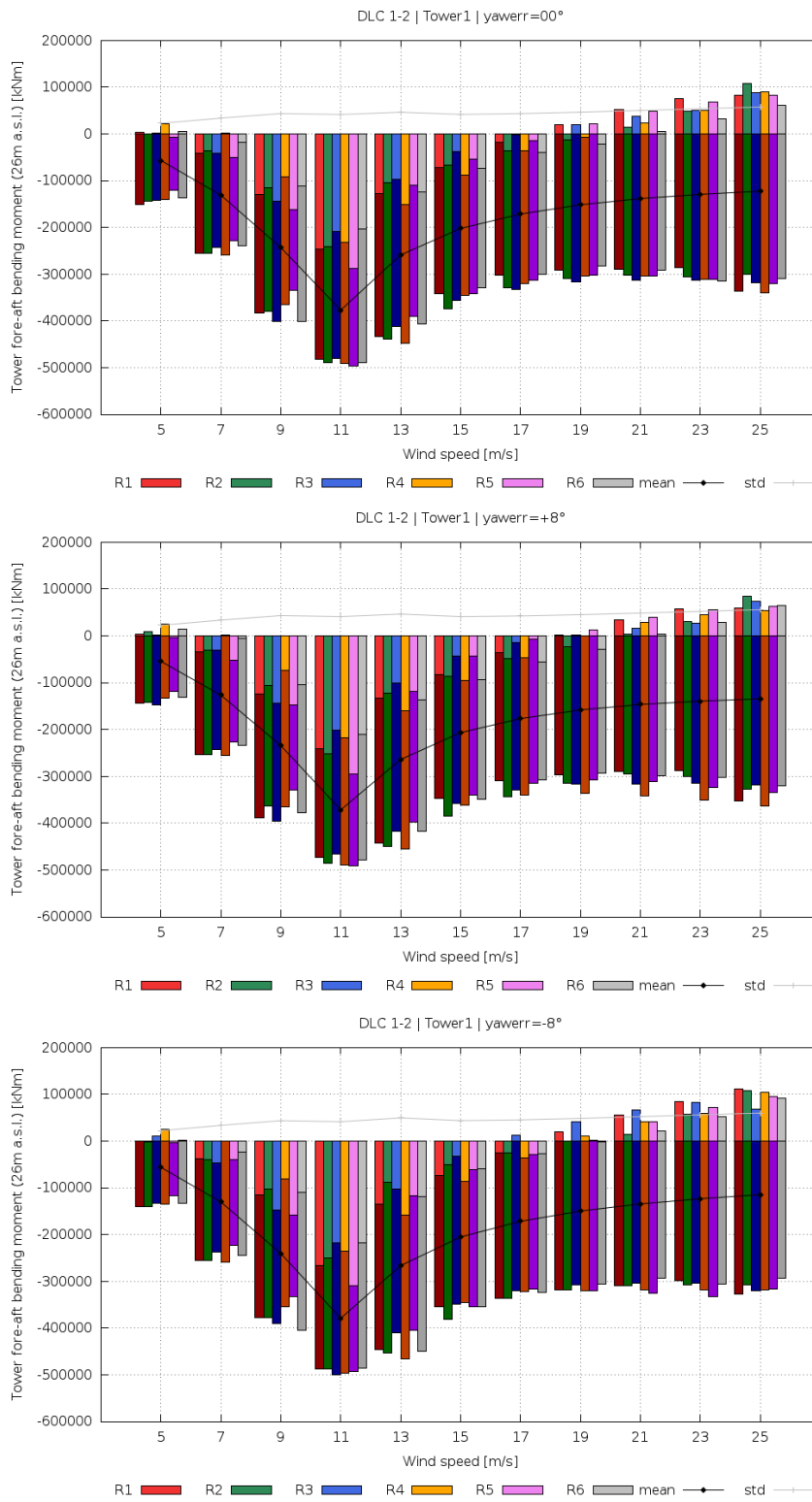
Figure 25   *Tower bottom (26m amsl) fore-aft bending moments for Tower 1 and yaw angles 0 and ±8 degrees as a function of the wind speed*
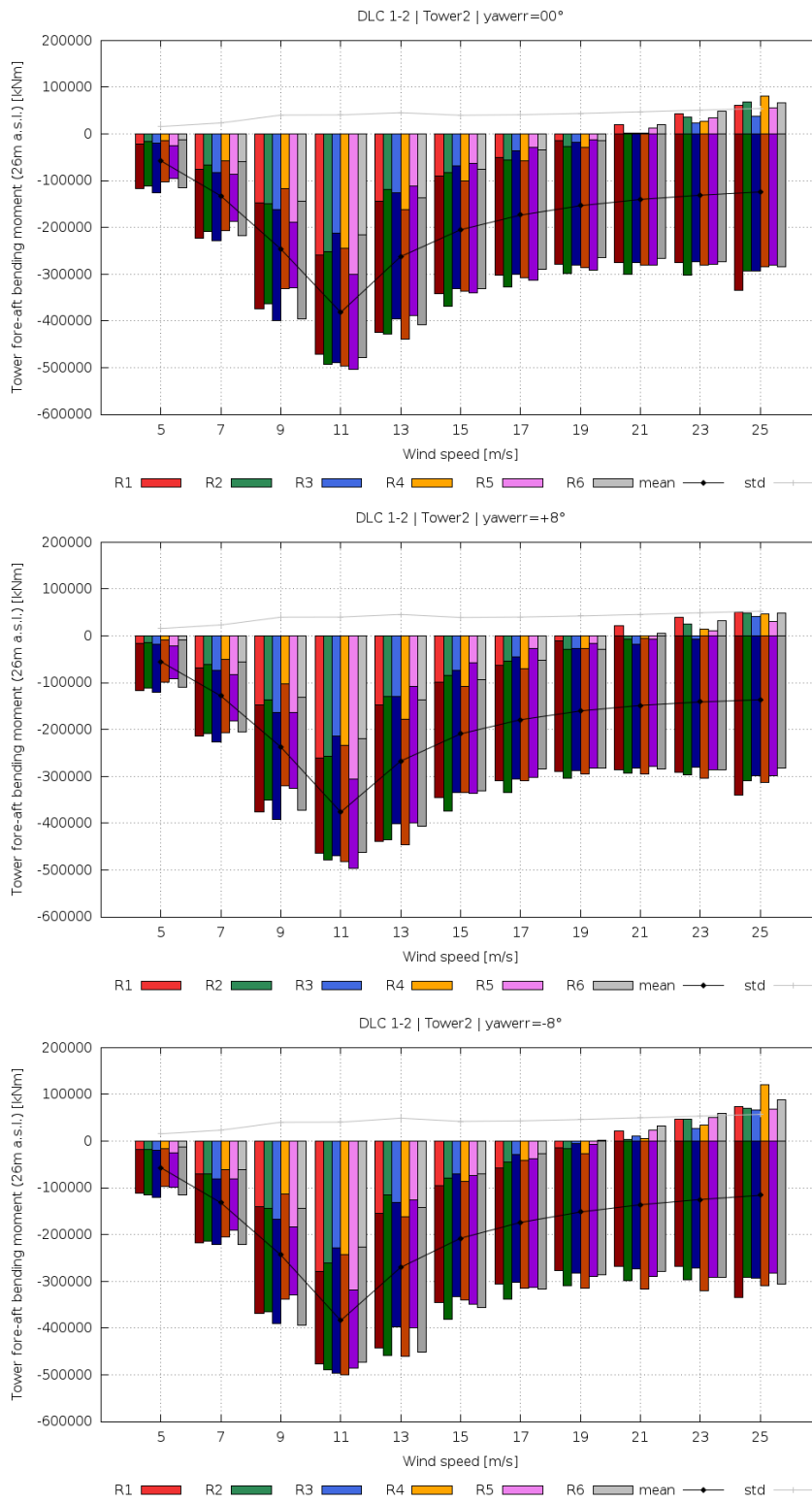
Figure 26 *Tower bottom (26m amsl) fore-aft bending moments for Tower 2 and yaw angles 0 and ±8 degrees as a function of the wind speed*
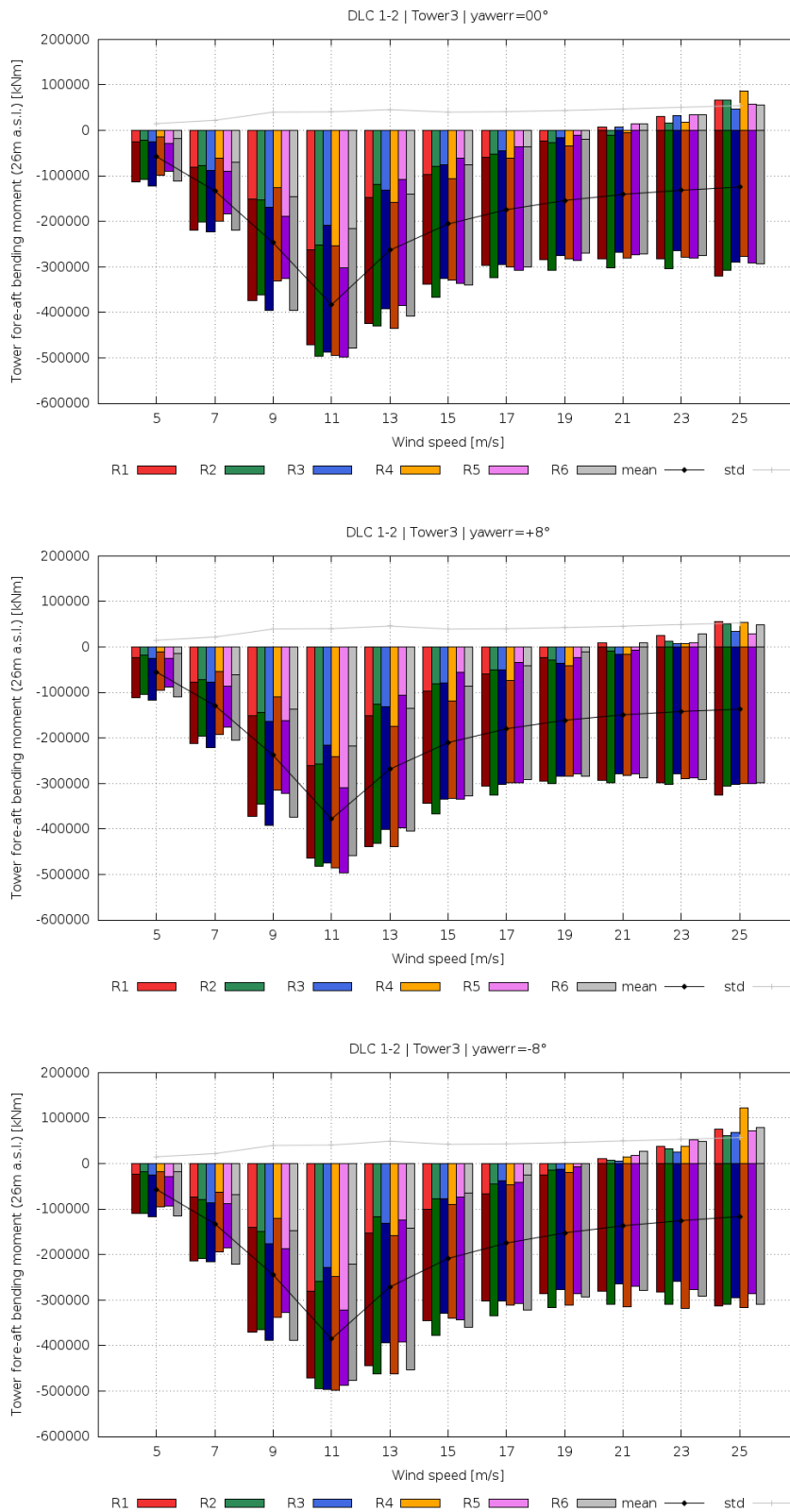
Innwind.EU, Deliverable 1.25, 20MW Reference Wind Turbine

Figure 27   *Tower bottom (26m amsl) fore-aft bending moments for Tower 3 and yaw angles 0 and ±8 degrees as a function of the wind speed*
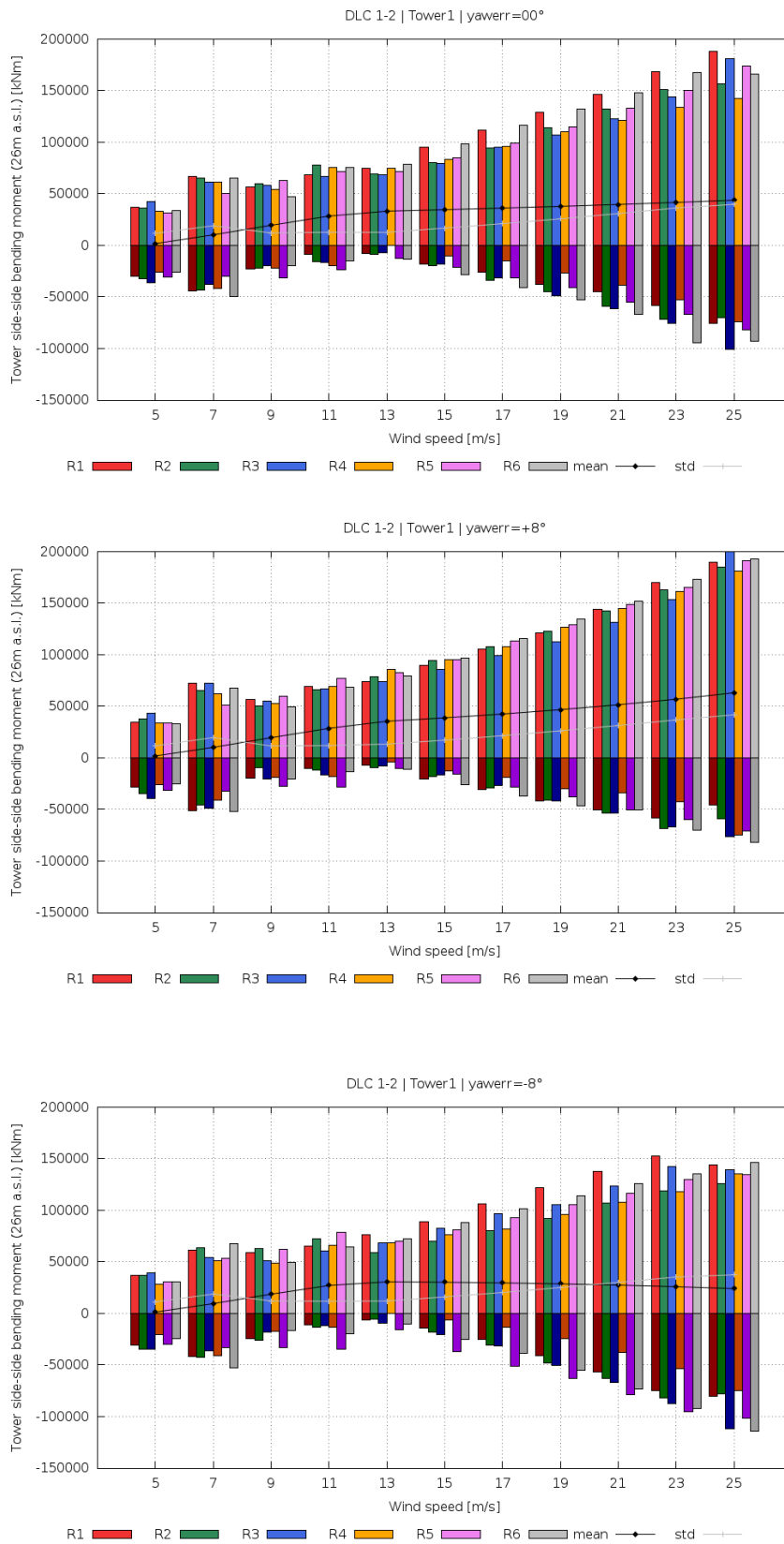
Figure 28   *Tower bottom (26m amsl) side-side bending moments for Tower 1 and yaw angles 0 and ±8 degrees as a function of the wind speed*
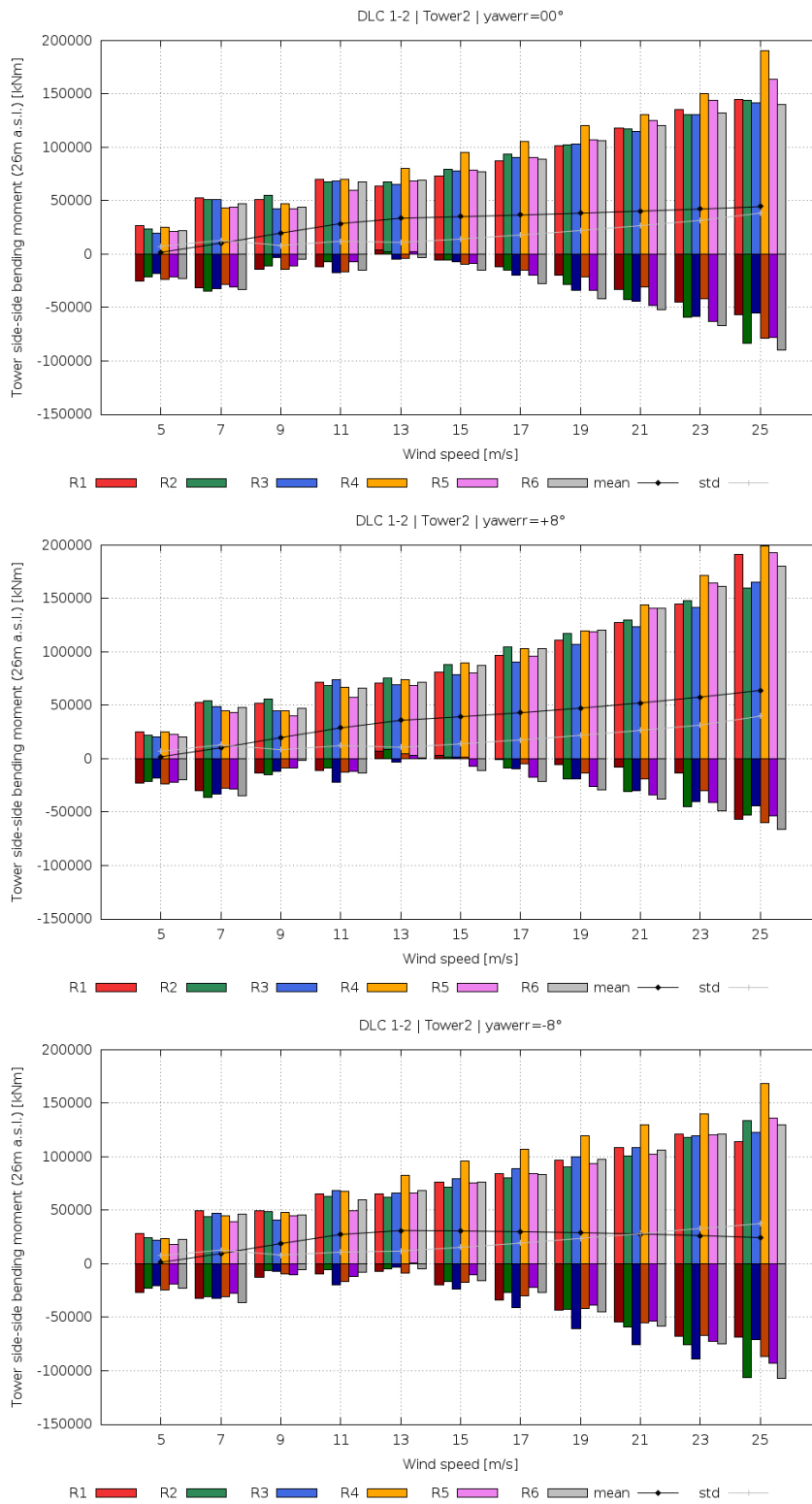
Figure 29   *Tower bottom (26m amsl) side-side bending moments for Tower 2 and yaw angles 0 and ±8 degrees as a function of the wind speed*

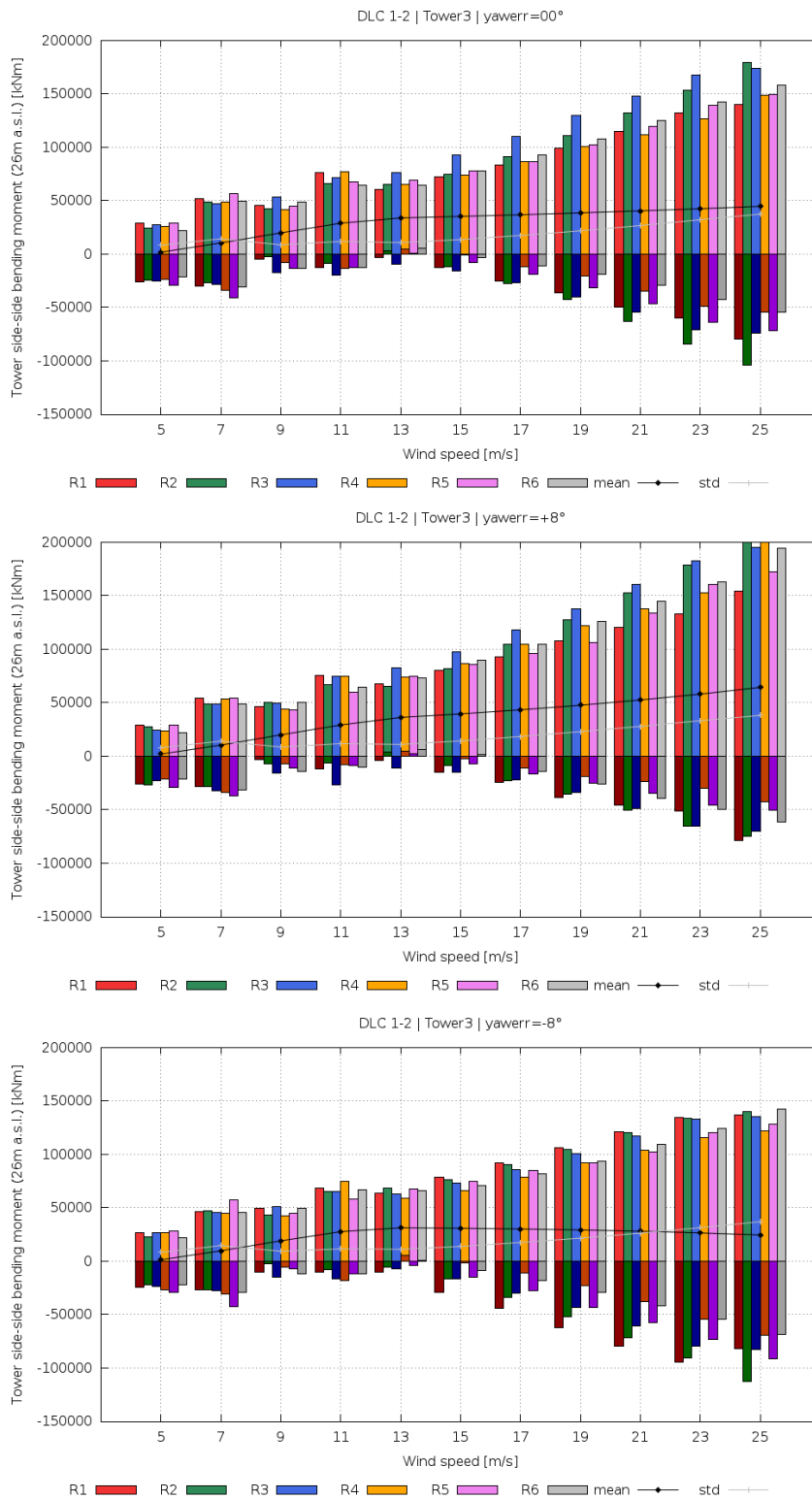*Innwind.EU, Deliverable 1.25, 20MW Reference Wind Turbine*

Figure 30   *Tower bottom (26m amsl) side-side bending moments for Tower 3 and yaw angles 0 and ±8 degrees as a function of the wind speed*

Figure 31   *Tower bottom (26m amsl) yaw moments for Tower 1 and yaw angles 0 and ±8 degrees as a function of the wind speed*

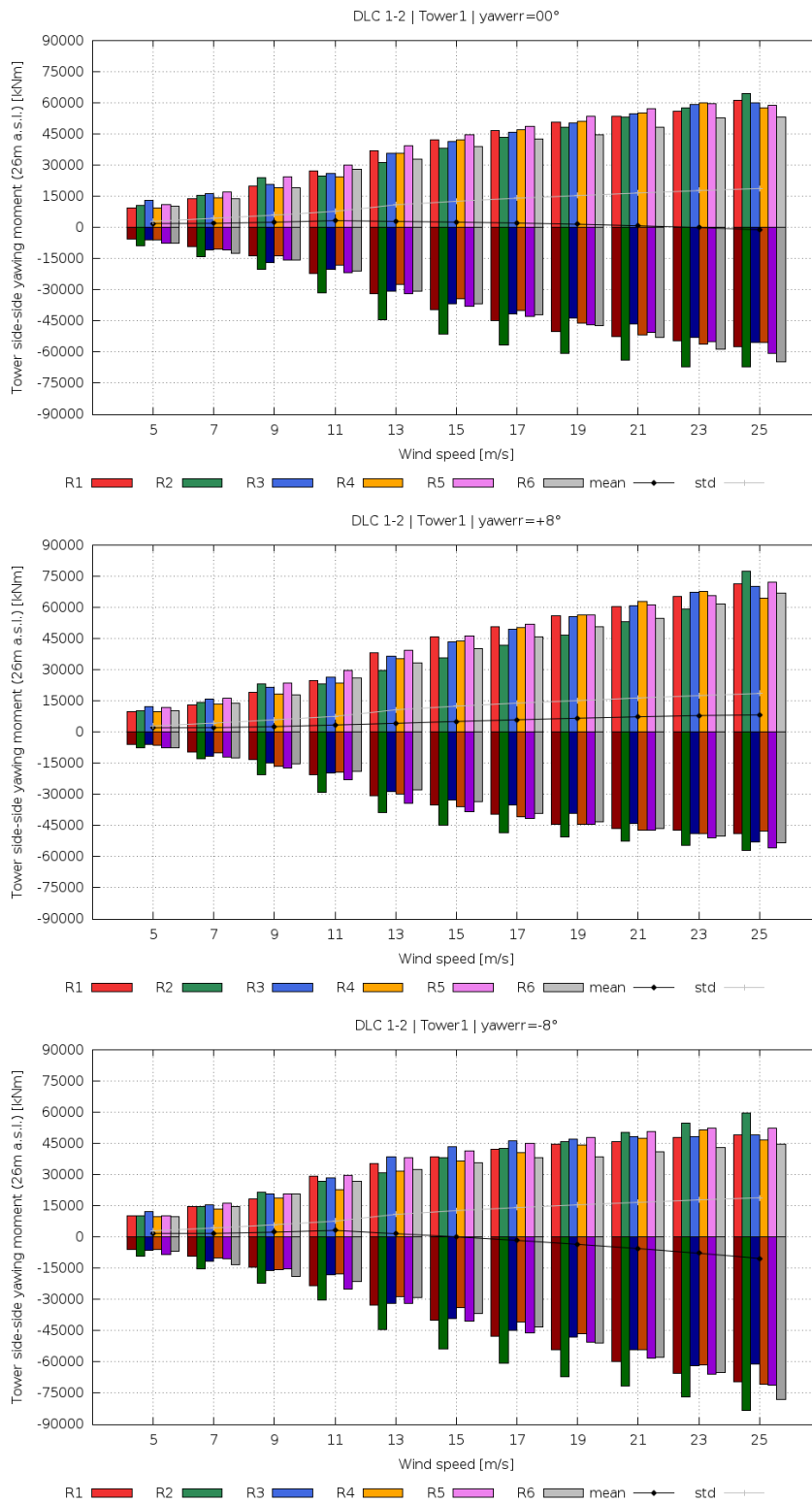*Innwind.EU, Deliverable 1.25, 20MW Reference Wind Turbine*

Figure 32   *Tower bottom (26m amsl) yaw moments for Tower 2 and yaw angles 0 and ±8 degrees as a function of the wind speed*

Figure 33   *Tower bottom (26m amsl) yaw moments for Tower 3 and yaw angles 0 and ±8 degrees as a function of the wind speed*
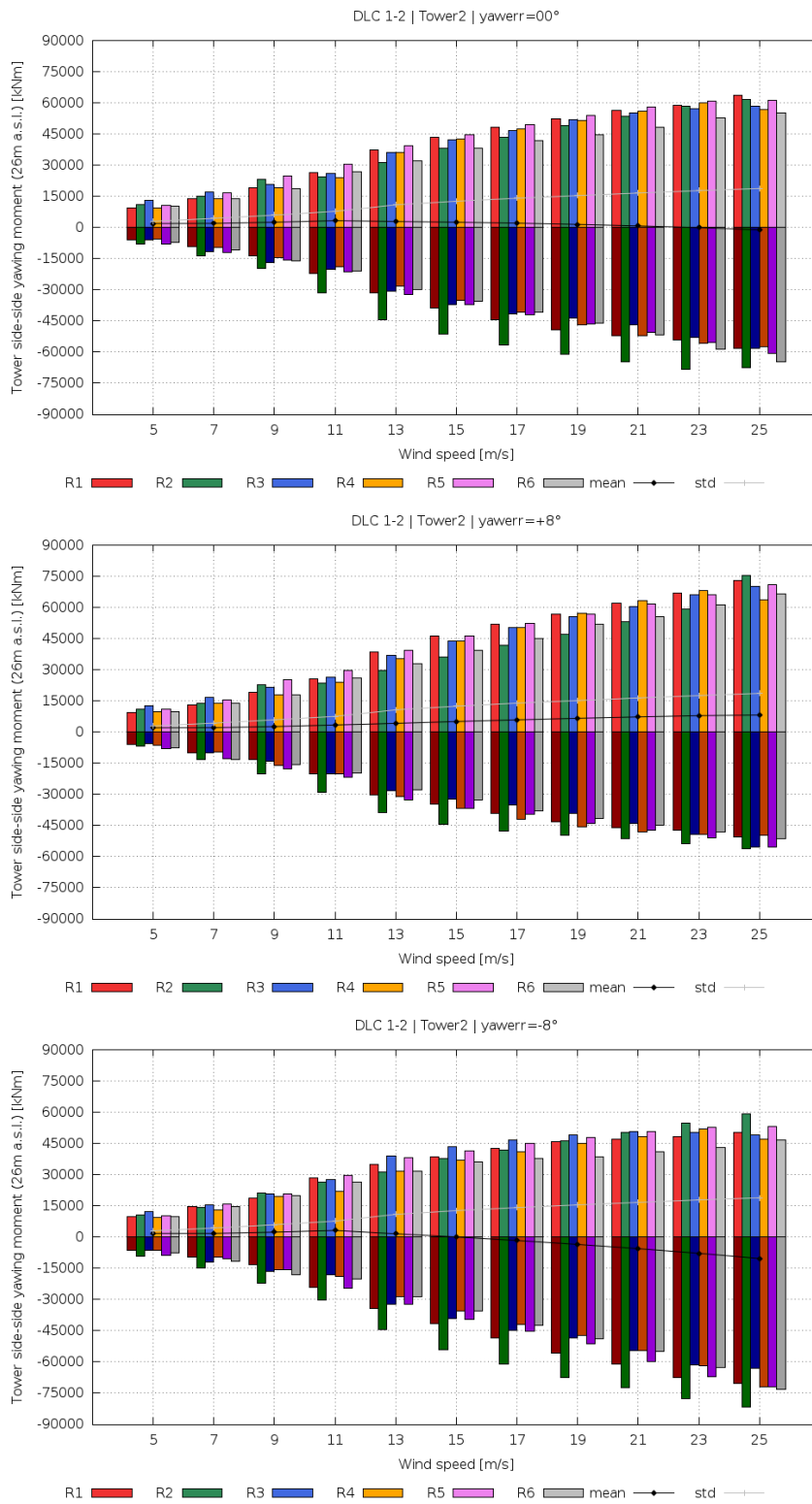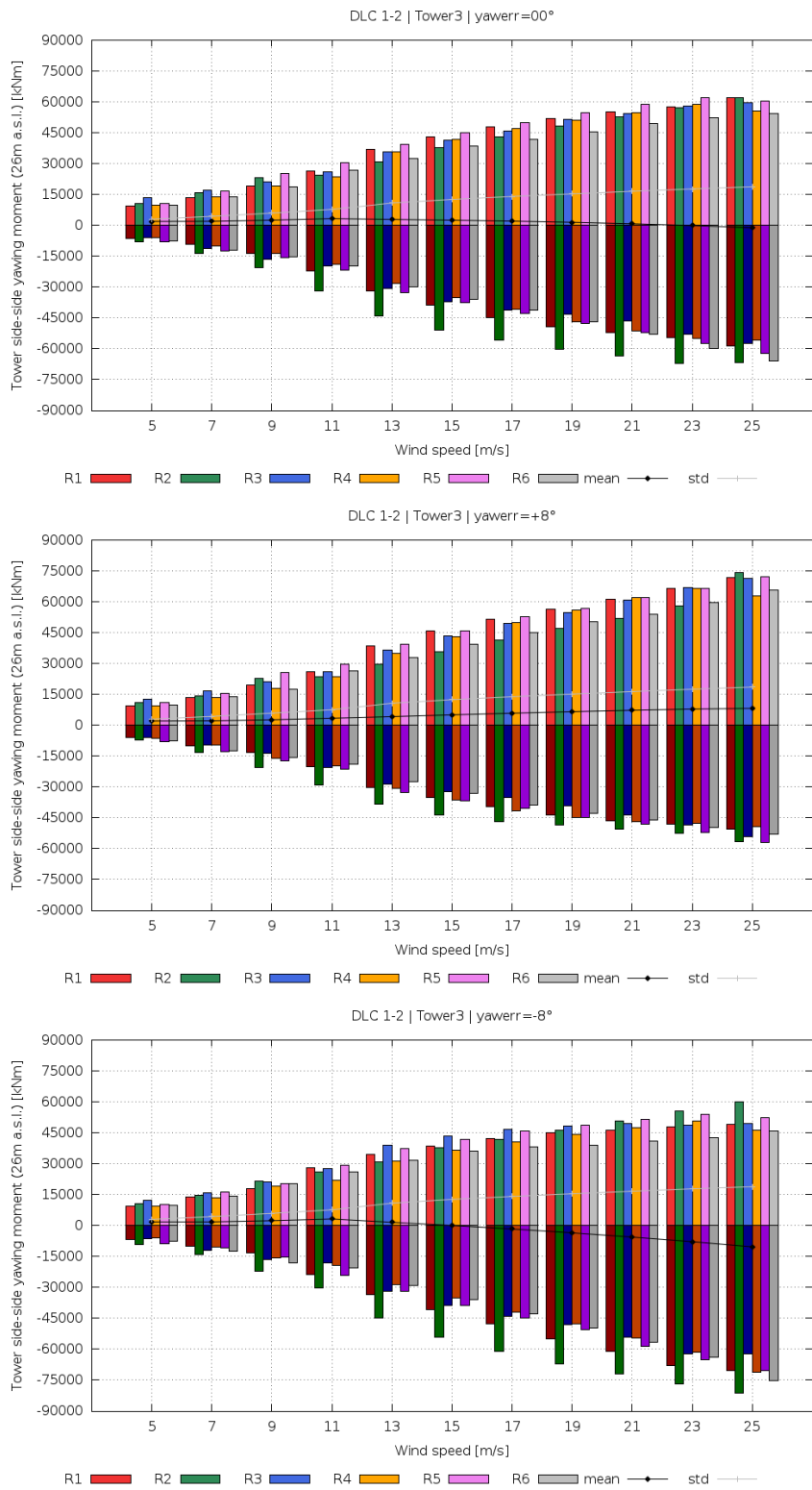
Innwind.EU, Deliverable 1.25, 20MW Reference Wind Turbine

Edgewise moment [kNm]

Uw (m/s)	tower 1			tower 2			tower 3		
	yaw00	yaw-8	yaw+8	yaw00	yaw-8	yaw+8	yaw00	yaw-8	yaw+8
5	7.676E+04	7.665E+04	7.653E+04	7.684E+04	7.674E+04	7.663E+04	7.685E+04	7.674E+04	7.664E+04
7	7.880E+04	7.879E+04	7.873E+04	7.883E+04	7.880E+04	7.874E+04	7.880E+04	7.874E+04	7.872E+04
9	8.313E+04	8.294E+04	8.312E+04	8.313E+04	8.286E+04	8.308E+04	8.301E+04	8.275E+04	8.299E+04
11	8.115E+04	8.097E+04	8.106E+04	8.117E+04	8.098E+04	8.110E+04	8.118E+04	8.098E+04	8.110E+04
13	8.293E+04	8.284E+04	8.293E+04	8.315E+04	8.301E+04	8.319E+04	8.319E+04	8.307E+04	8.324E+04
15	8.411E+04	8.386E+04	8.420E+04	8.441E+04	8.419E+04	8.458E+04	8.449E+04	8.428E+04	8.466E+04
17	8.556E+04	8.532E+04	8.559E+04	8.579E+04	8.560E+04	8.597E+04	8.587E+04	8.568E+04	8.606E+04
19	8.690E+04	8.665E+04	8.689E+04	8.711E+04	8.682E+04	8.725E+04	8.721E+04	8.688E+04	8.734E+04
21	8.830E+04	8.788E+04	8.834E+04	8.869E+04	8.814E+04	8.872E+04	8.880E+04	8.827E+04	8.883E+04
23	9.014E+04	8.974E+04	9.010E+04	9.059E+04	9.020E+04	9.051E+04	9.068E+04	9.039E+04	9.063E+04
25	9.172E+04	9.188E+04	9.168E+04	9.202E+04	9.238E+04	9.219E+04	9.218E+04	9.255E+04	9.236E+04

Flapwise moment [kNm]

Uw (m/s)	tower 1			tower 2			tower 3		
	yaw00	yaw-8	yaw+8	yaw00	yaw-8	yaw+8	yaw00	yaw-8	yaw+8
5	1.112E+04	1.093E+04	1.157E+04	1.119E+04	1.102E+04	1.161E+04	1.121E+04	1.103E+04	1.165E+04
7	1.665E+04	1.685E+04	1.643E+04	1.691E+04	1.717E+04	1.668E+04	1.690E+04	1.719E+04	1.672E+04
9	2.913E+04	3.024E+04	2.830E+04	2.935E+04	3.033E+04	2.847E+04	2.935E+04	3.028E+04	2.842E+04
11	3.757E+04	3.725E+04	3.634E+04	3.770E+04	3.734E+04	3.635E+04	3.771E+04	3.735E+04	3.637E+04
13	4.817E+04	4.788E+04	4.950E+04	4.833E+04	4.810E+04	4.964E+04	4.828E+04	4.806E+04	4.960E+04
15	5.110E+04	4.927E+04	5.357E+04	5.125E+04	4.953E+04	5.372E+04	5.121E+04	4.950E+04	5.364E+04
17	5.585E+04	5.238E+04	6.003E+04	5.600E+04	5.256E+04	6.022E+04	5.593E+04	5.252E+04	6.016E+04
19	6.055E+04	5.544E+04	6.685E+04	6.073E+04	5.554E+04	6.715E+04	6.066E+04	5.551E+04	6.711E+04
21	6.515E+04	5.839E+04	7.349E+04	6.538E+04	5.848E+04	7.383E+04	6.530E+04	5.845E+04	7.379E+04
23	6.949E+04	6.125E+04	8.003E+04	6.978E+04	6.145E+04	8.046E+04	6.965E+04	6.140E+04	8.043E+04
25	7.391E+04	6.597E+04	8.633E+04	7.394E+04	6.596E+04	8.633E+04	7.381E+04	6.583E+04	8.621E+04

Torsional moment [kNm]

Uw (m/s)	tower 1			tower 2			tower 3		
	yaw00	yaw-8	yaw+8	yaw00	yaw-8	yaw+8	yaw00	yaw-8	yaw+8
5	7.257E+02	7.255E+02	7.250E+02	7.256E+02	7.258E+02	7.253E+02	7.258E+02	7.259E+02	7.254E+02
7	6.758E+02	6.774E+02	6.799E+02	6.750E+02	6.777E+02	6.787E+02	6.748E+02	6.776E+02	6.788E+02
9	5.829E+02	5.821E+02	5.855E+02	5.845E+02	5.827E+02	5.857E+02	5.851E+02	5.822E+02	5.858E+02
11	4.987E+02	4.990E+02	4.994E+02	4.959E+02	5.016E+02	5.012E+02	4.966E+02	5.025E+02	5.024E+02
13	6.741E+02	6.630E+02	6.783E+02	6.773E+02	6.640E+02	6.798E+02	6.772E+02	6.641E+02	6.795E+02
15	7.901E+02	7.755E+02	8.128E+02	7.918E+02	7.778E+02	8.126E+02	7.924E+02	7.786E+02	8.132E+02
17	8.952E+02	8.720E+02	9.321E+02	8.982E+02	8.755E+02	9.337E+02	8.991E+02	8.767E+02	9.347E+02
19	9.885E+02	9.596E+02	1.042E+03	9.887E+02	9.616E+02	1.043E+03	9.900E+02	9.622E+02	1.046E+03
21	1.094E+03	1.042E+03	1.151E+03	1.099E+03	1.049E+03	1.161E+03	1.101E+03	1.050E+03	1.164E+03
23	1.213E+03	1.146E+03	1.268E+03	1.213E+03	1.154E+03	1.279E+03	1.216E+03	1.154E+03	1.286E+03
25	1.313E+03	1.253E+03	1.413E+03	1.317E+03	1.261E+03	1.414E+03	1.324E+03	1.268E+03	1.415E+03

Table 12   *Blade root equivalent loads (m=12). Three towers, three yaw angles per tower. From top edgewise, flapwise and torsional loads*

Fore-aft moment [kNm]

Uw (m/s)	tower 1			tower 2			tower 3		
	yaw00	yaw-8	yaw+8	yaw00	yaw-8	yaw+8	yaw00	yaw-8	yaw+8
5	5.435E+04	5.272E+04	5.473E+04	2.899E+04	2.855E+04	2.893E+04	2.512E+04	2.487E+04	2.509E+04
7	8.202E+04	8.191E+04	8.263E+04	4.486E+04	4.475E+04	4.541E+04	3.912E+04	3.887E+04	3.924E+04
9	7.598E+04	7.681E+04	7.631E+04	5.743E+04	5.756E+04	5.749E+04	5.498E+04	5.513E+04	5.489E+04
11	7.387E+04	7.259E+04	7.249E+04	6.629E+04	6.432E+04	6.334E+04	6.531E+04	6.390E+04	6.276E+04
13	9.408E+04	9.762E+04	9.396E+04	8.419E+04	8.819E+04	8.461E+04	8.323E+04	8.749E+04	8.386E+04
15	9.961E+04	1.029E+05	9.905E+04	8.722E+04	9.078E+04	8.693E+04	8.591E+04	8.937E+04	8.573E+04
17	1.096E+05	1.129E+05	1.086E+05	9.530E+04	9.925E+04	9.404E+04	9.358E+04	9.748E+04	9.278E+04
19	1.212E+05	1.243E+05	1.198E+05	1.053E+05	1.088E+05	1.034E+05	1.033E+05	1.069E+05	1.019E+05
21	1.336E+05	1.367E+05	1.318E+05	1.162E+05	1.199E+05	1.139E+05	1.138E+05	1.177E+05	1.124E+05
23	1.461E+05	1.498E+05	1.440E+05	1.279E+05	1.319E+05	1.252E+05	1.251E+05	1.293E+05	1.234E+05
25	1.598E+05	1.629E+05	1.559E+05	1.396E+05	1.446E+05	1.369E+05	1.376E+05	1.430E+05	1.351E+05

Side-side moment [kNm]

Uw (m/s)	tower 1			tower 2			tower 3		
	yaw00	yaw-8	yaw+8	yaw00	yaw-8	yaw+8	yaw00	yaw-8	yaw+8
5	3.104E+04	2.996E+04	3.155E+04	1.981E+04	2.043E+04	1.879E+04	2.211E+04	2.170E+04	2.175E+04
7	4.989E+04	4.900E+04	5.229E+04	3.466E+04	3.387E+04	3.513E+04	3.742E+04	3.680E+04	3.668E+04
9	3.490E+04	3.507E+04	3.307E+04	2.232E+04	2.224E+04	2.336E+04	2.323E+04	2.414E+04	2.344E+04
11	3.772E+04	3.574E+04	3.546E+04	3.303E+04	3.067E+04	3.380E+04	3.260E+04	3.141E+04	3.284E+04
13	3.576E+04	3.403E+04	3.775E+04	2.836E+04	3.055E+04	2.756E+04	2.737E+04	2.815E+04	2.825E+04
15	4.634E+04	4.438E+04	4.768E+04	3.642E+04	3.937E+04	3.525E+04	3.480E+04	3.515E+04	3.651E+04
17	5.783E+04	5.553E+04	5.880E+04	4.595E+04	4.926E+04	4.492E+04	4.481E+04	4.464E+04	4.739E+04
19	6.968E+04	6.777E+04	7.105E+04	5.649E+04	6.072E+04	5.548E+04	5.591E+04	5.523E+04	5.920E+04
21	8.294E+04	8.054E+04	8.416E+04	6.770E+04	7.139E+04	6.742E+04	6.851E+04	6.726E+04	7.172E+04
23	9.710E+04	9.412E+04	9.826E+04	7.985E+04	8.358E+04	8.014E+04	8.232E+04	8.004E+04	8.520E+04
25	1.067E+05	1.004E+05	1.120E+05	9.610E+04	9.414E+04	1.008E+05	9.418E+04	9.261E+04	9.639E+04

Torsional moment [kNm]

Uw (m/s)	tower 1			tower 2			tower 3		
	yaw00	yaw-8	yaw+8	yaw00	yaw-8	yaw+8	yaw00	yaw-8	yaw+8
5	7.237E+03	7.145E+03	7.203E+03	7.217E+03	7.143E+03	7.160E+03	7.217E+03	7.135E+03	7.150E+03
7	1.038E+04	1.028E+04	1.027E+04	1.033E+04	1.024E+04	1.018E+04	1.030E+04	1.020E+04	1.015E+04
9	1.443E+04	1.429E+04	1.444E+04	1.439E+04	1.426E+04	1.443E+04	1.429E+04	1.416E+04	1.435E+04
11	1.792E+04	1.771E+04	1.780E+04	1.792E+04	1.773E+04	1.783E+04	1.778E+04	1.757E+04	1.769E+04
13	2.386E+04	2.375E+04	2.371E+04	2.382E+04	2.375E+04	2.368E+04	2.363E+04	2.354E+04	2.347E+04
15	2.788E+04	2.781E+04	2.769E+04	2.784E+04	2.781E+04	2.762E+04	2.759E+04	2.757E+04	2.737E+04
17	3.141E+04	3.141E+04	3.119E+04	3.138E+04	3.138E+04	3.115E+04	3.113E+04	3.112E+04	3.091E+04
19	3.479E+04	3.480E+04	3.458E+04	3.476E+04	3.479E+04	3.460E+04	3.457E+04	3.453E+04	3.435E+04
21	3.813E+04	3.820E+04	3.792E+04	3.814E+04	3.821E+04	3.797E+04	3.794E+04	3.797E+04	3.772E+04
23	4.153E+04	4.164E+04	4.128E+04	4.153E+04	4.167E+04	4.134E+04	4.134E+04	4.141E+04	4.108E+04
25	4.463E+04	4.477E+04	4.451E+04	4.466E+04	4.475E+04	4.460E+04	4.445E+04	4.449E+04	4.436E+04

Table 13   *Tower bottom (26m amsl) equivalent loads (m=4). Three towers, three yaw angles per tower. From top fore-aft, side-side and yaw loads*

Deliverable 1.25b

Reliability Level Estimation of a 20MW Jacket Structure

October 2017

Agreement n.:	308974
Duration	November 2012 – October 2017
	DTU Wind

The research leading to these results has received funding from the European Community's Seventh Framework Programme under grant agreement

Document Name:	**Reliability Level Estimation of a 20MW Jacket Structure**
Document Number:	**Deliverable 1.25b**
Author:	**Tomas Gintautas, John Dalsgaard Soerensen (AAU)**
Document Type	Report
Dissemination level	PU
Review:	**John Dalsgaard Soerensen**
Date:	**October 2017**
WP:	**WP1: Conceptual Design**
Task:	**Task 1.2: Assessment of Innovation at the Subsystems Level**
Approval:	Approved by WP Leader

TABLE OF CONTENTS

(Innwind.EU, Deliverable 1.25b, Reliability Level Estimation of a 20MW Jacket Structure)

LIST OF FIGURES

(Innwind.EU, Deliverable 1.25b, Reliability Level Estimation of a 20MW Jacket Structure)

1. INTRODUCTION / SUMMARY

The objective of this report is to present and apply a reliability-based approach for assessment of the system reliability of fatigue critical details in very large support structures and to evaluate the potentials for verification of satisfactory reliability for fatigue critical details using inspections. Further to include the effect of correlation between failure modes in different fatigue failure modes, and to investigate the effect in generic case studies relevant for very large support structures.

Verification of sufficient reliability using safety factors as traditionally done in design standards such as the IEC 61400 series (and the Eurocodes) does not allow in a consistent way to account for the effect of inspections done during the design lifetime. This report describes the theoretical basis for reliability-based planning of inspections (Bayesian pre-posterior decision theory). This requires that a probabilistic fracture mechanics model is calibrated to result in the same reliability level as obtained using the SN-curve approach used in traditional design standards. This includes establishment of stochastic models for load and fatigue strength parameters. These steps are described in this report. It is noted that a system reliability-based assessment / planning of inspections are very computer-time demanding, and needs careful modelling of the uncertainties. In this report experience from JCSS (Joint Committee on Structural Safety) and from applications in other offshore industries is applied.

The results indicate large potentials in using inspections for increasing the design lifetime fulfilling requirements to a minimum reliability level. E.g. an example shows that 3-4 inspections during the design lifetime of 25 years may increase the safe lifetime from 13 years to 25 years. It is noted that for decision making on the use of inspections a cost consideration should be performed where the following costs are compared:

- costs of inspections and eventual maintenance/repair in case of detected cracks
- cost savings in a reduced cost of the support structure, incl. the cost of additional steel to be used in the support structure such that it fulfils the reliability requirements in the design standards

The case studies performed indicate that the correlation (mainly from common epistemic uncertainties) between different fatigue failure modes is limited and does not have a significant influence on the system reliability.

2. RELIABILITY-BASED INSPECTION PLANNING

Inspection planning procedures require in principle information on costs of design/manufacturing, failures, inspections and repairs. Often these are not available, and the inspection planning is based on the requirement that the annual probability of failure in all years has to satisfy a reliability constraint. This implies that the annual probabilities of fatigue failure for all years during the operational life of the structure has to fulfill:

$$P_{FAT_j} \leq P_{AC_j} \tag{1}$$

The implicit code requirements to the safety of the structures in regard to total collapse may be assessed through the annual probability of fatigue failure of critical details (in the last year in service) $P_{FAT,j}$ for a joint for which the consequences of failure are "substantial"

(Innwind.EU, Deliverable 1.25b, Reliability Level Estimation of a 20MW Jacket Structure)

(i.e. the Design Fatigue Factor (DFF) is equal to 10 for offshore structures in general (oil and gas) and equal to 3 for offshore wind turbines). This probability can be regarded an acceptance criteria i.e. P_{AC}. A typical maximum acceptable annual probability of collapse failure is in the in the range $10^{-4} - 3 \cdot 10^{-5}$ for unmanned structures, see e.g. [1] and [2]. On this basis it is possible to establish joint & member specific acceptance criteria in regard to fatigue failure. For each critical detail / joint j the conditional probability of structural collapse given fatigue failure of the considered joint $P_{COL|FAT,j}$ are determined and the individual joint acceptance criteria for the annual probability of joint fatigue failure are found as:

$$P_{AC_j} = \frac{P_{AC}}{P_{COL|FAT_j}} \tag{2}$$

The annual probability of fatigue failure $P_{FAT,j}$ may be determined on the basis of either a simplified probabilistic SN approach or a probabilistic fracture mechanics approach. As an alternative to the above approach where basis is taken in annual probabilities of failure it is equally possible to take basis in service life probabilities. However, as most installation concept risk analyses give requirements to the maximum allowable risk for structural collapse in terms of annual failure probabilities, these are used in the following.

Further, in risk- and reliability-based inspection planning the planning is often made with the assumption that no cracks are found at the inspections. If a crack is found, then a repair is typically performed and a new inspection plan has to be made based on the observation. If all inspections are made with the same time intervals, then the annual probability of fatigue failure as a function of time could be as illustrated in Figure 2.1.
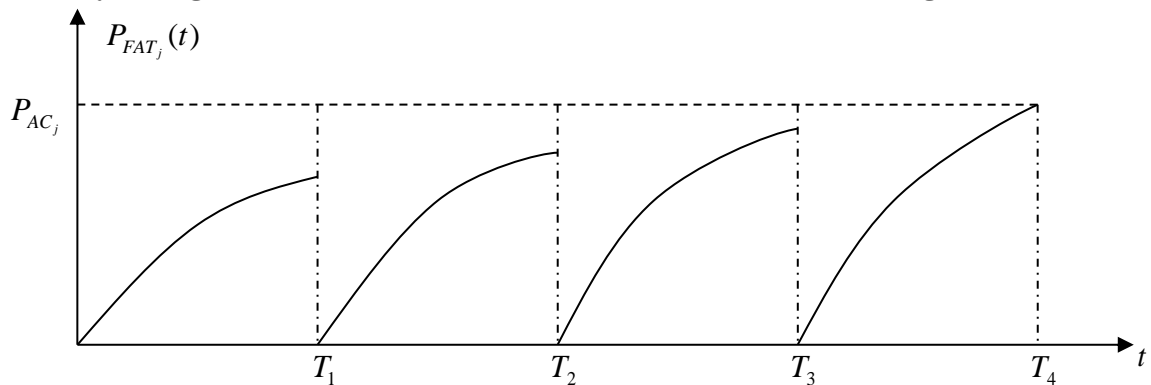

Figure 2.1. Illustration of inspection plan with equidistant inspections.

If inspections are made when the annual probability of fatigue failure exceeds the critical value then inspections are made with different time intervals, as illustrated in Figure 2.2. As assumed above, it is often assumed that the inspection planning can be based on the no-find assumption. This way of inspection planning is the one which if most often used. Often this approach results in increasing time intervals between inspections.

(Innwind.EU, Deliverable 1.25b, Reliability Level Estimation of a 20MW Jacket Structure)
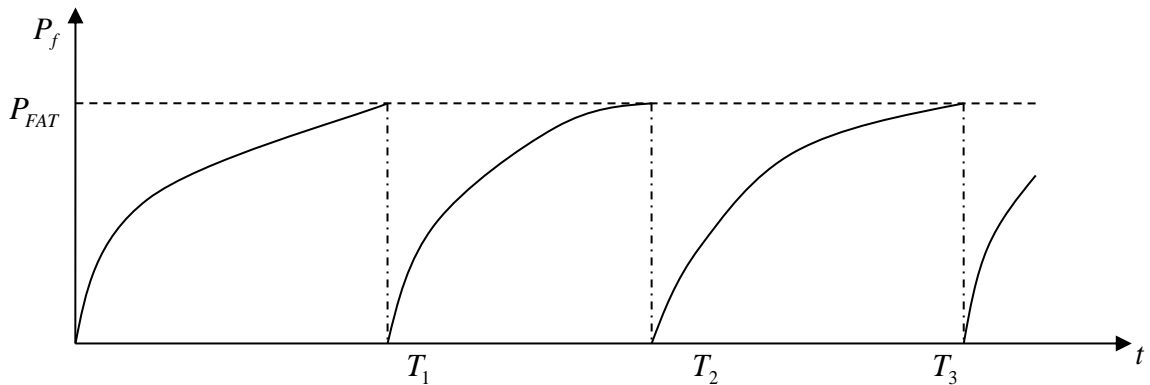
Figure 2.2. Illustration of inspection plan where inspections are performed when the annual probability of failure exceeds the maximum acceptable annual probability of failure.

1.1 Probabilistic modelling of inspections

The reliability of inspections can be modelled in different ways. Often POD (Probability Of Detection) curves are used to model the reliability of the inspections. If inspections are performed using an Eddy Current technique (below or above water) or a MPI technique (below water) the inspection reliability can be represented by following Probability Of Detection (POD) curve:

$$POD(x) = 1 - \frac{1}{1 + \left(\dfrac{x}{x_0}\right)^b} \tag{3}$$

where x is the crack size (length or depth) and e.g. X_0 = 15.78 mm and b = 1.079, [3].

For jacket structures [3] recommends general visual inspections (GVI) with remotely operated vehicles (ROV), cleaning and close visual inspections (cCVI) or eddy current inspections (EC). Parametric recommendations for different inspection techniques are given in the following Table 1. It should be noted, that high resolution image photos (HRI) are considered to conform to requirements of highest quality POD curve for Ccvi, thus making it feasible to use ROVs to clean the suspected crack locations and take HRIs for inspection.

Table 1: POD curve parameters for different inspection techniques.

Inspection type	Comment	X_0	b
Eddy Current	Below water and less good conditions above water	1.16	0.9
Ultrasonic	-	0.41	0.642
Visual inspection	Easy access	15.78	1.079
	Moderate access	37.15	0.954

Typically, Eddy current and Ultrasonic inspections are focused on crack depth detection (a-direction) while for Visual inspections, only crack width/length (c-direction) is possible to detect. Therefore, it is important to distinguish between these two types of crack detection and investigate benefits of such inspections towards increased reliability separately.

(Innwind.EU, Deliverable 1.25b, Reliability Level Estimation of a 20MW Jacket Structure)

If an inspection has been performed at time T_I and no cracks are detected then the probability of failure can be updated by

$$P_F^U\left(t\middle|\text{no - detection at time } T_I\right)= P\left(g(t)\leq 0\middle|h(T_I)>0\right) \text{ , } t>T_I \tag{4}$$

where $h(t)$ is a limit state modeling the crack detection. If the inspection technique is related to the crack length then $h(t)$ is written:

$$h(t)=c_d - c(t) \tag{5}$$

Here $c(t)$ is the crack length at time t and c_d is smallest detectable crack length. c_d is modelled by a stochastic variable with distribution function equal to the POD-curve:

$$F_{c_d}(x) = POD(x) \tag{6}$$

Similarly if the inspection technique is related to the crack depth then $h(t)$ is written:

$$h(t)=a_d - a(t) \tag{7}$$

where $a(t)$ is the crack length at time $_t$ and a_d is smallest detectable crack length. a_d is modelled by a stochastic variable with distribution function equal to the POD-curve:

$$F_{a_d}(x) = POD(x) \tag{8}$$

If two independent inspections are performed at time T_I and no cracks are detected then the probability of failure can be updated by

$$P_F^U\left(t\middle|\text{no - detection at time } T_I\right)= P\left(g(t)\leq 0\middle|h_1(T_I)>0\cap h_2(T_I)>0\right), t>T_I \tag{9}$$

where $h_1(t)=a_{d_1} - a(T_I)$ and $h_2(t)=a_{d_2} - a(T_I)$ are the limit states modeling the inspections.

3. PROBABILISTIC MODELLING OF FATIGUE

Probabilistic models for fatigue failure are in general established using the SN-approach together with the Miners rule of linear fatigue damage accumulation. SN-test results are used to model the uncertainty related to the SN-curves. However, the probabilistic model based on SN-curves cannot be used investigate the effect of inspections on the reliability levels since SN-curves do not have information about the crack size. Therefore, a probabilistic fracture mechanics approach is needed where an explicit measure of the fatigue crack is represented. Traditionally in reliability- and risk-based inspection planning (RBI) the probabilistic fracture mechanics model is calibrated to give the same reliability as function of time as obtained by the SN-approach. This approach is also applied in the following sections.

3.1 Stochastic model based on SN curves

Fatigue reliability is assessed using the SN-curve approach together with Miner's rule, combined in the following limit state equation:

(Innwind.EU, Deliverable 1.25b, Reliability Level Estimation of a 20MW Jacket Structure)

$$g = \Delta - \sum_{i,1} \frac{t\, n_i \left(C_{SCF} C_W \Delta\sigma_i \left(\dfrac{T}{t_{ref}}\right)^k \right)^{m_1}}{a_1} - \sum_{i,2} \frac{t\, n_i \left(C_{SCF} C_W \Delta\sigma_i \left(\dfrac{T}{t_{ref}}\right)^k \right)^{m_2}}{a_2} \geq 0 \qquad (10)$$

where C_{SCF} and C_{Load} are model uncertainties related to uncertainty in stress concentration factors and the fatigue load; Δ models model uncertainty related to Miner's rule. a_1 and a_2 are stochastic variables modelling uncertainty related to the SN-curve; m_1 and m_2 are slopes of a bi-linear SN curve; k is the thickness exponent for a given SN curve; t is the time in years; T is the thickness of the element; t_{ref} is reference thickness (32mm); n_i is the number of stress ranges $\Delta\sigma_i$ per year.

SN curves from [4] are used in fatigue analysis (curve parameters are given in Table 2). Curve D is applicable jacket leg elements, Curve F3 is applicable for jacket braces and Curve T is used for jacket joints. A full description of the stochastic model for fatigue reliability assessment is given in Table 2.

Table 2: Parameters for probabilistic fatigue damage model based on SN curves.

Variable	Distribution	Expected value	Standard deviation / COV	Comment
Curve T for jacket joints (in air) – DNV T-A				
m_1	D	3		Slope of SN curve
m_2	D	5		Slope of SN curve
$\log a_1$	N	12.164+2x0.2	SD= 0.2	T curve intercept, in seawater with CP
$\log a_2$	N	15.606+2x0.2	SD= 0.2	T curve intercept, in air
k	D	0.25	-	Thickness exponent
Curve T for jacket joints (in seawater, with cathodic protection) – DNV T-W				
m_1	D	3		Slope of SN curve
m_2	D	5		Slope of SN curve
$\log a_1$	N	11.764+2x0.2	SD= 0.2	T curve intercept, in seawater with CP
$\log a_1$	N	15.606+2x0.2	SD= 0.2	T curve intercept, in air
k	D	0.2	-	Thickness exponent
Model uncertainties				
Δ	N	1	COV = 0.30	Model uncertainty Miner's rule
C_{LOAD}	LN	1	COV = 0.06	Model uncertainty fatigue load
C_{SCF}	LN	1	COV = 0.055	Model uncertainty stress concentration factor
$\log a_1$ and $\log a_2$ are fully correlated.				

The total COV for the model uncertainty and the fatigue load is chosen to $\sqrt{COV_{LOAD}^2 + COV_{SCF}^2} = 0.08$. This represents a case where the fatigue load is estimated quite good and where the stress concentration factors are obtained based on detailed finite element analyses, see [5] for more details.

3.2 Fracture mechanis based stochastic model for fatigue crack growth

The applied fatigue crack growth model (based on fracture mechanics) is bi-linear and crack growth is considered in both 'c' and 'a' (depth and width) directions, see Figure 3.1, right side. The model is generally based on [6] with crack growth parameters adopted from [7] where necessary. The crack growth is typically described by the following coupled differential equations:

$$\frac{da}{dN} = A_a(\Delta K_a)^m \qquad a(N_0) = a_0 \tag{11}$$

$$\frac{dc}{dN} = A_c(\Delta K_c)^m \qquad c(N_0) = c_0 \tag{12}$$

here A_a, A_c and m are material parameters, a_0 and c_0 describe the crack depth a and crack length c, respectively, after N_1 cycles and where the stress intensity ranges are $\Delta K_a(\Delta\sigma)$ and $\Delta K_a(\Delta\sigma)$.

Failure is considered when a crack grows through the thickness of the monopile/transition piece steel and can be summarized in the following limit state function:

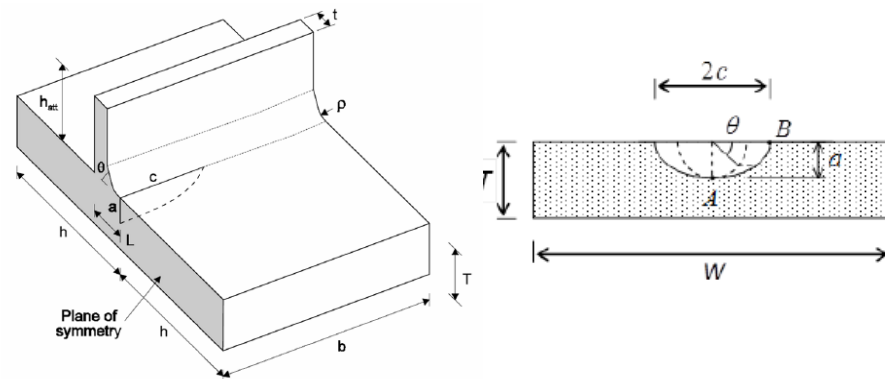$$g(X,t) = a_{cr} - a(t) \geq 0 \tag{13}$$

Figure 3.1: Weld geometry parameters for crack growth model, [64].

where t is time (in years) in the time interval between 0 and service life T_L. Crack dimensions at any given time within turbines service life can be calculated using following equations:

$$a(t) = \sum_{i,1} N_{i,1} A_1 \left(C_{SIF} \Delta K_{a,i,1} \right)^{m_1} + \sum_{j,1} N_{j,2} A_2 \left(C_{SIF} \Delta K_{a,j,2} \right)^{m_2} \tag{14}$$

$$c(t) = \sum_{i,1} N_{i,1} A_1 \left(C_{SIF} \Delta K_{c,i,1} \right)^{m_1} + \sum_{j,1} N_{j,2} A_2 \left(C_{SIF} \Delta K_{c,j,2} \right)^{m_2} \tag{15}$$

Equations (14) and (15) are a discretized version of (11) and (12), representing crack growth in two directions (depth 'a' and width 'c'), hence the summations. Also, use of sets

of two A and K parameters comes from the use of bi-linear crack growth model (A_1,K_1 for Stage A and A_2, K_2 for Stage B in Figure 3.2).

$$\Delta K_{i,a} = \left(M_{kma}M_{ma}(1-DOB) + M_{kba}M_{ba}DOB\right)C_{Load}C_{SCF}\Delta\sigma_i\sqrt{\pi a_i} \tag{16}$$

$$\Delta K_{i,c} = \left(M_{kmc}M_{mc}(1-DOB) + M_{kbc}M_{bc}DOB\right)C_{Load}C_{SCF}\Delta\sigma_i\sqrt{\pi a_i} \tag{17}$$

$$M_{km(b)a} = f_1\left(\frac{a}{T},\frac{a}{c}\right) + f_2\left(\frac{a}{T},\theta\right) + f_2\left(\frac{a}{T},\theta,\frac{L}{T}\right) \tag{18}$$

$$M_{km(b)c} = f_1\left(\frac{a}{T},\frac{c}{a},\frac{L}{T}\right)f_2\left(\frac{a}{T},\frac{a}{c},\theta\right)f_2\left(\frac{a}{T},\frac{a}{c},\theta,\frac{L}{T}\right) \tag{19}$$

$$M_{ma(c)} = \left[M_1 + M_2\left(\frac{a}{c}\right)^2 + M_3\left(\frac{a}{c}\right)^4\right]g\cdot f_\Theta/\Phi \tag{20}$$

$$M_{ba(c)} = M_{ma(c)}\cdot H \tag{21}$$

$$H = H_1 + (H_2 - H_1)\sin^q(\theta) \tag{22}$$

Here N_i is number of stress ranges $\Delta\sigma_i$ within considered lifetime window; A_1, A_2 m_1 and m_2 are material parameters based on crack growth environment for bi-linear crack growth curves; C_{SIF} is model uncertainty related to stress intensity magnification factors ($M_{km(b)a(c)}$ and $M_{m(b)a(c)}$); C_{LOAD} models uncertainty related to load (stress) modelling and C_{SCF} models uncertainty related to stress concentration factor calculation.

Stress intensity magnification factors based on weld and crack geometry (Figure 3.1) are calculated based on [3], [7] and [8] using f_1, f_2, f_3, M_1, M_2, g, f_Θ geometrical coefficients. θ is weld angle in on the left and Θ is the crack growth direction angle in 68 on the right (90 for growth in depth direction "a" and 0 for growth in width direction "c"). It should be noted here that membrane and bending loading was considered for the tubular joints, and the interaction between these two types of loading is represented by DOB-degree of bending, as recommended by [3] section 6.7. The following Table 3 summarizes all the parameters used for this analysis.

Table 3: Parameters for Crack growth (Fracture mechanics) probabilistic model

Variable	Distribution	Expected value	Standard deviation / COV	Comment
a_0	LN	Fitted to match SN results	COV= 0.66	Initial crack depth
c_0	LN	$a_0/0.62$	COV= 0.40	Initial crack width
a_{cr}	D	Depends on element geometry	-	Critical crack depth, thickens of the steel.
L	D	Depends on element geometry	-	Distance from weld edge to inner surface of the tubular element
T	D	Depends on element geometry	-	Thickness of tubular element

(Innwind.EU, Deliverable 1.25b, Reliability Level Estimation of a 20MW Jacket Structure)

In marine environment with Cathodic protection at -1100mV (Ag/AgCl)				
$\log(A_1)$	N	-17.32	SD= 0.11	FM curve parameter
$\log(A_2)$	N	-11.28	SD= 0.05	FM curve parameter
m_1	D	5.1	-	Slope FM curve
m_2	D	2.67	-	Slope FM curve
In Air				
$\log(A_1)$	N	-17.32	SD= 0.16	FM curve parameter
$\log(A_2)$	N	-12.23	SD= 0.09	FM curve parameter
m_1	D	5.1	-	Slope FM curve
m_2	D	2.88	-	Slope FM curve
Model uncertainties				
C_{LOAD}	LN	1	COV = 0.06	Model uncertainty fatigue load
C_{SCF}	LN	1	COV = 0.055	Model uncertainty stress concentration factor
C_{SIF}	LN	1	COV = 0.07	Model uncertainty related to stress magnification factor calculation

$\log A_1$ and $\log A_2$ are fully correlated.

General procedure of crack growth modelling using differential equations given in the beginning of this section is summarized in Figure 3.3.
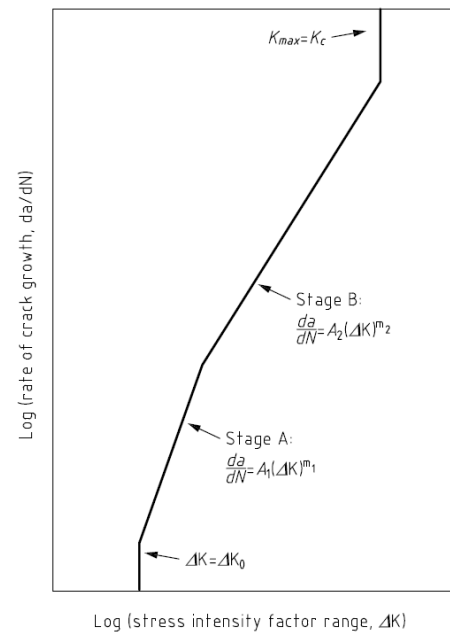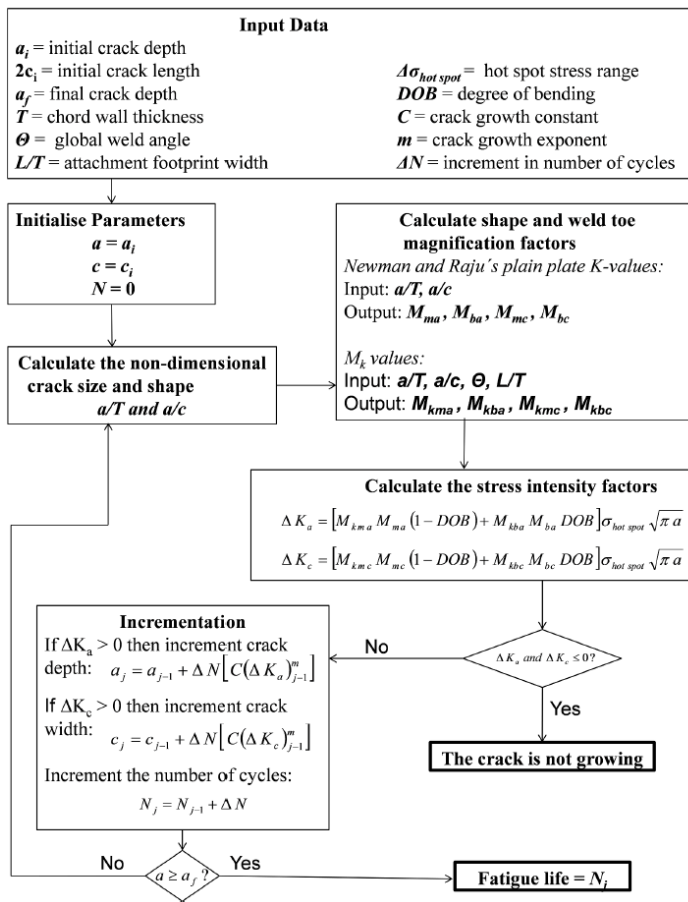

<div align="center">a   b</div>

Figure 3.3.: Procedure for crack growth calculation (a) [3] and Paris law sketch (b) [6]

The transition ("knee") point between stages A and B in Figure 3.3 is calculated based on realizations of $\log(A_1)$, $\log(A_1)$, m_1 and m_2 using the following equation:

$$\log(\Delta K_{trans}) = \frac{\log(A_1) - \log(A_2)}{m_2 - m_1} \tag{23}$$

As recommended in [3] the following additional geometrical parameters for tubular jacket joints/elements are assumed (based on HSE joint database data):

$$L_{Weld} = 1.17 \cdot T_{TP}$$
$$\theta_{Weld} = 43^0$$
$$DOB = 0.81$$

4. SYSTEM EFFECTS

Since the jacket substructure contains multiple structural members and system failure / total collapse / major damage may occur if one of the structural members fail, the system reliability is estimated considering a series system model consisting of potential failure in any of the structural members as elements in the series system model. It is noted that some additional load bearing capacity may exist in case of failure of a structural member. Assessment of this additional resistance requires non-linear finite element analysis which is outside the scope of this investigation. The system probability of failure for a series system with m elements / fatigue failure critical details is estimated by:

$$P_f^S = P\left(\bigcup_{i=1}^{m} \{g_i(\mathbf{X}) \leq 0\} \right) \approx 1 - \Phi_m(\boldsymbol{\beta}; \boldsymbol{\rho}) \tag{24}$$

where $\Phi m(.)$ is the standardized m-dimensional Normal distribution function, $\boldsymbol{\beta}$ is the vector with reliability indices and the elements in the correlation matrix, $\boldsymbol{\rho}$ are obtained from $\rho_{ij} = \alpha_i^T \alpha_j$. The α-vector a_j is obtained as

$$\boldsymbol{\alpha}_j = \left(0,0,\ldots,\alpha_{R_j},0,0,\ldots,0,\alpha_\delta,\alpha_L,\alpha_{X_{dyn}},\alpha_{X_{exp}},\alpha_{X_{aero}},\alpha_{X_{str}} \right)^T \tag{25}$$

where the index indicates which stochastic variable the α -value is connected to. It is noted that the 'fatigue strength' R for different structural members are assumed statistically independent.

The system reliability index is defined as

$$\beta_S = -\Phi^{-1}\left(P_f^S\right) \tag{26}$$

(Innwind.EU, Deliverable 1.25b, Reliability Level Estimation of a 20MW Jacket Structure)

5. RESULTS FOR 20MW JACKET STRUCTURE

This section shows the results of methodology presented in sections 1 through 4. The focus is on the 20 MW wind turbine reference jacket substructure, designed by Ramboll and documented in [9] and [10]. The following Figure 5.1 shows the locations of selected elements together with their notation as given in [9].

20 MW reference jacket:

- Considered Joints and Braces:
  - Node 50A0P0, brace 45ALT
  - Node 15AA00, brace 15A1V
  - Node 20A0O0, brace 15ALT
  - Node 13A0P0, brace 13ALV
- 12 stress point per location on brace side
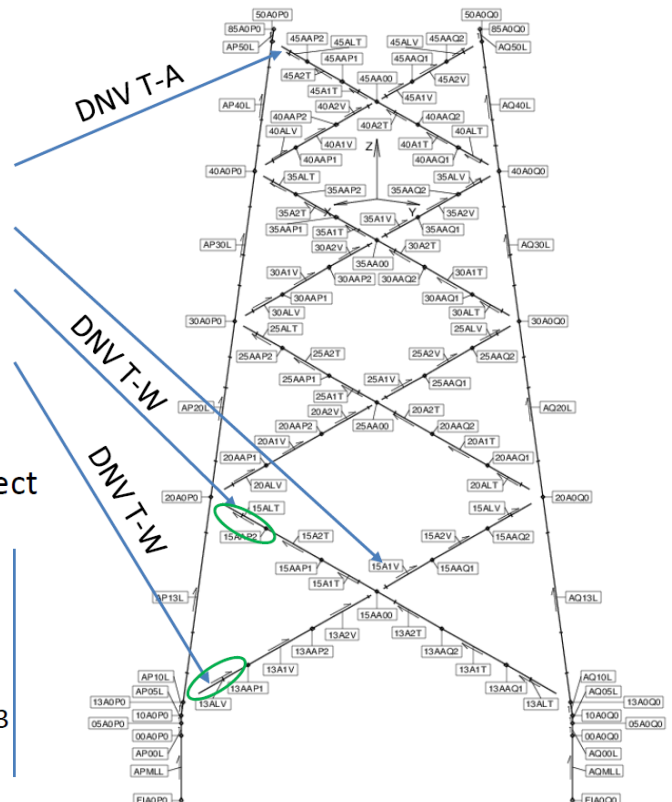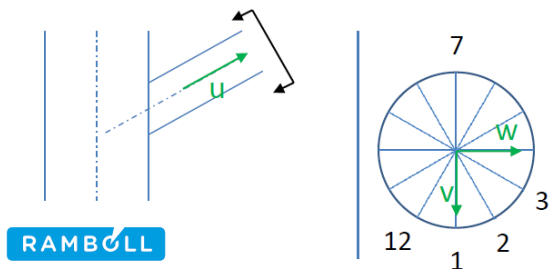- Includes SCF, safety, thickness effect

Figure 5.1.: Elements/nodes selected for the analysis [9],

4 different types of joints are selected for the reliability analysis and inspection planning. The considered elements/joints are as follows:
1. Node 13A0P0 – K joint with expected characteristic lifetime of 60 years (below mean water level). Tubular element thickness 34.9 mm.
2. Node 15AA00 – X joint with expected characteristic lifetime of 41 years (below mean water level). Tubular element thickness 31.8 mm.
3. Node 20A0P0 – K joint with expected characteristic lifetime of 45 years (below mean water level). Tubular element thickness 34.9mm.
4. Node 50A0P0 – K joint with expected characteristic lifetime of 85 years (above mean water level). Tubular element thickness 25.4mm.

5.1 Reliability level estimation for individual elements and Fracture mechanics model calibration

Stress range spectra were provided by WP4 partners for the joints mentioned above in terms of expected stress ranges and their respective half-cycle counts. The following Figure 5.2 shows the stress range spectra for the 4 selected joints. The 20MW wind

turbine jacket substructure design is not finalized yet and the stress range spectra used in this analysis is based on the "Preliminary design results" from [9]. Furthermore, it should be noted that the stress range spectra were provided at 12 nodes around the tubular member cross-section circumferentially. Only one most critical node per element was selected based on maximum equivalent damage stress range $\Delta\sigma_{eq}$:

$$\Delta\sigma_{eq} = \left[\frac{\sum_{i=1}^{n} N_i \Delta\sigma_i^{m}}{\sum_{i=1}^{n} N_i} \right]^{1/m} \tag{27}$$
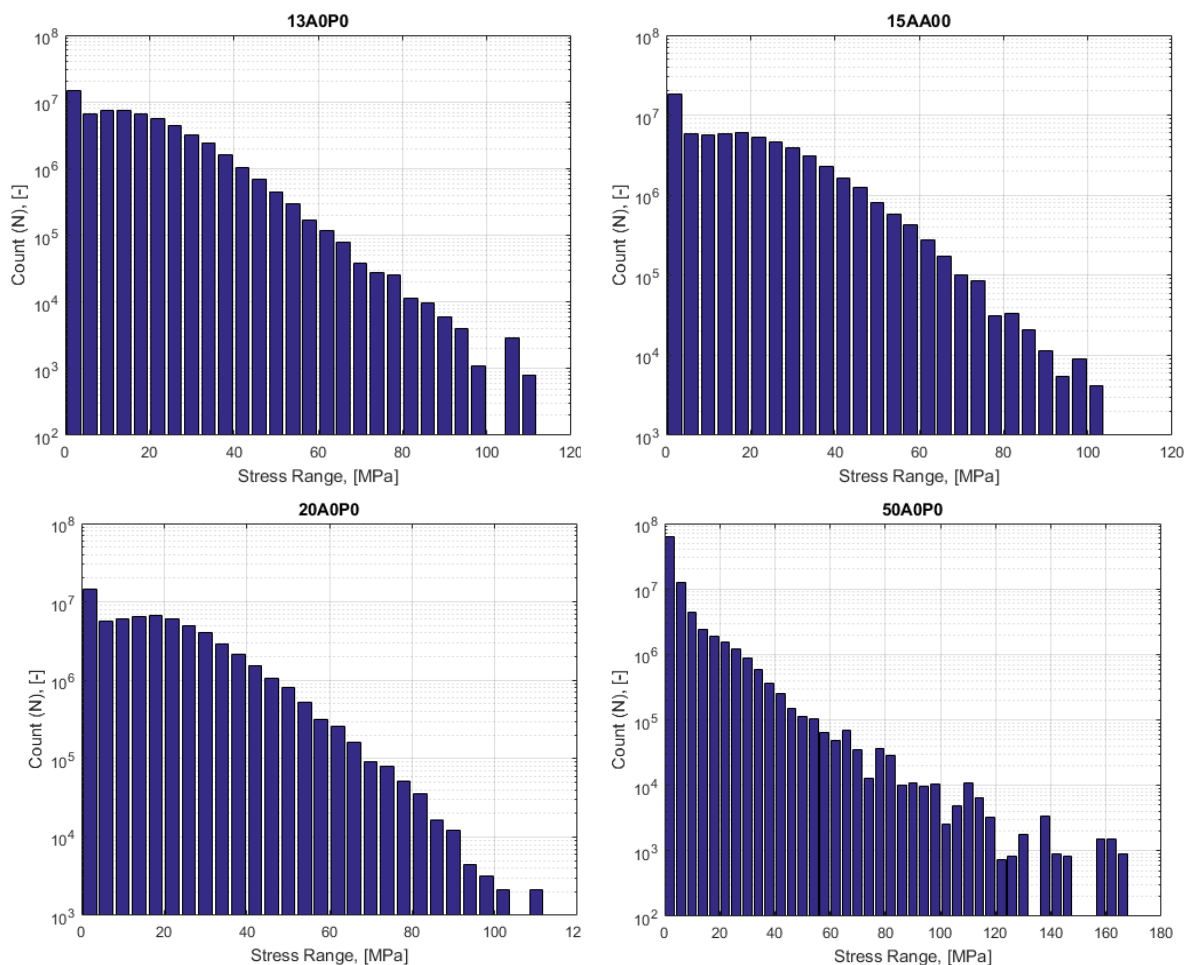

Figure 5.2.: Stress range spectra for the selected elements (most critical node), based on [9],

Using the stress range spectra, the reliability levels for all 4 elements are estimated using SN curve approach combined with miners rule, as described in section 3.1. It should be noted here that [9] provides only characteristic estimates of expected fatigue lives of the jacket elements – the fatigue load spectra used for fatigue life estimation have a safety factor γ_F=1.0 and modelling and load uncertainties are accounted for by using a Design Fatigue Factor (DFF=3). This implies increasing the required design life from 25 to 75 years. However, for probabilistic inspection planning, it is important to take the relevant uncertainties into account directly into the failure function (eq. (10)) through stochastic

variables, as defined in Table 2. The stochastic variables shown in Table 2 are equivalent to a safety factor of γ_F=1.25 (assuming SN-curve slope equal to 5) and are sufficient to conform with requirements of [2], [3], [4], [7] and general recommendations given in [5].

The accumulated probabilities of failure (and corresponding reliability indexes) are calculated using FORM (First Order Reliability Method). The following equation is then used to estimate the annual probability of failure in year t given survival up to year t:

$$\Delta P_{F,t} = \frac{P_{COL|FAT}\left(P(g(t) \le 0) - P(g(t-1) \le 0)\right)}{P(g(t) \le 0)} \qquad (28)$$

with annual reliability index obtained by:

$$\beta_{F,t} = -\Phi^{-1}\left(\Delta P_{F,t}\right) \qquad (29)$$

The following Figure 5.3 shows the accumulated and annual reliability indexes for all 4 selected elements. Required minimum annual reliability index of $\beta_{F,t}$=3.3 ($\Delta P_{F,t}$=5x10^{-4}) is used as target reliability, see [5] and IEC 61400-1 ed. 4 (2017) . This reliability level corresponds to minor / moderate consequences of failure and moderate / high cost of safety measure. It is noted that this reliability level corresponds to the reliability level for offshore structures that are unmanned or evacuated in severe storms and where other consequences of failure are not very significant.
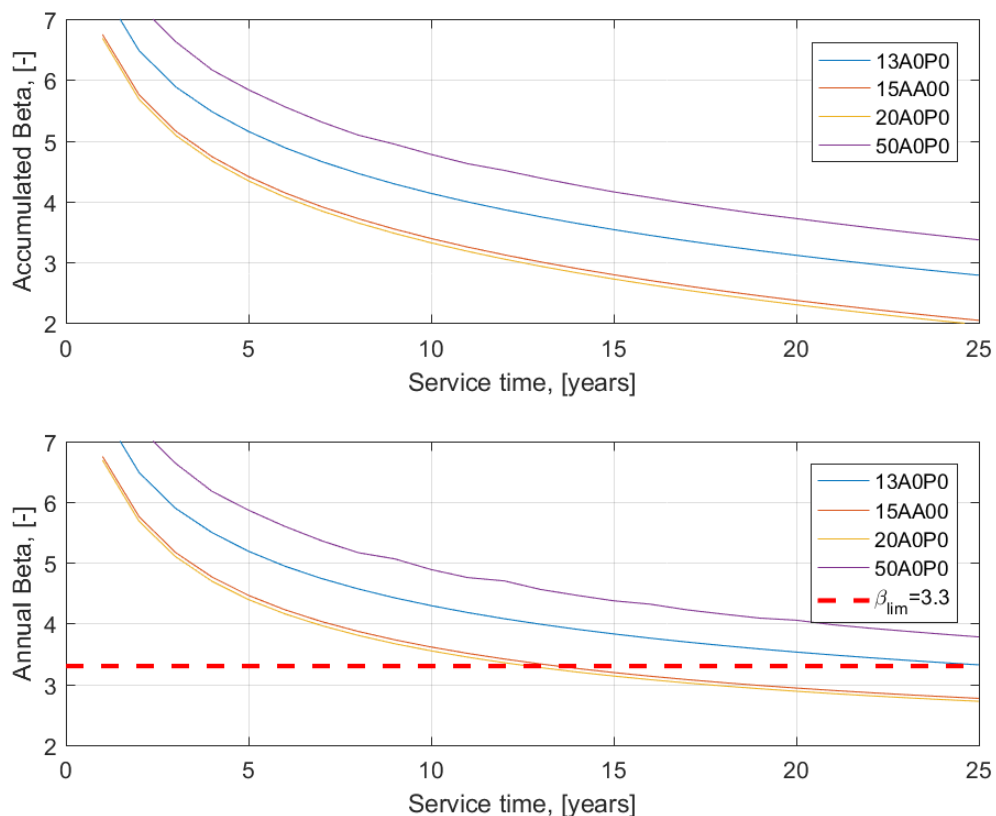

Figure 5.3.: Results of SN analysis of the selected elements.

It is seen that elements / fatigue critical details have different reliability levels and thus different expected 'safe' lifetimes, thus implying that system effects should be cosidered and annual system reliability should be estimated. This is done and documented in section 5.2. It is also seen that some elements have insufficient reliability. One possibility to increase the reliability is to perform inspections, see below following te approach described above.

Using the model described in set ion 3.2, Fracture Mechanics model is calibrated to give approximately the same annual reliability indices as function of time as obtained above with SN-curves from the [11]. The calibration parameter in the model is initial crack depth a_0. The calibration is performed in such a way that the predicted annual reliability indexes match at 10-25 years of service, because typically Fracture mechanics models are less reliable for the first few years of service. The following Figure 5.4 shows the results of FM model calibration for all 4 selected elements and it can be concluded that a very good match is obtained - the curves are very similar and "failure time" ($\beta_{F,t} \leq 3.3$) is predicted very accurately by the Fracture Mechanics model for all the elements.
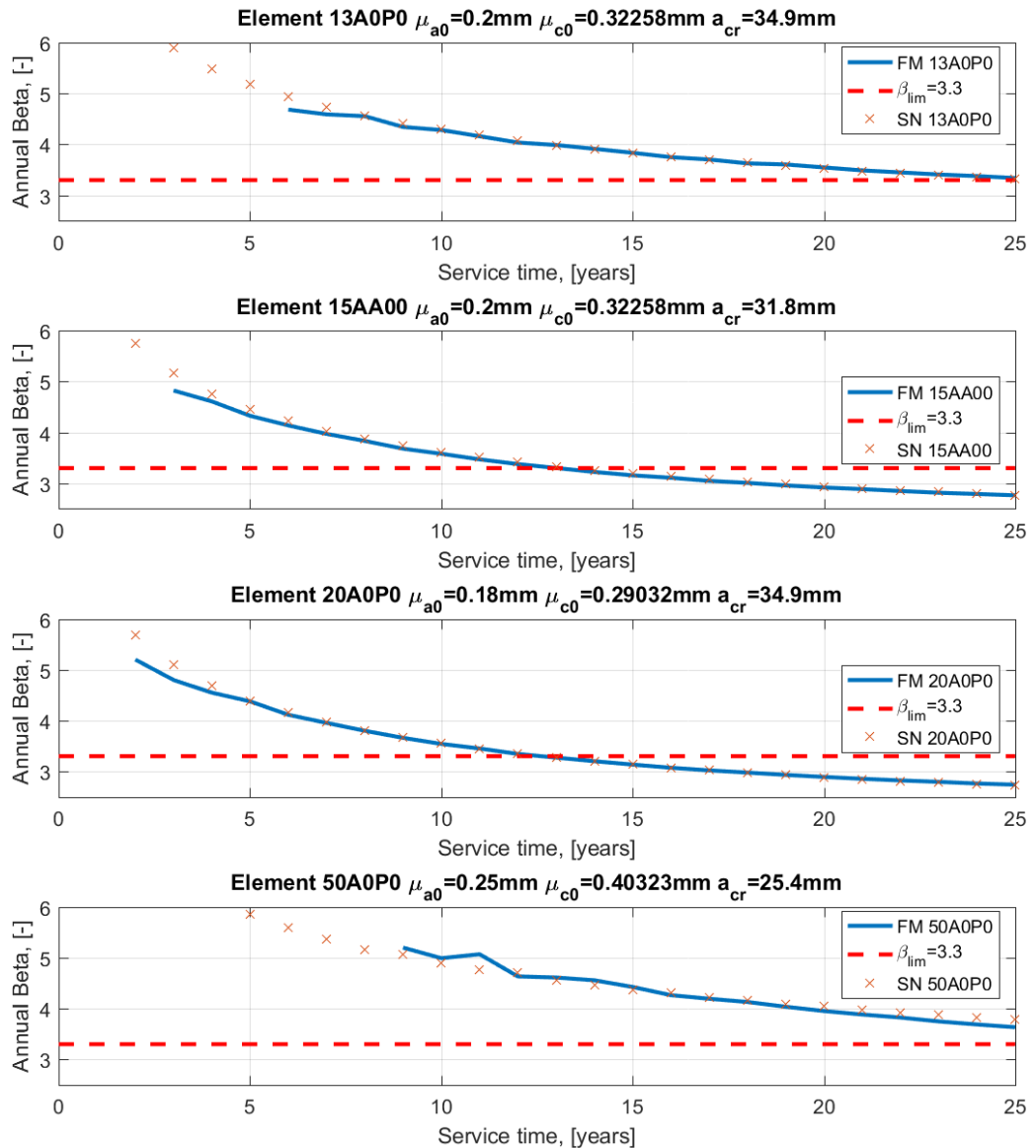
(Innwind.EU, Deliverable 1.25b, Reliability Level Estimation of a 20MW Jacket Structure)

Figure 5.4.: Results of FM model calibration for the selected elements.

5.2   System reliability and uncertainty correlation

As was mentioned in the previous sections, wind turbine jacket substructures consist of multiple tubular steel elements which have differing reliability indexes and thus different expected safe lifetimes. This implies the need for system reliability analysis. The jacket substructure elements are considered to be non-redundant, implying that failure of one

(Innwind.EU, Deliverable 1.25b, Reliability Level Estimation of a 20MW Jacket Structure)

element results in failure of the whole substructure – i.e. a series system behavior. The following Figure 5.5 shows the results of system reliability analysis.
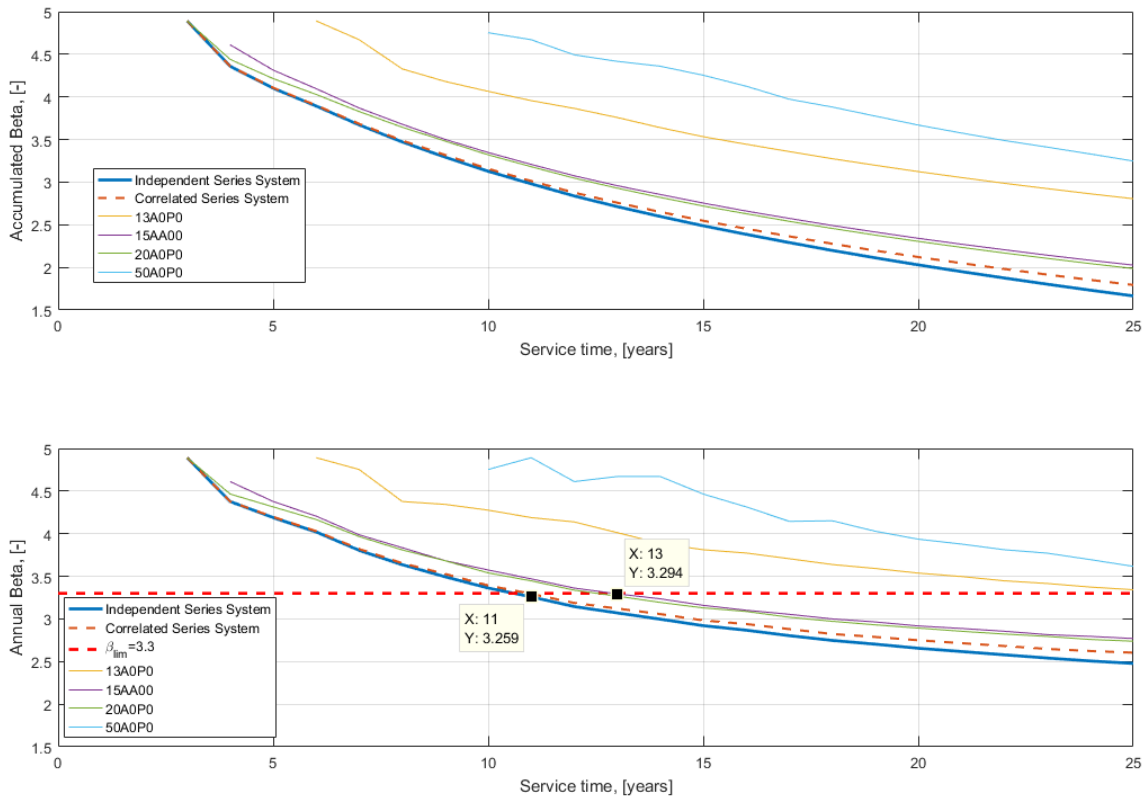

Figure 5.5.: Results of system reliability analysis with and without correlation.

It is seen that annual system reliability index (thick blue line) is significantly lower that annual reliabilities of individual elements (thin multicolored lines) – the expected system lifetime is 11 years whereas the lifetime of least reliable system element is ~13 years. This implies that in fact it is important and necessary to estimate system level reliability of jacket wind turbine substructures.

Another important aspect related to system reliability is correlation among failure elements/modes. Model uncertainties in Table 3 can be assumed to be fully correlated. The line "Correlated Series System" in Figure 5.5 assumes fully correlated (among failure elements) model uncertainties $C_{LOAD}, C_{SCF}, C_{SIF}$. In this case no significant change in annual system reliability index is achieved by assuming fully correlated model uncertainties, especially when it comes to "failure time" ($\beta_{F,t} \leq 3.3$). However, some improvement can be expected in the end of service life. Thus all further analyses below is done assuming fully correlated model uncertainties. Absence of significant difference between "correlated" and "independent" cases implies that some other variable/variables are driving the system behavior more extensively than model uncertainties. However, further correlation analysis is beyond the scope of this deliverable.

5.3 Effects of inspections

The calibrated FM model is used to introduce inspections in order to maintain annual reliability levels above the $\beta_{F,t} = 3.3$ target throughout the lifetime of the structure. The following figures show how different types of inspections, mentioned in section 1.1, can be utilized to maintain the acceptable system reliability levels.
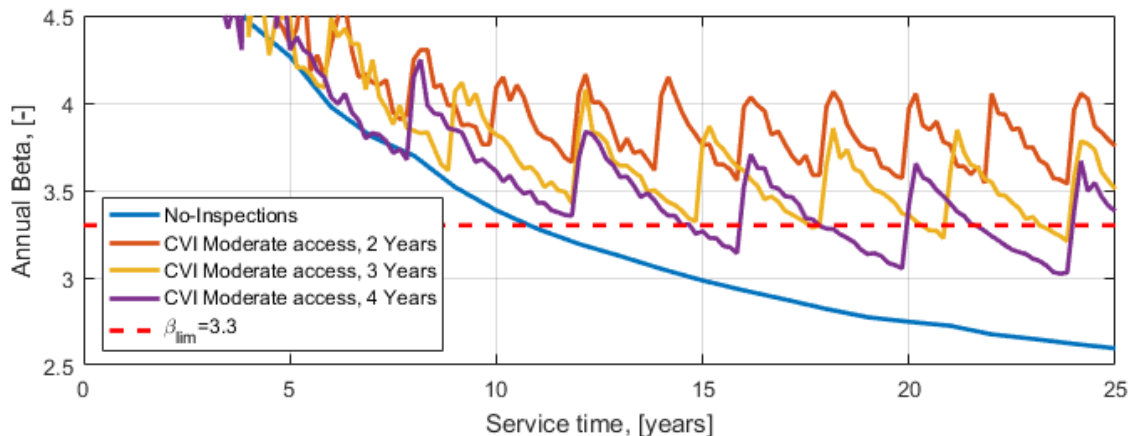

Figure 5.6.: Annual system reliability indexes using Close Visual Inspections assuming moderately easy access.
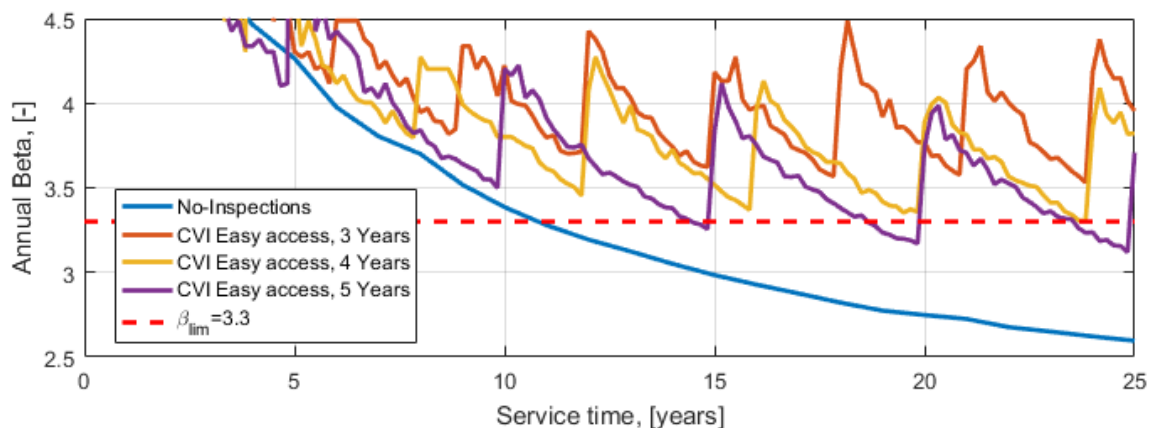

Figure 5.7.: Annual system reliability indexes using Close Visual Inspections assuming easy access.

It is visible in the Figure 5.6 that when access to the inspected nodes is considered "moderately difficult" inspections should be performed every 2.5-3 years in order to maintain acceptable reliability levels. Such inspection frequency would imply large expenses, therefore ROVs could be used instead of divers. Furthermore, as mentioned in [12], it is possible to use high resolution images made by ROVs to inspect the jacket joints/elements. Such high resolution images can be regarded as Close Visual inspections of highest quality, and POD curve with $X_0=15.78$mm average detectable crack can be utilized. Figure 5.7 shows the case of CVI with $X_0=15.78$mm and it is clear that by increasing the inspection quality (moving from $X_0=37.15$mm to $X_0=15.78$mm average detectable crack depth) the inspection intervals could be increased to 4 years. Further increase in inspection quality can be obtained using non-visual techniques, such as e.g. Eddy current inspections.
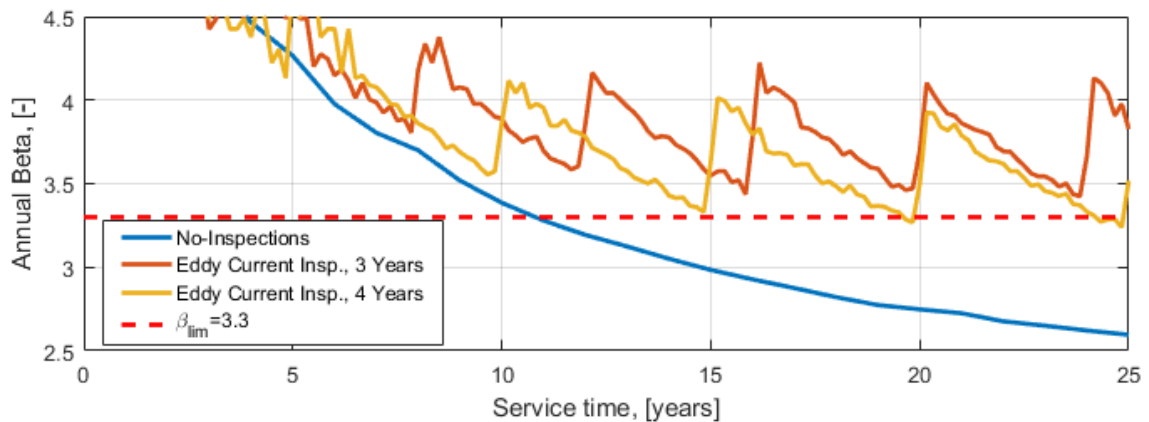
Figure 5.8.: Annual system reliability indexes using Eddy Current Inspections.

As it is seen from the Figure 5.8 above, using Eddy current inspections implies inspection intervals in the vicinity of 4 years – almost the same as was for the case for Close Visual inspections of high quality. However, it should be noted that Eddy Current inspections focus on detecting crack depths, rather than on crack lengths (Visual inspections). Since typical failure mode for welded steel details is formation of "through thickness cracks", use of "crack depth" detection techniques, such as Eddy current or Ultrasonic inspections, should be preferred as they allow for more direct detection and monitoring of the failure process.
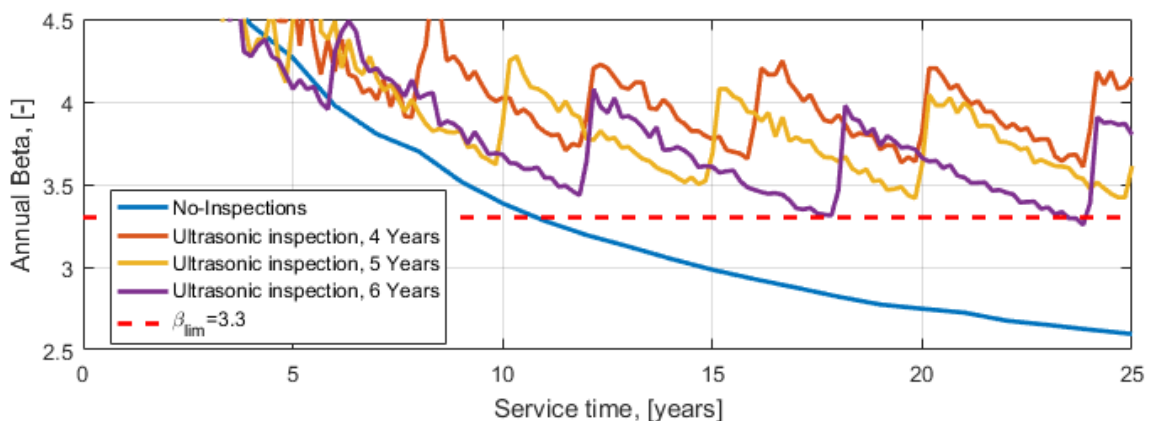

Figure 5.9.: Annual system reliability indexes using Ultrasonic Inspections.

Using an even more reliable crack detection method – Ultrasonic testing it is possible to increase the inspection intervals every further, to ~6 years. Also, it should be noted that [3] provides conservative estimates for POD (Probability of Detection) curve parameters and these parameters are also dependent on qualification of the inspection experts and their quality of work. It could be argued that by increasing the quality of crack detection techniques and inspection personnel competences, it would be possible to further increase the inspection intervals.

The following Figure 5.10 and Table 4 summarize the results of inspection planning for 20MW reference wind turbine jacket substructure (based on system reliability, using double the amount of Monte Carlo simulations than previous figures to achieve smoother reliability curves). It is noted that these results are based on a number of assumptions, especially the received information on stress range spectra. However, if new information

(Innwind.EU, Deliverable 1.25b, Reliability Level Estimation of a 20MW Jacket Structure)

on stress range spectra and the equivalent damage stress range become available the inspection planning can easily be updated.
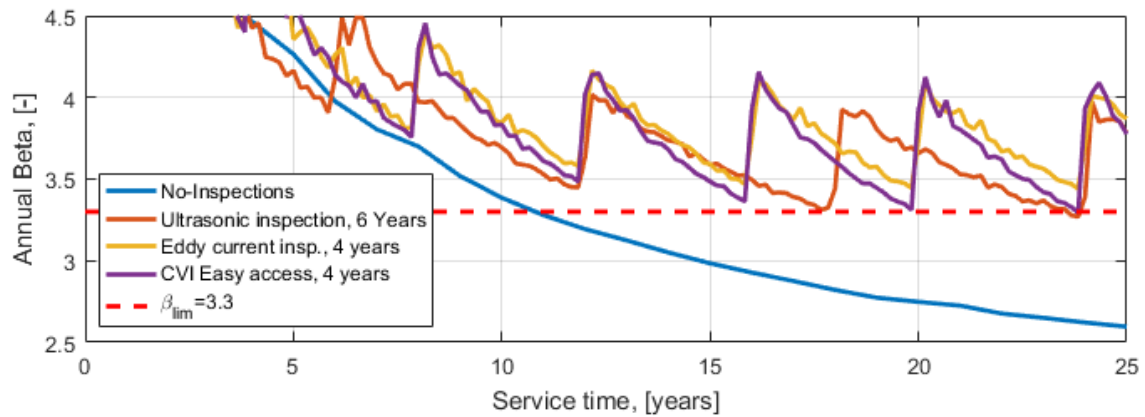

Figure 5.10.: Optimal inspection intervals for 20MW jacket substructure (system) using different inspection techniques.

Table 4: Suggested inspection strategies for jacket substructure system.

Inspection type	Suggested Inspection interval	x_0 ,mm	Comments
Eddy Current	~4 years	1.16	Below water and moderate working conditions above water.
Ultrasonic	~6 years	0.41	-
Visual inspection	~4 years	15.78	Cleaning and use of High resolution images by ROVs.
	~2.5-3 years	37.15	Manual inspections and cleaning by divers.

6. REFERENCES

[1] ISO 19902, "Petroleum and natural gas industries - Fixed steel offshore structures.," ISO, 2007.

[2] DNV, "Design of offshore wind turbine structures, OS-J101.," Det Norske Veritas, 2011.

[3] DNV GL, "RP-C 210. Probabilistic methods for planning of inspection for fatigue cracks in offshore Structures.," 2015.

[4] DNV, "Fatigue design of offshore structures, RP-C203.," DNV, 2010.

[5] J. Sørensen and H. Toft, "Safety Factors – IEC 61400-1 ed. 4 - background document.-0066 (EN).," DTU Wind Energy-E-Report, Copenhagen, 2014.

[6] JCSS , "Probabilistic Model Code - PART 3.12 Fatigue properties for metallic structures. Draft .," Joint Commitee for Structural Safety, 2012.

[7] BS 7910, "Guide to methods for assessing the acceptability of flaws in metallic structures.," British Standards Institution, London, 2013.

[8] D. BOWNESS and L. M.M.K., "Fracture mechanics assessment of fatigue cracks in offshore tubular structures. HSE Offshore Technology Report 2000/077 for HSE, EPSRC, and Chevron Oil.," The Stationery Office, London, 2002.

[9] S. Pontow, D. Kaufer, R. Shirzahdeh and M. Kuhn, "Deliverable D4.36 - Design Solutions for a Support Structure Concept for future 20MW," INNWIND.EU, Copnehagen, 2017.

(Innwind.EU, Deliverable 1.25b, Reliability Level Estimation of a 20MW Jacket Structure)

[10] D. Kaufer, "INNWIND.EU reference jacket 20MW," Ramboll, Hamburg, 2017.

[11] DNV RP-C203, "Fatigue design of Ofshore steel structures," Det Norske Veritas, 2014.

[12] DNV-GL, "Recomended Practice RP-0001. Probabilistic methods for planning of inspection for fatigue cracks in offshore structures," Det Norske Veritas - GL, 2015.

[13] *Lobitz DW, Veers PS, Eisler GR, Laino DJ, Migliore PG, Bir G. The Use of Twist-Coupled Blades to Enhance the Performance of Horizontal Axis Wind Turbines. Sandia Report SAND 2001-1303, Sandia National Laboratories, Albuquerque, NM, May 2001..*

[14] *Lobitz D, Veers PS, Laino D. Performance of twist-coupled blades on variable speed rotors. AIAA 2000-0062, 2000 ASME Wind Energy Symposium, Reno, January 10–13, 2000..*

[15] *Bottasso C.L., Campagnolo F., Croce A., "Multi-Disciplinary Constrained Optimization of Wind Turbines", Multibody System Dynamics, Vol. 27, N. 1, p. 21-53, 2012, ISSN: 1384-5640, doi: 10.1007/s11044-011-9271-x (2012)..*

[16] *Bottasso CL, Croce A. Cp-Lambda: User's Manual. Dipartimento di Ingegneria Aerospaziale, Politecnico di Milano, 2006–2011..*

[17] *A.Croce, Deliverable D2_22_PoliMI_16July2015.txt.*

[18] *Bottasso C.L., Campagnolo F., Croce A., Tibaldi C., "Optimization-based study of bend–twist coupled rotor blades for passive and integrated passive/active load alleviation", Wind Energy, Vol. 16, N.8, p1149-1166, 2013. DOI: 10.1002/we.1543 (2013)..*

[19] *Zahle, F., Tibaldi, C., Verelst, D. R., Bak, C., Bitche, R., and Blasques, J. P. A. A., Aero-Elastic Optimization of a 10MW Wind Turbine, Proceedings of the 33rd Wind Energy Symposium, Kissimmee, Florida, U.S.A., 2015.*

[20] *P.K. Chaviaropoulos, J. Beurskens and S.Voutsinas," Moving towards Large(r) Rotors – Is that a good idea?", Proc. EWEA 2013 Conference, Vienna, 2013.*

[21] *P.K. Chaviaropoulos and G. Sieros, "Design of Low Induction Rotors for use in large offshore wind farms", Proc. Scientific Track, EWEA 2014, Barcelona, 2014.*

[22] *P.K. Chaviaropoulos, G.Sieros, J.M. Prospathopoulos, K. Diakakis and S.G. Voutsinas, "Design and CFD-based Performance Verification of a Family of Low-Lift Airfoils", Proc. EWEA 2015, Paris, 2015.*

[23] *INNWIND.EU Deliverable 2.14.*

[24] P. Bortolotti, C. L. Bottasso and A. Croce, "Combined preliminary-detailed design of wind turbines," *Wind Energy Science,* vol. 1, pp. 71-88, 2016.

[25] *INNWIND.EU Deliverable 1.25b.*

[26] *INNWIND.EU Deliverable 1.25a, 20MW Reference Wind Turbine, Aeroelastic Data of the Onshore Version.*

[27] *INNWIND.EU Deliverable 2.12, New Airfoils for High Rotational Speed Wind Turbines, 2015.*

[28] *INNWIND.EU Deliverable 1.22.*

[29] *INNWIND.EU Deliverable 1.24.*

[30] *INNWIND.EU Deliverable 1.23.*

[31] *IEC 61400-1. Wind turbines – Part 1: Design Requirements, 2005.*

[32] *INNWIND.EU Deliverable 4.36.*

[33] "DNVGL-ST-0126, Support structures for wind turbines, 2016".

[34] "DNVGL-RP-C203, Fatigue Design of offshore steel structures, 2016".

[35] J. Serrano-González, "Technological evolution of onshore wind turbines-a market-based analysis," *Wind Energy,* 2016.

[36] W. H. Lio, "Fundamental performance similarities between individual pitch control strategies for wind turbines," *International Journal of Control,* vol. 90, no. 1, 2017.

[37] CDV IEC, "61400-1 ed.4. Wind Turbines - Part 1: Design requirements," IEC, Geneva, 2017.

(Innwind.EU, Deliverable 1.25b, Reliability Level Estimation of a 20MW Jacket Structure)

(Innwind.EU, Deliverable 1.25b, Reliability Level Estimation of a 20MW Jacket Structure)